POTENTIAL OF TERAHERTZ PULSED REFLECTOMETRY AND IMAGING FOR THE EARLY DIAGNOSIS OF CUTANEOUS MELANOMA

Martin Müller-Holtz

De Montfort University Leicester

Faculty of Health and Life Sciences / Faculty of Technology

This dissertation is submitted for the degree of Doctor of Philosophy

Sponsored by "Hope Against Cancer Foundation", Leicester

October 2019

DECLARATION

This dissertation is the result of my own work and includes nothing, which is the outcome of work done in collaboration except where specifically indicated in the text. It has not been previously submitted, in part or whole, to any university of institution for any degree, diploma, or other qualification.

Martin Müller-Holtz (BSc Computer Science, MSc Intelligent Systems)

Leicester

Potential of Terahertz Pulsed Reflectometry and Imaging for the early diagnosis of cutaneous melanoma

by
Martin Müller-Holtz

Submitted to the Faculty of Health and Life sciences & Faculty of Technology
on 28th of February 2019, in partial fulfillment of the
requirements for the degree of
Doctor of Philosophy

Abstract

In the last two decades the incidence rate of cutaneous malignant melanoma have been risen faster than any other form of cancer worldwide in the white-Caucasian population. The mortality rates over time show that an early diagnosis is the key point for quick treatment, which increase survival rates.

As a standard procedure dermatologists use a dermascope or the naked eye for evaluation of possible lesions, where experts have a higher chance of spotting infiltrated tissue than untrained persons.

Multiple investigations on diagnostic imaging for the detection of melanoma have been conducted in the past, like Ultrasound, Near-Infrared spectroscopy or Optical Coherence Tomography, with mixed, but not sufficient results to date.

In recent years terahertz radiation has shown to be a promising technology for the early detection of various types of cancers, i.e., colon (*ex-vivo*), breast (*ex-vivo*) and non-melanoma skin cancers (*ex-vivo* and *in-vivo*) as terahertz radiation is able to penetrate slightly into the bio-tissue but also deemed to be a non-ionising and therefore safe method for diagnosis of lesions *in-vivo*.

Investigations into the practicality and benefits of using terahertz reflectometry for the early diagnosis of melanoma has never been performed.

Therefore, as a pilot study, an investigation into the modalities of utilising terahertz technology on freshly excised human cutaneous melanoma is anticipated, which includes a comparison of the collected 3D terahertz images with visuals, comparison of histopathologists findings but also investigations about modelling skin and abnormalities of the skin using terahertz radiation.

Diverse and manifold results can be reported based on the study conducted, which show that there is a good potential of terahertz detecting abnormalities on a per patient basis of up to 78% sensitivity and 95% specificity respectively. However, skin is a very diverse medium and results of the modelling approach have to be seen very critically. As modality for a diagnostic tool, this investigation suggests that there is potential in detecting margins and active regions of cancerous region spreading, which may help to support the dermatologists to determine better margins for the excision of the lesion.

Acknowledgments

This research was taken out at De Montfort University Leicester, Faculty of Health and Life Sciences in cooperation with the Department of Dermatology at the Leicester Royal Infirmary (LRI) whereas I would like to thank everyone at the LRI involved in the project, especially Dr. J.D. Mckenna and Dr. Sara Arool for helping in tissue collection and patient recruitment. Furthermore, I would like to thank Mark Bamford and Phil Da Forno from the Histology Department at the LRI for providing valuable information and discussions.

Additionally I would like to thank my supervisors Professor Dr. Geoff Smith, Dr. Huseyin Seker and Dr. David Armitage for providing support and giving stimulus input to the project, not to mention the vital discussion we had during the project.

Moreover I would like to thank the Hope Against Cancer Foundation (HFCR) Charity, Leicester for providing me the possibility to work on a project that has found my deep interest and motivation for this manuscript. I am also grateful for the amount of people at the University who supported this research but also my fellow friends who supported me outside my research. And finally I would like to thank my family for their support.

Contents

List of Figures

List of Tables

List of Abbreviations

ANN	Artificial Neural Network
AUC	Area under the Curve
BCC	Basal Cell Carcinoma
BSFS	Backward Sequential Feature Selection
DT	Decision Tree
EVR	Extra-Visual Region
FFT	Fast Fourier Transform
FSFS	Forward Sequential Feature Selection
HFUS	High-Frequency Ultrasound
IVR	Inter-Visual Region
KNN	K-Nearest Neighbour
LDA	Linear Discriminant Analysis
LMM	Lentigo malignant melanoma
NIR	Near Infrared
NMM	Nodular malignant melanoma

PC-A . . . . . Photoconductive Antenna

PCA . . . . . Principle Component Analysis

PDT . . . . . Photodynamic Therapy

QDA . . . . . Quadratic Discriminant Analysis

RGP . . . . . Radial Growth Phase

RMSE . . . . . Root Mean Square Error

ROC . . . . . Receiver Operator Chart

SCC . . . . . Squamous Cell Carcinoma

SFS . . . . . Sequential Feature Selection

Si . . . . . Silica

SiO^2 . . . . . Silica-Quartz

SNR . . . . . Signal-to-Noise Ratio

SSMM . . . . . Superficial spreading malignant melanoma

TBP . . . . . Total Body Photography

TDS . . . . . Time Domain Spectroscopy

THz . . . . . Terahertz

TIL . . . . . Tumour Infiltrating Lymphocytes

TPI . . . . . Terahertz Pulsed Imaging

TPR . . . . . Terahertz pulsed reflectometry

. . . . . .

UV . . . . . Ultraviolet

VGP . . . . . Vertical Growth Phase

VPUF . . . . . Verdi-Pumped-Ultra-Fast

Chapter 1

Introduction

Incidence rates of melanoma, a cutaneous malignancy with the highest mortality rate of all skin cancers, have risen faster than they have for any other form of cancer in the last decade — especially in caucasian populations [1–7]—with an increase of 4.1% per annum [7].Diagnosis at an early stage increases the chance of successful treatment of the lesion. The treatment outcome will depend on the penetration depth of the carcinogenic lesion, as the risk of metastatic spread increases with an increase in the malignant tumour thickness. Patients whose melanoma thickness is less than 1 mm have a 94% survival rate over five years, whereas a 3 mm tumour reduces the chance of survival to 50% over five years [5].

Multiple staging/scoring systems to support visual examination are used to predict, diagnose, identify or stage cutaneous melanoma. Common techniques for clinical diagnoses of visible lesions include the ABCD rule (asynchronousness, border, colour, and diameter) and the seven-point checklist [8]. These systems are used to simplify the process whereby either an expert dermatologist or an untrained individual identifies melanoma.

In addition to these scoring methods and visual-examination techniques, technical imaging systems may improve the chance of identifying melanoma. Whilst

dermoscopy is the most common technique and the current gold-standard used over the last decade for the identification of malignant melanoma, technical imaging systems — such as total-body photography (TBP) [9], multispectral imaging, confocal microscopy, optical coherence tomography and near-infrared imaging [10] — have been investigated to support the diagnosis of cutaneous carcinoma.

These techniques, however, have not yet progressed into clinical practice; thus, there remains a clinical need for additional tools to enhance clinician decision making and improve the early recognition of melanoma, both to improve patient outcomes and to minimise the number of unnecessary, invasive and uncomfortable surgical procedures.

Terahertz-pulsed imaging (TPI) and spectroscopy (THz-TDS) are relatively new technical instruments currently under investigation for biological tissue and security applications [11], industrial observations (surface texture), astronomy, signal transmission [12], and analysis of pharmaceutical materials [13]. Terahertz-frequency electromagnetic radiation has a wavelength between 3 mm and 30 µm (equivalent to frequencies between 100 GHz to 10 THz). Materials have different absorption properties in the THz Region; for example, metal, because of its very high refractive index, is a full reflector and water is one of the strongest absorbers due to rotational transitions and intermolecular vibrations [14, 15]. Terahertz beams are also non-invasive because of their low energy output (4.4 meV at 1 THz) [16]. In pharmaceutical applications, the composition of tablets and coating analysis [17] are of interest, as they allow the non-destructive examination of tablets through packaging, for example.

The fact that water is one of the strongest absorbers in the terahertz regime led to investigations aimed at distinguishing between different kinds of biological tissues. Successful attempts to discriminate between cancerous and healthy tissues have been undertaken with non-melanoma skin cancer (basal-cell carcinoma

(BCC) and squamous-cell carcinoma (SCC)), breast cancer, cervical cancer and colon cancer [18]. Apart from cancerous tissue, other types of human soft tissue — such as skin, fat, bones, eyes, and teeth [16, 19–22] — have also been subjects of interest in recent years. These investigations provide evidence that terahertz radiation might also be able to distinguish between moles and melanoma. The differentiation of soft-body tissue can be attributed to the different complex refractive indices of the tissues under investigation, which may be compared to either the refractive index of air (n=1) or to that of water [16, 23, 24]. It has been suggested that the differences arise mostly from the different water concentrations of the tissue, which are caused by conformational changes in protein structures [25] and thus by a measurable difference of the water absorption of the tissue. However, Woodward et al. (2003) state that they were able to distinguish between dried-out healthy skin and dried-out BCC as well [26], which leads to the suggestion that different inter-molecular vibrations and rotations of proteins may be detectable in the terahertz regime [27–29]. These differences may be caused by the hydration water being influenced by two or more protein molecules which have different dynamical behaviours from that which they exhibit around single proteins [25, 30].

1.1 Outline of this report

This thesis is the result of a pilot study of the determinations of freshly excised cutaneous human melanoma scanned with terahertz reflectometry. To the author's best knowledge, this is the first time 3D images of *ex-vivo* human cutaneous melanoma have been gathered and compared to histology findings. Furthermore, a novel predictive modelling technique is evaluated here which is used to predict melanoma in the terahertz regime and to compare the results to visual images.

The overall aim of this study is to determine if and to what extent terahertz analysis could help dermatologists and individuals make decisions regarding the diagnosis of cutaneous melanoma.

1.2 Thesis structure

Chapter 2 provides an overview of the modalities of skin and skin-cancer types. Furthermore, current clinical-practise standards (GOLD standard) and staging systems applied to visual examination or images are described in detail and are compared regarding their specificity and sensitivity to melanoma diagnosis.

Chapter 3 introduces and compares current non-invasive imaging techniques applied to skin cancer and gives a detailed description of terahertz-systems techniques which are currently used for bio-medical applications. This is followed by a state-of-the-art literature review of bio-medical applications with a focus on cancer and skin cancer in the terahertz regime.

Preliminary investigation of terahertz modalities for bio-medical applications is discussed in Chapter 4. The first half of the Chapter deals with the general setup, pre-processing and image registration that have been used throughout the thesis. The second half covers miscellaneous experiments that have been evaluated before sample gathering, including wavelet de-noising and defining the time window for safely processing and handling patients' melanoma samples.

Chapter 5 evaluates a descriptive analysis of the samples covered. Visual and terahertz images are compared descriptively and discussed together with results from histopathology, which offers an indication of the underlying morphological features seen on histopathologists' slides compared to terahertz images.

Chapter 6 evaluates the features and feature-reduction techniques gathered from 3D terahertz data. Using the raw (denoised) waveforms, principle com-

ponent analysis (PCA) as input for various predictive-modelling techniques in comparison to the visual images shows similarities which indicate the applicability of THz technique for melanoma diagnosis. Results are investigated by the ReliefF algorithm to show which parts of the input variables are accountable for the results.

Chapter 7 deals with the physical principle used to describe human skin *ex-vivo* in the terahertz regime by converting the time-domain data into the frequency dependent, complex refractive index. Malignant samples are compared with healthy moles and described in terms of their refractive indices. The Chapter concludes by offering recommendations for further investigations into melanoma using terahertz devices.

The final Chapter, Chapter 8, concludes the thesis and offers a comprehensive outlook for further research.

Chapter 2

Modalities of human skin

In recent years, the incidence rate of cutaneous malignant melanoma has risen faster than that of any other form of cancer worldwide [3]. While the probability of developing any kind of cancer rises proportionally with age, malignant melanoma has increased rapidly in the of 20-30 years old age group. It has risen four-fold in caucasian men and eight-fold in caucasian women [31]. Recent studies in Croatia [2], Netherlands [1], the U.S. [4] and the U.K. [6] show a rapidly increasing incidence rate of melanoma over the last 50 to 60 years.

If diagnosed and treated early, the chances of survival are excellent but decrease gradually over time, as tumour growth progresses through deeper layers of the skin, eventually reaching the lymph system or blood vessels [32].

The following part provides a comprehensive overview of the topic of this investigation. It begins with an overview of the structure of human skin and then focuses on the three most common types of skin cancer: namely, basal-cell carcinoma, squamous-cell carcinoma and malignant melanoma (MM). This is followed by a discussion of the current screening modalities for diagnosing, staging and scoring suspicious cutaneous melanoma based on visual examination by experts or untrained individuals. The pattern-analysis algorithms used on

visuals are evaluated with respect to their sensitivity and specificity, which are discussed briefly.

2.1 Structure of human skin

The skin is the largest organ of the body. Depending on the literature, the skin is mainly divided into three layers: the epidermis, the dermis and the subcutis. The epidermis, the outer part of the skin, ranges in thickness from 0.05 mm at the eyelid up to 1.5 mm at the sole of the foot. Thickness depends on the location on the body. The epidermis is sub-divided into five regions, from the outer to the inner: stratum corneum (horny layer), stratum lucidum (only on soles and palms), stratum granulosum (granular layer), stratum spinosum (spinal or prickle cell layer) and the stratum basale (basal layer or stratum germinativum) [33]. The epidermis is followed by the dermis, the thickest part of skin, which consists of two layers: the papillary layer and the reticular layer. The subcutis (hypodermis) is found under and attached to the dermis and consists mainly of adipose tissue. Depending on the literature, the subcutis is not always considered part of the skin (cmp. [34, 35]). It functions as the anchor between the skin and the rest of the body. Figure 2-1 gives an overview of the layers of the skin.

2.1.1 The epidermis

The epidermis comprises up to five layers depending on the body region being considered. It reaches a thickness of 0.05 mm on the eyelids up to 1.5 mm on the palms and soles [36]. The epidermis consistently develops basal cells from the stratum basale towards the outer layers of the epidermis by invoking apoptosis and granulation. As the dead cells move towards the stratum corneum, they form a natural barrier against xerosis (drying out). They also form a protective, water-

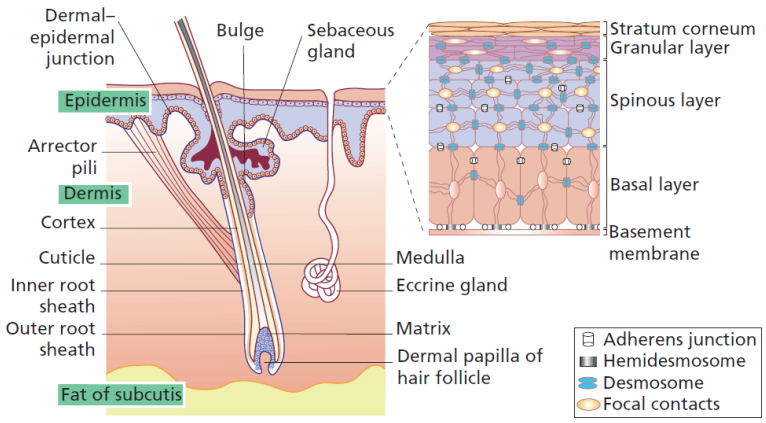

Figure 2-1: Overview of the composition of human skin (source [33])

repellent barrier. The five layers, in descending order from outer to inner are as follows:

- **stratum corneum (cornified layer)**

  The stratum corneum is the most outer layer of the epidermis and consists of 25 to 30 layers of flattened, dead keratinocytes. It is also known as the keratinised squameous layer. Dead keratinocytes are continuously shed and replaced by cells from the deeper layers—a process based on apoptosis, which describes the wanted, programmed process of cell death [37]. The stratum corneum consists mainly of keratin and lipid secretions from lamellar granules, which create an effective water-repellent barrier and protect the deeper layers from injury and microbial invasion [35].

- **stratum lucidum (clear/translucent layer)**

  The translucent layer is made out of three to five layers of flattened, dead keratinocytes and exists only in areas of the skin that are prone to friction, like the palms and the heel, where the skin is relatively thick compared to other regions of the body [36].

- **stratum granulosum (granular layer)**

The stratum granulosum forms the third, middle layer of the epidermis. Like the stratum lucidum, it consists of three to five layers of flattened keratinocytes. Lipids are released by membrane-enclosed lamellar granules which are present in the keratinocytes. This liquid fills the space between cells of the stratum corneum, the stratum granulosum and the stratum lucidum, and it acts as a water-repellent sealant that retards the loss of body fluids and denies entry to foreign materials [38]. In this layer, the keratinocytes appear flattened (squamous), as they lose their nuclei, and the cytoplasm appears in a granular form.

- **stratum spinosum (spinous layer)**

  The stratum spinosum—also referred to as the spinous or prickly layer [36] because the desmosomes, which act as intercellular bridges, appear microscopically as prickles—consists of eight to ten layers of keratinocytes [35]. As the basale cells begin to clone and replicate, they progress towards the upper layers of the epidermis and form the spinous layer. Furthermore, most Langerhans cells are found in this layer. These are immunologically active cells, also known as antigen-presenting cells, which cause immune reactions of the skin. Langerhans cells appear in all layers of the epidermis, but they are mostly found in the stratum spinosum [39].

- **stratum basale (basal/germinal layer, germinativum)**

  The stratum basale is the innermost layer of the epidermis and is attached to the dermis. At the interface between the epidermis and the dermis, the basement membrane consists mainly of dividing and non-dividing kertinocytes attached by hemidesmosomes.

  When keratinocytes divide and differentiate, they initially begin to move from the basal membrane towards the outer layers of the epidermis until

they reach the surface of the skin.

Melanocytes, which produce the pigment melanin, comprise a small proportion of the basal cell population. Characteristic features of melanocytes are dendritic processes, which stretch between relatively large numbers of neighbouring keratinocytes. Melanin accumulates in melanosomes that are transferred to the adjacent keratinocytes, where they remain as granules.

The pigmentation of the melanin inside the basal cells protects the body against ultraviolet radiation. The ratio of keratinocytes and melanocytes increases with the amount of exposure to light. Therefore, more melanin is typically found in the facial skin or outer arm than in the lower back or inner arms. The number of melanocytes is the same in equivalent body sites in white and black human skin, but the distribution and rate of production of melanin differ. Intrinsic ageing diminishes the melanocyte population.

Merkel cells are also found in the basal layer, with large numbers in touch-sensitive sites such as the fingertips and lips. They are closely associated with cutaneous nerves and are involved in light touch sensation [39].

2.1.2 The dermis

The dermis varies in thickness, ranging from 0.6 mm on the eyelids to 3 mm on the back, palms and soles. The dermis is directly attached to the epidermis and is comprised of a tough, supportive cell matrix. Two layers comprise the dermis: a thin papillary layer and a thicker reticular layer.

The papillary dermis lies below and connects with the epidermis. It contains thin, loosely arranged collagen fibres. Thicker bundles of collagen run parallel to the skin surface in the deeper reticular layer, which extends from the base of the papillary layer to the subcutaneous tissue. The dermis is made up of fibroblasts,

which produce collagen, elastin and structural proteoglycans together with immunocompetent mast cells and macrophages. Collagen fibres make up to 70% of the dermis, giving it strength and toughness. Elastin maintains normal elasticity and flexibility while proteoglycans provide viscosity and hydration. Embedded within the fibrous tissue of the dermis are the dermal vasculature, lymphatics, nervous cells and fibres, sweat glands, hair roots and small quantities of striated muscle [40].

2.1.3 The subcuties

The subcutaneous tissue (subcutis or hypodermis) consists of connectivity tissue and adipose tissue. It connects the dermis with the underlying periosteum and fascia and acts as a shifting layer. The adipose tissue mainly serves the purpose of thermal insulation, but it also functions as an energy accumulator and can grow up to a couple of centimetres [41]. It also features large blood-vessels and nerves.

2.2 Cutaneous malignancies

In general, cancer can be defined as a disease in which a group of abnormal cells grow uncontrollably by disregarding anti-grow signals from tumour-suppressor genes. Normal cells are constantly subjected to chemical-signal interactions that trigger cell division, apoptosis or differentiation into other cell types. Cancerous cells, on the other hand, develop autonomy from these signals, which results in uncontrolled growth and mutation by ignoring apoptosis but produce oncogenes (a constant growth, cell-division stage) [42] further to angiogenesis, a process of growing blood vessels around the malignancy to maintain nutrition.

The most common form of skin cancer is BCC [43], which is followed by SCC and MM. However, rare forms of non-melanoma skin-cancer types like Merkel-cell

or Langerhans-cell carcinoma also exist. The following section provides a brief overview of the three most common skin-cancer types in Caucasian population.

2.2.1 Basal-cell carcinoma

Basal-cell carcinoma is the most common malignancy in the Caucasian population [44], though it is also the one with the lowest mortality, as BCC rarely spreads [43]. BCC originates from the stratum basale, where the highest rate of cell division takes place. A recent study conducted and published in 2016 by Sánchez-Danés et al. suggests that the origin of BCC lies in the clonal dynamics of epidemical stem cells, which cause mutation and therefore abnormal cell growth [45]. Since BCC affects the basal cells, which are subject to apoptosis and are pushed towards the outer layers of the epidermis, the mortality rates for BCC are considerably lower than for other cutaneous cancers. BCC rarely reaches the lymph nodes or the blood-vessel stream; thus, the creation of metastasis is limited.

BCC patients often present with a non-healing sore of varying duration. The lesions are typically seen on the face, ears, scalp, neck or upper trunk, as BCC originates mainly in regions with high Sun (or other ultraviolet-radiation) exposure. A history of chronic recreational or occupational Sun exposure is commonly cited. Intense Sun exposure in childhood or young adulthood dramatically increases the probability of creating BCC [46]. The most common therapy is surgical excision. Since BCC rarely creates metastasis, it is usually not investigated by histopathologists and does not have to be reported to the NHS.

2.2.2 Squamous-cell carcinoma

The second most common skin malignancy is squamous-cell carcinoma, which accounts for approximately 20% of all non-melanoma skin cancers. It is typically found in persons aged 50 and above. Though the spread of metastasis is more

likely with SCC than with BCC, SCC is often diagnosed early due to its distinct features—especially ulceration and the appearance of "bumps", often with red patches. An early type of *in-situ* SCC is called Bowens disease. As with all skin cancers, SCC usually occurs in parts of the skin exposed to sunlight, but it appears twice as often in men and in regions around the head, face, neck and arms [47]. SCCs are found in the squamous cells, which form in the epidermis, as they are flattened keratinocytes, which follow the apoptosis. Due to the uncontrolled growth phase of SCC, the risk of reaching the lymph system to form metastasis in considerably higher than it is from BCC.

The general treatment of SCC is excision via a process called Moh's surgery [48], which describes the excision of the lesion layer by layer. Each excision sample is directly analysed by histopathologists using a microscope. This process is repeated until the lesion does not show any form of cancerous features in the cells [48].

Non-surgical treatments of SCC include "topical chemotherapy, topical immune response modifiers, photodynamic therapy (PDT), radiotherapy, and systemic chemotherapy" [33]; however, most of these treatments are either applied at the location of a premalignant state of *in-situ* lesions or where metastatic spread has occurred.

2.2.3 Melanoma

This and the upcoming sections describe the physical abnormalities of melanoma, progression and diagnosis, staging. A histopathology description is also offered for cutaneous malignant lesions of the skin. Genetic factors, molecular aspects and cell infiltration and prevention, therapies and risk factors—these topics lie beyond the scope of this thesis. A good overview of these topics is given by Whiteman (2011) [49]. This section focusses on the three most common types of cutaneous

melanoma among Caucasians: namely, superficial spreading melanoma (SSM), nodular melanoma (NM) and lentigo melanoma (LM). Other forms of melanoma include mucosal melanoma, which can be found (amongst other places) in the oral cavity, the eye, the inner organs, the brain and the central-nervous-system [50]; acral lentiginous melanoma, which accounts for 90% of melanoma in the black African population [51] and desmoplastic melanoma. These forms are mentioned for completeness but will not be discussed in detail.

Cutaneous melanoma has its origin in the melanocytes which lie between the dermis and the epidermis, close to the basement membrane. The out-of-control growth phase of melanocytes that may start the development of nevi and ulceration is called melanomagenesis.

Due to stimulation from ultraviolet (UV) radiation, melanin is continuously transferred from the melanocytes into the keratinocytes, causing a constant, extensive interaction between the keratinocytes and the adjacent melanocytes. The stimulation due to UV radiation can cause DNA alterations and thus create abnormalities in genetic pathways within the melanocyte [51]. Growth factors such as stem-cell factor, fibroblast growth factor and transforming growth factor are produced by the action of solar radiation on melanocytes and surrounding keratinocytes and fibroblasts [51].

From a histopathology view, malign invasion begins with the proliferation of melanocytes, a benign nevi, which is colloquially described as a freckle or mole (Step 1). The benign nevi presents a clear delimitation or demarcation and shows uniform pigmentation. The second step is the forming of a dysplastic nevi, which is a development of aberrant growth and originates either from existing moles or from a new location. Dysplastic nevi exhibit asymmetry and irregular borders and are usually still benign.

The radial growth phase (RGP) is the third stage. It is a phase of abnormal

horizontal growth of the lesion, but it does not penetrate into the dermal-epidermal junction [52]. Extensive growth of the RGP usually leads to the most common sub-type of melanoma: the SSM. Because the tumour cells do not grow into the dermis but rather stay at the basal membrane, it is unlikely that the malignancy will spread, as it has not yet reached the blood vessels or the lymph system. Histologically, the lesion now presents cytomorphological cancer. The Breslow thickness of this stage is typically less than 0.75 mm (Breslow Level I). At Breslow Level I, the infiltrated region can usually be completely removed by excision.

At the end of the RGP, the mutated melanocyitcism is replaced by a clonal change, which begins with a growth from RGP to the vertical growth phase (VGP), which offers a survival advance of the malignancy [53]. During the VGP, the tumour grows into the dermal-epidermal junction, reaching the papillary layer of the dermis and eventually the reticular layer, which often leads to nodules [53]. The tumour thickness is usually more than 1 mm and attains invasive potential. It can infiltrate the surrounding tissue and may form metastasis once the lymph-system or the blood-vessels are reached.

During the VGP, the body may elicit an "immunological reaction against the tumour which is judged by the presence and activity of the tumour infiltrating lymphocytes (TILs)" [54]. At the stage of the TIL, the tumour may spread and form metastasis, and immuno-reactions may appear which may destroy the primary tumour. This process is known as regression. It forms the last stage of melanoma development, in which the primary lesion is completely destroyed but only metastatic secondary lesions may be discovered. If the tumour penetrates into and beyond the subcuties, it may reach the underlying fascia or the periosteum. Histologically, this is the final, fifth step of the process. Figure 2-2 shows the differences and the depth of the RDP and the VGP.

If the RGP dominates over time (five to seven years), it is described as a

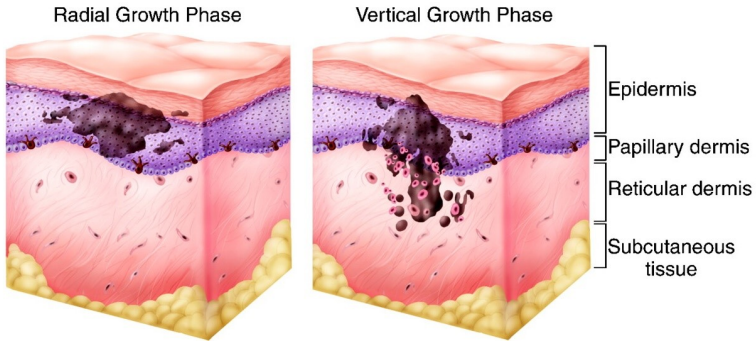

Figure 2-2: Radial and vertical growth phases of superficial spreading MM (altered, from [55])

subtype of melanoma called SSM, which is the most common type of melanoma and accounts for around 70% of all melanomas [33]. In SSM, the lesion appears as a freckle with brown / light-brown colouring and with asymmetric features and irregular edges.

Nodular melanoma (NM), which accounts for approximately 20% of all melanoma, has a relatively short RGP which is replaced by a rapid VGP and is presented with "sharply demarcated borders on the skin, often shiny with a slightly infiltrated base. The colour, generally darker and more uniform than that of SSM, may vary from black to unpigmented" [56].

The third most common form of MM is LM, which develops from lentigo malignant lesions (melanosis praecancerosa of Dubreuilh or Hutchinson's melanotic freckle) [56]. LM appears mainly in middle-aged persons from the fifth decade onwards but reaches its highest occurrence during the eighth and ninth decades. LM is primarily located at the face, neck and forearms due to Sun and UV exposure [57]. It emerges as a tan macule with irregular edges. As the tumour progresses, the colour typically changes to a darker, brown-black tone. The first horizontal phase, which is not-invasive, may have an active growth phase of up to 20 years. When the clonal phase change appears, VGP may develop, clinically presenting the LM as a pigmented nodule [56].

Having discussed the three most common types of melanoma and their typical pathways, a brief description of staging and tumour progression of MM is given next. This is followed by a discussion of current pattern-analysis techniques that may be applied to MM.

2.3 Tumour progression (pathophysiology) and staging systems for cutaneous melanoma

A biopsy of suspicious lesions is the gold standard for the diagnosis and therapy of malicious behaviour of the skin. After surgery, the sample is cut into slices of approximately four micrometres and studied by histopathologists via a microscope. The histopathologists determine tumour type and tumour depth by considering the morphological features of the lesion. If the lesion is to be malign, the thickness is measured and evaluated according to the Breslow Depth or TNM staging system. If metastasis or depth into the papillary layer of the dermis is measurable, further actions such as lymph-node biopsy are required.

The two phases of the melanoma progression, the RGP and VGP, form the basis for the classical staging systems for MM: the Clark and Breslow staging systems.

The Breslow classification system was introduced by Alexander Breslow in 1970. It divides the tumour thickness of the histopathology image into four stages (originally five stages) depending on the penetration depth into the skin [58]. The measurement is taken from the stratum granulosum of the epidermis until the deepest layer of invasion where the tumour is still visible. Consider Table 2.1: Breslow stages with tumour depth and five year survival rate [59]. In contrast to Clark's-Level (see below) the Breslow depth does not take different dermal and epidermal layers into account. While the Breslow depth is still one of the

Table 2.1: Breslow stages with tumour depth and five year survival rate [59]

Breslow stage	**Tumour depth**	**Approx. 5 year survival rate**
I	<1 mm	95-100%
II	1 – 2 mm	80-94%
III	2.1 – 4 mm	60-80%
IV	>4 mm	<60%

Table 2.2: Description of Clark's-Levels [61]

Clark's Level	**Depth description**
I	Melanoma confined of the epidermis (*in-situ*)
II	Invasion into the papillary layer of dermis
III	Invasion to the junction of the papillary and reticular layer of the dermis
IV	Invasion into subcutaneous fat

most used diagnostic and prognostic systems, it has been incorporated into and replaced by the AJCC TNM staging system discussed below. The Breslow depth also gives an accurate prognosis of survival and is classified into the following stages summarised in Table 2.1.

The Clark's-Level scheme is in many ways similar to the Breslow depth; however, instead of giving a tumour depth in mm, Clark recognizes five stages depending on how deeply the infiltrated area has passed (epi-)dermial layers [60].

The Clark's-Level and Breslow staging systems have been integrated and replaced by a staging system from the American Joint Committee on Cancer (AJCC), which divides stages depending on the TNM factor. TNM stands for primary tumour (T), regional lymph nodes (N) and distant metastasis (M). The TNM staging consists of four stages with divisions amongst them (A-C). It gives prognostic five-year survival rates and is based on a multivariate analysis of around 38,000 cases of melanoma [62]. See Table 2.3: TNM tumour depth staging (excerpt, altered [62]). Specifically for melanoma, each factor (T,N,M) is divided into sublevels (from 1 to

Table 2.3: TNM tumour depth staging (excerpt, altered [62])

T-Stage	Tumour depth	Ulceration / Mitosis status
1	<1 mm	a – without ulceration and mitosis $< 1mm^2$ b – with ulceration and mitosis $> 1mm^2$
2	1 – 2 mm	a – without ulceration b – with ulceration
3	2.1 – 4 mm	a – without ulceration b – with ulceration
4	>4 mm	a – without ulceration b – with ulceration

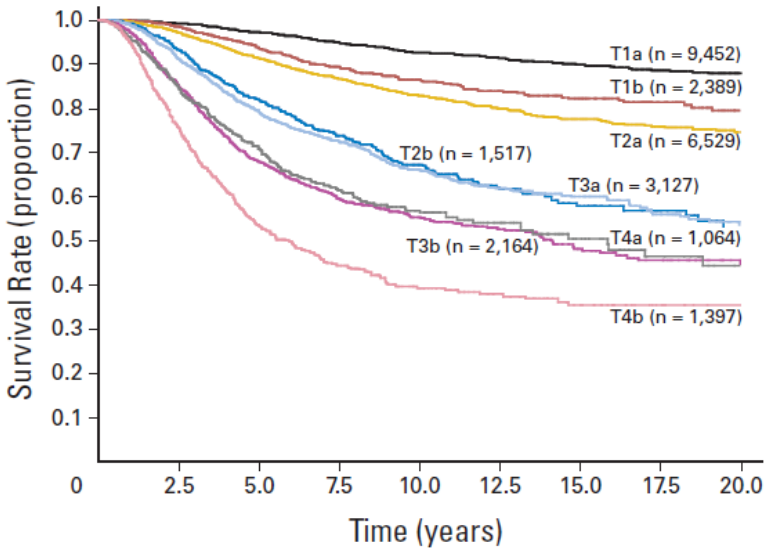

Figure 2-3: Survival rate over time depending on the tumour depth and ulceration / mitosis based on the TNM staging system (source [62])

4) to describe further states of each category, like ulceration, micrometastasis or distant metastasis. The stages of T1-4 also subdivide into a (without ulceration) and b (with ulceration). One of the most important factors for classification is still the tumour thickness, which is determined by T1-4. Ulceration / mitosis is summarised in Table 2.3.

As with Breslow depth and Clark's level, the survival rate over time strongly depends on tumour depth, as indicated in 2-3:

The final stages (I and II) are defined by the primary tumour thickness only.

They subdivide into subsections A-B for Stage I and subsections A-C for Stage II. Stage II is reached as soon as any micrometastatic behaviour within the lymph nodes become visible but divide into the stages IIIA up to IIIC, while the final Stage IV depends only on the distant metastasis. The full classification of the AJCC TNM staging for melanoma can be found in Appendix A.

2.4 Pattern analysis for the diagnosis of cutaneous lesions

When a suspicious lesion is identified as melanocytic in origin, it must be determined whether this lesion is benign, suspect or malignant. To differentiate between these three groups, various classification systems have been investigated. These systems rely on hundreds [8,63] of patients' data and/or images, and they are evaluated by expert dermatologists. The pattern-analysis systems have been developed from various analyses of histopathology results and expert knowledge and help to identify lesions using only a small amount of pattern description. Pattern analysis exists to support untrained or trained persons in decision making and to provide a structured mode of justification and a standardisation. Pattern recognition has historically been used by clinicians and histopathologists to differentiate benign lesions from malignant neoplasms [64].

The main classification systems for melanoma are based on pattern analysis. Six different approaches are most commonly used [65]: ABCD(E) classification, seven-and three-point checklist, Menzies method, the CASH algorithm and pattern analysis by Pehamberger. All of these methods will be discussed in this section followed by a comparison in terms of their respective specificity and sensitivity.

Sensitivity and specificity are statistical measures of the performance of a bi-

nary classification test and are widely used as standards for the quantification of results in determining and evaluating abnormalities in medicine. In general, they are used when a simple misclassification rate would not provide enough significance. The term sensitivity describes the "true positive rate" and is a measure of the proportion of actual positives which are identified (by an algorithm or individuals) as such. On the other hand, the term specificity describes the "true negative rate," which is the proportion correctly identified as negative. In a medical environment, the specificity is most often related to images or patients who do not show the condition under test. Sensitivity and specificity are closely related to statistical hypothesis testing with respect to Type 1 and Type 2 errors. A perfect prediction of data for a binary classification system would result in a sensitivity of 100% and a specificity of 100%; however, theoretically, any predictor will possess a minimum error bound known as the Bayes error rate [63, 66]. A more detailed description of the statistical evaluation of sensitivity, specificity and accuracy is offered in Chapter 4.2.

2.4.1 The ABCD(E) Rule

The currently most often used rule is the ABCD(E) rule, which considers asymmetry, border, colour, differential structure and sometimes evolution. It has become the quasi-standard for professional and untrained individuals and is highly promoted by all cancer organizations for use in identifying a suspicious lesions and seeking medical consultation. The asymmetric feature is mainly built on the fact that moles are typically round, but SSM often presents different structures on the sides of the lesion. The border factor describes a crisp, clearly differentiable border between the lesion and the surrounding skin, whereas MM are often present with unclear, blurry or irregular edges. The colour may show differentiable structure but also may show dark to black and blue or green patches, which may account

for ulceration in malign lesions. Formerly, for visual inspection by the naked eye, diameter was used instead of differential structure. A diameter larger than or equal to 6mm increases the chance of a malignancy. Various studies show, however, that diameter does not seem to be a valid parameter—especially for the early detection of melanoma, where the lesion might be smaller than 6mm (compare [67, 68]). The differential structure describes the structure of the lesion, which may contain dots, globules and structureless or homogeneous areas. For untrained individuals, the scoring system in Table 2.4 is not valid, as the scoring works only for trained persons who review many lesions over time. For untrained individuals, medical advice should be sought when two or more of the five variables are present. Each variable (ABCD) is multiplied by a score factor, and the sum, the final dermatoscopic score, is used to classify the lesion as either benign, suspicious or malignant [69]. This information is summarized in Table 2.4. The ABCD criteria represent a commonly used clinical guide for the diagnosis of early melanoma [70] because it considers factors—especially asymmetry and loss of clear border — which can be used to differentiate from moles. The evolution (E) factor is not always present in the guidelines but describes a general growth or translation of the lesion over time, which may be used to observe suspicious lesions using photography or total-body photography (TBP) over time to identify changes.

Since the ABCD rule is the most common rule used for the early diagnosis of melanoma, and because it is used by both untrained and trained persons, it has been subject to much research regarding its specificity and sensitivity. The overall accuracy of determining any form of melanoma gradually rises with the experience and the training of the subject. Trained and experienced dermatologists can reach an accuracy of 80%, a sensitivity of 91%, and a specificity of 99% [73]. However, these values degrade with less experienced persons down to 78% sensitivity and

Table 2.4: Description of ABCD rule with weighting and score factors [71, 72]

	Weighting factor	**Score**	**Min - Max value**
Asymmetry (A)	1.3	0-2	0 - 2.6
Border (B)	0.1	0-8	0 - 0.8
Colour (C)	0.5	1-6	0.5 - 3
Differential Structure (D)	0.5	0-5	0 - 2.5
Total Dermascopic Score (TDS)			0.5 - 8.9
Classified as Benign:			< 4.76
Classified as Suspicious:			4.76 - 5.45
Classified as Malign:			> 5.45

96% specificity. It can be assumed that these numbers further degrade for GPs [73].

A similar study reveals that 10 years or more experience for dermatologists improves sensitivity to 76% in comparison with 59%, 48% and 65% for dermatologists with less than 1, 1-3 and 3 to 10 years of experience [74], respectively.

2.4.2 Seven-point checklist

Another potentially useful diagnostic test is the revised seven-point checklist developed in the United Kingdom in 1998 by Argenziano et al. [8]. The seven criteria together with their scoring values are presented in Table 2.5. It was found that the seven-point checklist features a high sensitivity and a relatively low specificity. It has therefore been thought to be useful for ruling cutaneous melanoma out from the suspicious lesions if the test shows negative results. If this test was to be used without further diagnosis, the large number of false positives would lead to a higher possibility of unnecessary biopsies and therefore to more patients.

Studies of physicians' global assessments of melanomas vary widely for sensitivity (50% to 97%) but are consistent for specificity (96% to 99%). In addition, some studies have shown higher percentages of correct diagnoses of malignant

Table 2.5: The seven-point checklist according to Argenziano [8]

Criteria	Score
Major Criteria	
Atypical pigment network	2
Blue-white veil	2
Atypical vascular pattern	2
Minor Criteria	
Irregular streaks	1
Irregular pigmentation	1
Irregular dots/globules	1
Regression structures	1

melanoma by dermatologists than by non-dermatologists; however, all of these studies used lesion images rather than patient examinations [65]. In an early study of the seven-point checklist it has been found that three out of the seven criteria (i.e., change of size, shape and colour) were more likely to be linked with melanoma than others. The seven criteria have thus been divided into major and minor criteria [59, 75].

2.4.3 Three-point checklist

The results of the seven-point checklist have been used to create the three-point checklist, which is based on the evaluation of only three dermoscopic criteria: namely, asymmetry, atypical network and blue-white structures. These criteria are similar to the major criteria discussed in Table 2.6. Preliminary results demonstrate that the three-point checklist allows non-experts to reach sensitivity values for malignant skin lesions which are comparable to those obtained by experts [61]. A primarily study of non-experts and one trained dermatologist who was shown 169 images of cutaneous lesions showed that the sensitivity of the non-experts was even higher (96.3%) than that of the dermatologists (94.2%). However, the experiment also showed a very low rate of specificity of the non-experts, who scored

Table 2.6: Three-point checklist proposed by Argenziano [65]

Asymmetry	Asymmetry in colour and/or structures in 1 or 2 perpendicular axes
Atypical Network	Pigmented network with thickened lines and irregular distribution
Blue-white structures	Any blue and/or white colour within the lesion

32.8% compared to the 82.8% of dermatologists [76].

2.4.4 Menzies Method

In the Menzies method [77] for diagnosing melanoma, neither of the following negative features may be found: a single colour (tan, dark brown, grey, black, blue, and red, but white is not considered) and "point and axial symmetry of pigmentation" (which refers to pattern symmetry around any axis through the centre of the lesion) [78]. This criterion does not require the lesion to exhibit symmetry of shape. In addition, at least one positive feature must be found [65] to account for a malignancy. The negative and positive features are summarized in Table 2.7. The evaluation of the Menzies method revealed a sensitivity of up to 92% with a specificity of 71% for experienced dermatologists [79]. Indeed, another study suggests that the Menzies method is preferred by some less-experienced dermatologists due to the simplicity with which it rules out melanoma [80]. However, the results of specificity vary widely depending on the experience and the sample source of the study.

2.4.5 The CASH system

The CASH algorithm (which considers colour, architecture, symmetry, and homogeneity) is very similar to the ABCD rule. Both evaluate colour, symmetry, and dermoscopic structures. However, the CASH algorithm includes a new evaluation value called architecture, which is used for dermatologists to make an overall

Table 2.7: Features according to Menzies method [77]

Negative features
Point and axial symmetry of pigmentation
Presence of a single colour
Positive features
Blue-white veil
Multiple brown dots
Irregular dots/globules
Pseudopods
Radial streaming
Scar-like de-pigmentation
Peripheral black dots-globules
Multiple blue/grey dots
Broadened network
Multiple colours (5 or 6)

judgement of the organisation of the lesion. This is an important skill used in the more sophisticated, though difficult-to-learn, technique of pattern analysis. The CASH algorithm provides a regimented way of teaching pattern analysis to the novice dermoscopist. Another benefit of CASH is that it does not require any weighting factors to calculate a total score, thus making it quicker and easier to use [81]. For distinguishing between melanoma and neoplasm melanocytes, it received a sensitivity of 98% with a specificity of 68% [82], and it can be seen as comparable to the Menzies method.

2.4.6 Pattern Analysis by Pehamberger

Like the term pattern recognition used by histopathologists and dermatologists, the term pattern analysis as used by Pehamberger refers to a system to aid diagnosis malignancies based on dermoscopic features. It was described by Pehamberger et al. based on the analysis of more than 7000 pigmented skin lesions [65, 83]. Pehamberger pattern analysis is not just used for the identification of melanoma but

Table 2.8: Pattern Analysis by Pehamberger, (altered from [65])

Malignant Melanoma
Heterogeneous (colours and structures)
Asymmetry (colours and structures)
Irregular pigment network
Irregular border with abrupt peripheral margin
Structure less areas
Gray-blue or red-rose veils
Red
Pseudopods/radial streaming
Point and hairpin vessels

also for a various kinds of pigmented skin lesions. It is primarily used by experts dermatologists utilising a dermascope. For simplicity, only the relevant information is summarised in Table 2.8. The full table can be found in [65] and [64].

2.4.7 Comparison of methods

The pattern-analysis algorithms discussed in this Chapter are compared with respect to their sensitivity and specificity, as shown in Table 2.9. The data evaluated in Table 2.9 might be unlike the values obtained in the text, as sensitivity and specificity may exhibit a large variability depending both on the sample size and on the number and profession of the people who are evaluating the pattern-analysis algorithm. Therefore, it was anticipated to take the results of studies containing non-experts and large sample size as underlying criteria for Table 2.9.

While it is very unlikely that any study would show a 100% correct false positive and true negative rate, it can be seen that the seven-point checklist and the CASH algorithm must deal with low specificity while the sensitivity for all algorithms is above 80% for five out of the six algorithms under investigation. This result shows that all of these algorithms favour the determination of malignant melanoma over under-fitting, which would result in more patients having unnec-

Table 2.9: Comparison of visual pattern classification systems in accordance to their sensitivity and specificity

Algorithm	**Sensitivity**	**Specificity**	**Source**
3-point checklist	86%	71%	[10]
7-point checklist	78%	65%	[63,84]
ABCD(E) Rule	84%	75%	[63,84]
CASH algorithm	98%	68%	[10,82]
Menzies method	85%	85%	[84,85]
Pattern Analysis by Pehamberger	85%	79%	[63,84]

essary surgery and mole removal. However, it also shows that still up to 22% of melanoma would be falsely identified as a mole or non-critical abnormality such that surgery would not be seen as the favoured choice.

Furthermore, traditional pattern analysis is taken out and evaluated on the basis of qualitative data by experts who do not always define a measurement: e.g., for asymmetry or state of ulceration. It therefore relies heavily on the experts' ability to differentiate between MM and moles. Techniques that rely on the analysis of data gathered by quantification would be very beneficial in supporting the dermatologists' decision regarding whether a lesion is benign, suspicious or malign. They might also help inexperienced non-experts acquire a further degree of certainty. In the next Chapter, the standard clinical practice of patient evaluation for cutaneous melanoma is described before a discussion is offered about imaging technologies currently under investigation.

2.5 Clinical practice for the diagnosis of cutaneous melanoma

The following passage introduces the process of melanoma diagnosis and treatment, which can be summed up to the following steps: patient assessment (pa-

tients' background information), physical examination (screening), biopsy and histopathological reporting (staging), treatment, and follow-up check-ups.

Patients' background information can help identify higher-risk persons for melanoma by their skin type, sun-exposure (especially in the childhood), family history of melanoma, and number of multiple-common nevi and atypical nevi [86].

2.5.1 Physical examination

Physical examination usually starts with visual inspection of the suspicious lesion. Various pattern-analysis systems exist to help trained or untrained individuals identify lesions. However, trained persons are more likely to find suspicious lesions because their training and experience results in significantly higher specificity and sensitivity [87].

Depending on the lesion, it may be observed before any action is taken, for example by total body photography. Dermatology consultation is needed if a change in the nevi's colour, ulceration or size is recognized. In the majority of cases, the lesion has to be investigated by a dermatologist utilizing a dermascope.

2.5.2 Total body photography

Total body photography is typically used on patients containing multiple suspicious moles (more than 50) or a historic background in the family with multiple suspicious lesions that need to be monitored where the suspicion does not (yet) satisfy clinical surgery. Total body photography is used over time to determine changes of the suspicious lesions. The goal is to reduce the number of unnecessary biopsies and to facilitate the early detection of malignant lesions.

Total body photography consists of taking multiple visual images, at least 20, over the whole body (i.e., over the entire skin surface) at a particular time. These images establish a baseline for each individual and can be used as a comparison

during physical examinations to identify lesions that have changed in colour, size or position on the body. Such lesions are most likely to be of malign origin, and the usual treatment is excision.

2.5.3 Dermoscopy

If suspicious lesions are found, patients are forwarded to a dermatologist. Typically, a dermatoscope is used to examine the lesion of interest. With specialists trained in dermoscopy, there is considerable improvement in the sensitivity and specificity compared with naked eye examination. The accuracy by dermatoscopy is increased up to 20% in the case of sensitivity and up to 10% in the case of specificity compared to naked eye examination [88]. The sensitivity of clinical diagnosis by experienced dermatologists is about 70% [86].

Dermoscopy is a technique used to see a variety of patterns and structures in lesions that are not discernible to the naked eye. Examinations with dermascopes reveal several features that are helpful in differentiating between benign and malignant pigmented lesions. A dermascope is a magnifying glass with a light emitter that uses polarised light beams, which penetrate deeper into the skin than unpolarised light. Dermoscopy provides additional criteria for the diagnosis of melanoma [36].

However, in order to diagnose accurately, knowledge and experience are required. Experienced dermatologist may still fail to accurately diagnose the lesion as 20% or more cases of melanoma lack classic dermoscopy features of melanoma. The dermoscopy feature which is most commonly detected in thin melanomas (Breslow thickness of 0.75 mm) is an irregular pigment network. Atypical nevi often exhibit hyperpigmentation and bridging of the rete ridges, which give them a similar appearance by dermoscopy. Dermoscopy criteria for melanoma variants—such as amelanotic melanomas, desmoplastic melanomas, lentigo malignant

melanoma, or nevoid melanomas—are lacking. A patient's report of change in a lesion is an important risk factor for melanoma. Approximately 10% of melanomas yield no characteristic dermoscopy findings. The decision to perform a biopsy of a lesion with a moderate to high clinical suspicion for melanoma before dermoscopy observation should not be changed by the lack of dermoscopy criteria for melanoma [36].

The accuracy of the clinical diagnosis of cutaneous melanoma with the unaided eye is only about 60%. Dermoscopy has the potential to improve diagnostic accuracy and is therefore the standard tool of diagnosis for the dermatologist [89].

In this Chapter the structure of the human skin layers (epidermis, dermis and subcuties) have been introduced and the most common types of skin caner, namely basal-cell carcinoma, squameous-cell carcinoma and melanoma have been discussed. Furthermore, tumour progression and different scoring and staging systems have been described as well as current clinical practice procedure for the diagnosis of cutaneous melanoma has been given. In the next Chapter an overview of current non-invasive imaging techniques for the detection of melanoma is given before terahertz technology is introduced in detail and current research for the use of terahertz technology with bio-medical applications are given.

Chapter 3

Imaging modalities for the diganosis of cutaneous melanoma

Having discussed the structure of the human skin as well as the most common types of cutaneous malignancies, in this Chapter an overview of current imaging techniques using measurements at different wavelengths is given. Where obtainable, research papers have been included that demonstrate the ability to differentiate between malignancies and healthy skin in terms of sensitivity and specificity. Furthermore strength and weaknesses of the techniques will be discussed and summarised.

The second part introduces the terahertz spectral regime as a relatively new technology for bio-medical applications. This is followed by a discussion about measurement modes suitable for bio-medical sensing. The Chapter closes with a state-of-the-art review about medical investigation topics using terahertz rays with a focus on (but not limited to) the human skin as well as oncology. The final discussion of this chapter outlines opportunities, challenges and gaps of knowledge that forms the basis for this thesis.

3.1 Imaging technology for cutaneous melanoma detection

While the gold standard for suspicious pigmented skin lesions is still excision followed by microscopic analysis by histopathologists, other imaging-technology techniques have been studied in recent years in pursuit of non-invasive techniques for the early diagnosis of melanoma, preferably *in-vivo*. Since the very early phase of MM may be particularly difficult to identify due to similarities with moles or birthmarks, there is a considerable need for new technologies that may help the non-expert or dermatologist identify malignancies in pigmented skin lesions so as to improve health outcomes without biopsy or excision of lesions for testing.

The following section provides an overview of imaging techniques that have been investigated with the non-invasive diagnosis of melanoma. It excludes invasive imaging techniques such as fluorescence tomography and PET and techniques that are used to diagnose metastasis. The Chapter concludes by considering possible opportunities in which terahertz imaging could facilitate the diagnosis of malignant melanoma.

3.1.1 Multi-spectral Imaging (MSI)

The penetration depth of light is wavelength dependant. Multispectral images are sequences of images taken at different wavelengths of light, typically in the visible and infra-red spectrum (i.e., 400 – 970 nm). Multispectral imaging has been subject to research for the diagnosis of melanoma since the end of the 1990s. As a contactless optical method, multi-spectral imaging is regarded as a non-invasive, safe method. Halogen lamps, incandescent lamps, or white-light emitting diodes can be used as broadband illumination sources. Advanced image processing allows for mapping the main skin "absorbing chromophores—oxyhemoglobin,

deoxy-hemoglobin, and melanin" [90].

In a study conducted by Elbaum et al. the lesion is illuminated with 10 narrow band wavelengths and detected by a camera, which then creates 10 images of different wavelengths. Statistical pattern analysis is applied to the images to distinguish between healthy and infiltrated tissue and to give a prognosis of the outcome [91]. Images created by MSI feature a low noise level on high-resolution images with a field-of-view of approximately 2 cm x 2 cm. The study of Elbaum et al. shows that a linear classifier consisting of 13 parameters can differentiate melanoma from non-melanoma lesions with a sensitivity of 100% and a specificity of 85%. Furthermore, a non-linear classifier model using 12 parameters was able to achieve a sensitivity of 100% but with a specificity of only 75%.

Spectral images provide information on the distribution of collagen, melanin content, and blood-vessel distribution within skin lesions. A fully automated system using 15 spectral bands between 483 nm (blue) through 951 nm (near infrared) has been shown to achieve a 97% contour accuracy in a sample of 1,856 pigmented lesions. A follow-up study using multispectral analysis and an artificial neural network showed that it could recapitulate clinicians' assessments with 88% sensitivity and 80% specificity [10]. Table 3.1 gives a brief overview of the prediction techniques used to discriminate MM from other lesions based on MSI techniques. The sensitivity and the specificity values seem to differ greatly between the experiments, which may be due (amongst other factors) to sample size and sample selection criteria. Thus, these values must be regarded critically. Also, non-malignant melanoma from Table 3.1 may refer to healthy surrounding skin, other nevi or other skin cancers. Tomatis (2005) concludes that a higher amount of differentiation of the MM lesion should be taken into account (i.e., the vertical and horizontal size of the lesion) [92].

MSI is not eligible for full-body screening due a limited field-of-view, image

Table 3.1: Overview of predictive modelling techniques using MSI on MM with results in terms of sensitivity (SE) and specificity (SP)

Technique	**n**	**MM**	**Non-MM**	**SE %**	**SP %**	**AUC**	**Source**
Artificial Neural Network	1391	184	1207	80	76	0.85	[92]
parametric image algorithm	81	22	59	86	91	n/a	[94]
discriminant analysis	237	67	170	80	51	n/a	[95]
Artificial Neural Network	573	132	441	78	76	0.85	[96]
multivariate discriminant analysis	573	132	441	76	57	0.76	[96]
MSI on 8 bands using ANN (and Genetic Algorithm)	47	12	35	92	91	n/a	[97]

acquisition and processing time, but it does make it possible to investigate suspicious, atypical nevi. Furthermore, the training of the model requires expert knowledge to adjust the underlying mathematical or statistical model [93].

3.1.2 Ultrasound Imaging

Ultrasound imaging (sonography) is a longstanding medical-imaging modality with manifold applications in diagnosis, preventive examinations, therapy and image-guided surgery. Image-guided surgery uses either a single frequency or a range of frequencies, typically between 20 and 100 MHz. In dermatologic oncology, diagnosis relies mainly on surface indicators such as colour, shape and texture, whereas the two more reliable measures are the depth of the lesion and the number of skin layers that have been invaded [98]. Lassau et al. investigated the use of high-frequency ultrasound (HFUS) for the depth identification. They concluded that the depth of the lesions is indeed visible but that they were overestimated when compared to those of the histopathologists [99]. High-frequency transducers and 3D probes have opened new opportunities for performing non-invasive diagnostics using ultrasound images. However, changing dermatological practices require the development of robust segmentation algorithms [98].

The lower ultrasound wavelength at around 20 MHz has been shown to be advantageous for the determination of the penetration depth of cutaneous melanoma [100] and is thus used for thickness mapping. In a study carried out by Machet et al. [101], a trained model was able to determine the thickness of melanoma to $\pm$ 0.01 mm when compared with histopathologists' results. Furthermore, the margins of the lesion were correctly determined in 26 out of 31 patients. In a different meta-analysis of the use of ultrasound for excisional margin detection, the overall accuracy was 72%. It was also found that ultrasound was performed insufficiently when the real tumour depth was smaller than 1 mm, thus making this technique reliably usable only for malignancies $>$ 1 mm deep. Like HFUS, the disadvantage of ultrasound is that it tends to overestimate the penetration depth of the tumour compared to histopathologists' results. It was concluded that the overestimation is likely due to an inflammatory infiltration from under the melanoma which produces a hypoechoic area similar to the hypoechoic area from the melanoma. Thus, HFUS cannot be used to differentiate both areas. Furthermore, ultrasound cannot substitute for biopsy, as the differentiation between benign and malign tumours has not been quantified [102].

In the majority of the literature, ultrasound imaging has been used as a follow up to determine lymph-node metastasis prior to excision, which is due to the higher penetration depth at the ultrasound spectrum compared to other imaging techniques. While the literature suggests that ultrasound imaging cannot be used to identify skin cancer in general, but is used to detect metastasis spread around the lymph system [103], ultrasound imaging has been frequently used as a modality for the estimation of tumour depth and compared to histology findings, thereby resulting in a correlation between these two [101].

Even though major features of the sample are visible, HFUS does not provide cellular resolution and therefore can only be used in the follow-up of chronic and

inflammatory skin diseases on pre- and post-operative assessments of skin tumours (especially malignant melanoma and basal-cell carcinoma). It can also be used as a guide during surgical procedures [103].

3.1.3 Optical Coherence Tomography

Optical coherence tomography (OCT) is a low-coherence interferometry technique that produces cross-sectional images of tissue with a high resolution. The signal arises from light backscattered at index of refraction mismatches in the sample. OCT is very similar to ultrasound; however, it features higher resolution of about 5–15 µm, though the penetration depth is limited to a maximum of 1 mm [104].

While the layers of the skin (i.e. the epidermis, dermis, adnexal structures and blood vessels) can be seen, the basement membrane zone and cellular features cannot be visualized; therefore, OCT is of limited use in the early detection of melanoma [103] but allows for a maximum penetration depth up to the papillary dermis.

Some studies of non-melanoma skin cancer acknowledge a promising sensitivity of 79% to 94% and a specificity 85% to 96%; but these also state that the misclassification rate of atypical nevi and BCC is high, with a 50% error [105]. This is due to the limited penetration depth and the high backscattering intensity. The infiltration depth of melanoma can be measured only in thin tumours (up to 1 mm in thickness) because of the limitation of the light penetration depth into the skin [106] and the lateral resolution [107].

One of the first trials conducted by De Giorgi et al. (2005) studying melanocytic lesions with the use of OCT and dermoscopy found that OCT - in some cases - allows an *in-vivo* correlation between dermoscopic features and histopathologic results [108]. However current limits in resolution make a differentiation between benign and malign lesions difficult, Furthermore, OCTs limited penetration depth

makes it challenging to determine the depth of the infiltration [109, 110].

Most recently, Turani et al. (2019) have proposed an imaging algorithm called "optical properties extraction (OPE)" as post-processing step to improve the classification between non-melanoma and melanoma OCT images of 69 patients, which resulted in a 97% sensitivity and 98% specificity [111]. However, Turani claims that more subjects may need a more sophisticated classification algorithm then the one established [111].

3.1.4 Infrared Spectroscopy

In recent years, near infrared spectroscopy (NIR) has been widely explored in the field of cutaneous malignancies and covers a wavelength from 780 nm up to 3 micrometres.

NIR radiation is in resonance with molecular overtone and combination vibrations. As a consequence, the molar absorption with NIR is typically quite small. In contrast to mid-infrared, NIR has the advantage that it can penetrate deeper into the sample and is therefore useful in probing bulk material though it is not particularly sensitive.

The molecular overtone and combination bands seen in the NIR are typically very broad and overlap, thus leading to complex spectra. This makes it difficult to assign features to chemical components. Multivariate analysis, like principle component analysis, neural networks and partial least squares are frequently used to extract desired chemical information.

However, in recent years, near infrared spectroscopy has been investigated for the determination of melanoma: McIntosh et al. (2002) conducted an *in-vivo* experiments to study the differentiation of various pigmented skin lesions by using NIR from "actinic keratosis, basal-cell carcinoma, benign nevi, dysplastic nevi, actinic lentiginous and seborrheic keratosis" [112], which involved placing a fibre-

optic probe on the skin. Using linear discriminant analysis (LDA) as a calibration technique, they determined whether spectra could be classified according to the lesion type. This study resulted in accuracies of 70–98% in differentiating benign from pre-malignant or malignant lesions [112].

Wald et al. (2015) have used Fourier-transform IR (FTIR) on histological slides of melanoma and a supervised partial least squares discriminant analysis (PLS-DA) to detect various types of cells that typically appear in and around melanoma with an accuracy of over 90%. Furthermore, a comparison of primary tumours of the disease has been performed with the result that differentiation between patients showing Stage I or II and Stage III and Stage IV could be shown. The unsupervised model of the PLS-DA has a relatively high sensitivity of 88.9% and a good rate specificity of 70.6%. It also gave a good demonstration of the usefulness of NIR in the clinical prediction of malignant melanoma lesions [113].

In 2018, Rey-Barroso et al. [114] studied the usefulness of extended NIR (exNIR) based on an InGaAs sensor (which covered a wavelength of 995 to 1613 nm) covered with a combination of a previously developed combined NIR with visible-light multispectral analysis. Rey-Barroso et al. found that the higher wavelength is suitable for the evaluation of deeper skin layers due to the high penetration depth of the photons at these wavelengths. By comparing various classifications systems, Rey-Barroso et al. achieved a sensitivity of 78.6% with a specificity of 84.6% after comparing 14 melanoma with 39 nevi from Caucasian patients *in-vivo*.

Furthermore, in 2011, Herman et al. showed the potential of thermal infrared imaging for the determination of malign regions due to differences in the thermal behaviour. The suspicious region was cooled down for one minute with a stream of cold air. After this, an infrared camera photographed the lesion every couple seconds. When the skin returns to normal, significant differences can be seen in

the tumour region. This is because cancer tumours re-heat faster than surrounding tissue [115].

3.1.5 Confocal Scanning Laser Microscopy

Confocal microscopy is an optical imaging technique used to increase optical resolution and the contrast of a micrograph by using point illumination and a spatial pinhole to eliminate out-of-focus light in specimens that are thicker than the focal plane. In the literature, it is also often referred as reflectance confocal microscopy (RCM). It facilitates the reconstruction of three-dimensional structures from images up to a resolution reaching histologic detail [116]. The penetration depth of CSLM in skin is limited to 200 to 300 µm up to the level of the papillary layer of the dermis [117].

While confocal microscopy allows the visualisation of structures with greater resolution deeper into the skin than conventional CSLM, it can still image only relatively shallow structures. For imaging deeper into skin tissue, OCT is perhaps better suited [103].

A meta-analysis by Stevenson et al. (2013) systematically reviews papers concerning CSLM for the detection of melanoma. The authors found promising studies that showed a sensitivity between 91% to 97% with a specificity of 68% up to 81% and with a number of lesions ranging from 85 to 351 specimens [118]. The average prevalence of melanoma in the studies included in the review was 36%. However, given the baseline studies analysed in the context of CSLM being used as an add-on to dermoscopy, the authors conclude that CSLM does not have the potential to replace dermoscopy, as its image-acquisition time is remarkable higher than that of expert dermatologists.

3.1.6 Comparison of imaging techniques

While OCT has the potential to be used to detect local superficial metastasis, it currently lacks the resolution needed to detect early-stage metastasis of melanoma. In conclusion, despite an extensive range of non-invasive imaging techniques, there is still a need for imaging techniques with a high resolution which can be used to determine whether or not a melanoma tumour has invaded through the basement membrane, as this is critical in the staging and treatment of these very difficult-to-treat cancers [103].

CSLM features very high resolution (up to the cellular level) but is limited with regard to depth penetration, which makes this technique feasible for further investigations in BCC. However, it is unlikely to become a non-invasive technique for the detection of melanoma [119, 120].

Ultrasound and high-frequency ultrasound have been investigated to differentiate the melanoma of healthy tissue, but they have not been found useful for the detection of early stage melanoma in particular, as it is limited to the lateral and axial resolution and penetration depth. However, these methods can be used to determine if the lymph system is already infiltrated by melanoma [121].

Despite the variety of techniques available for detecting melanoma, there remains a critical need for a high-resolution technique which can answer the question whether tumours have invaded through the basement membrane [103]. Table 3.2 gives an overview of current imaging techniques summarized by their spatial and depth resolution, dis/advantages and mode of operation.

Table 3.2: Comparison of non-invasive imaging techniques for the diagnosis of MM

Technique	Axial resolution	Lateral resolution	Features Depth information	Mode of operation	Strengths	Weakness	Source
OCT	10-20 µm	20 µm	Up to 2 mm	reflectance	High resolution for visualization of the epidermis and dermis	Limited sensitivity precludes early detection of melanoma, limited lateral resolution	[103, 106, 122–124]
CSLM	3–5 µm	0.5-1.0 µm	Up to 300 µm	fluorescence and reflectance	High resolution, images the epidermis and the dermis noninvasively with cellular-level resolution	Expensive, time consuming, limited depth penetration	[103, 119, 120, 124–126]
Ultrasound	up to 200 µm	approx. 1 mm	3.8 mm (at 20 MHz)	reflectance	thickness of melanoma estimation for melanoma $<$ 1mm	no useball for melanoma $>$1mm, , no cellular resolution	[103, 121]
HFUS	50 µm	100 µm	1 mm (at 100 MHz)	reflectance	Detection of spread into the lymph system	Of limited use to detect primary melanoma tumours, no celluar resolution	[99, 102]
NIR	15 µm	40 µm	0.5 up to 15 mm	transmittance	Detect intramolecular bonds, has the ability to differentiate	Contains overtones and noise which requires further (computational) analysis	[127, 128]
THz	40 µm	200 µm	Up to 1.5 mm	reflectance and transmittance	Detect intermolecular bonds, high absorption of water	Noisy signals, high water absorption and limited depth information	[16, 124, 129]

Having summarised the current non-invasive imaging techniques for the early detection of melanoma, I now give an overview about terahertz technologies, the setup modes and the application to current bio-medical applications. The Chapter ends by showing the potentially usefulness of terahertz technology for the detection of melanoma.

3.2 Terahertz technology

The term terahertz regime has been around for approximately two decades. Though it first appeared in 1976, it has only attracted research since the late 1990s and was thus previously referred to as the terahertz gap due to the lack of suitable devices for emitting and detecting terahertz radiation. With new advances in physics and ultrafast laser development, new terahertz devices have been created in recent decades that are cost-effective, portable and stable and are thus allowed to perform experiments at room temperature with an acceptable signal-to-noise ratio (SNR). The first commercial devices have been available since the 1990s, and they have been improved over the last years such that the devices are smaller, more cost effective and more reliable.

3.2.1 Foundations of terahertz technology

The terahertz frequency range, also referred as sub-millimetre band, is broadly defined as the region between infrared and microwave and covers a spectral range from 300 GHz up to 3 THz [24], which corresponds to a wavelength ranging from 1000 µm to 100 µm. This definition of the spectral range is not fixed and depends on who is writing about it. In this thesis, the definition given above is used, as it is applicable to the frequency range given by the device used throughout the thesis.

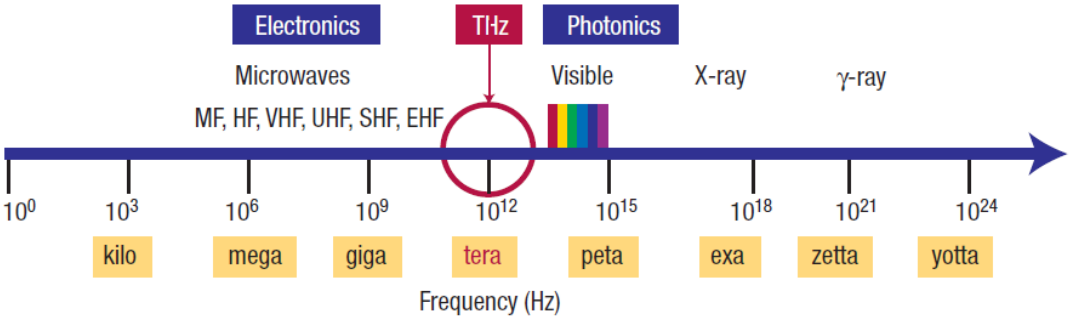

Figure 3-1: The electro-magnetic spectrum (altered from [130])

Due to a lack of suitable emitters and detectors, the terahertz regime was referred to as the "terahertz gap" before the late 90s. Traditionally, the terahertz band lies in a region where conventional electro-optical and electromagnetical devices do not reach the required wavelength. From the microwave side, traditional electronic components such a transistors, have a principle limit of working up to 300 GHz. From the optical side, on the other hand, semiconductors only operate down to a frequency of 30 THz, which creates a situation in which traditional electric components do not operate in the region between 300 GHz up to 30 THz [130].

In the last two decades, progress in physics, the creation of laser sources, and fibrebased laser systems and semiconductor manufacturing have made it possible to create terahertz devices that yield a stable output, are more cost efficient and may operate at room temperatures. The low energy output of these systems remains a challenge, however.

The hunt for suitable components for the creation and detection of terahertz rays is ongoing. In fact, current research of this topic is so broad that discussion of it could easily fill a complete thesis of its own. Therefore, this section focuses on the fundamentals of detecting and emitting terahertz light which is suitable for medical systems—i.e., machines that cover a broad THz range and are suitable for use at normal temperature.

All terahertz systems are of high-power electromagnetic waves fired on some kind of substrate that emits a terahertz beam. In almost all cases, a laser is used for this purpose. Pulsed terahertz emission and detection requires a high-power femtosecond pulse, which is most commonly produced by mode-locked lasers [131]. Optical rectification and photoconductive antennas are the two main principles that are able to create pulsed terahertz broadband emission and detection [130].

3.2.2 Terahertz creation and detection with the TPS3000

The Teraview TPS3000 uses a Titanium-Sapphire (Ti:Sa) Laser provided by the company Coherent Inc. The Ti:Sa laser utilises the principle of mode-locking using the Kerr-effect. High intensities create a perceptible influence between the electric-field and the index of refraction which changes the optical properties due to a realignment of free carriers [132]. This procedure has certain advantages: At first the Kerr-effect induces a Kerr-lense which creates an (auto) self-focussing beam within the crystal. Secondly, since the light-beam wanders between the mirrors, it is automatically pulsed when exiting the laser system [133].

The most common device for emission and detection of Terahertz waves are the photoconductive antennas which utilises a photo carrier transport to create a Hertzian dipole [134]. "A PC antenna is an electrical switch exploiting the increase in electrical conductivity of semiconductors and insulators when they are exposed to light. The photoconductivity results from an increase in the number of free carriers—electrons and holes—generated by photons. The photon energy must be sufficiently large to overcome the bandgap of the material" [135]. A PC-A typically consists of a semiconductor material, such as low-temperature grown Gallium arsenide (ltGaAs), Indium arsenide (InAs) or Indium phosphide (InP) which is embedded in the centre of two metallic strips. Emitters use a dc-bias of a couple of volts to create a potential difference between the anode and the cathode.

When an ultrashort laser pulse of up to 100 fs hits the semiconductor substrate and the energy is equal or greater than the bandgap free charge carriers are created and the semiconductor becomes photoconductive. Due to the impressed voltage, the free charge carriers are accelerated towards the anode which creates a time dependent dipole and therefore a time dependent electrical field. The lifetime of the pulse created is approximately 1 ps as the electron-hole-pairs begin to recombine.

The carrier acceleration and recombination phases define the width of the output pulse and it is therefore of importance to accelerate the recombination time down to an overall width of 1ps. This is done by using fast intraband relaxation as well as defect levels, which further accelerate the recombination of the photon with the electron.

The output of the PC-A, the THz radiation is highly divergent because the size of the source is much smaller than the terahertz wavelength. Thus a silicon lense attached behind the PC-A to collimate the THz radiation is a critical component for the THz emitter [136]. Silicon is best suited for the component because the refractive index matches well with typical substrate materials, the linear absorption is very low at the THz frequencies, dispersion over the whole THz spectrum is almost negligible, and the fabrication of high-quality components is reasonably simple [135, 137].

The detector using a PC-A is very similar to the emitter, however instead of a DC-bias an ampere meter is used to measure the difference of the energy arrived at the detector. The detector acts like an optical switch only measuring the THz signal when the laser probe pulse opens the switched gate for the duration of a couple of fs. This is important for a gated detection of the terahertz signal in order to provide high stability with a low energy terahertz output as well as to reduce the effects of noise and blackbody radiation.

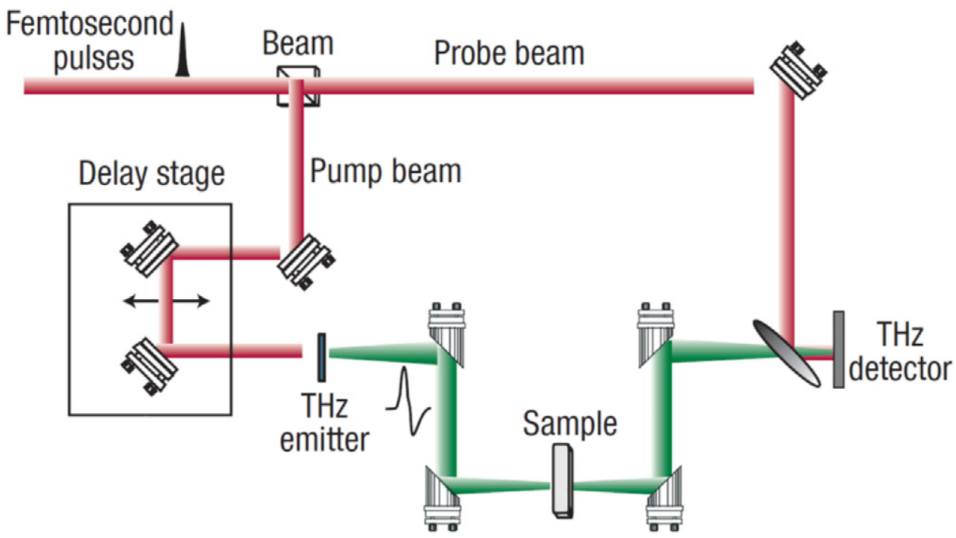

Figure 3-2: Schematic of a terahertz setup in transmission mode (altered from [130, 138])

3.2.3 Terahertz modes

The TPS3000 can be operated in multiple modes. In this section, the most commonly used, transmission and reflection mode will be described. At the end of the section, a brief overview about other configurations suitable for bio-medical imaging will be provided as well as new devices created for that field of study While throughout this thesis the angle based reflection mode will be the preferred choice of the imaging of biological tissue, a comparison between the two modes in regards of advantages and disadvantages is anticipated, thus a brief description of the transmission mode and interferometer based modes are provided.

In transmission mode, a terahertz pulse is fired on the substrate of investigation passing through it. The transmitted beam is detected by the PC antenna. Depending on the substrate, the terahertz pulse changes its index of refraction but also bounces back at the interfaces of the substrate due to internal reflection, dispersion and absorption, causing a loss of transmitted energy through the media. The electric field is measured before and after propagation through the

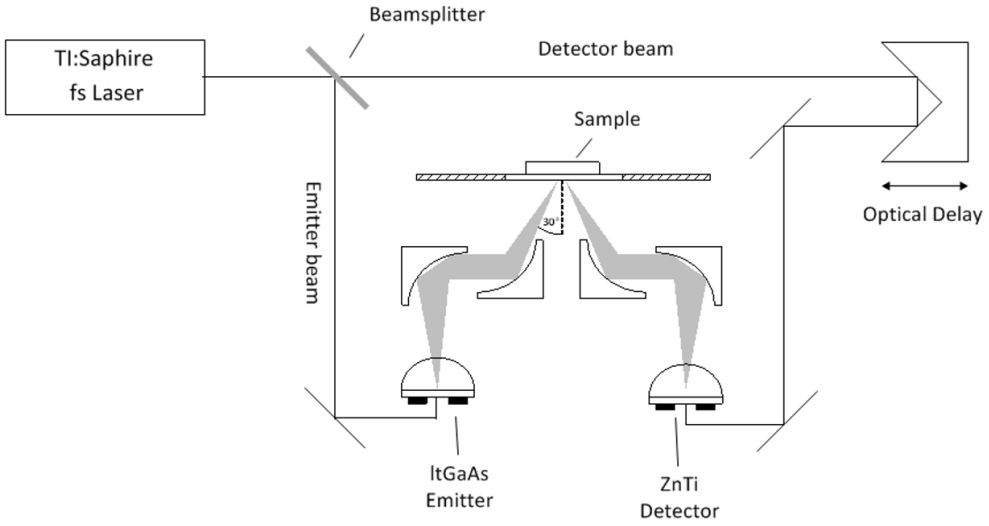

Figure 3-3: Simplified schematic of a terahertz setup in reflection mode

sample. Since the electric field is measured, both, the refractive index (n) and the absorption coefficient (α) can be measured simultaneously. A schematic of the setup is give in Figure 3-2.

Typical applications are found in the pharmaceutical environment for the quantification of polymorphs, the discrimination of transformation dynamics, analysis of tablet coating as well as coating thickness and chemical mapping and imaging of tablets [139]. Bio-medical samples have been investigated through transmission mode scanning as well, like monitoring the hydration of leaves from plants [140, 141].

One of the major hurdles for biomedical applications lies in the poor THz transmittance of polar liquids, which makes it difficult to extract information about solute molecules [142]. To overcome these difficulties, the transmission sample chamber can be modified using parabolic mirrors to change a transmission beam into a reflection beam.

In terahertz pulsed reflection mode, the terahertz beam gets redirected onto the sample interface using parabolic mirrors. Using the TPS3000 the apparatus consists of 8 mirrors, redirecting the beam towards the sample interface with a

fixed angle of 30 degrees. A simplified schematic of the general setup is provided in Figure 3-3.

The reflection mode allows to acquire information about the changes of the refractive index at the interface between two media, therefore making it suitable to pass through multiple layers of materials. However in order to obtain quantitative results, exact focusing to the desired interface is required, which can be difficult to achieve. While in transmission mode, a measurement of the empty sample chamber can be used as a reference (considering that the energy of the incidence beam equals the energy of the collector beam), in reflection mode a second medium needs to be acquired with known optical properties in order to retrieve a reference beam. This is most frequently done using a golden plated mirror, with a reflectivity close to 1. Furthermore, in cases of non-solid materials, a sample holder is required with the following properties: The sample holder must be non-absorpting and must contain a stable and constant refractive index over a wide terahertz frequency spectrum. Currently most often used sample holders are silica based quartzes which fulfil these requirements.

Another method is reflectance interferometry (which acts similar to a Michelson interferometer) was introduced by Johnson et al. [143, 144]. In this case, the reference and the sample beam are coupled with a phase shift of 180 degres. Because the receiver collects the combined beam, the reference beams cancels out the incident beam leaving the interference between those two, which can be used to enhance the reflection results from the material under investigation. Another advantage is that the beam is focused onto the sample without any angle of incidence, which will reduce (and simplify) the phase-dependant Fresnel equations to the once from normal incidence (compare [132]). One disadvantage would rely in the THz beamsplitter as shown in Figure 3-4, a 50% transparent mirror, which divides the beam into the sample and reference beam, as the already low power

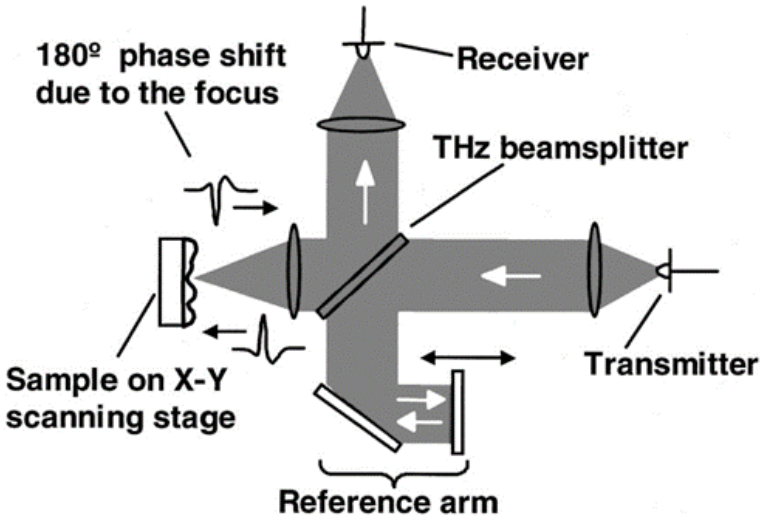

Figure 3-4: Terahertz reflectance interferometry (adapted from [144])

outcome of a sample beam is further declined due to the split.

3.2.4 External terahertz probes

With the constant research and development of cheaper, yet smaller devices, in recent years two devices have become available that are suitable in performing medical studies *in-vivo*. The external terahertz reflected scanner from Teraview is available as an additional add-on to the TPS3000. The probe head, which is connected to the laser system consists of the terahertz emitter and the detector and features a line scan of 15 pixels using rotating prisms [145] as shown in Figure 3-5. The principle setup is the same as described in the last section. The THz emitter and detector are connected via fibre optic couplers to the laser system. The external system allows greater flexibility when measuring samples *in-vivo* and has been used to characterise the skin of the palms, as due to the thickness of the stratum corneum a secondary interface is visible on the reflected pulses [146].

An endoscopic device with a size of 2x4x6 mm has been developed Ji et al. [148] in 2009 which for the first time demonstrated the use of terahertz imaging from the mouth and tongue region *in-vivo* as illustrated in Figure 3-6. Furthermore,

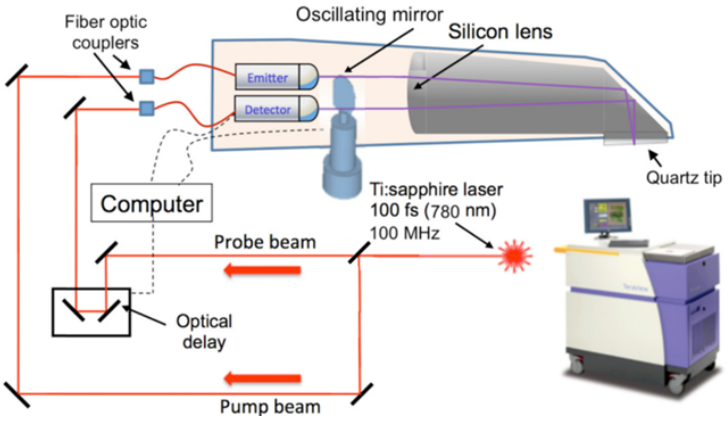

Figure 3-5: External terahertz reflected scanner (altered, from [147])

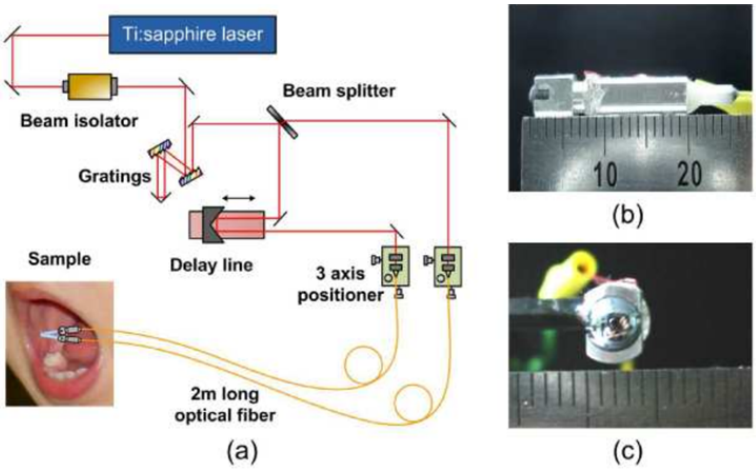

Figure 3-6: Endoscopic Terahertz device schematic (from [144])

Doradlla et al. (2014) have demonstrated another endoscopic device which uses CW-mode lasers which is able to detect polarization specific changes of a sample using reflection and transmission mode simultaneously [149]. Up to now, no quantified results are found in the literature concerning the opportunities to detect skin cancer by these devices, however, the University College London in collaboration with the University Hospitals London are currently taking a phase 2 study on the detection of non-melanoma skin cancers using the external handheld probe but results have not been published yet.

Most recently, Pickwell-MacPherson et al. (2017) have designed a table-top interface apparatus for the TPS3000 suitable to measure the epithelial tissue *in-*

vivo [150]. The design is similar to a gantry created at De Montfort University, which I call the "one-point reflectance"-module as no scanning motor is attached to the system making it impossible to obtain images from the device. Our device can be operated on top of the TPS3000 sample chamber making it possible to measure reflection using the quartz sample holder, but also external probes are attached to the top of the device suitable to scan a reflection without the need to the sample holder However, in our early studies I found that the maximum reflection from the external probes is very complicated to measure and this has not been used for this study.

3.2.5 Terahertz radiation for bio-medical sensing

In recent years, terahertz technology has attracted some interest in bio-medical engineering. This is reflected in the number of publications that appear per year in professional magazines and conference publications. While terahertz technology is a niche in the wide field of medical and biomedical applications, a growth of interest can be observed, as shown by Figure 3-7. This growth may be explained by the development of smaller and therefore more portable, more applicable (they work at room temperature) and less cost-intensive devices which are due to new developments in physics. These include laser devices developed in the last two decades that operate in CW and pulsed mode.

While terahertz as a modality for the investigation of biological tissue has to compete with various other techniques, it has advantages relative to infrared spectroscopy (NIR), for example, because of its lower level of Rayleigh scattering and the ability to access lower-frequency vibrational modes (of proteins and/or molecules) [151]. The low photon energy of 4.14 meV (at 1 THz) makes it a non-ionising, safe method [152] to use for studies conducted both *in-vivo* and *ex-vivo*.

This Section aims to give an overview of biomedical applications using tera-

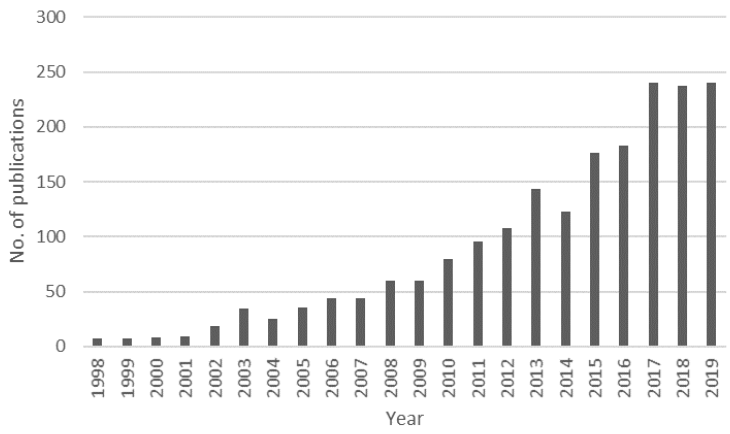

Figure 3-7: Number of publications using the keywords "terahertz" and "medicine", "biomedical", "medical" or "biology", retrieved from ScienceDirect 29.08.2019

hertz technology with a focus on cancer detection.

Energies corresponding to molecular rotations, hydrogen bonding stretches and torsions and bond vibrations lie within the terahertz range. Water in particular plays an important role in biological systems, with a network of water molecules surrounding and influencing the dynamical behaviour of biomolecules, such as proteins [25]. Proteins are structures made of a large number of atoms, and terahertz technology can be used to probe the collective vibrational modes of whole molecules, as different molecules vibrate differently.

All of the mentioned modes (transmission and reflection) have been used for the study of bio-medical applications using terahertz radiation. However, as mentioned above, due to the limitations of transmission measurements with respect to the strong absorbance from bio-medical media, terahertz technology is typically used when the sample is very thin (up to 500 µm), when the sample has been dried to reduce water vapour effects, and for medical applications that is most often excited tissue which has been sliced (normal while undergoing standard histopathology procedures).

Terahertz technology has been of increasing interest in the field of bio-medicine

regarding the detection of skin burns [153] or basal-cell carcinoma (whether *ex-vivo* and *in-vivo*) [154] and detectable alterations of the hydrogen bond network in the protein structure of infiltrated tissue [155].

The first appearance of the applied-medical applications of terahertz systems appeared in the late 90s by research conducted by Arnone et al. [156], which in essence describes the terahertz setup from the last Chapter in transmission and reflection mode. Various healthy tissues have been taken from chicken and from pork—such as liver, kidney and skin tissues—to demonstrate the advantages of terahertz rays on excised and dried-out tissue. Furthermore, the use of TPI on a human tooth was demonstrated and showed the differentiation of enamel and cavity [156].

Loeffler et al. used terahertz dark-field imaging to show structural changes caused by the diffraction of canine skin tissue containing cancerous tissue in transmission mode. It was concluded that the deflection loss at low THz frequencies might provide a suitable method for margin detection of carcinogenic tissue [157], as the standard procedure of histopathology is similar: Histopathologists look for structural (and morphological) differences at the margins of the tumour region.

In 2002/2003, Woodward and Wallace et al. [26, 154, 158] carried out extensive studies of the detection of BCC *in-vitro* and *in-vivo* by using terahertz pulsed imaging (in reflection mode). This is the first time terahertz was used for *in-vivo* studies in the time and frequency domain [158]. The study yielded results comparable to those of histopathologists. It was shown that BCC gives a positive contrast when compared to healthy skin, whereas skin inflammation gives a negative contrast. It was concluded that this result is most likely because the keratinocyte within the BCC contains more water and therefore absorbs the terahertz energy more strongly than healthy tissue. They also investigated the stratum corneum thickness, which might be visible on the samples as well; however, it was found

that this depends on the position of the body, as the thickness of the SC can change greatly. A secondary reflection from the SC interface was recognisable at body positions in which the SC is typically thick, especially the palm. Samples obtained from the neck and head showed an SC thickness smaller than 20 µm, which is beyond the resolution limit of terahertz beams [26].

Similar results are reported by Pickwell-MacPherson and Cole et al. [159–161] who investigated the response of THz radiation to normal skin *in-vivo*. Since the stratum corneum of the forearm is typical 10 µm which lies beyond the resolving capabilities of a typical TPI system, the reflected waveform from the volar forearm was dominated by the reflection of the epidermis, and the optical properties of this layer could be measured. On the palm, wich has a bigger stratum corneum, the system was able to resolve the stratum corneum as the layered structure showing multiple reflections and thus the possibility to calculate the thickness out of the optical delay between the reflected peaks [162]. Having investigated normal skin *in-vivo*, Woodward et al. (2003) have also acquired *in-vivo* images of skin cancer (BCC) [158]. Wallace et al. [154] described a portable TPI reflection system which was used to image 18 BCCs *ex-vivo* and five *in-vivo*. They found regions of diseased tissue identified in the THz images correlated well with histology and therefore implying that the technique could be used *in-vivo* to delineate tumour margins pre-operatively [162]. Analysis of the reflected terahertz pulses reflected from infiltrated and healthy tissue showed a broadening of the reflected THz pulse when compared with normal tissue due to unknown changes in the frequency-dependent absorption and refractive index [163,164]. By combining spectroscopy measurements [155] and the finite-difference time-domain model with Debye theory [159], Pickwell-MacPherson et al. [165] were able to demonstrate that the contrast visible in the images was due to in the refractive index and absorption of the tissue [162, 165].

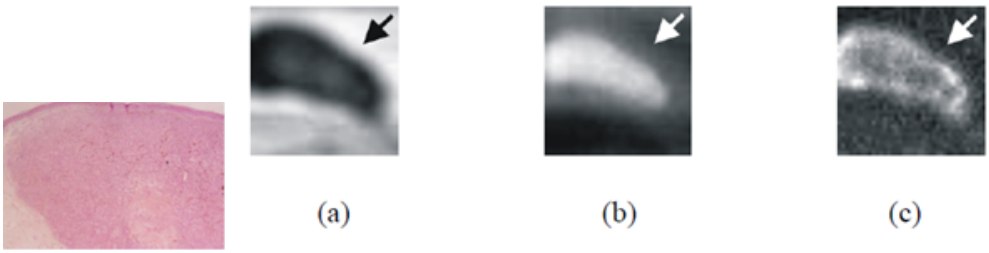

Figure 3-8: Images from melanoma sample, where a) is the relative pulse amplitude, b) time delay between reference and sample pulse and c) FWHM of the pulse, the arrow indicates the epidermis layer (from [166]).

In terms of skin cancer, BCC and SCC have been subjected to wide study in combination with terahertz radiation. However, little information can be found when inspecting melanoma-infiltrated tissue. In fact, at the time of this writing there are five scientific papers which describe melanoma and terahertz. The first melanoma inspection using terahertz was introduced by Berry et al. [166] in 2004 using excised, sliced melanoma and BCC samples prepared for histology. They were dehydrated and fixed in formalin, as the imaging-acquisition time may require over 24 hours. Three "features" from the time-domain waveforms were chosen for k-means multi-spectral imaging: i.e., the relative pulse amplitude, the time delay relative to reference pulse and the full-width at half-maximum (FWHM) of the positive pulse peak.

Berry et al. conclude that terahertz images offer the possibility of providing information from deeper structures than are currently available to the pathologist from stained slides. "Whilst the edges of the tumours appear to have been defined, it is necessary to confirm this experimentally. Similarly, the differences between tumour types that have been suggested in this study require further investigation, and in particular it is essential to include location-specific diagnoses using one or more reference techniques, and samples of healthy tissue for comparison" [166].

Two more papers were published by Sim et al. [167, 168] in 2013 on a freshly excited oral melanoma which was directly frozen using dry ice in the operation

room. The authors performed temperature studies on the sample at 20 degrees Celsius and concluded that a higher quantitative difference is obtained using the frozen sample than the one kept at room temperature. The terahertz sample from Figure 3-9 was obtained using terahertz-reflection geometry after excision. The diseased tissue was clearly visible at both temperatures. The freshly excised oral melanoma was 15 x 12 mm in size and contained both healthy and melanoma sections. It had a thickness of approximately 3 mm [168].

In 2019 Vilagosh et al. build a computational phantom of frozen melanoma at 0.45 terahertz and discussed the differences between a sample at room temperature and a frozen sample. They state that the depth limitation, due to the high absorption coefficient of water (80-350 cm^{-1} at 0.1 to 2 terahertz [169] at room temperature, is limited to 0.2 up to 0.3 mm for biological tissue when assuming that the tissue consists of about 70% up to 85% water content [170]. However, for ice, the absorption coefficient of water is much lower (1 - 7 cm^{-1}) and thus the penetration depth could be enhanced. They have chosen 0.45 terahertz as "the disparity results is 90% of the incident signal surviving to a depth of 1.0 mm in ice, compared to a mere $<$0.0001% of the signal surviving in liquid water" [171]. For the simulation they concluded that low terahertz frequencies could indeed provide a differentiation between melanoma and skin up to a depth of 4mm, due to the different water content of skin being around 70% and melanoma about 80 to 85% [171].

A recent study carried out by Zaytsev et al. [172, 173] (2015) investigates dysplasia (an enlargement of an organ associated as a pre-step to cancer) on skin using terahertz imaging *in-vivo*. The authors conclude that the dysplasia (on four patients) shows a different permittivity and dielectric loss (ε' and ε") at low terahertz frequencies (0.3 to 0.5 THz) and at higher frequencies (0.8 to 0.9 THz) than does healthy skin tissue and non-dysplastic nevi [172]. A follow-up study on

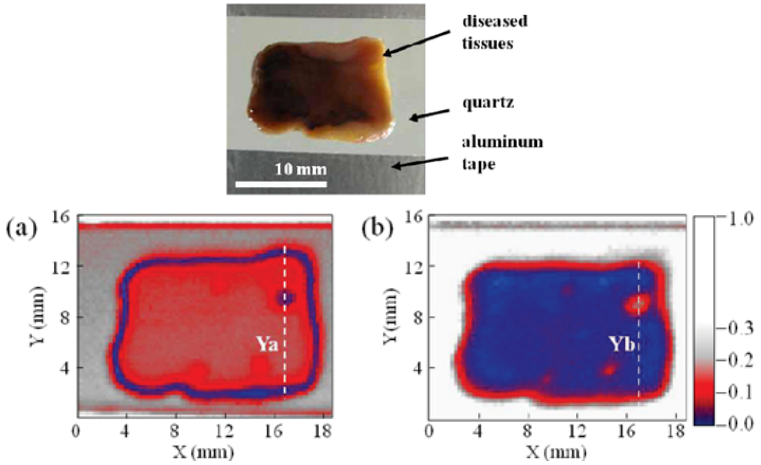

Figure 3-9: Images obtained from Sim et al. showing a photograph of the excited melanoma sample (top), a) maximum amplitude at -20 degrees Celsius and b) maximum amplitude at 20 degrees Celsius [168].

the complex refractive index showed significant changes between BCC and skin at frequencies between 0.8 and 1 THz; however, dysplastic and non-dysplastic nevi do not seem to distinguish between it and skin. The absorption coefficient, however, shows a change in BCC when compared to non-dysplastic nevus and healthy skin. It was concluded that significant differences between the THz characteristics of healthy skin and pathology may be observed and that THz-pulsed spectroscopy could become an effective tool for skin neoplasm diagnosis [173].

In 2017, Park et al. [174] performed a study on metastasis of frozen, excised lymph nodes of mice which were infected by murine melanoma cells for 30 and 15 days. Cellular interfaces in the dichotomized melanoma images were strongly correlated with the histological results. It was concluded that the image-processing technique is able to distinguish between metastatic and normal lymph nodes and may be useful as a supplementary technique for cryogenic pathologic examinations.

3.3 Potential for terahertz in melanoma diagnostics and imaging

Terahertz has been shown to be a promising technology for the detection of various (human) cancerous tissues. In particular, recent studies of BCC and SCC suggest the possibility of the detection of melanoma as well. Recent studies of the potential of terahertz for cutaneous melanoma are rare, which opens the opportunity for a study of terahertz technology's general ability to diagnose cutaneous melanoma *ex-vivo* as a tool to support dermatologists. Since melanoma originates from the dermal-epidermal junction at the stratum basale, which is deeper than BCC or SCC, it cannot be said with certainty that THz is applicable as a diagnosis tool. Because secondary peaks are visible at the stratum-corneum interface at the palms, where the SC is typically thick, there is a possibility that MM might reflect a secondary peak as well, due to changes in the RI. Alternatively, though melanoma might not be directly visible because of the infiltration thickness, differences in the surrounding tissue of the skin caused by changes in the apoptosis of the upper layers of the epidermis (on top of the MM) may be visible. Furthermore, terahertz might be useful for the detection of early stages of melanoma during the RGP, which would describe SSMM. And finally, if differences in the skin structure can be observed, terahertz reflectometry might be useful for margin detection, which could be of help to dermatologists during excision of suspicious lesions. As a consequence, while in this thesis the properties of freshly excised MM *ex-vivo* are investigated, the data acquisition is performed from the top of the skin rather on than sliced samples from histology to study the opportunity for using terahertz for the detection of melanoma *in-vivo*, e.g., with the help of a handheld probe.

In this Chapter, imaging modalities for the detection of cutaneous melanoma

have been discussed and terahertz technology has been introduced. Terahertz modes and external probes have been introduced and a literature review about the current status of bio-medical applications in the field of terahertz research has been given. The Chapter ended with a brief outlook about the potential use of terahertz technology for the detection of melanoma. In the next Chapter, the principle methods as well as noise-reduction techniques for the use of terahertz with freshly excised cutaneous melanoma are developed. Segmentation as the input for classification projects is introduced. Furthermore a study of the time window of chicken as a phantom for freshly excised melanoma will be performed.

Chapter 4

Method Development

The upcoming Chapters four, five and six broadly follow the steps that need to be performed for building computational models. The process starts with the sample data acquisition. As a second steps data cleaning is performed which deals with normalisation of the given data set, denoising and handling of null-variables as well as transformation of the data. The process also includes feature extraction and, for supervised systems, definition of classes for the classification process as well as feature selection. To create a supervised model, the labelled feature set is divided into training and test sets in order to determine the goodness of the model and to enhance the model during the training phase. The process is visualised in Figure 4-1.

This Chapter on method development describes the setup, measurement of

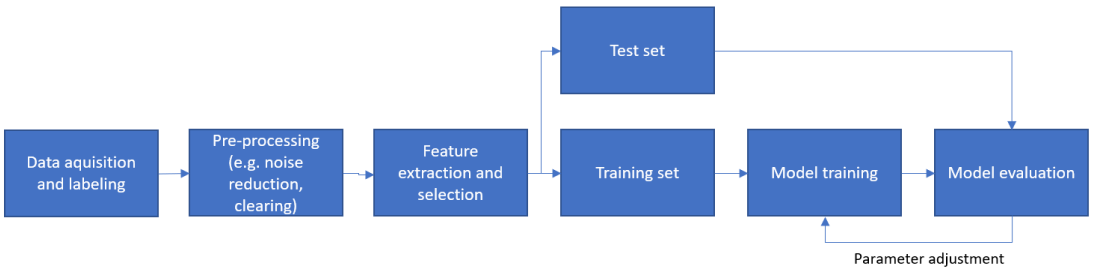

Figure 4-1: Steps for data analysis and supervised model building

the skin samples and transformations of the time-domain waveform which will be used in further Chapters. It is broadly divided into the "principle methodology and transformation" part (Section 4.1) but also covers some miscellaneous studies which were made before the melanoma samples were obtained. This includes a preliminary investigation of wavelet denoising (Section 4.2), which is typically applied to the raw terahertz waveforms before any transformations are performed and is a basic step before feature extraction. After the denoising, a description is given of the retrieval of features; pre-processing steps, such as straightening and segmentation of the visual images; and terahertz images (Section 4.3), which have been used for this study to compare visual images with the terahertz data obtained from the melanoma samples. Furthermore, a preliminary study (Section 4.4) using chicken skin was performed before human skin samples were obtained so as to define the time window in which it is safe to scan the future melanoma samples to prevent them from degradation. This was needed to obtain ethical approval from the LRI and the East Midlands Research Committee.

4.1 Principle methodology and setup for 2D and 3D Terahertz

This Chapter covers the basic setup used to scan the MM, which forms the basis of the thesis. Furthermore, transformations from the energy time-domain waveform are discussed. These include the transformation of the time-domain intensity waveform and Fourier transformation and the further processing conducted to obtain obtaining the frequency-dependent complex refractive index and the complex permittivity. Most of the transformations are used later to extract features from the data obtained for further processing and modelling.

4.1.1 Terahertz setup

Terahertz waves were generated using a Teraview TPS3000 in combination with the Imaga module provided by Teraview, Cambridge, UK. Terahertz waves are generated by firing a femto-second-laser beam at a superconductive dipole switch (ltGaAs). For focusing reasons, directly behind that switch there is a highly resistive hyperhemispherical silicon lens. By using a beam splitter, the beam is divided into a reference beam and a sample beam. The reference beam is used to detect the THz wave by using an optical gated switch.

For the purpose of measuring biological tissue, it is almost always necessary to use terahertz in reflectance mode rather than in transmission mode. The reflectance module redirects the beam to the sample with an incidence angle of 30°. Since the THz-signal is very sensitive to the exact position of the sample, a SiO_2 quartz sample holder with a refractive index of 2.08 is used. The SiO_2-sample holder has a negligible absorbance but changes the incidence beam angle towards the sample to 14.5° (based on an initial angle of 30°) because of its refractive index.

4.1.2 The time-domain waveform

THz waveforms detected from angle-based reflectometry are recorded using the propriety software provided by Teraview, with a maximum peak centred at unity of the time window to make measurements comparable with each other. The time window has been selected to be 35 ps (5 Volts) with a resolution of 17 fs, which results in a THz waveform consisting of 2,048 data points. This window size is chosen to capture the largest amount of data while avoiding Fabry Perot (multiple reflections) effects from the underlying quartz sample holder, as a secondary reflection must be filtered out via bandpass filters to further process the data—especially to avoid secondary harmonics in the frequency domain.

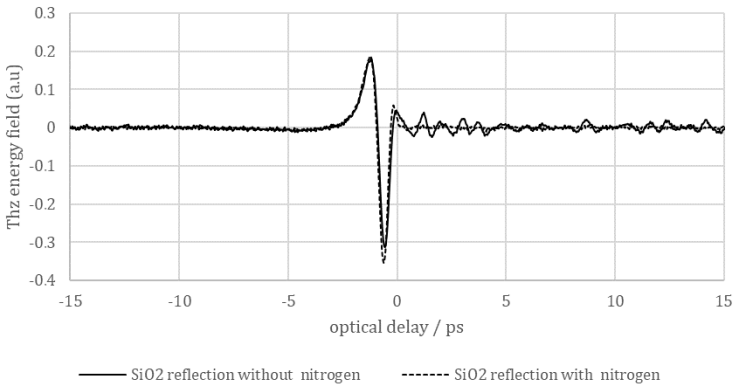

Figure 4-2: Air – Sample holder reflection from the top of the quartz with and without purging the underlying sample chamber with nitrogen.

To produce 3D images, an x,y-stepper motor has been setup to capture a region of 2x2 cm with a resolution 0.2 mm. This has resulted in a 3D image the size of 100x100 waveforms, which equals 10,000 waveforms in total for each sample. Beforehand, the x,y adjustment was set up to the centre of the quartz sample holder for reproducibility and comparability. A window size of 2x2 cm captures the whole circular sample holder and parts of the surrounding metal gantry as well.

To avoid water-vapour artefacts from the beam travelling through air under the sample holder, the underlying chamber is purged with nitrogen; the differences with / without nitrogen are shown in the resulting waveforms in Figure 4-2. To ensure that the chamber has been completely purged, experiments are performed five minutes after purging with nitrogen began.

4.1.3 Hilbert Transform for intensity transform

To transform an energy waveform in the time domain into its corresponding intensity waveform, one is required to transform the real-valued collected waveform into its analytical signal. The resulting intensity function has no negative values and removes the phase information from the original signal.

By transforming the energy waveform $E(t)$ into the intensity function $I(t)$, the complex conjugate of the real-valued signal is required. This may be easily obtained by utilising the Hilbert transform, which is conventionally used in signal processing to obtain the complex envelope of a real-valued signal.

The Hilbert transform is obtained by convolving $E(t)$ with $1/\pi t$. In the frequency domain, this is equivalent to shifting the phase of the negative frequency components by $+\pi/2/2$ and of the positive frequency components by $-\pi/2$ [175].

Figure 4-3 shows the process of a THz TD waveform transformed into its corresponding analytical signal and its corresponding intensity function using the quartz sample holder in contact with air.

The definition of the Hilbert transform Hf of a function f is as follows:

$$H \cdot f(t) = \frac{1}{\pi} \int_{-\infty}^{\infty} \frac{f(x)}{t-x} dx \tag{4.1}$$

By transforming a real-valued signal to an analytical signal, an envelope of the real-valued signal is established. The envelope is calculated by creating the analytic signal of the input using the Hilbert transform. An analytic signal is a complex signal in which the real part is the original signal and the imaginary part is the Hilbert transform of the original signal.

Mathematically, the envelope $e(t)$ of a signal $x(t)$ is defined as the magnitude of the analytic signal, as is shown by the following equation:

$$\text{envelope} = \sqrt{E(t)^2 + \hat{E}(t)^2} \tag{4.2}$$

where is $\hat{E}(t)$ the conjugate complex of the real-valued signal $E(t)$.

The relationship between the measured energy field and the intensity is given as follows:

$$I \propto |E|^2 \tag{4.3}$$

Since the Energy E rather than E^2 is measured, it can be seen from Equation 4.4 that one has to multiply E with its conjugate complex. However, since the signal is real valued only, the Hilbert-transform is applied to transform the real signal into an analytical signal, which is then transformed according to Equation (4.3). From Equations (4.2) and (4.3), it can be seen that

$$|E|^2 = E\bar{E} = \text{envelope} = \sqrt{E(t)^2 + \hat{E}(t)^2} \tag{4.4}$$

The intensity waveform may be beneficial for further processing, as it might be easier to interpret and process because the phases are not taken into account by the intensity function. Furthermore, it could make the results comparable to other frequently used techniques: e.g., TD-NIR, which measures intensity rather than energy.

4.1.4 Fourier Transform for frequency spectrum

The discrete Fourier transform is used to dissemble a finite time-domain signal into its sinusoidal components, using

$$y_k = \sum_{j=1}^{n} \omega^{jk} x_j \tag{4.5}$$

where ω is

$$\omega = e^{-2\pi i/n} \tag{4.6}$$

The Fourier transformation provides the frequency-dependant magnitude and the corresponding phases that are used to dissemble the time-domain waveform into its sinusoidal components and forms the basis for further transformations, such as the frequency-dependant refractive index and absorption but also the complex permittivity. Since the phase information is typically wrapped around,

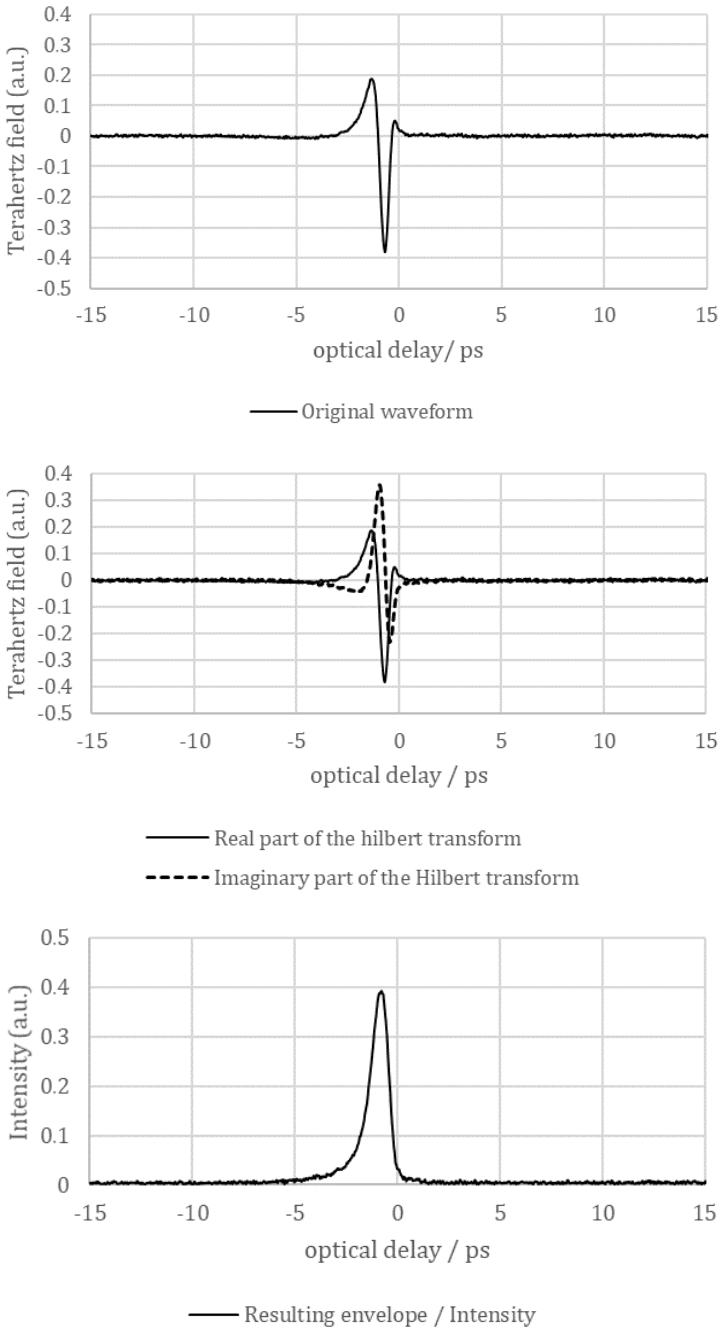

Figure 4-3: Original THz beam of air in contact with the sample holder (top), converted to the analytical signal with real and imaginary part (centre) and resulting intensity TD waveform after transform (bottom).

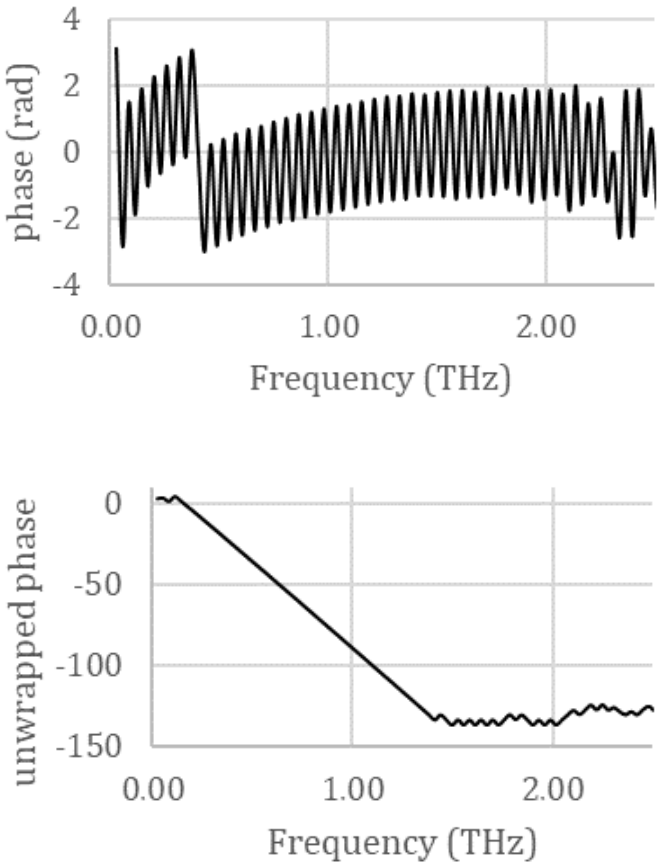

Figure 4-4: Wrapped phase (top) and unwrapped phase (bottom) of air in contact with the sample holder.

phase unwrapping is also performed to correct phase angles and enhance plots, as illustrated in Figure 4-4 taken from the sample holder in contact with air in refection geometry.

The unwrapped phase plot from Figure 4-4 seems to indicate that a stable phase can be obtained between 0.3 and 1.3 THz, which corresponds with the magnitude image shown in Figure 4-5.

4.1.5 Frequency dependent complex refractive index

The refractive index (n) gives the optical properties of the material under investigation in terms of the optical density compared to the speed of light in vacuo.

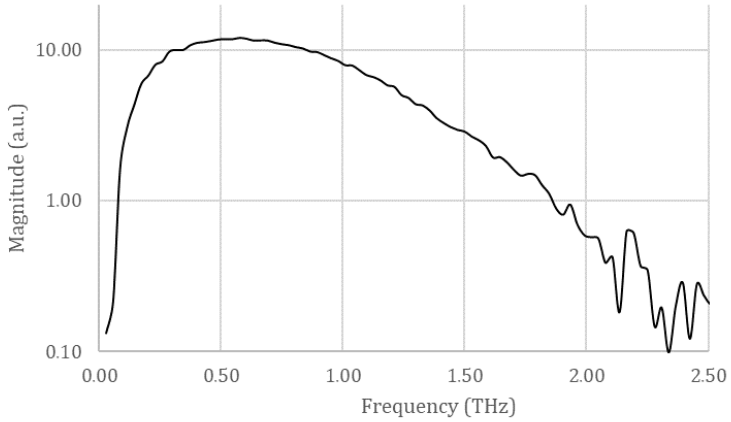

Figure 4-5: Magnitude of the sample holder in contact with air.

It is defined as the dimensionless unit dividing the speed of light of the medium (c_{medium}) with the one in vacuo (c_{vacuo}):

$$n = \frac{c_{medium}}{c_{vacuo}} \tag{4.7}$$

If the medium has absorptive properties, the frequency-dependant refractive index becomes complex, wherein the imaginary part is the extinction coefficient (κ).

$$\hat{n} = n + j\kappa \tag{4.8}$$

Since the absorption coefficient (α) is dependent on the angular frequency (ω), the extinction coefficient is used to obtain the absorption as follows:

$$\alpha = 2\kappa \frac{\omega}{c_{vacuo}} \tag{4.9}$$

To obtain the refractive index of an unknown material, a second measurement of a material with known refractive index (or a full reflective mirror) is required. This is obtained by utilising the Fresnel equations and is discussed in detail in Chapter 7.1.

4.1.6 Complex Permittivity

The complex permittivity is used to describe the electro-magnetical properties of materials and can be obtained from the complex refractive index. The connection can be made through the Kramers-König relationship, which has been used to improve sample characterisation in the terahertz regime (compare [176] and [177]). The relationship is given by

$$(n + j\kappa)^2 = (\epsilon_r' + i\epsilon_r'')\mu_r \tag{4.10}$$

where ϵ_r' and ϵ_r'' are the real and imaginary parts of the permittivity and μ_r is the magnetically permeability. Considering a negligible magnetically permeability ($\mu = 1$), the conversion from equation 4.11 is simply:

$$\epsilon_r' = n^2 - \kappa^2 \tag{4.11}$$

and

$$\epsilon_r'' = 2n\kappa \tag{4.12}$$

Both, the refractive index and the permittivity have been used to investigate skin cancer samples in the terahertz regime.

4.2 Noise reduction using the wavelet transform

The low systems energy, which is typically in the femto- up to nanojoule range [178] provides a relatively low signal output. In addition, signals reflecting from the surface of (or inside) biological tissue can be weak, as they contain a large amount of water, which is one of the strongest absorbers in the THz regime.

In the case of the detection of metal in a biological tissue, measurements have to

be taken in reflectance mode, as the metal, being an almost perfect reflector [179], does not allow the terahertz beam to pass through. It should also be stressed that, to detect signals in reflectance mode, the incidence beam has to travel twice as far through the sample material before it reaches the detector, which further attenuates the signal strength.

A simple method for noise reduction is to average the signal; however, this method increases the data-acquisition time and may not be suitable for *ex-vivo* biological measurements, as the tissue is prone to drying out.

Alternatively, noise can be reduced by using digital signal-processing filters based on high-pass or low-pass filters. One of the best known de-noising algorithms is the wavelet family, which denoises a signal using an iterative algorithm. However, suitable mother-wavelets and scales have to be chosen to ensure that the process will not over-fit (over-denoise) and therefore lose the original signal.

A number of authors have used wavelet analysis to good effect in terahertz imaging: Ferguson et al. describe the usefulness of wavelets and Wiener deconvolution filtering for de-noising terahertz imaging in transmission mode [180]. Yin et al. used wavelets to restore topographic images out of transmission mode measurements [181] while Hadjiloucas (et al.) studied denoising and system identification in the wavelet domain to enhance the frequency range in THz images [182]. Chen et al. used wavelets in the frequency domain in reflection imaging to deconvolve a signal obtained from a human palm *in-vivo* [183].

Therefore, for this study, the aim is to find suitable denoising algorithms using the wavelet transform to enhance the visualisation of the penetration depth of a metal microneedle within a biological tissue (*ex-vivo*) using terahertz imaging in reflectance mode. The microneedle embedded in skin acts as a phantom of a secondary reflection from inside the skin sample. The aim is to find a suitable denoising technique that would not alter the primary reflection—i.e., from the

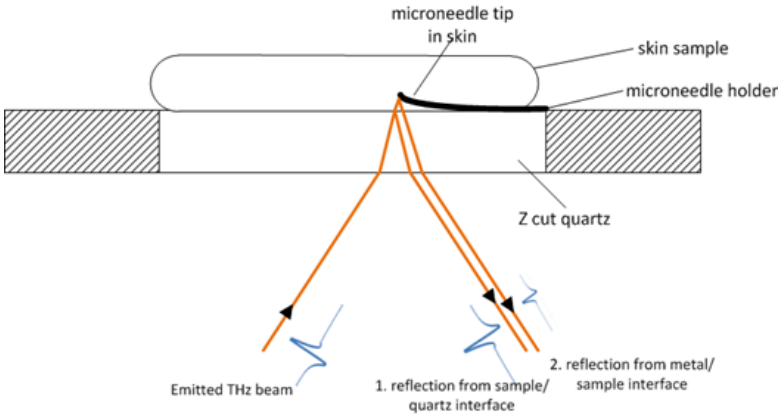

Figure 4-6: Schematic of the reflection measured from the sample and the microneedle.

skin / sample holder reflection—as it needs to be used for further processing. It is also necessary to enhance the secondary reflection and remove noise from data obtained from inside the skin.

4.2.1 Tissue preparation

Fresh pig tissue was obtained from a veterinary school in Loughborough, and the skin from the back of the ear was dissected, as this is similar to human skin [184, 185]. For each measurement, the sample was slightly wiped to reduce water artefacts at the skin / quartz interface. Depending on the size of the sample, a 3D image scan took between 10 and 15 min. at an x,y-resolution of 0.2mm.

A microneedle with a length of 1mm and a width of 200 microns was inserted into the skin. A 3D image was acquired with and without the microneedle. In the time domain, the microneedle was visualised by a second reflection of the incidence waveform reflecting from the metal/skin interface, as indicated in Figure 4-6. Three samples (4, 10, and 12) were chosen for this study, as the secondary reflection was clearly visible without wavelet denoising beforehand.

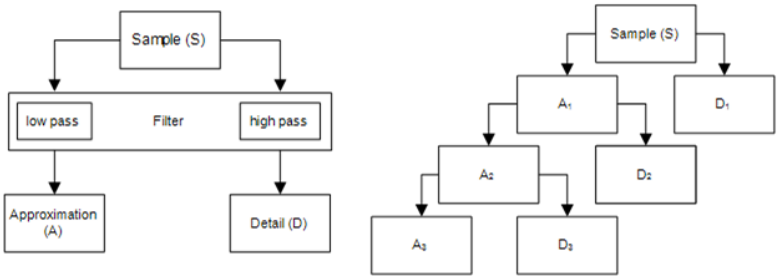

Figure 4-7: Schematic process of the wavelet denoising process.

4.2.2 Wavelet transforms for denoising and reconstruction

The wavelet transform attempts to remove noise from signal but retains the original signal by utilising a multi-level decomposition approach. In each step, the sample (S) is divided by a low-pass and a high-pass filter into two new waveforms, called Approximation (A) and Detail (D). Using the approximation from the last scale as the input for the next filter process, an iterative multi-level process is used until the maximum number of scales are reached. It is noteworthy, that the Approximation and Detail data are down-sampled and contain half the size of the initial wave.

To quantify and compare results from the wavelet transforms, the signal-to-noise ratio (SNR) is used, which is defined as the maximum energy peak (E_{Max}) divided by the standard deviation of (the assumed) noise (σ):

$$SNR = \frac{E_{Max}}{\sigma_{noise}} \tag{4.13}$$

The maximum energy peak is used, as it is important to maintain the maximum peak for further analysis when creating the ratios of the reference wave and the sample wave.

The Wavelet Transform is used with a soft, fixed threshold function [133] determined from unscaled white noise.

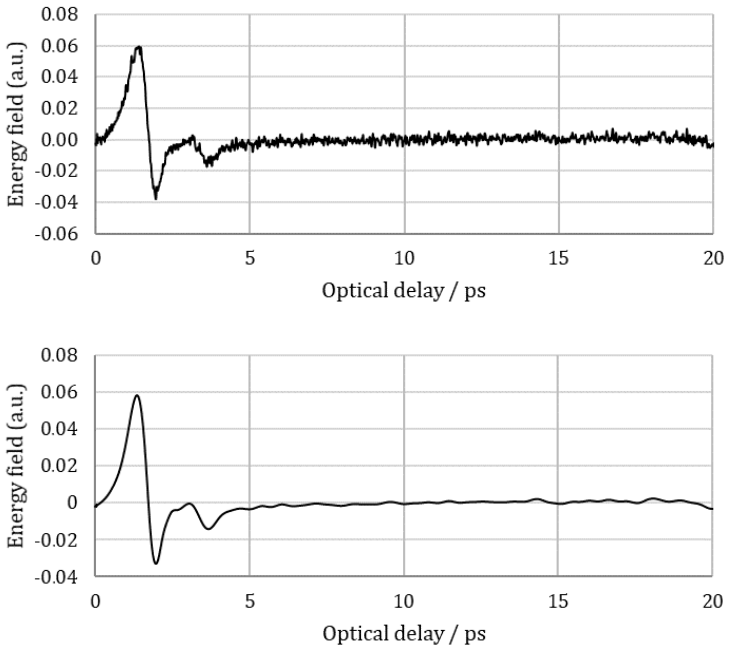

Figure 4-8: Original waveform (top) and wavelet de-noised waveform (bottom) of sample 4. A second reflection is clearly visible at around 3 ps.

4.2.3 Results: Wavelet denoising

The standard deviation of noise was defined as the optical delay between approximately 10 ps to 15 ps (points 1000 to 1500) in the waveform, as this is the region in which no significant data is reflected. We choose the region only up to 15 ps because, a small negative peak is shown on all data collected at around 20ps, which is most likely due to an internal reflection from the silica lens.

Figure 4-8 (top) shows the original waveform reflected from Sample 4. The initial peak (E_{Max}) is the reflection from the quartz/skin interface, and the second (negative) peak is the reflection from the microneedle. The phase change of the microneedle reflection is due to the full reflecting metal causing a phase shift of 180 degrees, which is a boundary condition of the Fresnel equation.

The first analysis was carried out using the Daubechies 4 mother wavelet on different scales to determine at which scale the denoising process would begin to overfit. As shown in Table 4.1 and Figure 4-9, using three different samples, the

Table 4.1: SNR of sample 4,10 and 12 using Debauchies 4 with scales 1 to 8

Scale	Sample 4 SNR	Sample 10 SNR	Sample 12 SNR
Raw	40.07	61.4	126.67
DB4-1	41.83	63.42	130.85
DB4-2	51.20	71.36	147.60
DB4-3	67.14	87.31	172.90
DB4-4	87.62	118.60	213.24
DB4-5	108.82	130.21	224.83
DB4-6	98.38	95.19	187.70
DB4-7	90.89	31.48	50.12
DB4-8	78.52	17.44	8.25

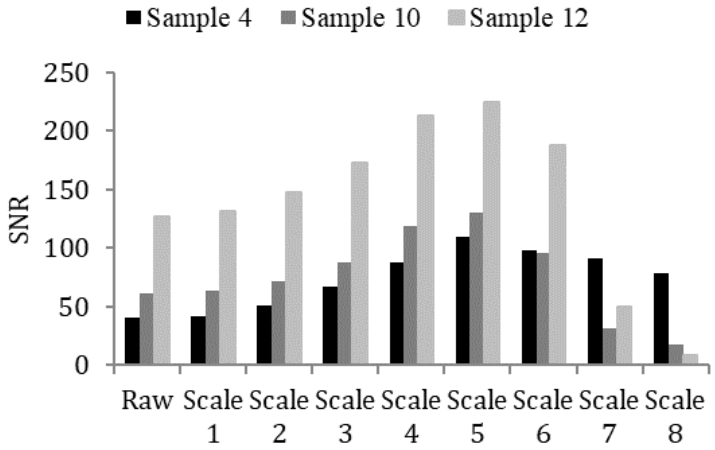

Figure 4-9: Signal to noise ratio of sample 4,10,12 using DB4 on different levels

SNR improves until the maximum values of $SNR_{sample4} = 108.82$, $SNR_{sample10} = 130.21$ and $SNR_{sample12} = 224.83$ are reached and before a decrease in the SNR is observed at scale 6 and beyond. This has been observed on all mother-wavelets under investigation (data not shown).

The energy maximum peak value from the time-domain waveform has been taken as quantification as a measure of the signals stability (durability). The maximum peak remains stable until the fifth scale of the wavelet transform before it begins to degrade on all samples, as shown in Figure 4-10. The maximum peak differences between the three samples are most likely due to fluctuations in

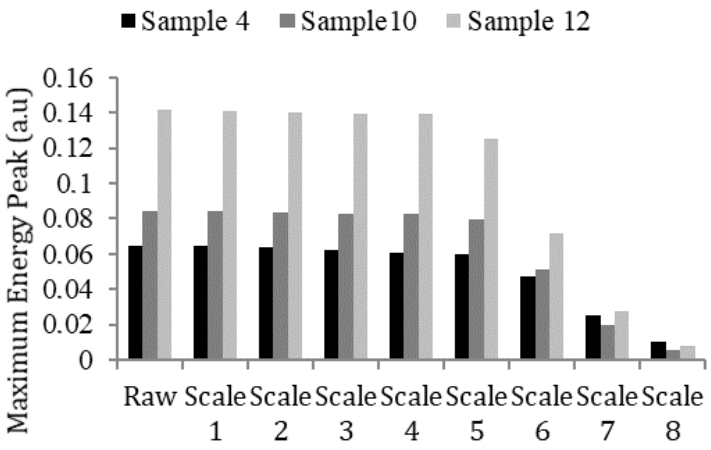

Figure 4-10: Maximum energy peak values of the raw and the denoised waveforms of samples 4, 10 and 12

laser emission energy but may be normalised to the reference and/or the baseline measurement for further research.

Further analysis was carried out using the DeBauchies 1 to 10, Symlets 2 to 8, Coiflet 1 to 5, Haar and the discrete approximation of the discrete Meyer (dmey) wavelet on all samples on Scale 5 to find the most suitable mother-wavelet, which further improves the SNR (Table 4.2). All mother wavelets increase the SNR significantly; however, the discrete Meyer wavelet showed the best performance with an improvement of the SNR by factors of 2.8 (Sample 4), 2.2 (Sample 10) and 1.8 (Sample 12).

Furthermore wavelet analysis was performed on the quartz/air interface and the quartz/mirror reference interface without a biological sample and with the equivalent maximum SNR results on discrete Meyer Scale 5, with $SNR_{Air} = 168.68$ (from original 76.31) and $SNR_{Mirror} = 129.86$ (from original 79.52).

In a key result, we found that the Meyer mother wavelet on the fifth scale would produce the most reliable result, as is shown in Figure 4-10 before and after wavelet denoising.

Table 4.2: SNR of samples 4,10 and 12 using different mother wavelets on scale 5.

Wavelet	**Sample 4**	**Sample10**	**Sample 12**
Original	40.07	61.46	126.67
Coif1	110.31	126.49	222.92
Coif2	108.69	130.41	224.97
Coif3	107.79	131.54	225.82
Coif4	107.15	132.03	226.38
Coif5	106.68	132.29	226.78
Sym2	110.40	126.22	222.78
Sym3	109.45	128.92	224.13
Sym4	108.82	130.21	224.83
Sym5	108.34	130.95	225.30
Sym6	107.95	131.40	225.66
Sym7	107.61	131.71	225.97
Sym8	107.32	131.92	226.22
DB1	112.04	118.71	219.28
DB2	110.40	126.22	222.78
DB3	109.45	128.92	224.13
DB4	108.82	130.21	224.83
DB5	108.34	130.95	225.30
DB6	107.95	131.40	225.66
DB7	107.61	131.71	225.97
DB8	107.32	131.92	226.22
DB9	107.07	132.08	226.45
DB10	106.85	132.20	226.64
Dmeyer	112.00	133.23	227.48
Haar	112.04	118.71	219.28

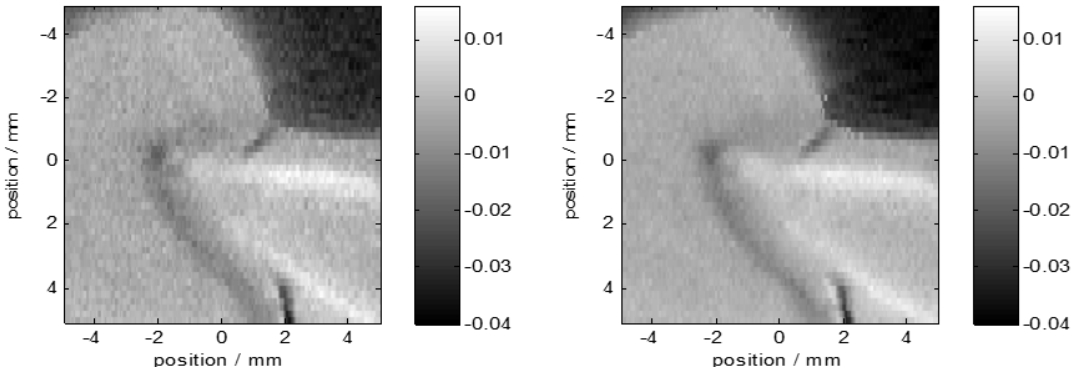

Figure 4-11: Original peak reflectance image of skin sample 4 with the microneedle (left) and wavelet denoised result of the same peak reflectance (right).

4.2.4 Conclusion

This study analyses wavelet denoising and reconstruction, which were used to identify a microneedle in freshly excised pig skin. It has been demonstrated that the fifth scale of the wavelet transform increases the SNR. Furthermore, the wavelet families Haar, Meyer, Daubechies, Symlet and Coiflet were used to increase the signal-to-noise ratio. Overall, the Meyer mother-wavelet outperformed the other wavelets using five scales with an SNR improvement factor between 1.8 and 2.8.

The technique might be used to enhance the usefulness of terahertz in combination with targeted drug delivery via microneedle channelling technology, thereby allowing more precise targeting of cancerous tissue and / or to observe the healing process.

This method might be used to improve the reflection signal from different layers of biological tissue. It may be used in conjunction with penetration-enhancing agents (i.e., glycerol) [186] to further improve the signal-to-noise ratio *in-vivo* and *ex-vivo*.

4.3 Segmentation based on visual images of lesions

Visual images were collected right before the examination with the terahertz machine on the sample holder by performing an overhead shot with a conventional digital camera (Olympus VG-160). To quantitatively compare the visual images taken before the terahertz scanning from under the quartz, a number of preprocessing steps are needed to accurately map the THz data onto the visual image and to perform feature extraction. The skin terahertz data collected needs to be separated from the surrounding air and air-gaps that may occur and may need to be filtered out. On the visual image, the regions of clearly infiltrated tissue need to be separated from the presumably healthy tissue. By using image-registration

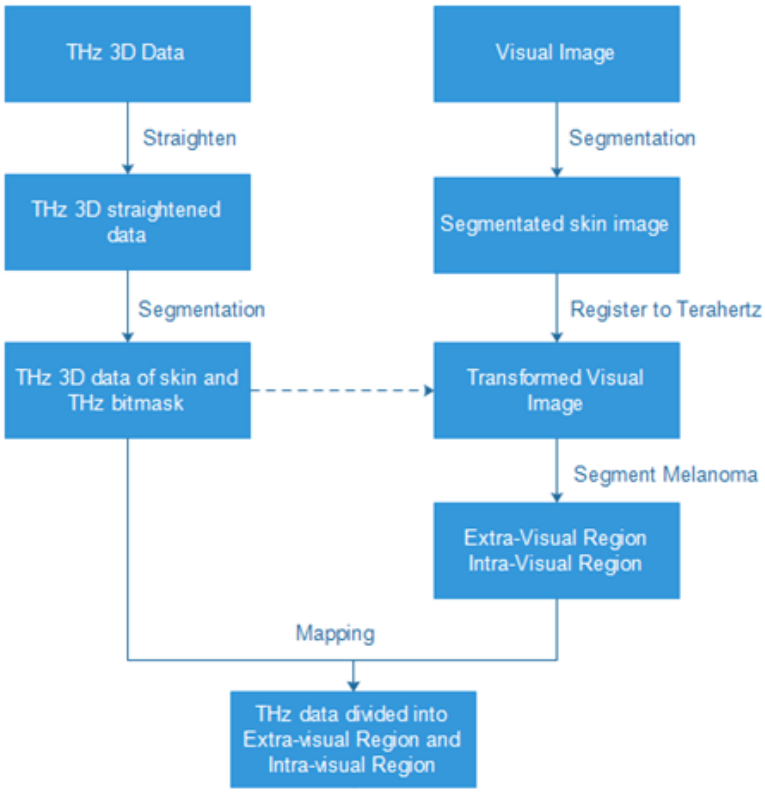

Figure 4-12: Overview of pre-processing steps for segmentation and mapping of visual images onto terahertz data.

methods, the visual image will be mapped on the terahertz image by reducing the resolution and performing translation, rotation and scaling.

Figure 4-12 identifies the steps needed to perform feature extraction and segment the terahertz data into inter-visual (IVR) and extra-visual regions (EVR). This method was applied to all malign samples collected to compare the features from the terahertz data with the visual images. In the following section, these steps are discussed in detail.

4.3.1 Straightening (rectifying) Terahertz data

Though all practical steps were performed in the initial setup of the terahertz machine to gain the maximum energy reflected by the sample, misalignments may appear during the setup of the x and y-stages which cannot be ruled out by

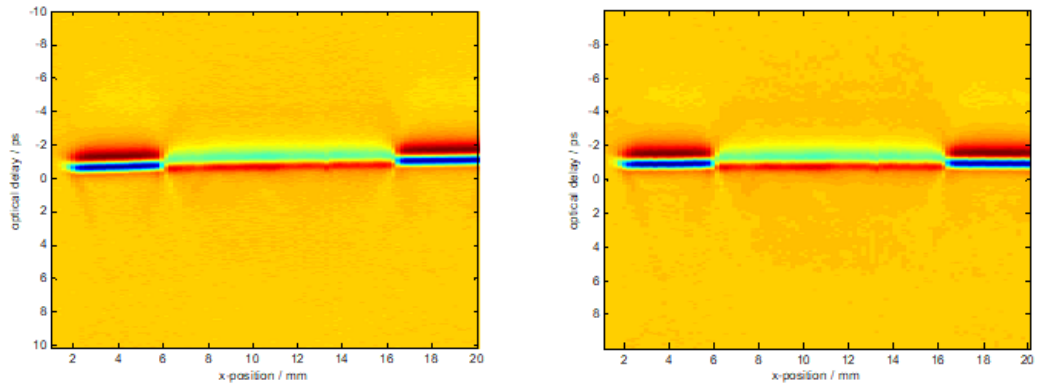

Figure 4-13: B-Scan of a sample surrounded by air before (left) and after (right) the correction process.

adjusting the mirrors and moving the top of the sample holder to the focus of the terahertz beam. Such misalignments are difficult to circumvent, as they appear to be in a range of a couple of microns, but they are reversible using simple linear functions:

$$f(x,y) = (\frac{\Delta od}{\Delta x}(x - x_1) + od_1, \frac{\Delta od}{\Delta y}(y - y_1) + od_1) \tag{4.14}$$

where od is the optical delay, x is the position on the x-axis and y is the position at the y-axis.

Since the scans capture the surrounding quartz/air interface around the sample, points at the top-left and bottom-right are chosen. The optical delay positions of the maximum peaks are compared to each other and aligned by applying Equation 4.14 to each time-domain waveform.

An example is shown in Figure 4-13, which represents a B-Scan through a skin sample which was mis-aligned on purpose to show the data before and after applying the two linear functions from Equation 4.15. This simple procedure has the advantage that it preserves relative shifts of the waveforms and phase shifts (by 180 degrees).

4.3.2 Skin segmentation and air-gap filtering

Segmentation is a semi-automated process of dividing an image into regions of interest. We use binary segmentation to divide the data into "skin" and "everything else". This is not only useful to extract the skin sample from the surrounding air but also to detect and remove possible air-gaps and other artefacts.

Segmentation is a process of separating the sample from the rest of the collected data (i.e., the metal sample rig and air). We use a semi-automated segmentation approach in which one waveform of the sample is selected as a kind of reference waveform. Using a similarity function, the algorithm compares all other waveforms to the one chosen. If the compared waveform has a similarity above a certain threshold, it belongs to the sample; otherwise it will be discarded.

All waveforms are compared with a pre-chosen waveform of the skin using a cross-correlation algorithm. A fixed threshold is determined by the R^2 value. Good results were achieved using an R^2 value of 0.85.

The mean ($\bar{x}$) of a waveform is defined as the sum of all values x of the waveform divided by the number of values (n):

$$\bar{x} = \frac{1}{n}\sum_{i=1}^{n} x_i \tag{4.15}$$

The covariance of two waveforms (x,y) with equal lengths (n) describes the variance between those two and is defined as follows:

$$cov = \frac{1}{n-1}\sum_{i=1}^{n}(x_i - \bar{x})(y_i - \bar{y}) \tag{4.16}$$

The correlation coefficient (ρ) between two waveforms is then calculated as follows:

$$\rho = \frac{cov(x,y)}{\sqrt{cov(x,x)cov(y,y)}} \tag{4.17}$$

The r-square (R^2) value is then simply

$$R^2 = \rho^2 \tag{4.18}$$

The R^2 value is used as a measure of fit throughout this analysis. Figures 4-14 and 4-15 show the segmentation and air-gaps filtering on Sample 2 and the resulting bitmask. To further exclude noise that may appear around the edges of the air-gaps, further edge detection has been applied which enlarges the air-gap area as shown in Figure 4-15 (right).

4.3.3 Image registration of visual image

To register the visual image, a segmentation process similar to that described in the previous Chapter is applied. As the first step, the visual sample is divided into the skin sample and the background part (data not shown), leaving only the skin sample for further processing. To compare the visual images with the terahertz data, the images need to be altered to fit on the terahertz images by scaling them down and translating them on top of the terahertz images, which is also known as registering the visual image on the terahertz image.

Image registration is an important step in image processing in which two (or more) images of the same scene are brought in relation with each other. Image registration typically requires one of the image to be the reference image—that is, the image onto which the other data should be mapped. It is also referred to as a fixed image, as operations are performed on the other image (moving image) to map those on top of each other, as shown in Figure 4-16

For the comparison of a visual image with the terahertz image, the terahertz maximum-energy feature was chosen as the fixed, reference image, as the terahertz data is in 3D and is typically of lower resolution than the visual image. Also, by

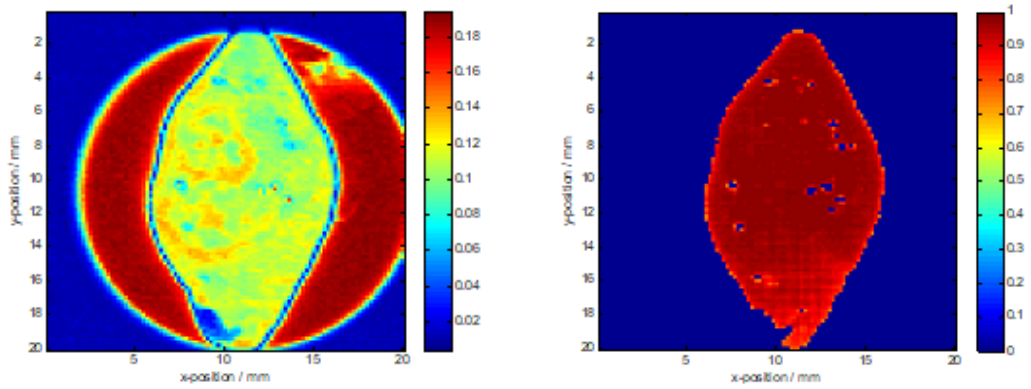

Figure 4-14: Terahertz segmentation of human skin sample 2. Maximum energy peak image in false colour (left), false colour R^2 value (>0.85) compared with an arbitrary point of the skin. The colourbar represents the R^2 value.

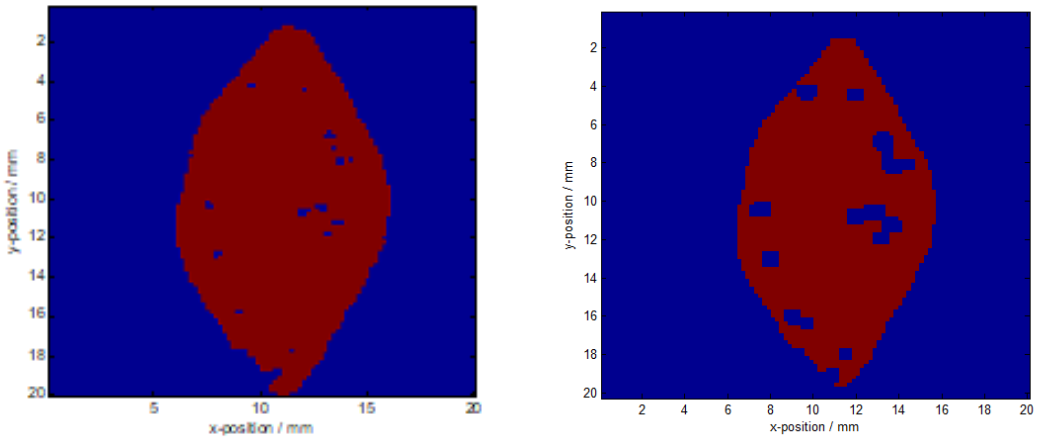

Figure 4-15: Bitmask after segmentation of sample 2 with visible air gaps (left), bitmask of sample 2 with edges expanded to further reduce noise (right).

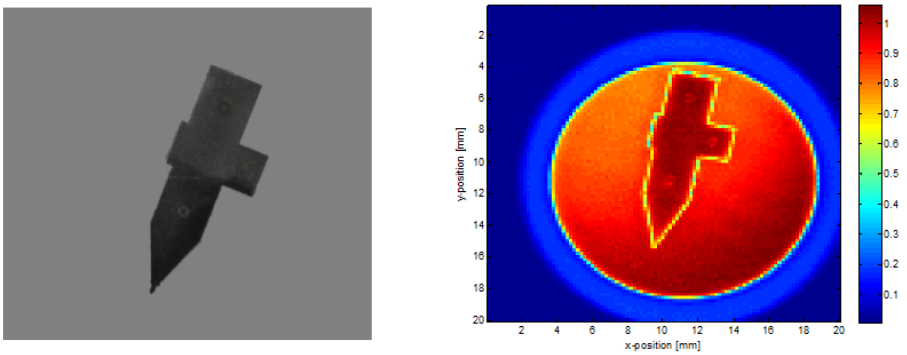

Figure 4-16: Phantom of a microneedle holder as grayscaled visual image (left) and its corresponding Terahertz maximum energy peak image (right).

distorting an image, one typically needs to interpolate intensity values from neighbouring pixels, which in the 3D terahertz waveform would not be advantageous, as it would increase the data space without adding relevant information to the data.

The operations performed on the visual image are translation, rotation, skewing and shearing. Before image registration is performed on the visual image, the visual image is pre-processed, which means that it has been transformed into intensity values (colour information is lost) and the background has been cut.

To demonstrate the image registration procedure, a microneedle holder was scanned in terahertz and a picture with an ordinary camera was made, as is detailed in Figure 4-16. Because the images do not have comparable intensity values, an automatic approach was not chosen; instead, an extrinsic controlpoint procedure was used. The control-point procedure works by selecting similar points, or points of interest, like sharp edges, on both images. A minimum of four or more points is required. In data obtained from skin, 10 to 15 points are typically chosen. Since the phantom (the microneedle holder) has a geometry suitable to demonstrate the procedure, 11 points were chosen on the edges of the microneedle, as indicated in Figure 4-17.

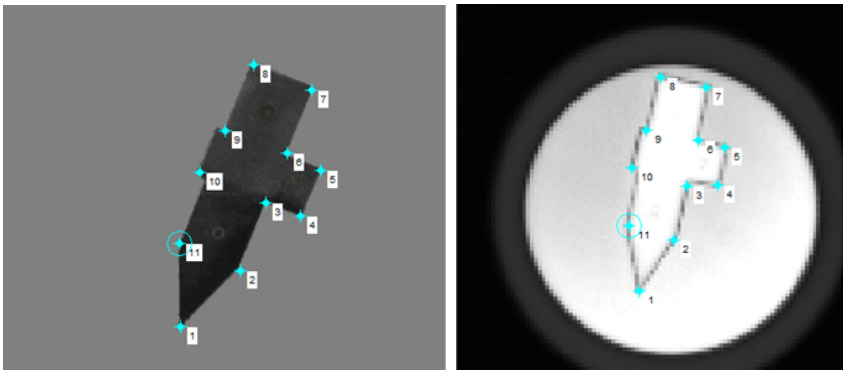

Figure 4-17: Image registration of the microneedle holder to create a similarity matrix of the visible intensity image (left) and terahertz image maximum peak image (right)

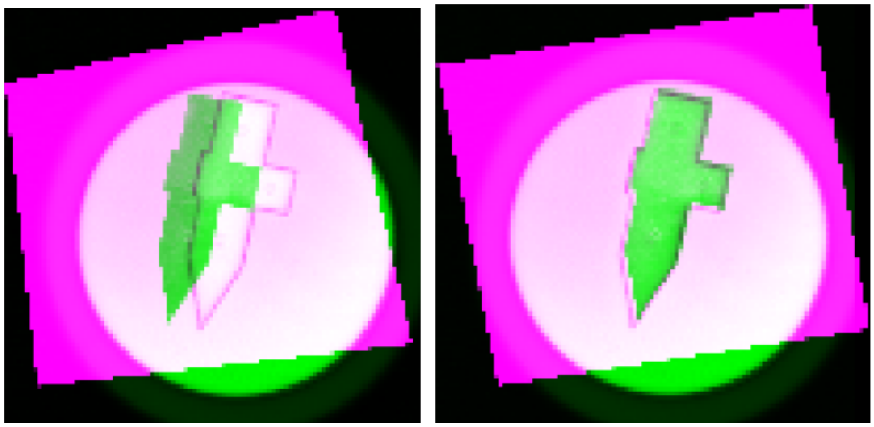

Figure 4-18: False colour image registration after mapping (left) and mapping plus translation (right) of the visual (purple) and the terahertz image (green).

While the visual image can be slightly distorted depending on the angle of the camera to the sample, the visual image gets mapped on top of the terahertz images by using a projective algorithm that utilises translation, rotation and scaling.

To show the successful procedure and to provide visual validation, both images are then mapped onto each other (using a false colour overlay, Figure 4-18). Unwanted distortions would attract attention at the edges of the microneedle holder, and the procedure with different or more control points would need to be repeated.

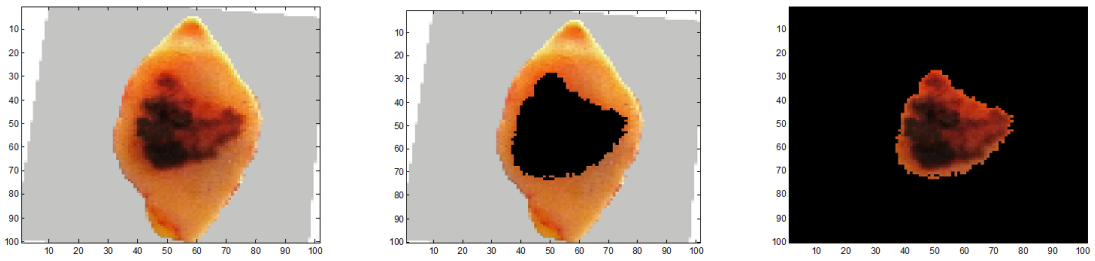

Figure 4-19: Original visual image (left) and segmented images of the extra-visual region (centre) and inter-visual region (right)

4.3.4 Skin segmentation into 'intra-visual region' and 'extra-visual region'

The image data from the visuals is now in the same size and rotation / transformation as the 3D terahertz data. In this step, a second segmentation is used to divide the visual and the terahertz data into the classes labelled 'intra-visual region (IVR) and 'extra-visual region (EVR)'. For this purpose, an arbitrary point (pixel) in the visual image is selected that is inside the pigmented lesion (i.e., for an intensity-based image the darker area of the skin, as shown in Figure 4-19. The segmentation is then performed based on a threshold of the intensity (typically, 0.2 was used). With this procedure, the created region of IVR and EVR is then applied to the terahertz waveforms.

4.4 Study on the time window for skin tissue experiments

Processed chicken was obtained from a local butcher. The chicken skin was detached from the rest of the tissue and divided into three parts of roughly the same size (1 cm). Sample 1 was placed in saline solution for twenty minutes. Sample 2 was not altered, and Sample 3 was wiped with wad of cotton wool prior to the

start of the experiment.

All three samples were placed on the sample holder and put on the gantry. Scans of all samples were performed four times at an interval of 30 minutes. While a full scan takes approximately 15 minutes, the samples, and the sample holder (etc.) were not moved from their original positions. This ensured that sample positions remained roughly the same throughout the experiment.

4.4.1 Statistical Analysis

From each sample, a centerfield of 10x10 pixels (which corresponds to 2x2mm) was taken. To evaluate statistical data, the variability and standard deviation of each sample were measured. Furthermore, a cross-correlation comparing each scan with the first scan was performed to determine how much the data has in common after a certain time has passed, as the primary aim of this study is to evaluate the differences from the original scan with the scans taken at a later point in time. Using this procedure, we compared the three samples over time, thus finding changes that appear over time.

4.4.2 Results

The frequency-dependant refractive index was also calculated to evaluate the dehydration. Because the refractive index of water is relatively high (around 2) and the refractive index of air is 1, we expect the experiment to reflect the dehydration by a degrading refractive index.

The first thing to notice after the scans are completed is that wet tissue has a larger border than tissue which was previously wiped. This is due to the afflicted water that surrounds the tissue of Sample 1 (kept in saline) and Sample 2 (not processed), as can be seen from Figure 4-20. Figure 4-20 shows the sample's maximum energy peak normalised to the maximum energy peak of all scans (0.1960,

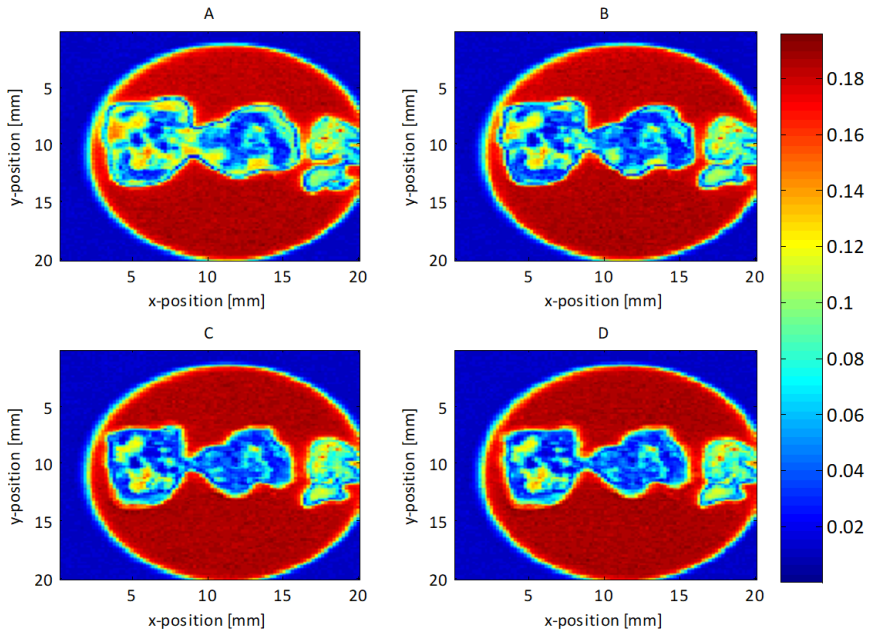

Figure 4-20: Samples 1-3 repeated scan after 0 minutes (top left), 30 minutes (top right), 60 minutes (bottom left) and 90 minutes (bottom right), where sample 1 kept in saline (left sample), unaltered sample 2 (middle sample) and sample 3 wiped sample (right sample).

which is the top value of the colourbar). The left sample (Sample 1) has been kept in saline while the sample in the centre (Sample 2) has not been altered and the right sample (Sample 3) has been wiped. Furthermore, changes in the variability of the maximum peak can be observed from samples 1 and 2 when comparing scan1 (0 minutes) with the second scan taken after 30 minutes (compare Figure 4-20 a and b). The variability and the maximum energy seems to be lower and more constant at scans 3 and 4, as can be seen from Figure 4-20 c and d). The colourbar shows the maximum energy peak.

Because water is highly absorptive in the terahertz regime, we expect the samples' maximum energy peak to rise over time because, due to dehydration, more energy is reflected back from the quartz sample interface. Over all samples, comparing scans 1 to 4, we find that the maximum values do indeed decrease, as does the minimum peak value, as shown in Table 4.3.

Table 4.3: Maximum and minimum energy peaks over time of all samples

Scan	Maximum Energy peak (a.u.)	Minimum Energy peak (a.u.)
1	0.1930	-0.3817
2	0.1942	-0.3804
3	0.1944	-0.3796
4	0.1960	-0.3998

Table 4.4: Degradation over time and sample showing the variability, standard deviation and R and R-square values (compared to the first scan) over time

Scan	Time / min.	Type	Variance	Standard Deviation	R	R^2
1	0	Normal	3.72E-04	0.0193	1.0000	1.0000
2	30	Normal	3.79E-04	0.0195	0.7020	0.4928
3	60	Normal	4.35E-04	0.0209	0.6736	0.4537
4	90	Normal	4.22E-04	0.0205	0.5898	0.3479
1	0	Saline	1.30E-03	0.0365	1.0000	1.0000
2	30	Saline	1.30E-03	0.0359	0.9746	0.9498
3	60	Saline	1.20E-03	0.0343	0.6093	0.3712
4	90	Saline	1.20E-03	0.0347	0.6058	0.3670
1	0	Wiped	6.26E-04	0.0250	1.0000	1.0000
2	30	Wiped	4.86E-04	0.0220	0.7977	0.6363
3	60	Wiped	4.56E-04	0.0214	0.6275	0.3938
4	90	Wiped	5.11E-04	0.0226	0.6084	0.3702

Comparing each sample over time reveals a rising standard deviation. To compare the samples over time with each other, the cross-correlation function with regards to the first scan was calculated. After 30 minutes, the correlation drops significantly for the sample that has not been altered and the wiped sample, while the sample kept in saline still shows a strong correlation, as can be seen from Figure 4-21. After 60 minutes, the correlation drops down to between 0.4 and 0.5 for all samples.

This leads the conclusion that a sample kept in saline (though it does dry out) does not significantly change the results over the first 30 minutes, while the other

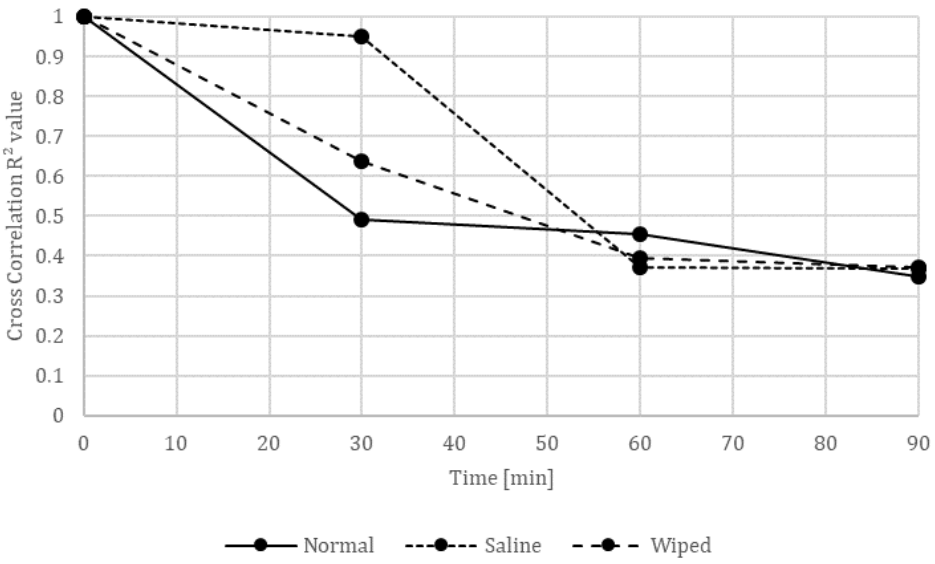

Figure 4-21: R^2 comparison of samples over time.

samples degrade faster.

4.4.3 Conclusion

Applying these results to human skin (which is thicker than chicken skin), we conclude that the time-dependant window for future experiments should not exceed 30 minutes, as samples are kept in saline during transport. We also conclude that, though the absorbance of water is very strong, it is best to keep samples in saline before the experiment, as it is important to not destroy the sample due to dehydration, as the human samples need to be returned to histopathology. This trade-off might lower our expectations for future experiments .

In this Chapter, the data collection and transformation has been discussed. Furthermore, a noise reduction technique using wavelets on chicken skin has been evaluated and the time window for the collection of human skin data has been set. In the next Chapter, we aim to give a descriptive analysis of the sample data collected and provide information from the dermatologist.

Chapter 5

Sample Collection and Descriptive Analysis

In this chapter, a descriptive analysis of the collected samples is given to provide information about the principle structure of the gathered data and to offer a comparison with histopathologists' findings. The results agree with those of the principle dermatologists and the field of histopathology. Since the data comes from different patients with different malignancies, it is worth describing the differences and similarities of the excised samples. Therefore, a brief description of each sample is given which includes dermatology findings and images of the visual and dermoscopy images in comparison with the TD THz maximum energy peak image.

5.1 Sample collection and preparation

Samples were collected closely after excision and held in saline for transportation form the LRI to the university laboratory. The project was granted and meets research-ethics standards according to the university's standard operating procedures for tissue handling, the East Midlands Research Ethics Committee (13/EM/0365) and the Universities Hospital of Leicester (UHL 11280). Patient

information sheets and consent forms were given to and signed by the patients. Data was collected in an anonymised form, and there is no direct link between the patients' personal information and the data gathered for this study. After data collection, the samples were placed in formalin to fix the proteins. They were then transported back to the LRI so that standard histopathology procedures could be performed on them. To avoid degradation of the proteins, no sample was scanned for longer than 30 minutes.

With the exception of Patient 1 (samples 1.1, 1.2 and 1.3), all samples contain a form of cutaneous melanoma and were excised in accordance with standard procedures, leaving a safety margin between the lesion and the skin of a couple of mm, as melanoma might have developed in the underlying regions of the skin that is not visible to the naked eye nor the dermascope. Confirmation of the success of the full removal of the lesion was reported after histopathology analysis.

5.1.1 Results: Visual descriptive analysis of THz maximum peak images in comparison with visuals

Before quantitative analysis occurs, it is good to have a visual and descriptive analysis of the terahertz maximum peak images compared to the visual images per patient. This will help us discuss features seen in the images and might facilitate the discovery of explanations for histopathologists.

Patient 1

Patient 1 presented with benign nevi. Five lesions from various sides of the body were removed due to cosmetic surgery. Three of them were large enough to be included in this study. The samples contain only moles and no surrounding skin, as this would be seen as an unnecessary excision. The images of Patient 1 show samples 1, 2 and 3 of the maximum energy peak of the terahertz waveforms and images taken from a visual camera where the black bar represents 5mm. Some

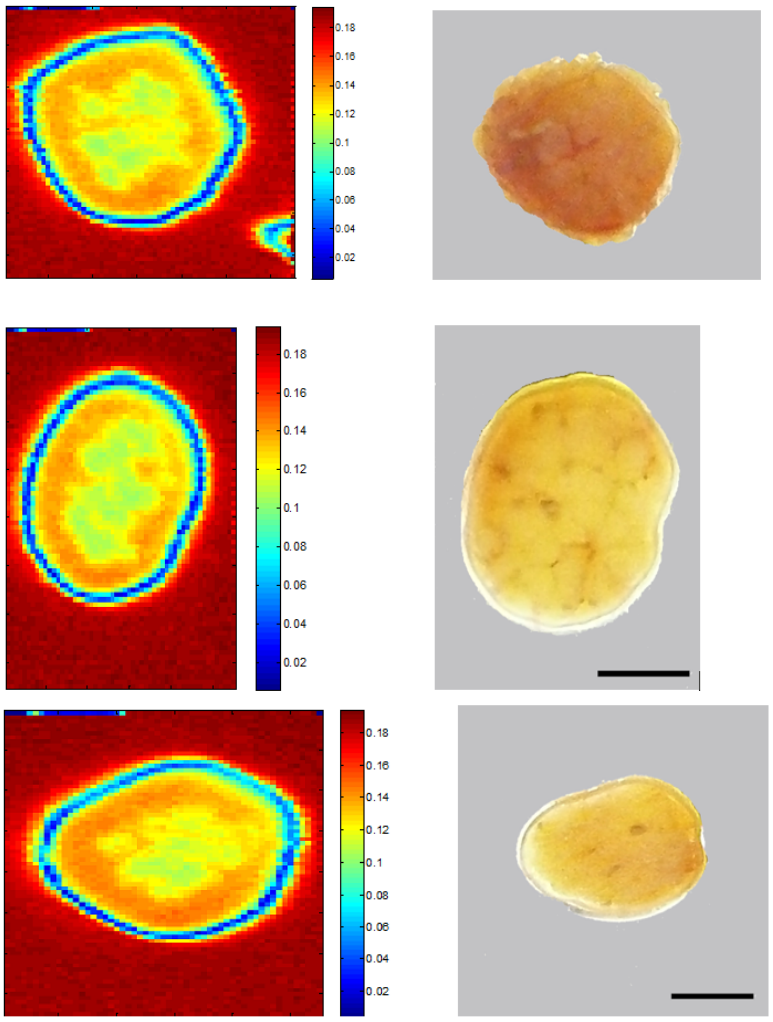

Figure 5-1: Three samples from patient 1 with their representation in the Terahertz time domain using the maximum energy peak (left) and the visual taken from a conventional digital camera (right). The black bar on the visuals represents 5mm.

structures are visible in both the terahertz and the visual image but appear mainly in the centre of the terahertz image.

Patient 2

Patient 2 presented with superficial spreading melanoma with some tendencies towards nodular melanoma on the west side of the sample. Irregular borders and ulceration with change in colour are visible on the dermascopic image (Figure 5-1 (top)). Figure 5-1 (centre) shows the freshly excised sample taken from under

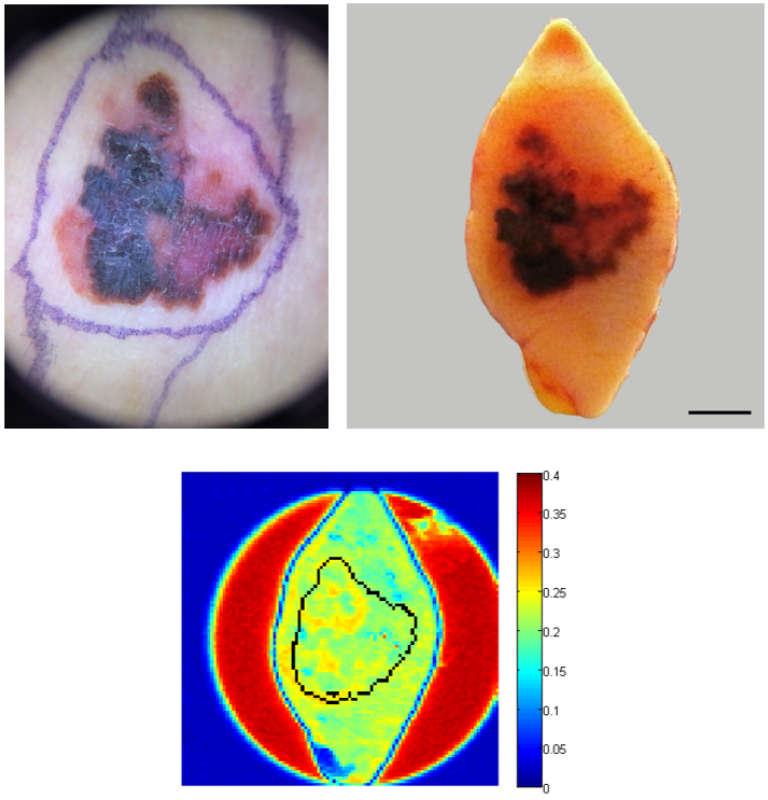

Figure 5-2: Images obtained from patient 2, *in-vivo* image taken with dermascope (top left), flattened, freshly excised sample on sample holder *ex-vivo* (top right) and corresponding Terahertz maximum peak image with lesion border (bottom)

the sample holder. There is a clear loss in pattern and colour visibility between the dermascopic image and the visual image; however, irregular borders are still visible. The terahertz maximum peak-energy image shows features around the border of the lesion that are evident on the visual images as well. Furthermore, a higher maximum energy (around 0.25, yellow) in Figure 5-1 (bottom) shows a higher reflectivity in patterns inside the lesion.

Patient 3

Patient 3 (female) presented with a neoplasm on the right lateral chest. Unfortunately, due to age-related changes in the connective tissue, which have caused declining elasticity and are accompanied by wrinkling of the skin, Sample 3 could not be further analysed and was removed from further investigations. The wrin-

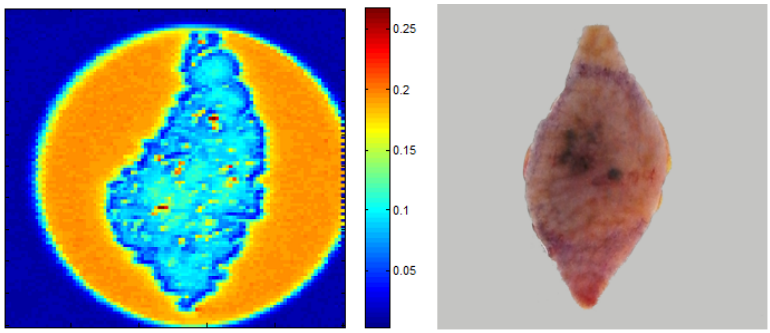

Figure 5-3: Terahertz maximum peak (left) and visual image (left) of patient 3

kling effects of the dermis result in a terahertz image for which the algorithms for image registration fail. Furthermore, the wrinkling created a large number of air gaps between the sample and the sample holder so that the sample could not be further analysed.

Patient 4

Patient 4 (male) presented with a form of nodular melanoma on the top right shoulder. Asymmetric, irregular borders are visible towards the south of the main lesion, which shows a slight form of superficial spreading melanoma. The main lesion is dark-brown to black and elevated. The terahertz image shows a strong decrease in reflected energy in the centre of the nodular lesion; around the lesion, a kind of "halo" is seen with a higher reflection peak (around 0.28 to 0.32). The grey / white hair visible on Figure 5-4 (right) is not visible on the terahertz regime, but the saline-water surrounding the hair is visible.

Patient 5

Like Patient 4, Patient 5 (female) presented with a nodular melanoma featuring irregular borders and asymmetric behaviour with slight appearance of superficial spreading MM, which suggests that the RGP was relatively short before it devolved into the VGP. The specimen was taken from the back and is smaller than the other samples collected. For comparison with histopathology, a suture is present on the south of the surface of the sample that is not visible in the terahertz

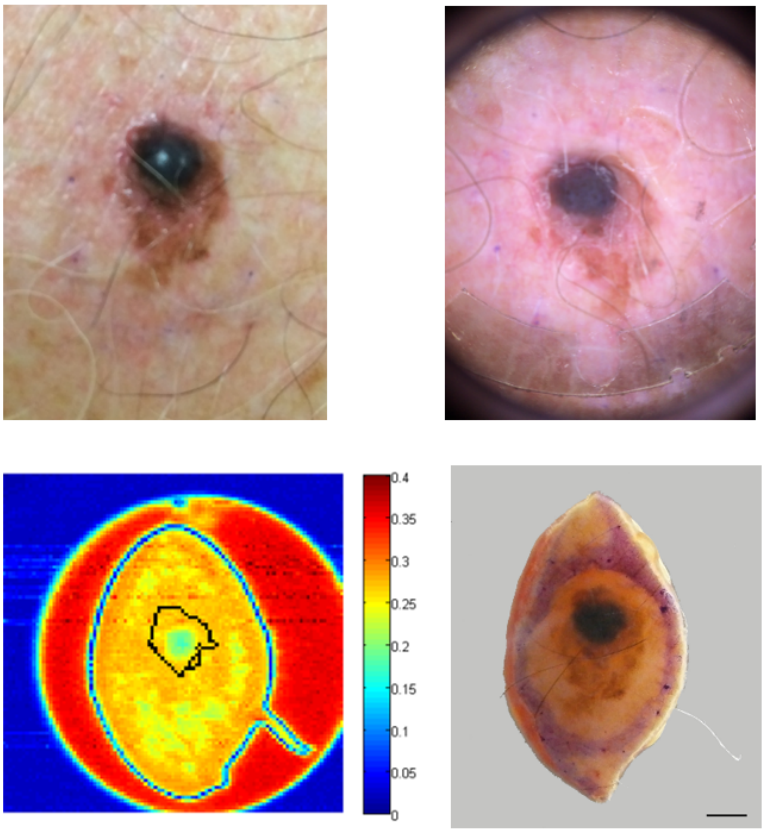

Figure 5-4: Visual of the lesion before excision (top left) and through a dermascope (top right) of Patient 4. Terahertz maximum energy peak (bottom left) and excised visual image (bottom right)

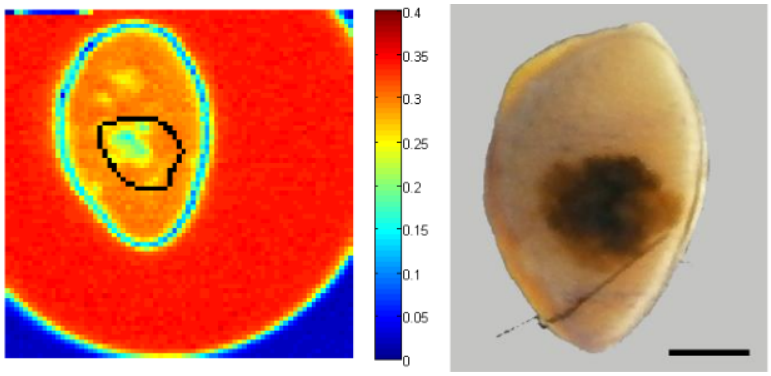

Figure 5-5: Patient 5 Terahertz maximum energy peak (left) and visual image (right)

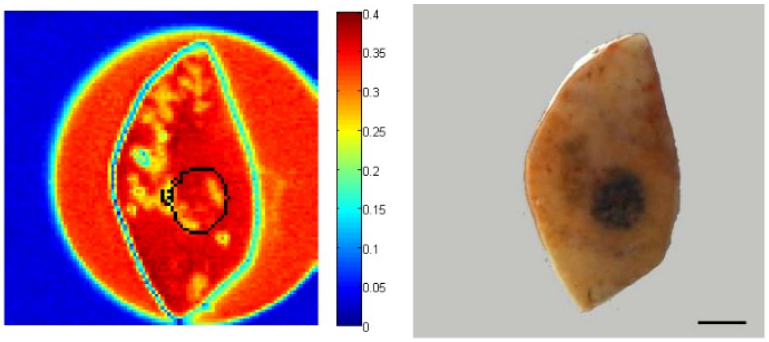

Figure 5-6: Patent 6 Terahertz maximum peak image (left) and corresponding visual image (right)

regime.

Patient 6

Patient 6 presented with a form of nodular melanoma. The main lesion is uniform in colour and symmetry, and no ulceration is visible. Towards the west of the main lesion is a form of superficial spreading MM, which is difficult to catch in the terahertz image.

While the data collected from Patient 6 is used throughout this thesis, it was found that the specimen acts and reacts unlike all other samples chosen for evaluation, which makes it more difficult to describe than the other ones.

Patient 7

Patient seven (male, aged 84) presented with a form of nodular melanoma

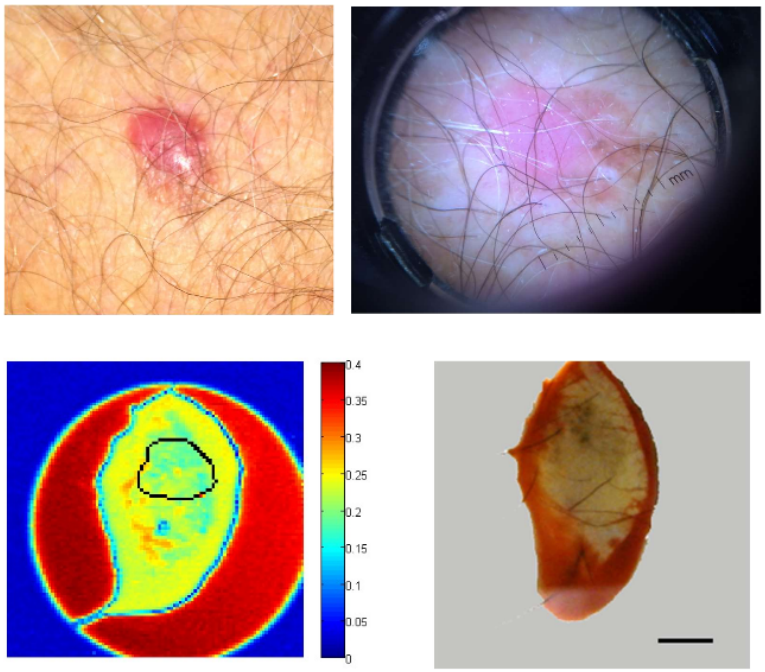

Figure 5-7: Images from patient 7 taken before excision (top left), with a dermascope (top right), the resulting Terahertz maximum energy image (bottom left) and visual taken with a conventional camera from the bottom of the quartz interface (bottom right)

from the left anterior. In contrast to the other lesions, this melanoma presents an elevated nevi with irregular border structure and colours ranging towards the red region (in contrast to other samples, where the colour goes towards brown/ black / bluish like lesions). Due to the colour of the neoplasm, the segmentation algorithm dividing the sample into the IVR and EVR failed and was performed manually. The excised sample of Patient 7 was pressed on the sample holder using a gantry created at the university specifically for this experiment. A suture is present at the medial edge. The suture is for later comparison with histopathology results and is situated at the south of the lesion. Pressing down the sample results in a difficult-to-obtain terahertz image, as the inner liquid is pressed out, which is clearly visible on Figure 5-7 (bottom images) due to the presence of blood around the neoplasm.

Patient 8

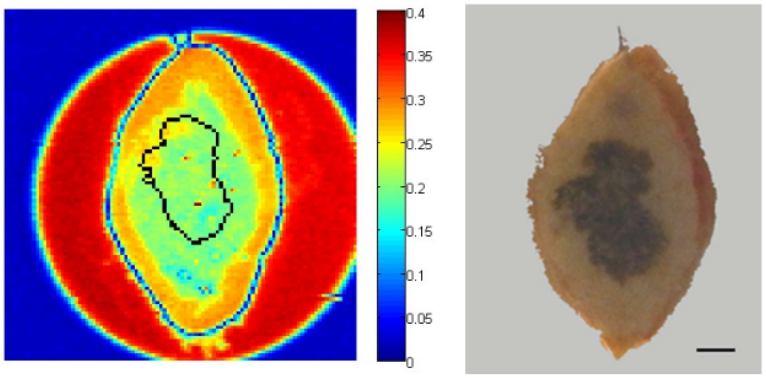

Figure 5-8: Terahertz maximum peak image of sample from patient 8 (left) and the corresponding visual image (right)

Patient 8, a male aged 78 years, shows superficial spreading MM. The specimen was removed from the right shoulder and shows strong irregular borders. A suture has been stained on the top of the sample. Sample 8 was pressed down on the quartz using the gantry, which has created strong water effects around the sample that are strongly visible on the terahertz image.

Patient 9

Patient 9 is a 67-year-old female who presented with a lesion on the right lower leg. Figure 5-9 (top left) shows the lesion prior to excision. The image was taken with a normal camera *in-vivo*. The top-right image shows the lesion taken through the dermascope (*in-vivo*). The neoplasm shows two kind of melanoma. The western region shows superficial spreading melanoma with irregular borders, while the east (and south – east) regions show light ulceration and darker colouring. The sample was pressed using the gantry. A visual image and the terahertz image were taken. Like the results on Sample 2, there seems to be a higher reflectivity on the border of the lesion (marked black on the terahertz image of Figure 5-9). The suture is located on the south of the sample. High reflectivity appears red on the top to top-left border of the sample There seem to be correlations between the reflectivity and the structure of the skin.

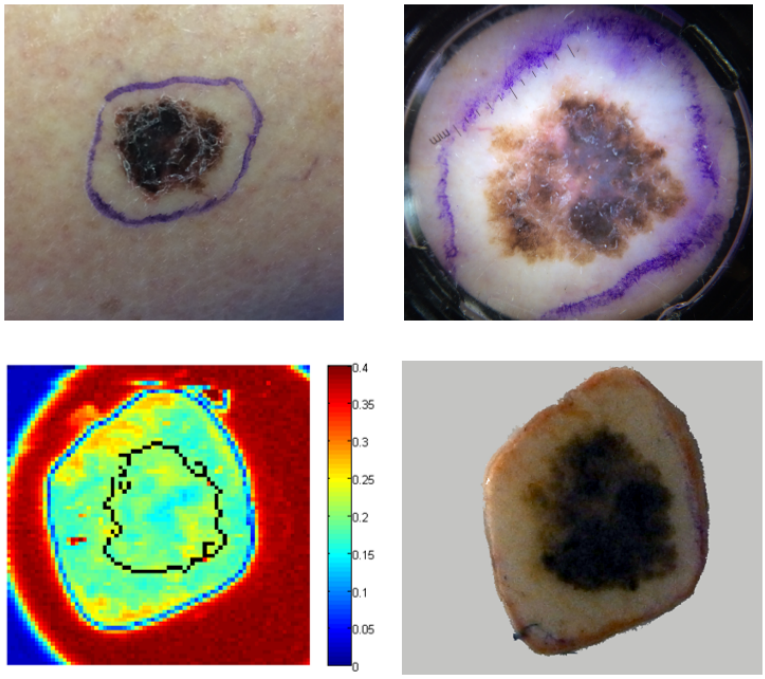

Figure 5-9: Images of patient 9 taken before excision (top left), with a dermascope (top right), the resulting Terahertz maximum energy peak (bottom left) and the corresponding visual taken with a conventional camera (bottom right)

5.2 Conclusion

The figures shown in this section were presented to histopathologists. Confirmation was given regarding the malignancy of the samples, and features were discussed with the following conclusions:

- The samples which are presented with a superficial spreading MM often show border interfaces between the IVR and EVR, which is especially strong on samples 2 and 9. Because SSMM has a long RGP, it might be that these areas consist of fibroblasts, which are produced when MM infiltrates the surrounding tissue. While further studies would be required to corroborate this hypothesis, if true, THz reflectometry could be potentially beneficial for dermatologists who would identify active borders of the lesion that are not visible to the naked eye prior to surgery. This could be potentially useful for preventing secondary surgery after histopathology if the malignancy has

Table 5.1: Overview of patient information collected.

Sample	Gender	Age	Position on body	Type of MM
Sample 2	male	78	right leg	superficial
Sample 3	female	72	lateral chest	n/a
Sample 4	male	69	right shoulder	nodular
Sample 5	female	77	back	nodular
Sample 6	female	62	left shoulder	nodular & superficial
Sample 7	male	84	left anterior	superficial
Sample 8	male	78	right shoulder	superficial
Sample 9	female	67	lower leg	superficial

infiltrated tissue not caught by the first excision.

- The samples presented with nodular MM are clearly visible on both the visual and the terahertz maximum energy images (samples 4 and 5). Since these samples have a short RGP but a rapidly evolving VGP, they show strong regular borders which allow for clear differentiation of the EVR and IVR. While secondary peaks in the waveforms were not visible (data not shown), it can be assumed that terahertz is not able to penetrate deeply enough into the skin to determine the thickness of the infiltrated lesion

Patient information obtained from the dermatologist is presented in Table 5.1. All patients are in the age range of 67 to 84 and collected data contains mostly superficial spreading melanoma but also nodular melanoma.

Table 5.2 shows the number of data collected classified into IVR and EVR and the corresponding percentage. Sample 2 contains the largest amount of infiltrated tissue with 36%, whereas Sample 4 only contains roughly 7% of the IVR.

To the best of the author's knowledge, eight terahertz images were obtained for the first time from freshly excised human malignant melanoma, three from moles prior to histopathology analysis. For descriptive analysis, images of the terahertz maximum peaks of each sample were presented to dermatologists and

Table 5.2: Overview of sample collection and classification in EVR and IVR.

Sample	**Overall data waveforms**	**Classified as EVR**	**Classified as IVR**	**EVR in %**	**IVR in%**
Sample 2	2549	1626	923	63.79	36.21
Sample 4	2523	2349	174	93.10	6.90
Sample 5	935	775	160	82.89	17.11
Sample 6	2310	2072	238	89.70	10.30
Sample 7	2196	1793	403	81.65	18.35
Sample 8	2493	1926	567	77.26	22.74
Sample 9	1931	1353	578	70.07	29.93

histopathologists with the conclusion that nodular melanoma which shows clear, strong borders is completely visible on the terahertz images. Samples containing SSMM showed a more complex structure, and it is believed that these structures could be produced by fibroblasts during the RGP because, during the infiltration of the healthy tissue with the malignance, fibroblasts are present as a side product during the transformation. This result should encourage further investigation of the behaviour of SSMM using terahertz reflectometry, as this procedure could help dermatologists determine the region to be excised more precisely.

In this chapter, samples collected from the UHL have been discussed. A visual comparison of the maximum energy peak terahertz images with the images taken prior scanning and dermatology images - where available- were provided. Based on the segmentation each sample has been divided into the corresponding intra-visual and extra-visual region based on the colour of the visual images.

The collected data will be analysed in the next chapter in comparison to the visual IVR and EVR. Various supervised predictive modelling techniques will be used to determine the number of positive classifications of the EVR and the IVR when compared to the visual images.

Chapter 6

Multivariate Analysis For The Diagnosis of Melanoma

In the last chapter, a comparison of the visual images and the maximum energy peak of the terahertz images was evaluated. A single-variable analysis for the distinction of IVR and EVR was conducted, but it showed no significant difference. Due to the majority of features extracted, there is a chance that a combination of them could help to distinguish between the IVR and EVR; furthermore, it is good practise to evaluate the data in terms of its goodness and to find relationships between the features taken. For this reason, a multi-feature analysis is anticipated with the aim of assessing the quality of the input data and investigating the underlying structure of the data collected. To achieve these goals, experiments were performed based on the full-feature set, and on subsets using the ReliefF algorithm, and also using linear-combinations based on principle component analysis (PCA). These features serve as input to various predictive modelling techniques, which might help to explain the inner layout of the data. With increasing complexity, a number of methods—from linear discriminant analysis to artificial neural networks—have been chosen as prediction models to differentiate between the IVR

and EVR regions; since these regions are based on segmentation and are known, the whole process in this chapter is called "informed" or supervised. To validate the results from the predictive models, we performed 10-fold cross-validation to estimate the general fitness of the model, as some of them are known to overfit.

This chapter reports on experiments performed based on the data obtained from each sample individually so as to explore the feasibility of distinguishing between the IVR and the EVR. Predictive modelling techniques are applied to the raw waveforms, the first 75 components of the PCA, the components of the PCA discovered to be of importance by the ReliefF algorithm and manually chosen variables obtained from the raw waveforms.

Furthermore we apply the same modelling techniques on the full dataset to predict if there is a general rule to distinguish the IVR from the EVR.

6.1 Methods for feature extraction

Based on the division of the patient sample data into the IVR and the EVR, various predictive modelling techniques with increasing complexity have been applied to the raw waveforms. The waveforms were normalised by subtracting each sample waveform with an average of 10 surrounding air waveforms. Using a PCA, we can significantly reduce the number of dimensions in feature space by using linear combinations of such. The PCA needs only to use the feature-space and is uninformed, as it does not take the segmentation between IVR and EVR into account but performs a noise reduction or reduction of the feature space by calculating the importance of each feature space. In addition, the ReliefF algorithm (which is an informed algorithm) was applied to the PCA to further reduce the number of variables in the feature set, whereas the ReliefF algorithm tries to find the features best correlated with the variables by importance (score) to determine

which features best predict the classification outcome.

This study was conducted using *Matlab*2014 with self-written scripts utilising the Statistics Toolbox.

6.2 Feature extraction

6.2.1 Raw Dataset

The raw dataset contains all of the waveforms of the skin per sample classified into the IVR and EVR. The data was normalised by using a simple subtraction of the baseline, which is a waveform with the vicinity of the sample.

The gathered terahertz 3D data has been transformed into a 2D waterfall images to visually analyse the data and find regions of interest as well as presumably false positives, e.g. regions that may appear as secondary reflection. The colourbar represents the terahertz energy field and has been set to low maximum and minimum values (-0.07 to 0.7). This is to visualise data otherwise hidden features due to the presence of the maximum and minimum energy peaks. A resulting waterfall image is shown in Figure 6-1 showing the skin data at the top and surrounding air at the bottom. A reflection is visible at around 35ps but cannot account for a secondary peak from the skin, as it appears in the air-values as well (see Appendix B). Similar peaks have been found at the end of all samples (see Appendix B) which is most likely an internal reflection from the silicon lens. None of the samples show a clear secondary peak outside of the main energy wave and we conclude that most of the information is most likely to be found between approximately 12ps and 35ps. Furthermore, because of the high water absorption from inside the skin it is not feasible to detect any reflection further away from the main incidence beam than 10ps. Therefore, the data chosen has been limited to a range between 10ps and 30ps as indicated by 6-1.

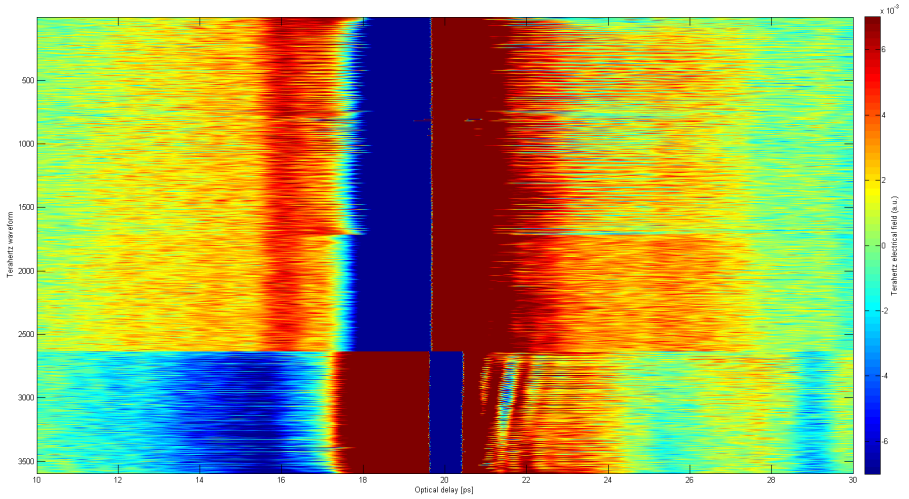

Figure 6-1: False colour waterfall diagram from patient 2 of the sample (top) and air (bottom) waveforms transformed into 2D.

To correctly subtract the waveforms, they were normalised on the optical delay with the maximum peak position, which has been set to a constant 19 ps. The surrounding air waveforms were normalised using their negative peak to 19 ps as well. To avoid false positives, the full waveforms were cut to an optical delay between 13 and 40 ps. To visualise the data collected, false-colour waterfall diagrams were created for each sample, which can be found in Appendix B.

6.2.2 Principle component analysis (PCA)

Principle component analysis has frequently been used in the past on bio-medical terahertz data to reduce the dimension of the collected features [21, 187, 188]. The aim of the PCA is to project the original multidimensional data (features) into a lower-dimension space while maintaining most of the variability of the data. This is achieved by restructuring the original variables to maximise the variance using linear transformations. The newly found variables are orthogonal and are therefore uncorrelated relative to each other.

The orthogonals are shifted and rotated such that the first orthogonal is placed

where the most variance of the dataset can be found. Thus, the first component always has the largest amount of information, thereby suggesting that the largest variance would contain the highest amount of information, which is able to explain the dataset. Each of the following components have the highest amount of information left from the further found components and lie at an angle of 90° to the orthogonals.

To perform a dimension reduction, the first 20 components of each item of sample data was used, as no change in the information gain per component from all samples could be identified anymore. Also, the ReliefF algorithm was applied to each sample individually, as it further reduces the number of variables and may help improve the prediction of the EVR and IVR.

6.2.3 ReliefF-Algorithm

The ReliefF algorithm is a multivariate feature extraction algorithm often used in environments where the results are expected to be correlated non-linearly. In contrast to the PCA, it takes the expected result into account and is therefore informed. The algorithm weights the features of the training set by calculating the Euclidean distance to all other features. The nearest features that belong to the same class are called the nearest hit and get rewarded, while the training data that belongs to the second class, called the nearest-miss, gets penalized. Since a "good" feature is evaluated by the ability to separate the two classes, the distances to the nearest-hit class should be small while the distance to the nearest-miss class should be large. The weights are calculated and adjusted iteratively by using the following equation:

$$W_i = W_i - (x_i - nearHit_i)^2 + (x_i - nearMiss_i)^2 \tag{6.1}$$

The ReliefF algorithm is typically applied after the model prediction has been evaluated, and it gives information about which features have the highest impact on the decision-making process. Once these "important" features have been evaluated, one may run the predictive model on a subset of the features again and thereby gain a feature reduction.

6.2.4 Manual chosen variables

The manual chosen dataset form out of the raw waveforms is one way to create feature extraction and selection. 30 variables were manually extracted from each waveform. These variables might be able to show a better prediction and/or offer an explanation of the waveforms, as they take the full-width-at-half-maximum (FWHM) and the area-under-the-curve (AUC) and secondary peaks found behind the primary energy peak into account.

The feature extraction uses significant positions in the waveform and its transformations to reduce the number of dimensions. All feature are normalised to there corresponding baseline values. The first 14 variables describe the main pulse. As this is were most of the energy is reflected back from the skin, it can be assumed that most information lies within this pulse. Next to the maximum and minimum energy peaks, the Full-Width-At-Half-Maximum (FWHM) of the positive and the neagtive waves are collected as well as the Area-Under-the-Curve (AUC). The AUC contains the behaviour of the slope after the maximum energy peak, as a faster gradient towards the intercept accounts a stronger absorption. Furthermore, since the intensity waveforms are computed using the Hilbert transform from the original energy waveforms, one can expect a strong coupling between these variables. A visual representation of the extracted variables for all samples can be found in Appendix D. The features collected from a terahertz time-domain waveform are as shown in Table 6.1. Secondary peaks are collected to determine

Table 6.1: Extracted features from a Terahertz waveform

1	Maximum Energy peak
2	Maximum Energy peak position (in ps)
3	Minimum Energy peak
4	Minimum Energy peak position (in ps)
5	Maximum / Minimum Energy peak
6	Maximum - Minimum Energy peak
7	Maximum Intensity
8	Maximum Intensity position (in ps)
9	FWHM of positive energy wave
10	FWHM of negative energy wave
11	FWHM of intensity wave
12	AUC – positive energy wave
13	AUC – negative energy wave
14	AUC – intensity wave
15-20	First 5 highest secondary peaks after main peak
21-25	First 5 highest secondary peak positions (in ps) after main peak
26	Mean peak height of the 5 secondary peaks
27	Total number of secondary peaks found

if an internal reflection from inside the skin due to a change of the refractive properties of the medium appears. Secondary peaks are difficult to detect as they could be incorporated within the maximum-energy waveform and when they are too close together, they might not be detectable or they might be visible as a shoulder within the maximum energy peak, which is likewise not detected as a secondary peak, as is shown in Figure 6-2.

6.2.5 Evaluation of predictive models (objective function)

As is normal for medical investigations, we use introduce the terms specificity, sensitivity and accuracy here. These terms describe the "goodness " of the underlying predictive model. The model creates some kind of classifier using training data and then tests the classifier against previously unseen data. Each test data presented to the model has one of the following four outcomes compared to the

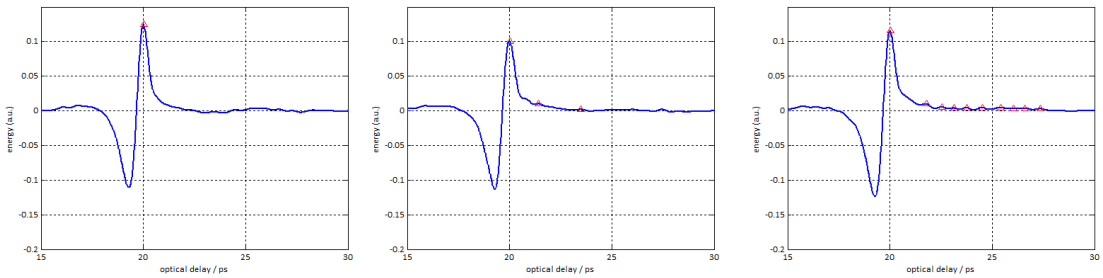

Figure 6-2: Three exemplary shown waveforms from sample 2 showing no secondary peaks (left), secondary peaks with a non-detected shoulder (centre) and 9 secondary detected peaks (right).

		Predicted class: IVR	Predicted class: EVR
True class	IVR	True positive	False positive
	EVR	False negative	True negative

Figure 6-3: Relationship of "true class" versus "predicted class" outcome.

true class: "true positive (TP)" means that the algorithm correctly classified the data as "healthy", and "true negative (TN)" is correctly classified as "infiltrated". On the opposite end, where the model predicted wrongly, the outcome false into the "false positive (FP)" class meaning data classified as "infiltrated" has been wrongly identified as "healthy" and "false negative (FN)", data that has been classified as "healthy" has been wrongly predicted to be "infiltrated". The relationship between the classes are illustrated in Figure 6-3.

The sensitivity is then described as the ability of the algorithm to identify the "healthy" class correctly and is calculated as follows:

$$Sensitivity = \frac{true\ positive}{true\ positive - false\ negative} \tag{6.2}$$

Similarly, the specificity is a value that describes how good the algorithm has put data labelled as infiltrated into the correct infiltrated class. It is calculated by the number of true negatives divided by number of false positive plus the number of true negatives.

$$Specificity = \frac{true\ negative}{true\ negative - false\ positive} \tag{6.3}$$

Furthermore, we describe the outcome with the term accuracy, which describes the algorithms' overall precision on correct classification. It is defined as follows:

$$Accuracy = \frac{true\ positive + true\ negative}{true\ positive + false\ positive + true\ negative + false\ negative} \tag{6.4}$$

The objective function to evaluate the goodness of the predictive modelling would be to simultaneously maximise both the sensitivity and the specificity. The accuracy variable could have been used as the objective function but is only rational if the binary classes contain data of roughly the same size, as the accuracy would otherwise be in favour of the class that contains more sample data. Another possibility is to use the area-under-the-curve (AUC) of the receiver-operator chart (ROC). Though mostly used for regression, the ROC is simply a plot of the specificity over 1 – sensitivity. The AUC of the ROC then gives a number between 0.5 and 1, where 0.5 means complete randomness and 1 is fully predicted. Since the AUC takes both sensitivity and specificity into account, this variable was chosen as the objective function for the predictive modelling techniques used.

Two tests were performed on the data itself. The first uses the full-data set for the predictive modelling to investigate the general ability to depict the data. This procedure is known as resubstitution. Since some modelling techniques are

known to overfit and it is also important to find out how the model would react to previously unseen data, 10-fold cross-validation was also performed for each experiment on a single sample. For the whole dataset, Leave-One-Out-Cross-Correlation is used. In this case the test data contains all samples except one, which is the training data.

6.3 Predictive modelling methods

Predictive modelling techniques are discussed in this chapter. Each model has been tested on each individual sample (patient) to gain an overview of the goodness of the data and to determine which predictive model might be used (i.e., which is in good correlation with the IVR and EVR) for further analysis. The objective function is to minimize the misclassification rate, which equals a maximisation of the accuracy.

6.3.1 Linear and Quadratic Discriminate Analysis (LDA / QDA)

Linear Discriminate Analysis tries to separate the features (x_1 to x_n) by using a Linear-weighted combination as the discriminator of the features in the form of

$$D = \beta_1 x_1 + \beta_2 x_2 + ... + \beta_n x_n \tag{6.5}$$

The task is to estimate the discriminant coefficients β_1 to β_n by the given test data (X). The discriminator is estimated by calculating the between-group covariance matrix (B) and the within-group covariance matrix (W). Described as Fishers problem, the task is now to maximize β in the form

$$\lambda = \frac{B_d}{W_d} = \frac{\beta' B \beta}{\beta' W \beta} \rightarrow \max f for \beta \tag{6.6}$$

The solution to Equation 6.5 is found by optimizing its eigenvalue of W-1B, which is a linear discriminant. To classify a new sample u, the mean value of both classes x1 and x2 are calculated. The sample is then classified using the following:

$$|\beta'(u - \bar{x_1})| - |\beta'(u - \bar{x_2})| \begin{cases} < 0 & group1 \\ \geq 0 & group2 \end{cases} \tag{6.7}$$

which means that, if the projection of the sample is closer to the mean of class x1 than to x2 (the equation gives <0) then it belongs to Class 1. Otherwise it belongs to Class 2. The LDA works properly only if the variables can be linearly separated and do not correlate very well with each other [189].

While LDA assumes the same covariance of all classes, QDA computes a different covariance for each class. Essentially, LDA computes a separate the samples for each class (using training points that belonged to it), but the covariance is computed using the entire training data. LDA uses a covariance matrix using the entire training data to compute the correspondence to each class, whereas QDA computes a separate covariance and mean for each possible output class.

6.3.2 Support-vector machines (SVM)

A support-vector machine is a classifier that tries to divide the training data into two classes using a hyperplane. The best hyperplane is the one that has the largest margin between the two classes. Margin means the maximal width of the slab parallel to the hyperplane that has no interior data points. The support vectors are the data points that are closest to the separating hyperplane.

The hyperplane is calculated as a decision-function and is given by the normal

vector (w) and the bias (b). The objective is put in a class based on the sign of the decision function. Thus, if the decision function returns a positive sign, the object xi is above the hyperplane; otherwise it is under the hyperplane. Objects that lie directly on the hyperplane are not separable. Furthermore, a slack-variable ζ is introduced to improve cases for which the test data is not linearly separable, which creates the optimisation problem of

$$\frac{1}{2}||w||_2^2 + C\sum_{i=1}^{m}\zeta_i \tag{6.8}$$

6.3.3 K-nearest Neighbours (KNN)

The k-nearest-neighbour classification is a simple instance-based learning algorithm in which a new "data-object" is put in the class that is closest to its neighbour object (or class) based on maximum-likelihood.

During the training of the KNN algorithm, the data gets partitioned into the (so-called) Voronoi-partitioning, which creates regions divided by hyperplanes. Choosing a suitable size for K is crucial to the algorithm, as a small value creates a larger sensitivity against outliers, and a K that is too high might misclassify the data because too many neighbouring clusters (or classes) are used in the process. Therefore, before testing the KNN algorithm, the size K is evaluated over all patients. As a rule of thumb, k should be around the size of the square-root of the feature dimension.

6.3.4 Decision Trees (DT)

Decision trees (DTs) are among the most favoured of machine-learning algorithms for clinical diagnosis and prediction modelling [190]. In contrast to methods like the ANN, which acts like a black box to the outer world, DTs have the ability to clearly explain the final decision and the process of making that decision.

Decision trees, also known as classification trees, create a binary tree-like structure for the separation by using a division criterion for each node starting from a rootnode in a tree-like structure. Internal nodes describe one question or one feature either in an inequality or equality way and build more internal nodes starting from the root node. In each node only one variable is considered for the decision making also known as attribute test condition , until a leaf node (a final node with no descendants) is reached. The leaf node contains the classification (or result) outcome, which in the case of binary classification is either 0 or 1. The training data is used to construct the tree using certain criteria to prevent over and/or under fitting. Constructing (binary) decision trees with a large number of features that may contain heavy noise can be difficult, as a DT might over fit, which could lead to a DT in which a node only has one feature of one training set; therefore in addition to describing a "split criterion" to create a node, it is also important to describe a "stop-split" criterion to prevent overfitting and reduce the influence of noise [190, 191]. A typical split criterion is built on an impurity function (or information gain) on a feature chosen by its information gain, which is defined as

$$I(y) = f(P(X|y_1), P(X|y_2)) \tag{6.9}$$

where f is an arbitrary function and P(X|y) is the probability that the observation X containing the features belongs to a class y with the indices 1,2 for binary classification. A typical function f for the impurity is the entropy H function is given by,

$$H(y) = -\sum_{y} P(X|y) \log_2 P(X|y) \tag{6.10}$$

where P is the probability that the observation X belongs to class y and the sum over all classes y [191]. Using the information-gain function above on all

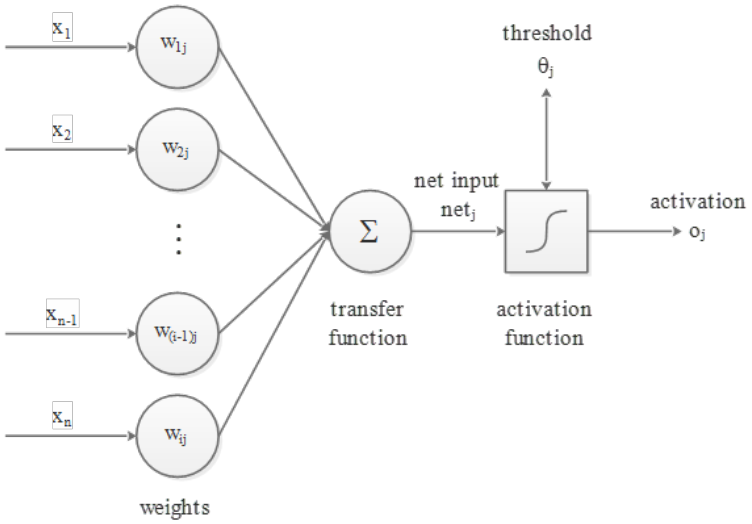

Figure 6-4: Classical structure of a perceptron with input weights and activation function

features, one can now select the feature with the highest information gain with respect to the resulting class Y.

6.3.5 Artificial Neural Networks (ANNs)

Artificial Neural Networks are inspired by the concept of neurons found in biology. A neuron (or a perceptron) is fired when it receives several stimulations from various, weighted neurons on a previous layer that surpass (are higher) than a certain threshold (activation function). The activation function is often a rectangle (binary) function that fires when the sum of the weights of the connected fired neurons are over the threshold. Otherwise a sigmoid function is commonly used as an activation function. Because each input is weighted and the sum of these inputs cause activation only when a certain threshold is exceeded, a single perceptron acts exactly as the LDA. It is a linearly separable classifier, depicted in 6-4.

By creating a layer of perceptrons, all of which are connected, and by weighting them with respect to all input variables, it is possible to create a more complex classifier. As for pattern recognition, one hidden layer is sufficient ; this neural

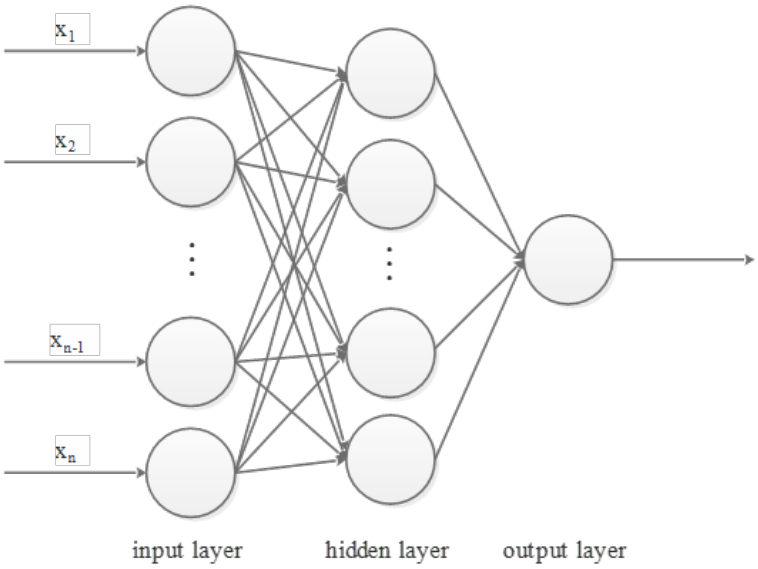

Figure 6-5: Principle construct of an ANN with one hidden layer and one output neuron for binary classification

network acts as a multi-linear classifier.

By putting multiple neurons in layers, the network can be trained (adjusted, supervised learning etc.). For classification problems with a given test-set pattern, recognition ANNs are chosen when the sigmoid "fire rule" of the neuron is adjusted to the outcome of the test-data presented to the NN . The task is to minimize the error between rightly and wrongly predicted classes. Because training patterns with known results are needed, this structure is a 'classical' supervised learning algorithm. The sigmoid-activation function is defined as

$$f(x) = \frac{1}{1 + e^{-steepness\ x})} \tag{6.11}$$

For neural networks, the data has to be divided into three sets: namely, the training set, the test set and a validation set, which is used to prevent the ANN from overfitting. For the purpose for pattern recognition, which includes classification problems, a feed-forward neural network with error backpropagation is used. When initialising the network, the gain of the sigmoid-activation functions

and the weights are set randomly. The first data from the training set is presented to the ANN and is forwarded through the hidden layer into the output layer. At the output layer, a comparison of the actual and the desired outcomes is made before adjusting the internal weights and gains of each neuron backwards through the network (backpropagation).

The feed forward net input function is defined as follows:

$$net_j = \Theta_j \sum_i^n x_i w_i \tag{6.12}$$

where net_j is the input net, Θ_j is the threshold, x_i is the output of the neurons from the previous layer and w_i is the weight from the previous neuron of the previous layer. In the hidden layer, the output of the neurons is calculated using the activation function from Equation 6.11

$$o_j = f(net_j) \tag{6.13}$$

For the output layer, it is simply this:

$$o_j = net_j \tag{6.14}$$

Once data has been passed through all layers, the root mean square error is determined by:

$$RMSE = \Theta_j \sum_{i=1}^n \frac{(d_i - a_i)^2}{2} \tag{6.15}$$

where d_i is the desired output, a_i is the actual, calculated output and n is the number of observations presented as training sets.

The RMSE gives an overall performance estimate for the ANN. To determine the error of the weights of the neurons connected with each other, before adjusting

the weights, one uses the so -called delta rule for error determination [192]. For the output layer, the delta rule is defined as follows:

$$\delta_{out,j} = (a_j d_i) f'(d_i) \tag{6.16}$$

It is then defined backwards through the hidden layers as follows:

$$\delta_k = f'(net_i)\delta_j w_{kj} \tag{6.17}$$

where δ_k is the error of the neuron of layer k, δ_j is the error of the neurons of the previous layer and w_{kj} is the weight of the connection between neurons of k and j. To finally adjust the weight at position ij, a typical gradient descent algorithm is used which introduces a learning rate (alpha) to adjust the weights. To further improve the speed of the algorithm, a conjugate gradient-descent algorithm is used which also introduces a momentum (y). The learning rate is adjusted automatically according to the RMSE. A small RMSE decreases the learning rate and a high RMSE increases the learning rate. This is in a way similar to the added momentum, which converges faster on plateaus (where the error rate is close to constant) and slower at higher error rates.

The change of the weight of a connection between a neuron at layer i and a neuron at layer $k(\Delta w_{ij})$ is calculated by

$$\Delta w_{ij} = \alpha\ (\delta_j d_j) + \gamma\ \Delta w_{ij}(n) \tag{6.18}$$

where α is the learning rate and γ is the momentum.

6.4 Results: Single Sample

Each sample has been applied to the predictive modelling techniques as, a) a full training set and b) a 10-fold cross-validated set. The accuracy, sensitivity, specificity and the AUC have been recorded. Furthermore, the average and the standard deviation have been calculated.

6.4.1 Raw data

Applying the predictive algorithm techniques to the raw waveforms shows a good determination of the specificity (between 0.94 and 0.98) and a lower, yet still significant sensitivity (between 0.65 and 0.82) on the whole training set. The values are lowered when using 10-fold CC and vary for sensitivities between 0.57 and 0.74 and specificities between 0.91 and 0.94. Especially the results of the LDA, the KNN and the NN show a correlation between the raw input data and the classification parameters, whereas all of them have a high specificity (0.94 (LDA), 0.95 (KNN) and 0.96 (NN)) and a significant lower sensitivity of 0.76 (LDA), 0.74 (KNN) and 0.77 (NN). As can be seen from Tables 6.2 to 6.7, all classification algorithms are good at classifying EVR samples as such but fail to identify the IVR correctly, as is summarised in Figure 6-6 and Figure 6-7 respectively. Also, while the SVM performs well with the whole training set, it fails to determine the specificity and sensitivity of the 10-fold CC, which gives raise to the assumption that the SVM overfits. Even though the KNN shows high specificity and moderate sensitivity it would not be the favour of choice, as the standard deviation is higher than from the ANN and the LDA.

To further investigate which of the raw waveforms variables are useful for the classification process, the ReliefF algorithm has been applied to each sample. It shows that both the data behind the maximum energy peak and the data before

Table 6.2: Results of the LDA applied to raw waveforms

	Training Set				10-fold cross validation			
Sample	Accuracy	Sensitivity	Specificity	AUC	Accuracy	Sensitivity	Specificity	AUC
2	0.89	0.82	0.92	0.87	0.86	0.79	0.89	0.84
4	0.96	0.69	0.98	0.79	0.95	0.64	0.98	0.81
5	0.95	0.75	0.99	0.87	0.91	0.66	0.97	0.81
6	0.96	0.72	0.99	0.85	0.95	0.66	0.98	0.82
7	0.91	0.78	0.94	0.86	0.89	0.72	0.93	0.82
8	0.87	0.72	0.92	0.82	0.84	0.64	0.90	0.77
9	0.91	0.86	0.93	0.90	0.89	0.83	0.92	0.87
Avg	**0.92**	**0.76**	**0.95**	**0.85**	**0.90**	**0.71**	**0.94**	**0.82**
Std	0.03	0.06	0.03	0.03	0.04	0.07	0.03	0.03

Table 6.3: Results of the QDA applied to raw waveforms

	Training Set				10-fold cross validation			
Sample	Accuracy	Sensitivity	Specificity	AUC	Accuracy	Sensitivity	Specificity	AUC
2	0.74	0.63	0.95	0.79	0.74	0.63	0.95	0.79
4	0.55	0.52	0.93	0.72	0.55	0.52	0.93	0.72
5	0.78	0.75	0.96	0.85	0.79	0.75	0.96	0.85
6	0.68	0.64	0.90	0.77	0.68	0.64	0.90	0.77
7	0.80	0.77	0.94	0.85	0.80	0.77	0.94	0.85
8	0.70	0.63	0.96	0.80	0.70	0.63	0.96	0.79
9	0.72	0.62	0.93	0.78	0.71	0.62	0.93	0.78
Avg	**0.71**	**0.65**	**0.94**	**0.80**	**0.71**	**0.65**	**0.94**	**0.79**
Std	0.08	0.08	0.02	0.04	0.08	0.08	0.02	0.04

Table 6.4: Results of the SVM applied to raw waveforms

	Training Set				10-fold cross validation			
Sample	Accuracy	Sensitivity	Specificity	AUC	Accuracy	Sensitivity	Specificity	AUC
2	0.93	0.88	0.96	0.92	0.89	0.81	0.93	0.87
4	0.97	0.63	1.00	0.81	0.96	0.47	1.00	0.73
5	0.97	0.86	1.00	0.93	0.93	0.68	0.99	0.83
6	0.98	0.78	1.00	0.89	0.96	0.67	1.00	0.83
7	0.94	0.84	0.97	0.90	0.78	0.50	0.87	0.68
8	0.92	0.84	0.94	0.89	0.86	0.69	0.91	0.80
9	0.93	0.85	0.96	0.91	0.87	0.74	0.92	0.83
Avg	**0.95**	**0.81**	**0.98**	**0.89**	**0.89**	**0.65**	**0.94**	**0.80**
Std	0.02	0.08	0.02	0.04	0.06	0.12	0.05	0.06

Table 6.5: Results of the KNN (n=10) applied to raw waveforms

	Training Set				10-fold cross validation			
Sample	Accuracy	Sensitivity	Specificity	AUC	Accuracy	Sensitivity	Specificity	AUC
2	0.92	0.91	0.92	0.92	0.88	0.83	0.91	0.87
4	0.97	0.60	1.00	0.80	0.96	0.48	1.00	0.74
5	0.95	0.83	0.98	0.90	0.93	0.70	0.98	0.84
6	0.97	0.78	1.00	0.89	0.96	0.68	0.99	0.84
7	0.92	0.80	0.94	0.87	0.90	0.67	0.95	0.81
8	0.88	0.89	0.88	0.89	0.84	0.77	0.86	0.82
9	0.89	0.86	0.91	0.88	0.87	0.80	0.90	0.85
Avg	**0.93**	**0.81**	**0.95**	**0.88**	**0.91**	**0.71**	**0.94**	**0.82**
Std	0.03	0.10	0.04	0.04	0.04	0.11	0.05	0.04

Table 6.6: Results of the ANN (20 neurons) applied to raw waveforms

	Training Set				10-fold cross validation			
Sample	Accuracy	Sensitivity	Specificity	AUC	Accuracy	Sensitivity	Specificity	AUC
2	0.83	0.93	0.94	0.94	0.87	0.81	0.93	0.87
4	0.97	0.70	0.99	0.85	0.97	0.63	0.99	0.81
5	0.94	0.80	0.95	0.88	0.95	0.79	0.95	0.87
6	0.95	0.73	0.98	0.85	0.97	0.75	0.99	0.87
7	0.88	0.72	0.94	0.83	0.91	0.70	0.96	0.83
8	0.85	0.81	0.93	0.87	0.87	0.73	0.91	0.82
9	0.84	0.73	0.90	0.82	0.88	0.77	0.93	0.85
Avg	**0.89**	**0.77**	**0.95**	**0.86**	**0.92**	**0.74**	**0.95**	**0.85**
Std	0.05	0.07	0.03	0.04	0.04	0.06	0.03	0.02

Table 6.7: Results of the DT (minimum leaf size 20 samples) applied to raw waveforms

	Training Set				10-fold cross validation			
Sample	Accuracy	Sensitivity	Specificity	AUC	Accuracy	Sensitivity	Specificity	AUC
2	0.93	0.88	0.96	0.92	0.79	0.70	0.84	0.77
4	0.97	0.64	0.99	0.82	0.94	0.45	0.97	0.71
5	0.95	0.84	0.98	0.91	0.87	0.61	0.92	0.77
6	0.96	0.80	0.98	0.89	0.92	0.53	0.96	0.74
7	0.95	0.86	0.96	0.91	0.85	0.55	0.92	0.73
8	0.94	0.84	0.97	0.90	0.78	0.50	0.87	0.68
9	0.91	0.84	0.94	0.89	0.80	0.68	0.86	0.77
Avg	**0.94**	**0.82**	**0.97**	**0.89**	**0.85**	**0.57**	**0.91**	**0.74**
Std	0.02	0.08	0.01	0.03	0.06	0.08	0.05	0.03

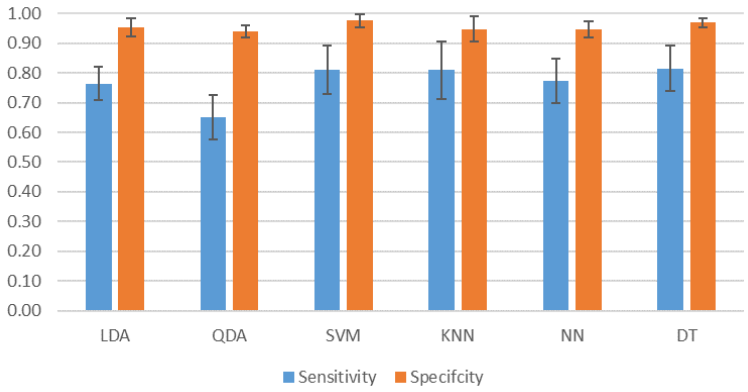

Figure 6-6: Sensitivity and specificity with corresponding standard deviation of the average values from predictive modelling methods on the whole training set using raw waveforms

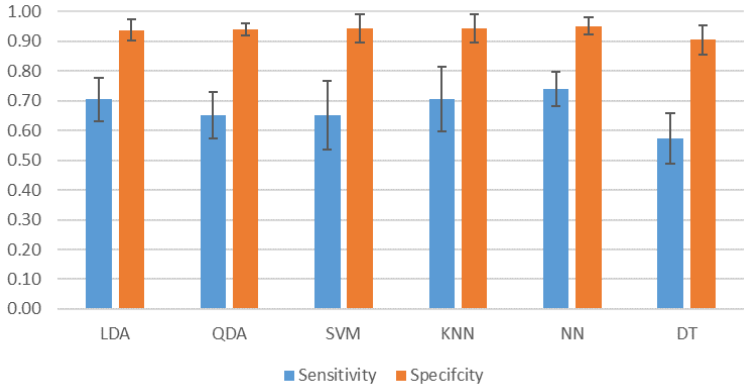

Figure 6-7: Sensitivity and specificity with corresponding standard deviation of the average values from predictive modelling methods on 10-fold cross validation using raw waveforms

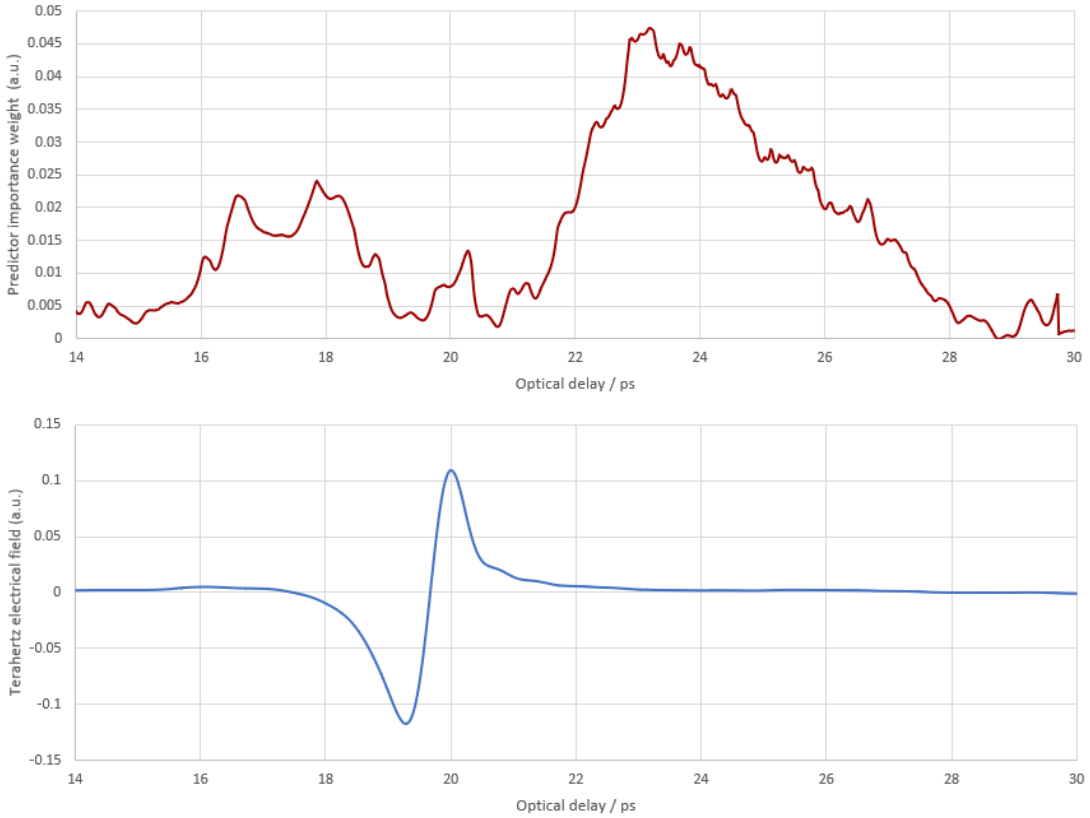

Figure 6-8: Results of the ReliefF predictor importance weights accumulated over all samples (top), arbitrary sample waveform from sample 2 (bottom).

the main energy peak are especially important. Figure 6-8 shows the accumulated predictor importance weight over the optical delay. Results of the ReliefF of each sample can be found in Appendix B. It is interesting to note that the predictor importance weight is low around the maximum peak, which could be because of the normalisation of that peak or because the incident (main) peak conceals underlying information due to its intensity. But it can be said that the main information for the classification of IVR and EVR lies in a range between 16ps and 29ps.

Table 6.8: Percentage explained principal component per sample.

Component	Sample 2	Sample 4	Sample 5	Sample 6	Sample 7	Sample 8	Sample 9
1	48.70	32.45	49.03	46.67	51.49	63.89	48.70
2	23.14	28.23	30.51	22.80	16.81	12.37	23.14
3	11.71	7.40	5.20	11.07	11.45	7.88	11.71
4	3.47	4.96	4.21	4.74	8.35	3.27	3.47
5	2.97	2.51	1.75	2.42	2.04	2.44	2.97
6	1.49	1.94	1.52	2.33	1.76	1.46	1.49
7	1.18	1.42	0.92	1.31	1.19	1.12	1.18
8	0.66	1.34	0.66	0.78	0.96	0.92	0.66
9	0.49	1.21	0.49	0.63	0.54	0.70	0.49
10	0.42	1.16	0.39	0.47	0.35	0.56	0.42
11	0.31	1.08	0.28	0.36	0.28	0.41	0.31
12	0.29	1.06	0.24	0.32	0.23	0.30	0.29
13	0.22	0.99	0.22	0.26	0.19	0.24	0.22
14	0.20	0.88	0.19	0.23	0.18	0.21	0.20
15	0.19	0.79	0.18	0.21	0.16	0.19	0.19
16	0.17	0.70	0.17	0.19	0.15	0.16	0.17
17	0.16	0.68	0.17	0.19	0.14	0.16	0.16
18	0.15	0.65	0.17	0.18	0.13	0.14	0.15
19	0.15	0.63	0.16	0.18	0.13	0.14	0.15
20	0.15	0.57	0.16	0.18	0.13	0.13	0.15
Sum	**95.52**	**90.65**	**96.64**	**95.51**	**96.64**	**96.68**	**96.23**

6.4.2 PCA (first 20 PCs)

The first 20 PCs of the PCA have been chosen as the information gain sinks down to 0.5 (Sample 4) to 0.1 at around the 20th component but also the total information is at around 95%, except for sample 4, which is around 90%, indicated in Table 6.8. Also visible from Table 6.8 is that the first components do not explain the variance in the data very well, as the values are only between 32% and 64% of the first PC, which indicates a large amount of noise and many differences in the data itself. A graphical representation of the first three components of each sample can be found in Appendix C.

The results of the PCA (first 20 components) show a slight decrease in sensitivity and specificity compared to the raw data, which is most likely due to the reduction of variables from 800 (raw waveforms) down to 20 (components). Like the raw waveforms, the PCA manages to detect specificity well (0.80 to 0.98), but it does not show a good agreement for sensitivity (0.66 to 0.76). The NN performs

Table 6.9: Results of the LDA applied to the first 20 components of the PCA

	Training Set				10-fold cross validation			
Sample	Accuracy	Sensitivity	Specificity	AUC	Accuracy	Sensitivity	Specificity	AUC
2	0.85	0.77	0.89	0.83	0.85	0.77	0.89	0.83
4	0.96	0.69	0.99	0.73	0.95	0.64	0.99	0.82
5	0.93	0.69	0.98	0.84	0.93	0.68	0.98	0.83
6	0.94	0.53	0.99	0.76	0.94	0.51	0.99	0.75
7	0.89	0.71	0.93	0.82	0.88	0.68	0.92	0.80
8	0.85	0.65	0.91	0.78	0.84	0.63	0.90	0.77
9	0.87	0.81	0.90	0.85	0.87	0.81	0.89	0.85
Avg	**0.90**	**0.69**	**0.94**	**0.80**	**0.89**	**0.68**	**0.94**	**0.81**
Std	0.04	0.08	0.04	0.04	0.04	0.09	0.04	0.03

Table 6.10: Results of the QDA applied to the first 20 components of the PCA

	Training Set				10-fold cross validation			
Sample	Accuracy	Sensitivity	Specificity	AUC	Accuracy	Sensitivity	Specificity	AUC
2	0.77	0.81	0.69	0.75	0.76	0.81	0.69	0.75
4	0.92	0.61	0.83	0.72	0.91	0.60	0.83	0.72
5	0.91	0.54	0.89	0.71	0.90	0.51	0.89	0.70
6	0.95	0.80	0.88	0.84	0.95	0.78	0.88	0.83
7	0.88	0.65	0.80	0.73	0.87	0.63	0.80	0.72
8	0.80	0.79	0.77	0.78	0.80	0.79	0.77	0.78
9	0.78	0.76	0.75	0.76	0.78	0.76	0.75	0.75
Avg	**0.86**	**0.71**	**0.80**	**0.76**	**0.85**	**0.70**	**0.80**	**0.75**
Std	0.07	0.10	0.07	0.04	0.07	0.11	0.07	0.04

best with an AUC of 0.85 (specificity of 0.94 and sensitivity of 0.76). As with the raw waveform data, the SVM and the DT seem to overfit due to the significant fall of sensitivity between the training set and the 10-fold CC, as indicated by Figure 6-9 and Figure 6-10.

6.4.3 PCA with Relieff-Algorithm

Applying the ReliefF-algorithm to the PCA further reduces the number of chosen components between 4 and 16 summarised in Table 6.15. However, further reducing the number of variables results in a reduced accuracy with a sensitivity between 0.54 and 0.76 as well as in specificity between 0.84 and 0.94. Similar to the previous shown results, the KNN and the ANN perform best with a an AUC

Table 6.11: Results of the SVM applied to the first 75 components of the PCA

	Training Set				10-fold cross validation			
Sample	Accuracy	Sensitivity	Specificity	AUC	Accuracy	Sensitivity	Specificity	AUC
2	0.95	0.91	0.97	0.94	0.90	0.82	0.94	0.88
4	0.98	0.70	1.00	0.85	0.96	0.45	1.00	0.72
5	0.98	0.88	1.00	0.94	0.93	0.64	0.99	0.81
6	0.99	0.87	1.00	0.93	0.96	0.66	1.00	0.83
7	0.91	0.80	0.94	0.87	0.82	0.57	0.89	0.73
8	0.93	0.86	0.96	0.91	0.86	0.67	0.92	0.79
9	0.94	0.90	0.96	0.93	0.90	0.78	0.95	0.86
Avg	**0.95**	**0.84**	**0.98**	**0.91**	**0.90**	**0.66**	**0.95**	**0.80**
Std	0.03	0.07	0.02	0.03	0.05	0.11	0.04	0.06

Table 6.12: Results of the KNN (with n=10) applied to the first 20 components of the PCA

	Training Set				10-fold cross validation			
Sample	Accuracy	Sensitivity	Specificity	AUC	Accuracy	Sensitivity	Specificity	AUC
2	0.92	0.92	0.92	0.92	0.90	0.85	0.92	0.89
4	0.97	0.58	1.00	0.79	0.96	0.50	1.00	0.75
5	0.95	0.84	0.98	0.91	0.93	0.74	0.97	0.86
6	0.97	0.76	0.99	0.88	0.96	0.65	0.99	0.82
7	0.92	0.80	0.94	0.87	0.89	0.64	0.95	0.79
8	0.88	0.85	0.89	0.87	0.85	0.76	0.87	0.82
9	0.89	0.86	0.91	0.88	0.86	0.79	0.89	0.84
Avg	**0.93**	**0.80**	**0.95**	**0.87**	**0.91**	**0.71**	**0.94**	**0.82**
Std	0.03	0.10	0.04	0.04	0.04	0.11	0.05	0.04

Table 6.13: Results of the ANN (with 20 neurons) applied to the first 20 components of the PCA

	Training Set				10-fold cross validation			
Sample	Accuracy	Sensitivity	Specificity	AUC	Accuracy	Sensitivity	Specificity	AUC
2	0.83	0.93	0.94	0.94	0.83	0.76	0.93	0.85
4	0.97	0.70	0.99	0.85	0.96	0.62	0.99	0.81
5	0.94	0.71	0.98	0.85	0.96	0.83	0.95	0.89
6	0.98	0.82	1.00	0.91	0.96	0.80	0.99	0.89
7	0.90	0.78	0.95	0.86	0.90	0.78	0.95	0.86
8	0.86	0.81	0.92	0.87	0.83	0.68	0.92	0.80
9	0.89	0.82	0.91	0.87	0.87	0.87	0.88	0.87
Avg	**0.91**	**0.80**	**0.96**	**0.88**	**0.90**	**0.76**	**0.94**	**0.85**
Std	0.05	0.07	0.03	0.03	0.05	0.08	0.04	0.03

Table 6.14: Results of the DT (minimum leaf size of 20 samples) applied to the first 20 components of the PCA

	Training Set				10-fold cross validation			
Sample	Accuracy	Sensitivity	Specificity	AUC	Accuracy	Sensitivity	Specificity	AUC
2	0.92	0.87	0.95	0.91	0.85	0.78	0.88	0.83
4	0.97	0.68	0.99	0.84	0.95	0.52	0.98	0.75
5	0.96	0.88	0.98	0.93	0.90	0.70	0.94	0.82
6	0.96	0.76	0.98	0.87	0.93	0.64	0.96	0.80
7	0.94	0.82	0.97	0.89	0.87	0.61	0.93	0.77
8	0.91	0.80	0.94	0.87	0.82	0.57	0.89	0.73
9	0.91	0.84	0.94	0.89	0.82	0.73	0.86	0.80
Avg	**0.94**	**0.81**	**0.97**	**0.89**	**0.88**	**0.65**	**0.92**	**0.79**
Std	0.02	0.06	0.02	0.03	0.05	0.09	0.04	0.03

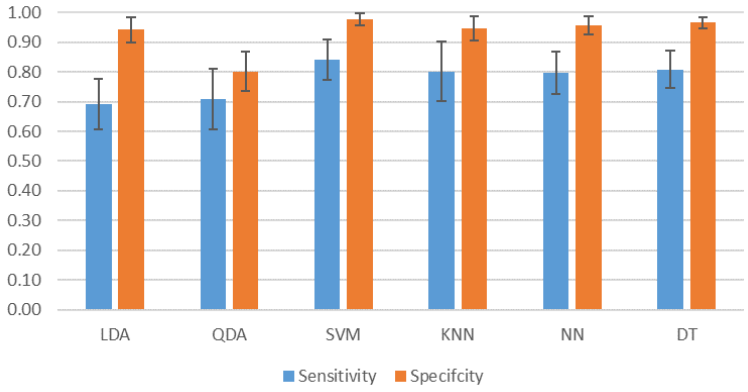

Figure 6-9: Sensitivity and specificity with corresponding standard deviation of the average values from predictive modelling methods on the whole training set using the first 20 components of the PCA

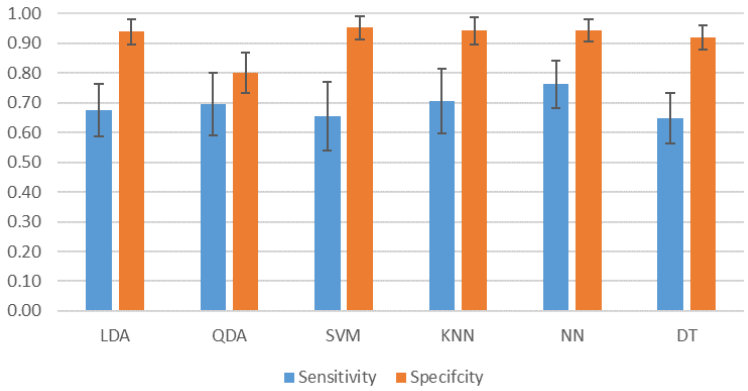

Figure 6-10: Sensitivity and specificity with corresponding standard deviation of the average values from predictive modelling methods on the 10 fold cross validated set using the first 20 components of the PCA

Table 6.15: Number of components chosen by the ReliefF algorithm per sample.

	No. Components
Sample 2	4
Sample 4	10
Sample 5	16
Sample 6	14
Sample 7	8
Sample 8	5
Sample 9	9

Table 6.16: Results of the LDA applied to the the PCA with ReliefF-algorithm

	Training Set				10-fold cross validation			
Sample	Accuracy	Sensitivity	Specificity	AUC	Accuracy	Sensitivity	Specificity	AUC
2	0.74	0.57	0.83	0.70	0.74	0.58	0.83	0.70
4	0.95	0.69	0.99	0.67	0.95	0.64	0.99	0.82
5	0.90	0.59	0.96	0.78	0.90	0.59	0.97	0.78
6	0.93	0.45	0.99	0.72	0.93	0.44	0.99	0.72
7	0.87	0.60	0.93	0.77	0.87	0.60	0.93	0.77
8	0.76	0.04	0.97	0.50	0.75	0.04	0.97	0.50
9	0.87	0.81	0.90	0.85	0.87	0.81	0.89	0.85
Avg	**0.86**	**0.54**	**0.94**	**0.71**	**0.86**	**0.53**	**0.94**	**0.73**
Std	0.08	0.23	0.05	0.10	0.08	0.22	0.06	0.11

value of 0.77 and a specificity of up to 0.94 and sensitivity of around 0.6 in the 10-fold cv data.

6.4.4 Manual chosen variables

The manually-chosen-variables set performs worse in comparison to all previously chosen datasets with a maximum specificity of 0.96 (SVM) and a maximum sensitivity of 0.76 (QDA). The neural network performs best with an AUC of 0.79 (sensitivity=0.65 and specificty of 0.94), as shown in Table 6.26 and Figure 6-14.

To further investigate the significant variables of the manually-chosen-dataset, the ReliefF algorithm was applied to the dataset to determine which variables are significant to the determination of the EVR and the IVR. These are summarised in Figure 6-15. The results show little significance using the variables $E_{max}-position$

Table 6.17: Results of the QDA applied to the the PCA with ReliefF-algorithm

	Training Set				10-fold cross validation			
Sample	Accuracy	Sensitivity	Specificity	AUC	Accuracy	Sensitivity	Specificity	AUC
2	0.75	0.61	0.66	0.78	0.74	0.60	0.66	0.78
4	0.94	0.38	0.98	0.68	0.94	0.38	0.98	0.68
5	0.89	0.49	0.97	0.73	0.88	0.48	0.97	0.72
6	0.94	0.60	0.98	0.79	0.94	0.58	0.98	0.78
7	0.86	0.68	0.91	0.79	0.86	0.67	0.91	0.79
8	0.70	0.63	0.66	0.74	0.70	0.62	0.66	0.74
9	0.78	0.66	0.75	0.81	0.78	0.65	0.75	0.80
Avg	**0.84**	**0.58**	**0.84**	**0.76**	**0.84**	**0.57**	**0.84**	**0.76**
Std	0.09	0.10	0.14	0.04	0.09	0.10	0.14	0.04

Table 6.18: Results of the SVM applied to the the PCA with ReliefF-algorithm

	Training Set				10-fold cross validation			
Sample	Accuracy	Sensitivity	Specificity	AUC	Accuracy	Sensitivity	Specificity	AUC
2	0.88	0.86	0.90	0.88	0.80	0.72	0.84	0.78
4	0.96	0.48	1.00	0.74	0.96	0.41	1.00	0.71
5	0.95	0.75	0.99	0.87	0.91	0.58	0.98	0.78
6	0.97	0.72	1.00	0.86	0.96	0.63	0.99	0.81
7	0.88	0.66	0.94	0.80	0.77	0.47	0.86	0.66
8	0.86	0.58	0.94	0.76	0.81	0.44	0.92	0.68
9	0.94	0.90	0.96	0.93	0.90	0.78	0.95	0.86
Avg	**0.92**	**0.71**	**0.96**	**0.83**	**0.87**	**0.58**	**0.93**	**0.75**
Std	0.04	0.14	0.03	0.06	0.07	0.13	0.06	0.07

Table 6.19: Results of the KNN (with n=10) applied to the the PCA with ReliefF-algorithm

	Training Set				10-fold cross validation			
Sample	Accuracy	Sensitivity	Specificity	AUC	Accuracy	Sensitivity	Specificity	AUC
2	0.83	0.87	0.81	0.84	0.79	0.73	0.82	0.77
4	0.97	0.56	1.00	0.78	0.96	0.41	1.00	0.70
5	0.93	0.78	0.96	0.87	0.91	0.68	0.96	0.82
6	0.96	0.66	0.99	0.83	0.95	0.57	0.99	0.78
7	0.91	0.74	0.94	0.84	0.88	0.61	0.94	0.77
8	0.83	0.69	0.87	0.78	0.79	0.53	0.87	0.70
9	0.89	0.86	0.91	0.88	0.86	0.79	0.89	0.84
Avg	**0.90**	**0.74**	**0.93**	**0.83**	**0.88**	**0.62**	**0.92**	**0.77**
Std	0.05	0.10	0.06	0.04	0.06	0.12	0.06	0.05

Table 6.20: Results of the ANN (with 20 neurons) applied to the the PCA with ReliefF-algorithm

	Training Set				10-fold cross validation			
Sample	Accuracy	Sensitivity	Specificity	AUC	Accuracy	Sensitivity	Specificity	AUC
2	0.78	0.93	0.94	0.94	0.78	0.70	0.93	0.81
4	0.97	0.70	0.99	0.85	0.94	0.41	0.99	0.70
5	0.94	0.72	0.98	0.85	0.89	0.65	0.95	0.80
6	0.95	0.65	0.99	0.82	0.94	0.59	0.98	0.79
7	0.89	0.72	0.94	0.83	0.88	0.62	0.94	0.78
8	0.82	0.81	0.94	0.88	0.77	0.32	0.93	0.62
9	0.89	0.82	0.91	0.87	0.87	0.87	0.88	0.87
Avg	**0.89**	**0.76**	**0.96**	**0.86**	**0.87**	**0.59**	**0.94**	**0.77**
Std	0.07	0.09	0.03	0.04	0.06	0.17	0.04	0.08

Table 6.21: Results of the DT (with minimum leaf size of 20 samples) applied to the the PCA with ReliefF-algorithm

	Training Set				10-fold cross validation			
Sample	Accuracy	Sensitivity	Specificity	AUC	Accuracy	Sensitivity	Specificity	AUC
2	0.87	0.82	0.89	0.86	0.76	0.68	0.81	0.75
4	0.97	0.70	0.99	0.84	0.95	0.56	0.98	0.77
5	0.94	0.79	0.98	0.88	0.89	0.63	0.94	0.78
6	0.96	0.73	0.98	0.85	0.93	0.59	0.97	0.78
7	0.92	0.71	0.97	0.84	0.87	0.60	0.94	0.77
8	0.88	0.66	0.94	0.80	0.77	0.47	0.86	0.66
9	0.91	0.84	0.94	0.89	0.82	0.73	0.86	0.80
Avg	**0.92**	**0.75**	**0.96**	**0.85**	**0.86**	**0.61**	**0.91**	**0.76**
Std	0.04	0.06	0.03	0.03	0.07	0.08	0.06	0.04

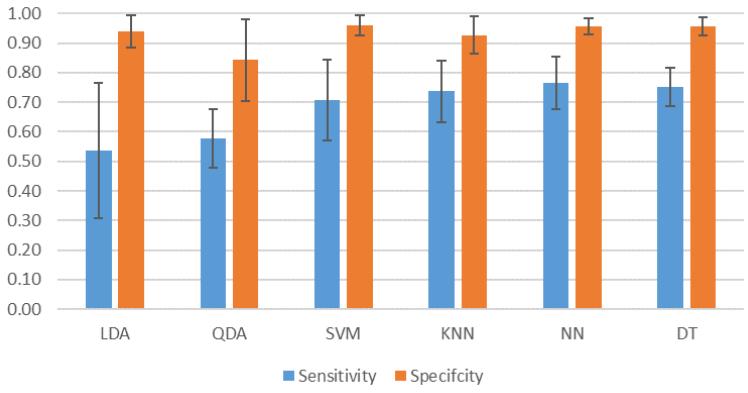

Figure 6-11: Sensitivity and specificity with corresponding standard deviation of the average values from predictive modelling methods on the whole training set using the components of the PCA extracted from the ReliefF-algorithm

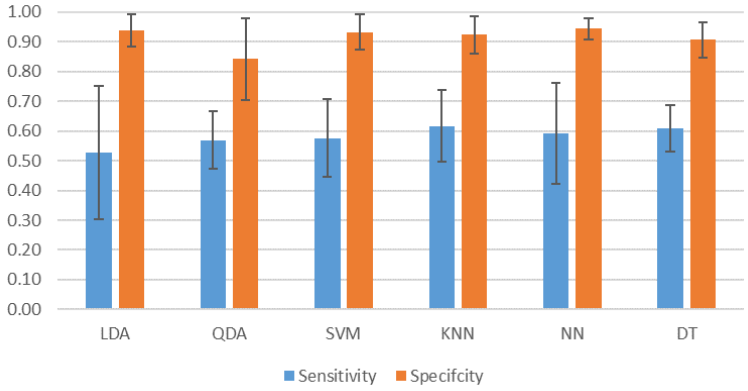

Figure 6-12: Sensitivity and specificity with corresponding standard deviation of the average values from predictive modelling methods on the 10 fold cross validated set using the components of the PCA extracted from the ReliefF-algorithm

Table 6.22: Results of the LDA applied to manual chosen variables

	Training Set				10-fold cross validation			
Sample	Accuracy	Sensitivity	Specificity	AUC	Accuracy	Sensitivity	Specificity	AUC
2	0.83	0.71	0.89	0.80	0.82	0.76	0.86	0.81
4	0.95	0.41	0.99	0.70	0.95	0.41	0.99	0.70
5	0.93	0.64	0.99	0.81	0.92	0.61	0.99	0.80
6	0.93	0.50	0.98	0.74	0.93	0.47	0.98	0.73
7	0.85	0.53	0.93	0.73	0.85	0.58	0.91	0.75
8	0.79	0.23	0.96	0.59	0.79	0.26	0.94	0.60
9	0.87	0.79	0.90	0.85	0.86	0.77	0.90	0.84
Avg	**0.88**	**0.55**	**0.95**	**0.75**	**0.87**	**0.55**	**0.94**	**0.75**
Std	0.06	0.18	0.04	0.08	0.06	0.17	0.05	0.07

Table 6.23: Results of the QDA applied to manual chosen variables

	Training Set				10-fold cross validation			
Sample	Accuracy	Sensitivity	Specificity	AUC	Accuracy	Sensitivity	Specificity	AUC
2	0.71	0.93	0.59	0.76	0.71	0.94	0.59	0.77
4	0.88	0.61	0.90	0.76	0.88	0.57	0.90	0.74
5	0.89	0.68	0.93	0.80	0.89	0.67	0.93	0.80
6	0.88	0.66	0.90	0.78	0.87	0.65	0.90	0.78
7	0.79	0.84	0.78	0.81	0.79	0.84	0.78	0.81
8	0.67	0.81	0.63	0.72	0.67	0.81	0.62	0.72
9	0.69	0.86	0.62	0.74	0.69	0.85	0.62	0.74
Avg	**0.79**	**0.77**	**0.77**	**0.77**	**0.79**	**0.76**	**0.76**	**0.76**
Std	0.09	0.11	0.14	0.03	0.09	0.12	0.14	0.03

Table 6.24: Results of the SVM applied to manual chosen variables

	Training Set				10-fold cross validation			
Sample	Accuracy	Sensitivity	Specificity	AUC	Accuracy	Sensitivity	Specificity	AUC
2	0.94	0.91	0.95	0.93	0.87	0.79	0.91	0.85
4	0.97	0.56	1.00	0.78	0.96	0.42	1.00	0.71
5	0.95	0.74	1.00	0.87	0.91	0.54	0.99	0.77
6	0.97	0.74	1.00	0.87	0.95	0.54	1.00	0.77
7	0.93	0.70	0.98	0.84	0.88	0.56	0.95	0.75
8	0.85	0.50	0.96	0.73	0.81	0.40	0.92	0.66
9	0.93	0.88	0.95	0.92	0.87	0.77	0.92	0.85
Avg	**0.94**	**0.72**	**0.98**	**0.85**	**0.89**	**0.58**	**0.95**	**0.77**
Std	0.04	0.14	0.02	0.07	0.05	0.14	0.04	0.06

Table 6.25: Results of the KNN (n=10) applied to manual chosen variables

	Training Set				10-fold cross validation			
Sample	Accuracy	Sensitivity	Specificity	AUC	Accuracy	Sensitivity	Specificity	AUC
2	0.80	0.65	0.88	0.77	0.69	0.47	0.81	0.64
4	0.94	0.20	1.00	0.60	0.94	0.15	1.00	0.57
5	0.87	0.28	1.00	0.64	0.86	0.18	1.00	0.59
6	0.91	0.15	1.00	0.57	0.90	0.09	1.00	0.54
7	0.85	0.40	0.95	0.67	0.81	0.17	0.96	0.56
8	0.80	0.49	0.88	0.69	0.74	0.32	0.87	0.59
9	0.78	0.62	0.84	0.73	0.72	0.48	0.82	0.65
Avg	**0.85**	**0.40**	**0.94**	**0.67**	**0.81**	**0.27**	**0.92**	**0.59**
Std	0.06	0.19	0.06	0.06	0.09	0.15	0.08	0.04

Table 6.26: Results of the NN (n=16) applied to manual chosen variables

	Training Set				10-fold cross validation			
Sample	Accuracy	Sensitivity	Specificity	AUC	Accuracy	Sensitivity	Specificity	AUC
2	0.86	0.80	0.90	0.94	0.84	0.79	0.87	0.83
4	0.94	0.44	0.99	0.94	0.96	0.49	0.99	0.74
5	0.86	0.55	0.92	0.93	0.93	0.68	0.98	0.83
6	0.93	0.62	0.98	0.95	0.96	0.73	0.99	0.86
7	0.87	0.54	0.95	0.92	0.88	0.59	0.95	0.77
8	0.75	0.30	0.91	0.83	0.81	0.44	0.92	0.68
9	0.90	0.81	0.94	0.95	0.88	0.80	0.92	0.86
Avg	**0.87**	**0.58**	**0.94**	**0.92**	**0.89**	**0.65**	**0.94**	**0.79**
Std	0.06	0.17	0.03	0.04	0.05	0.13	0.04	0.06

Table 6.27: Results of the DT (minimum leaf size = 20) applied to manual chosen variables

	Training Set				10-fold cross validation			
Sample	Accuracy	Sensitivity	Specificity	AUC	Accuracy	Sensitivity	Specificity	AUC
2	0.87	0.79	0.92	0.85	0.81	0.69	0.88	0.78
4	0.96	0.49	1.00	0.74	0.95	0.42	0.98	0.70
5	0.94	0.75	0.98	0.87	0.89	0.65	0.94	0.79
6	0.96	0.76	0.98	0.87	0.93	0.54	0.97	0.76
7	0.92	0.76	0.95	0.86	0.85	0.52	0.92	0.72
8	0.89	0.71	0.95	0.83	0.78	0.48	0.87	0.67
9	0.90	0.84	0.93	0.89	0.81	0.69	0.86	0.77
Avg	**0.92**	**0.73**	**0.96**	**0.84**	**0.86**	**0.57**	**0.92**	**0.74**
Std	0.03	0.11	0.03	0.04	0.06	0.10	0.05	0.04

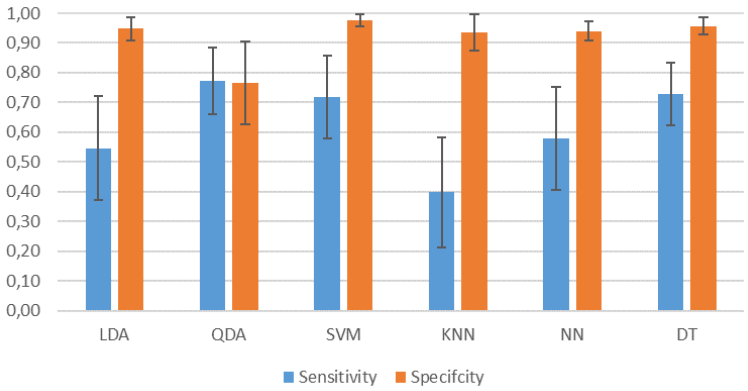

Figure 6-13: Sensitivity and specificity with corresponding standard deviation of the average values from predictive modelling methods on the whole training set using manual chosen variables.

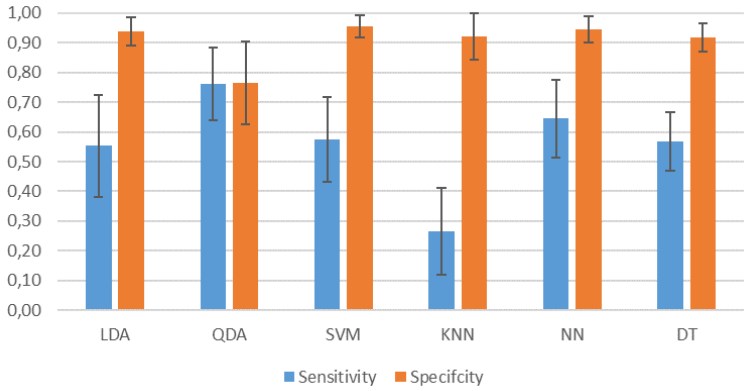

Figure 6-14: Sensitivity and specificity with corresponding standard deviation of the average values from predictive modelling methods on the 10 fold cross validated set using using manual chosen variables.

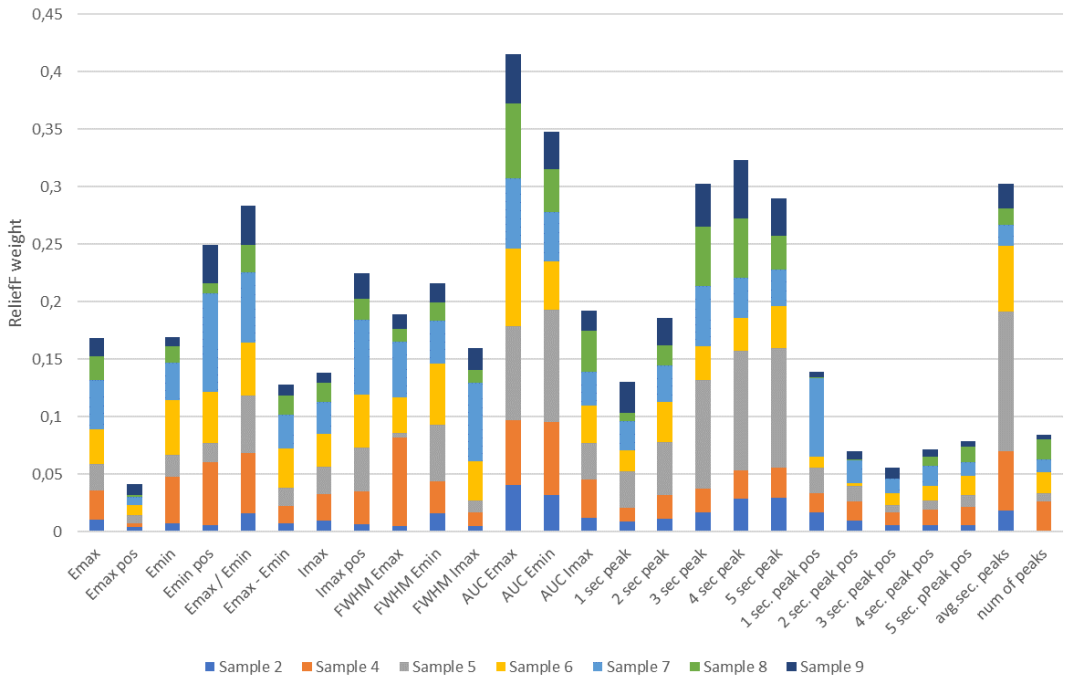

Figure 6-15: Importance weights of the ReliefF algorithm applied to manual-chosen-dataset, stacked per sample

as well as the positions of the secondary peaks. The largest importance is shown on the area-under-the-curve of the $E_{maximum}$ and the $E_{minimum}$ as indicated in Figure 6-15. For samples 5 and 8 further significance is shown in the secondary peaks heights of the 3rd, 4th and 5th peaks, whereas Sample 4 gives biggest significance to the FWHM of the $E_{maximum}$. The behaviour of Sample 4 may be explained by the fact that the first secondary peak might be very close to the first maximum and therefore stretches the initial waveform early enough to be caught by the FWHM value. Furthermore, the AUC of the maximum energy wave which contains the largest significance may be accounted for by multiple reflections from within the sample that are not separated into distinct secondary waves but are rather incorporated into the maximum energy wave.

6.5 Results: Raw data of all-sample-set

In this section, the predictive modelling techniques have been applied on the full sample normalised raw data. Using Leave-One-Out-Sample-Cross-Validation the intention is to find out if a model trained on seven of the eight samples can predict the IVR and the EVR of the excluded sample.

Applying the full data set of the raw normalised waveforms does not show good results. In the majority of cases, the prediction of the previously unseen sample fails. In many cases the $true\,positive - false\,negative$ or $true\,negative - false\,positive$ are zero, which leads to a division by zero problem and thus the accuracy, sensitivity or specificity cannot be determined. Furthermore due to the size of the dataset, the neural network and the decision tree have been dropped due to computational limitations.

Table 6.28: Results on the LDA performed on the whole raw dataset

Sample Left Out	Accuracy	Sensitivity	Specificity	AUC
9	0.70	0.70	NaN	0.69
8	NaN	0.77	NaN	NaN
7	NaN	0.82	NaN	NaN
6	0.90	0.90	0.01	0.43
5	NaN	NaN	0.17	NaN
4	0.37	1.00	0.10	0.49
2	0.65	0.65	0.01	0.46

Table 6.29: Results on the QDA performed on the whole raw dataset

Sample Left Out	Accuracy	Sensitivity	Specificity	AUC
9	NaN	0.70	NaN	NaN
8	NaN	0.77	NaN	NaN
7	NaN	0.82	NaN	NaN
6	NaN	0.90	NaN	NaN
5	NaN	0.83	NaN	NaN
4	0.77	0.92	0.03	0.48
2	NaN	0.65	NaN	NaN

Table 6.30: Results on the SVM performed on the whole raw dataset

Sample Left Out	Accuracy	Sensitivity	Specificity	AUC
9	0.72	0.72	0.71	0.54
8	NaN	0.77	NaN	NaN
7	NaN	0.82	NaN	NaN
6	0.88	0.90	0.21	0.51
5	0.80	0.87	0.41	0.63
4	0.93	0.93	0.17	0.50
2	0.69	0.69	0.68	0.58

Table 6.31: Results on the KNN performed on the whole raw dataset

Sample Left Out	Accuracy	Sensitivity	Specificity	AUC
9	0.65	0.73	0.39	0.91
8	NaN	0.77	NaN	NaN
7	NaN	0.82	NaN	NaN
6	NaN	NaN	0.10	NaN
5	0.83	0.83	1.00	0.91
4	NaN	0.93	NaN	NaN
2	0.65	0.65	0.75	0.89

6.6 Conclusion and discussion

Values obtained from the above experiments using the full feature set, the PCA and the ReliefF algorithm yield a couple statements that can be given regarding the data itself and the layout of the data:

The quality of the input data seems to be mixed, which can be seen because of the large differences between the best- and worst-fitted sample. In most cases, Sample 4 performs worse over all models which is most liekly due to the small sample size of the IVR.

To differentiate between the IVR and EVR, a linear modelling system performs well on the full raw dataset with a sensitivity 0.72 of and a specificity of 0.94, which shows that there is a linear separable dependency in the data. The results can be improved slightly by using a neural network which acts as a multi-linear classifier with a sensitivity of 0.79 and a specificity of 0.96. Using the ReliefF algorithm to determine the variables that show a positive prediction shows that

almost all variables that contain the positive or negative energy waves are positive prediction values. Since the early negative wave shows a positive prediction value as well, which is reflected at the main interfaces between the sample holder and the skin, this could mean that the malignancy is indeed already visible at the stratum corneum and further into the epidermis. Also, the slack behind the positive energy peak, which must be inside the tissue, shows positive prediction values, which could mean that different absorption rates are present between the IVR and EVR.

A quadratic, ring or rectangular modelling system does not seem to be the best choice, as the systems quality with respect to the AUC is low (or modest) or the prediction model seems to overfit dramatically one the raw dataset as well as the PCA.

By reducing the number of variables using the PCA and cutting after 20 components, the sensitivity and specificity decreases, which may be explained due to the high amount of noise in the data. However, it is interesting to see that the specificity always stays high (>90%) using the LDA on all datasets.

By using manually chosen variables a modest trade off can be found using the QDA on the, with a sensitivity of 0.76 and a specificity of 0.96. Using the ReliefF algorithm on the the results shows that the most important variables are AUC of $E_{minimum}$ and $E_{maximum}$ and the average peak heights chosen from secondary peaks. However, the AUC of the maximum energy peak mostly contains the secondary peaks, and these can be seen as overtones on the waveform. While it is difficult to detect secondary peaks in the data, the ReliefF analysis shows that some samples, especially samples 5 and 2, seem to show a positive prediction, which could be an internal reflection from the epidermis.

Applying the full dataset of all samples to the prediction methods and using a Leave-One-Sample-Out-Cross-Validation to inspect if a system can detect a

previously unseen cutaneous liaison does not show a positive result. This could be because of the simple normalisation with the baseline. The sample data seems to be too different to be comparable with each other. Furthermore, the positive predictor weights from the ReliafF algorithm applied to each sample show different areas of interest, making it difficult to find similarities in the data, however positive predictors can be found just before the positive incident beam as well as far behind the first incident which could indicate that the malignancy is already close to the epidermis. If and to what extend the positive predictor weights correlate with the depth of the lesions is beyond the scope of this study and requires further information from the histopathologists.

In this chapter, various models have been trained to determine if the IVR and the EVR are distinguishable by a) taking each sample separately and b) taking the whole dataset to determine if the IVR of one sample could be predicted by the other samples. In the next chapter, an investigation of the refractive index of the malicious lesions taken out and compared to non-melanoma samples.

Chapter 7

Investigation of the Refractive Index of MM Samples

The last chapters examined the use of predictive models on features extracted mostly from raw data. To try to explain these results and to give a more physical-theory based background, this chapter converts the waveforms to refractive indices spectra in the terahertz regime which allows us to investigate the cancerous samples with the samples taken from cosmetic surgery and compare the technique used to other techniques.

7.1 Conformation study on the determination of the complex refractive index using solid materials

Based on the theoretical foundations of the Fresnel equations for the determination of the refractive index in the frequency domain, a validation is anticipated using quartz slides with one and two interfaces. Thus, this experiment divides into two steps. First, we measure each quartz slide separately from the bottom (air-

Table 7.1: Substrates taken for the experiments. The refractive index was taken transmission mode measurements between 0.1 and 1.1 THz plus standard deviation apart from BK7 3mm which was taken between 0.1 and 0.7 THz.

Glass Sample	**Thickness / mm**	**Refractive Index**	**StdDev**
SiO_2 -Quartz	2.10	2.08	0.00
Fused Silica	1.08	1.97	0.01
Fused Silica	1.65	1.94	0.01
Pyrex	1.69	2.10	0.01
Pyrex	3.29	2.10	0.02
BK7	1.01	2.52	0.03
BK7	3.00	2.56	0.10

quartz interface) and compare our results with values previously obtained from transmission mode shown in . Second, we put the solid materials on top of the quartz sample holder and measure the interface between them.

It has also been found that, in the literature, the simplified Fresnel equations are often used to calculate the refractive index and the absorption coefficient. A theoretical comparison of the full and simplified Fresnel equations is needed to show the impact of the equations for calculation of the refractive index.

7.1.1 Windows slides materials

Three different types of window slides, fused silica, Pyrex and BK7 with different thicknesses were obtained from ESCO Products (New Jersey, NY, USA), and the sample holder, a C-axis parallel quartz crystalline window (SKU: Q-W-38-2) was obtained from ISP-Optics. The refractive indices are measured in transmission and in reflection mode; the properties of the substrates are given in Table 7.1 and Figure 7-1 shows the frequency dependant refractive index from transmission mode.

To measure differences of substrates with known refractive index and known thickness, the terahertz machine was set-up in reflection mode using an incidence

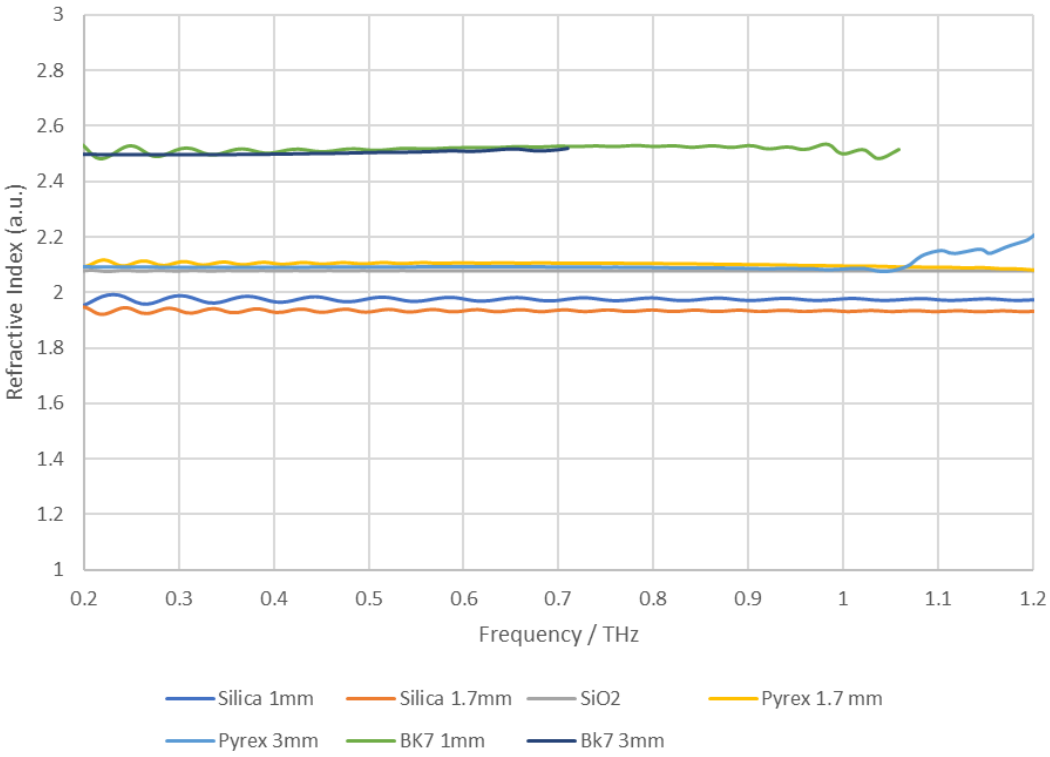

Figure 7-1: Quartz substrates taken from transmission mode measurements

angle of 30° and elliptical, gold-plated mirrors. The underlying chamber was filled with nitrogen to remove artefacts from air, including especially the water content within the air.

Prior to measurements of the glass slides, the sample position was adjusted with a focusing screw by placing a gold reflector on the sample position and focusing on the maximum reflected energy peak; thus, measurements were taken using the bottom of a probe as the focus.

Measurements in reflectance mode were taken within a scan range (bandwidth) of 29 ps (4V) and a wave resolution of 2,048 points. 29 ps were chosen to capture only the desired reflection of the quartz and the quartz-quartz interface, thereby surpassing any further secondary reflections (also called Fabry-Perrot effects) that would interfere with the results [193].

The time-domain waveform was obtained directly from the machine and a

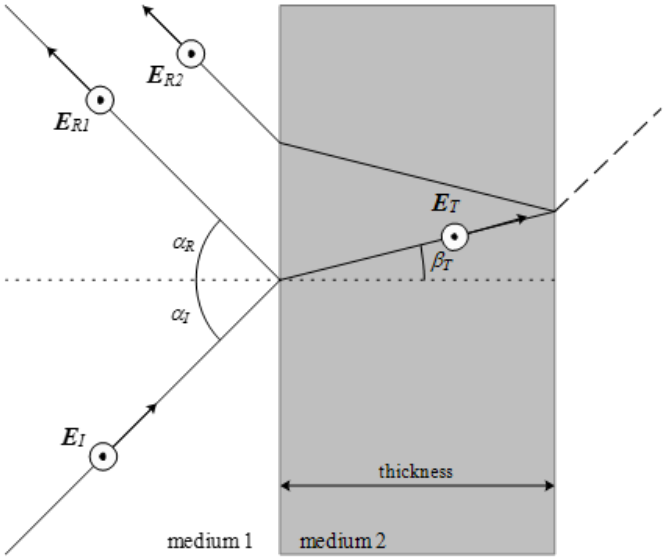

Figure 7-2: Schematic of the geometry of an electromagnetic wave travelling through a medium

reference was taken using a gold-plated mirror. The mirror must be positioned exactly at the same spot as the samples, as minimal misalignments (in the range of microns) create differences in the phase which significantly alters the results [194].

7.1.2 Theoretical description of single interface Fresnel equations and determination of the refractive index

For Method 1, the focus of the terahertz beam has been aligned to the bottom substrate, measuring E_{R1} as shown in Figure 7-2. Because the measurement of the incidence wave E_I is not applicable in reflection geometry, a gold plated mirror was used as reference, the reflection of which was almost 100%. In theory, $E_{reference}$ can be equated with the incident time-domain beam ($E_{incidence}$). After transforming the time-domain data into frequency space using the Fast Fourier Transformation (FFT), the following equations are applied to the sample reflection:

$$r_s = \frac{E_{sample}}{E_{reference}} = \frac{n_1 \cos(\alpha) - n_2 \cos(\beta)}{n_1 \cos(\alpha) + n_2 \cos(\beta)} \tag{7.1}$$

$$r_p = \frac{E_{sample}}{E_{reference}} = \frac{n_2 \cos(\alpha) - n_1 \cos(\beta)}{n_2 \cos(\alpha) + n_1 \cos(\beta)} \tag{7.2}$$

The refractive index of a medium is defined by its material dependent speed of light divided by the speed of light in vacuum, resulting in

$$n_{medium} = \frac{c_{medium}}{c_{vacuo}} \tag{7.3}$$

Together with the Snell's law, which describes the change of direction of (any) wave going from one medium to another, defined as:

$$\frac{\sin(\alpha)}{\sin(\beta)} = \frac{n_1}{n_2} \equiv \beta = \sin^{-1}(\sin(\alpha)\frac{n_1}{n_2}) \tag{7.4}$$

Method 1a In Method 1a, the raw data is used without any manipulation. The obtained (raw) time-domain data is transformed into the Fourier space using the fast Fourier transform, and the equations 7.1 to 7.4 are applied.

Method 1b In Method 1b, the maximum energy position of the samples (the optical delay at the maximum peak of the energy time-domain waveform) is compared with that of the reference (mirror) one. Since small fluctuations cannot be avoided, we shift the sample waveform on the reference waveform so that their maximum peaks have the same optical delay position.

7.1.3 Theoretical description of double interface Fresnel equations and determination of the refractive index

In Method 2, the quartz substrates were put on top of the sample holder and the beam was focussed between the two interfaces, as shown in Figure 7-3C. The substrates were clamped together with the sample holder to reduce the effects of air gaps which could alter the stability of the refractive index. Since the reflected

beam transmits through the sample holder and reflects back from the interface between the sample holder and the substrate, the equations for the determination of the refractive index become more complicated. We use the following:

$$\frac{E_{sample}}{E_{refrence}} = \frac{t^{\parallel}_{1,2}\, t^{\parallel}_{2,1}\, r^{\parallel}_{2,3} + t^{\perp}_{1,2}\, t^{\perp}_{2,1}\, r^{\perp}_{2,3}}{t^{\parallel}_{1,2}\, t^{\parallel}_{2,1} + t^{\perp}_{1,2}\, t^{\perp}_{2,1}} \tag{7.5}$$

where t stands for transmittance and r for reflectance. The symbol $\parallel$ indicates the parallel and $\perp$ indicates the perpendicular part of the resulting wave. The subscripts 1,2 represent the air-sample holder interface; 2,1 is the sample holder-air interface and 2,3 is the sample holder and substrate interface. The equations for the transmittance and reflectance part the parallel and perpendicular parts are as follows:

$$\hat{r}^{\perp}_{i,j} = \frac{\hat{n}_i \cos(\Theta_i) - \hat{n}_j \cos(\Theta_j)}{\hat{n}_i \cos(\Theta_i) + \hat{n}_j \cos(\Theta_j)} \tag{7.6}$$

$$\hat{r}^{\parallel}_{i,j} = \frac{\hat{n}_j \cos(\Theta_i) - \hat{n}_i \cos(\Theta_j)}{\hat{n}_j \cos(\Theta_i) + \hat{n}_i \cos(\Theta_j)} \tag{7.7}$$

$$\hat{t}^{\perp}_{i,j} = \frac{2\hat{n}_i \cos(\Theta_i)}{\hat{n}_i \cos(\Theta_i) + \hat{n}_j \cos(\Theta_j)} \tag{7.8}$$

$$\hat{t}^{\parallel}_{i,j} = \frac{2\hat{n}_i \cos(\Theta_i)}{\hat{n}_j \cos(\Theta_i) + \hat{n}_i \cos(\Theta_j)} \tag{7.9}$$

Equations 7.6 to 7.9 are inserted into equation 7.5 and solved numerically due to the complexity of the resulting equation. As explained regarding Method 1, we also apply Snell's law to Equation 7.5 to eliminate the second unknown angle of the material, thus leaving only the refractive index of the substrate as the unknown variable. For a detailed description of the Fresnel equation, we refer the reader to [132].

Method 2a) quartz-quartz interface using gold plated mirror as reference

Using the quartz as sample holder, the terahertz beam was aligned to be

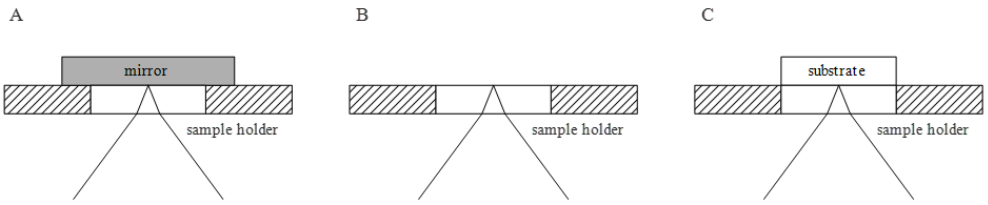

Figure 7-3: Measuring modes for substrates on a sample holder

focused on the centre between Medium 1 (sample holder) and Medium 2 (quartz substrate). The incidence (E_i) beam was calculated from a mirror reflection on top of the quartz, which had been measured independently before the substrate measurements.

Method 2b), quartz-quartz interface using air as reference The reference waveform may be calculated using any material with known refractive index and absorption coefficient. In this case, we use the sample holder in contact with air. Since the substrate lies on top of the sample holder, we measure the air (also known as baseline) by focussing on top of the quartz sample holder, as shown in Figure 7-3B, and by assuming a constant refractive index of 1 and a negligible absorbance for air.

Method 2b has the advantage that, when one is measuring biological tissue as a 2D image, one (almost) always encounters surrounding air interfaces as well, thereby reducing the need to gather additional reflection data from the mirror. Practically, this is also useful, as the conditions for the second (reflection) measurement may change, and tiny changes may lead to large differences when converting to the refractive index.

7.1.4 Results

Solid materials have been scanned. Figure 7-4 shows the time-domain results of the scan, including the mirror reference. Due to a reflection phase change of 180 degrees, what would have been the maximum peak of the incidence beam

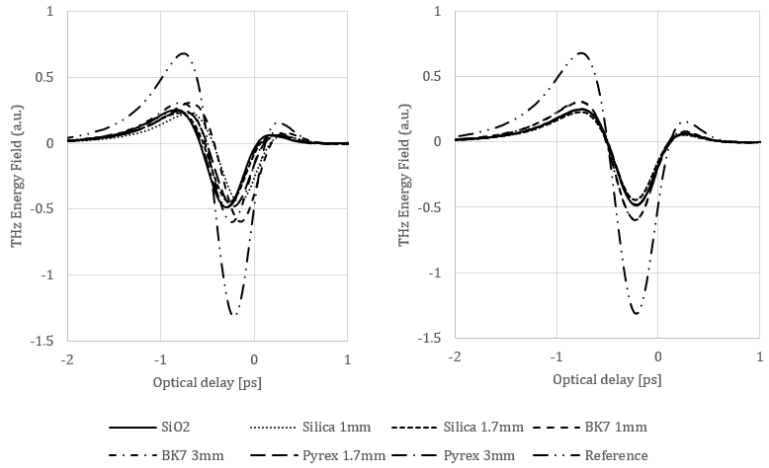

Figure 7-4: Original quartz substrates (left) and adjusted to the minimum peak of the reference (right)

Table 7.2: Maximum peak shifts of the Terahertz Time Domain waveform to align to the maximum peak of the reference waveform.

	SiO_2	**Silica 1mm**	**Silica 1.7mm**	**BK7 1mm**	**BK7 3mm**	**Pyrex 1.7mm**	**Pyrex 3mm**
Shift in pixels	6	-5	4	-3	1	1	5
Shift in ps	0.0814	-0.0678	0.0542	-0.0407	0.0135	0.0135	0.0678

now becomes a negative (minimum) peak. As can be seen in Figure 7-4 (left), the peak positions are not uniform and have been adjusted (Figure 7-4 (right)). These shifts are most likely due to tiny misalignments and are of a practical nature, as the shifts are within a couple of femto seconds, as shown in Table 7.2.

Before applying the Fresnel equations to the raw terahertz data, the fast Fourier transform was applied to the data, thereby converting the signals from the time domain into frequency space. In a range up to approximately 1.3 terahertz, the reflection data of unique materials with different heights overlay each other. Silica shows the smallest magnitude, followed by Pyrex and BK7, as shown in Figure 7-4.

Applying the Fresnel equations from the equations set in Section 7.1.4, the

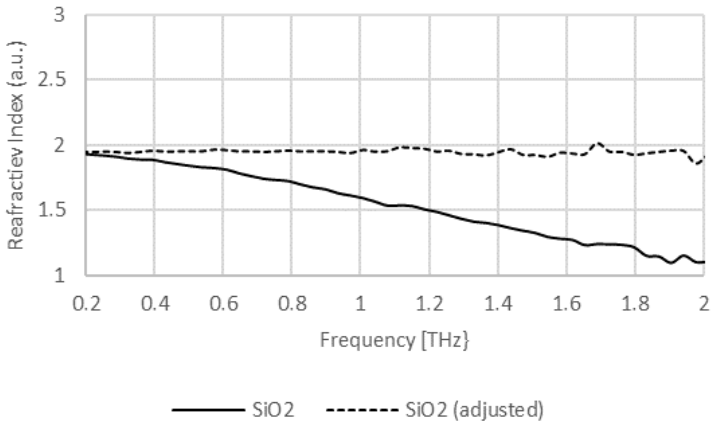

Figure 7-5: Refractive index of SiO_2 using Method 1a) raw data and Method 1b) adjusted data

reflectance optic system configured with parabolic mirrors creates an incidence beam with an angle of 30 degrees. Since Snell's Law is applicable here, the reflected angle from the samples needs to be 30 degrees as well.

Comparison of Method 1a and 1b:

On Method 1b, the maximum peak of the SiO_2 quartz sample shifted by 0.0679 ps (6 pixels). The result of Methods 1a and 1b changes dramatically, as the smallest misalignments between the sample and the reference lead to significant phase differences between them, which causes an unstable refractive index. This is demonstrated in Figure 7-5.

The same methodology was applied to all samples and a constant refractive index was retrieved which is comparable to the values obtained from prior taken transmission mode measurements. To quantify our results, the mean and the standard deviation from a frequency range between 0.3 and 1.3 THz was calculated as this seems to be the regime where the refractive index stays constant. Our results are in good agreement with the values obtained in transmission mode and shows an absolute error of under 1%, as summarised in Table 7.3.

In conclusion, we have demonstrated the need for the maximum peak align-

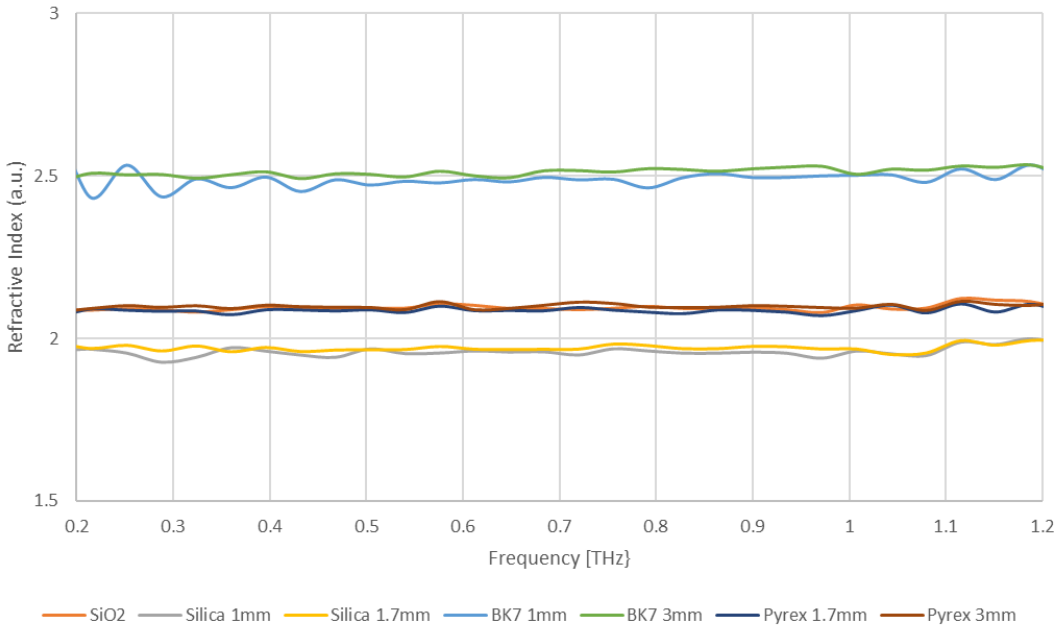

Figure 7-6: Adjusted refractive indices (Method 1b) of single substrates

Table 7.3: Comparison of mean refractive index from reflection and transmission mode measurements including the relative and absolute error (in %).

	$\mathbf{RI_{reflection}}$	**StdDev**	$\mathbf{RI_{transmission}}$	**rel. Error**	**abs. Error / %**
SiO_2	2.07	0.01	2.07	0.00	0.0
Silica 1mm	1.97	0.01	1.97	0.00	0.0
Silica 1.7mm	1.96	0.01	1.94	0.02	1.0
BK7 1mm	2.49	0.02	2.51	0.02	0.8
BK7 3mm	2.51	0.02	2.52	0.01	0.4
Pyrex 1.7mm	2.09	0.01	2.10	0.01	0.5
Pyrex 3mm	2.10	0.01	2.10	0.00	0.0

ment to improve the accuracy of the refractive index of single solid materials measured in terahertz reflection mode.

Method 2: Investigation of substrate in contact with the sample holder - Comparison of Method 2a and 2b

On Method 2a, the mirror was used as the reference, whereas on Method 2b, we use the baseline and calculate the reference from there. As can be seen from Figure 7-7, though the resulting waveforms are almost identical with an E_max of 1.08 and 1.06, the position of the mirror reference and the calculated reference differ greatly, by 0.12ps (equivalent to 10px). Not taking this shift into account results in unstable refractive materials of the substrates under investigation (compare 7-8 (left)), whereas taking the air as reference results in a relatively stable and constant refractive index in a frequency range up to approximately 1.3 THz (Figure 7-8 (right)). By calculating the refractive index of air from the reference taken from air, the refractive index has to be exactly 1 (Figure 7-8) with a standard deviation 0 (compare Table 7.4 and Table 7.5).

To further quantify the results, the average of the refractive index between 0.3 and 1.3 THz was calculated and the standard deviation was taken. The mean values have been compared with the transmission ones including their relative and absolute errors between them. The results of Method 2a are shown in Table 7.4 and the results of Method 2b are shown in Table 7.5.

While from Method 2b, the minimum error is above 2% and the maximum error is around 13% compared to the values obtained from transmission mode measurements. Using the air as a reference medium results in a low error compared to the literature (Table 7.5) and a constant refractive index (Figure 7-8)). We therefore prefer this Method when dealing with more complex materials.

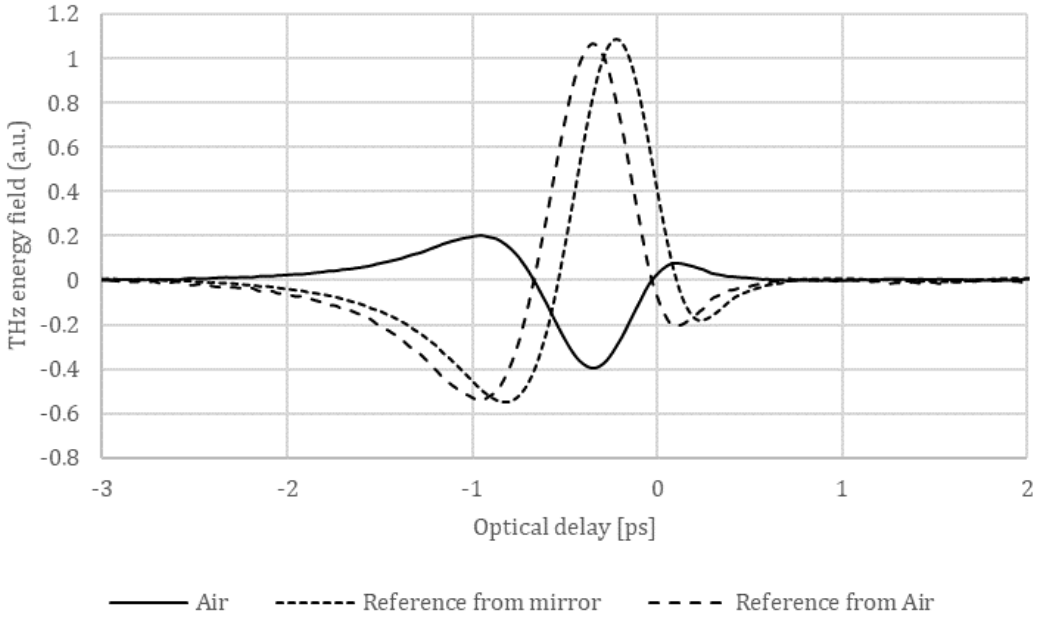

Figure 7-7: Real quartz-mirror reflection and calculated reference taken from a measurement of quartz in contact with air.

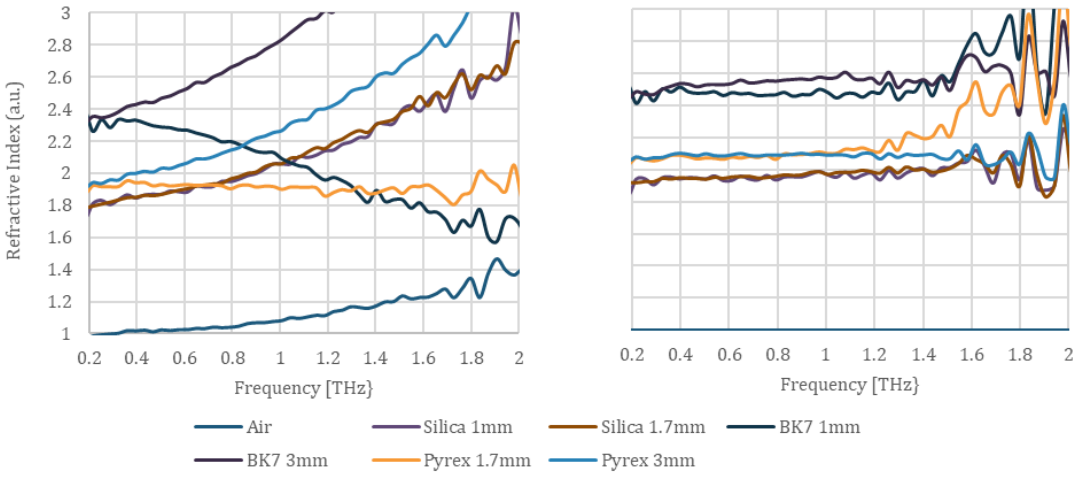

Figure 7-8: Comparison of Method 2a refractive index calculated with the mirror as reference (left) and 2b, refractive index calculated with air as reference (right).

Table 7.4: Comparison of the mean refractive index obtained from Method 2a with the transmission values.

	$\mathbf{RI_{reflection}}$	**StdDev**	$\mathbf{RI_{transmission}}$	**rel. Error**	**abs. Error / %**
Air	1.07	0.05	1	0.07	7.0
Silica 1mm	1.99	0.12	1.95	0.04	2.1
Silica 1.7mm	2.01	0.13	1.94	0.07	3.6
BK7 1mm	2.15	0.14	2.51	0.36	14.3
BK7 3mm	2.72	0.23	2.52	0.20	7.9
Pyrex 1.7mm	1.91	0.02	2.10	0.19	9.0
Pyrex 3mm	2.19	0.17	2.10	0.09	4.3

Table 7.5: Comparison of the mean refractive index obtained from Method 2b with the transmission values.

	$\mathbf{RI_{reflection}}$	**StdDev**	$\mathbf{RI_{transmission}}$	**rel. Error**	**abs. Error / %**
Air	1.00	0.05	1	0.00	0.0
Silica 1mm	1.96	0.12	1.95	0.01	0.5
Silica 1.7mm	1.97	0.13	1.94	0.03	1.5
BK7 1mm	2.47	0.14	2.51	0.04	1.6
BK7 3mm	2.55	0.23	2.52	0.03	1.2
Pyrex 1.7mm	2.10	0.02	2.10	0.00	0.0
Pyrex 3mm	2.09	0.17	2.10	0.01	0.5

7.1.5 Conclusion

In conclusion, we have compared the use of the mirror and the use of an air measurement as references to calculate the frequency-dependant, complex refractive index of solid quartz materials. It has been shown that use of an air measurement as reference leads to more feasible and accurate results. We assume that this is due to surface roughness between two solid materials and inescapable influences of practical misalignments in the micro-meter regime.

For solid materials that have a negligible absorption coefficient, it would be feasible to align the waveforms with the reference maximum peak to account for misalignments, as demonstrated with Method 1; however, when working towards the scanning of a 3D image of biological tissue, we assume that those shifts might contain valuable information of the sample under investigation. Shifts in the waveform compared to the reference waveform are expected especially when the sample has a high absorption.

Furthermore, this technique is practical for terahertz imaging techniques of liquids and biological tissues. This is true for two reasons. First, it can be assumed that liquids and non-rigid materials will not create a gap due to surface roughness between the sample holder and the substrates. Furthermore, by scanning excised biological tissue on top the sample holder using step-motors to create an image, the surrounding air interface can be used as a reference, thereby reducing the need for a second (mirror) measurement to be taken, which might influence the outcome due to baseline minimal shifts, as demonstrated with Method 1 in this article.

While other methods exist with which to obtain the refractive index—such as [195], which obtains the refractive index of aqueous alcohol and sugar solutions on a quartz sample holder—they have the problem that they need to take the bottom of the quartz into account, which lowers the possible bandwidth of the

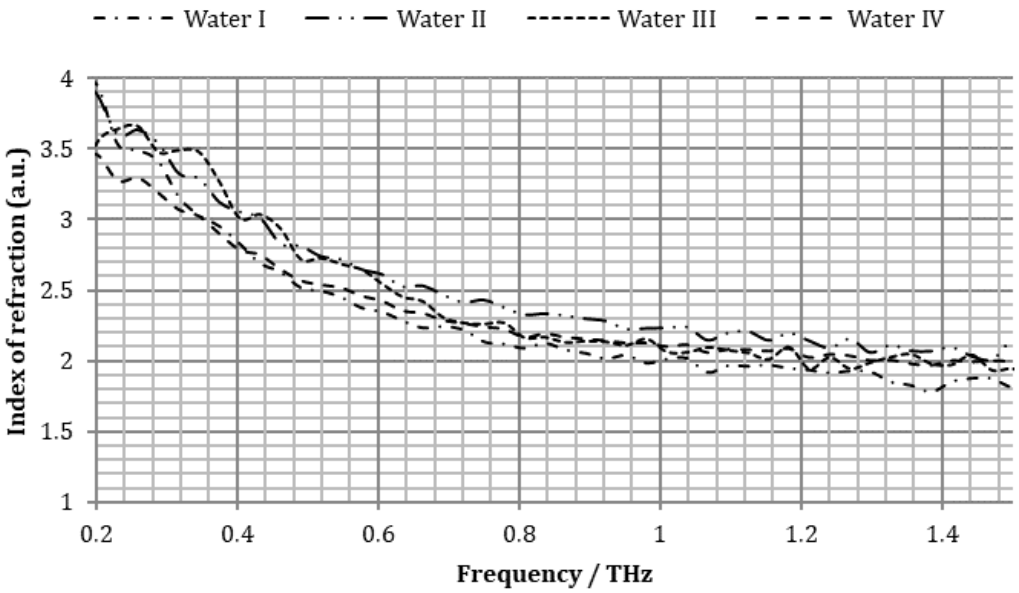

Figure 7-9: Measured refractive index of de-ionised water using the calculated baseline

material under investigation.

7.1.6 Validating data of de-ionised water

Using the corrected baseline, we investigate a more complex material: de-ionised water, which changes the index of refraction over time and has a high absorbance in the terahertz regime [196]. Distilled water was chosen for validation of our methodology, as we are working towards building an understanding of water in interaction with other materials. Figure 7-9 shows the frequency dependent refractive index of the sample measurements.

De-ionised water has been very well investigated in recent years, which allows a good verification with the literature values obtained from [24, 197, 198].

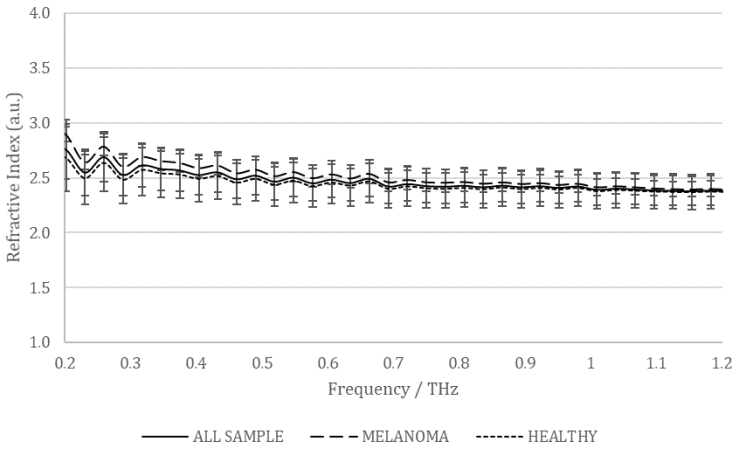

Figure 7-10: Averaged frequency dependant refractive index of sample 2 (N=3178) including IVR and EVR with standard deviation from 0.l to 1.2 THz.

7.2 Results: Refractive Index Analysis of Image Data from melanoma patients

Having established the methodology to obtain the refractive index from samples on top of the sample holder, we apply these findings to the skin data. The refractive index is evaluated on all samples from a frequency between 0.2 and 1.2 THz has a higher frequency increases the noise up to an unmeasurable amount. Furthermore, a frequency lower than 0.2 Terahertz is unreliable with Terahertz rays. The averaged frequency dependent RI of Sample 2 shows a lower refractive index of the extra-visual region compared to the intra-visual region, which could indicate that the EVR is less hydrated then the IVR, however, the data shows no statistical significance due to a high standard deviation, which increases on lower frequencies, shown as error bars in Figure 7-10. In principle, it can be said that a lower frequency comprises a bigger difference in the RI but also a higher standard deviation. At higher frequencies the differences between IVR and EVR becoming increasingly indistinguishable, which could be an indication of a lower penetration depth at higher frequencies however has been found to be comparable to other

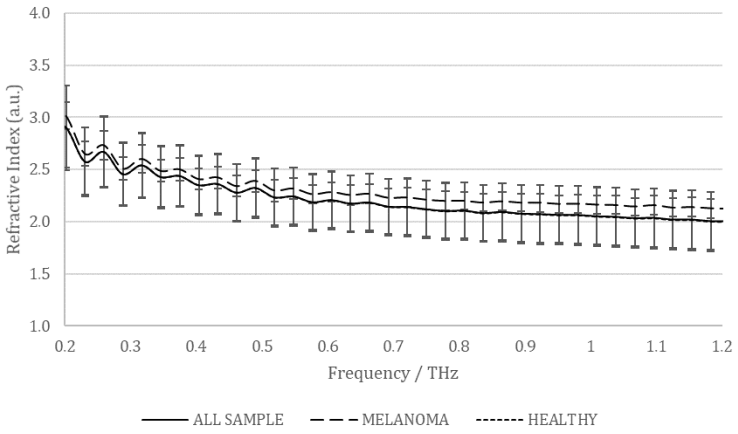

Figure 7-11: Averaged frequency dependant refractive index of sample 4 (N=2966) including IVR and EVR with standard deviation from 0.l to 1.2 THz.

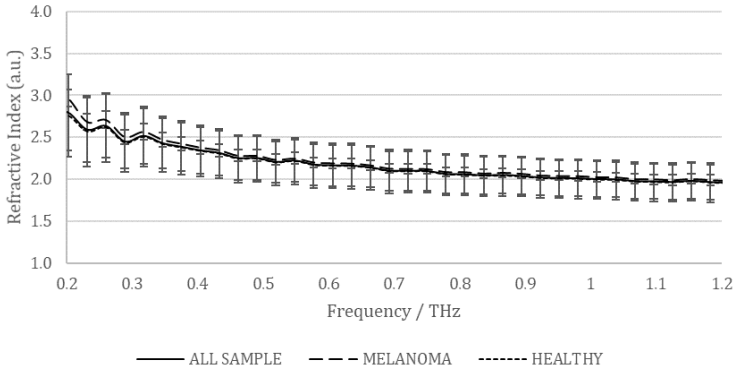

Figure 7-12: Averaged frequency dependant refractive index of sample 5 (N=1102) including IVR and EVR with standard deviation from 0.l to 1.2 THz.

studies found in the literature. Peak differences and shoulders on frequencies close to each other are most likely noise due to the calculation of the RI requiring a previously measured baseline (or reference). Similar results are observed on all other samples and are shown in figures 7-10 to 7-16.

7.3 Refractive Index fitting

The refractive index curves discussed in the last section lead to the problem, that even though in some cases the IVR is higher than the EVR at very low frequen-

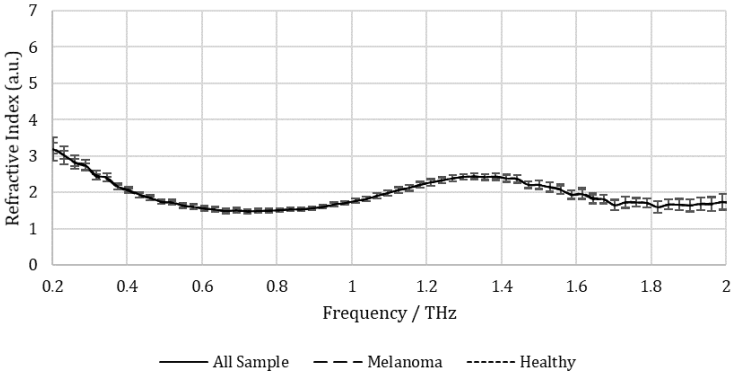

Figure 7-13: Averaged frequency dependant refractive index of sample 6 (N=2591) including IVR and EVR with standard deviation from 0.l to 2 THz.

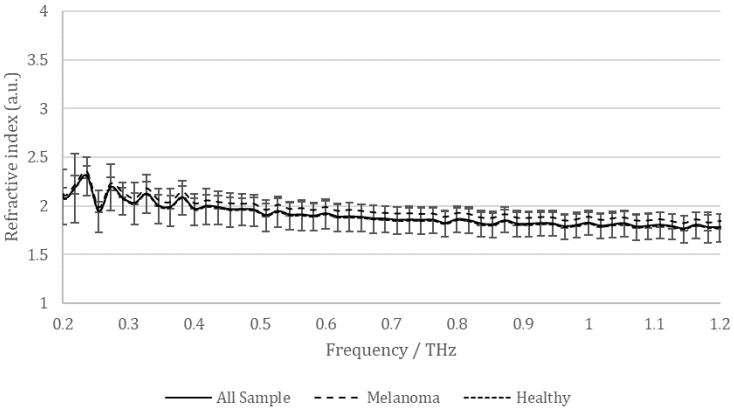

Figure 7-14: Averaged frequency dependant refractive index of sample 7 (N=2507) including IVR and EVR with standard deviation from 0.l to 1.2 THz.

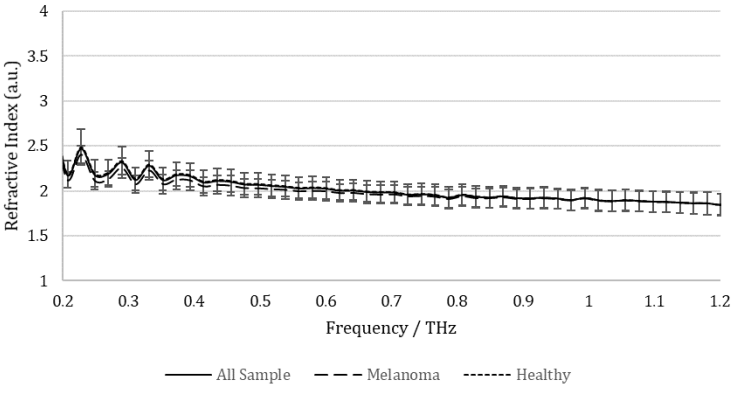

Figure 7-15: Averaged frequency dependant refractive index of sample 8 (N=2757) including IVR and EVR with standard deviation from 0.l to 1.2 THz.

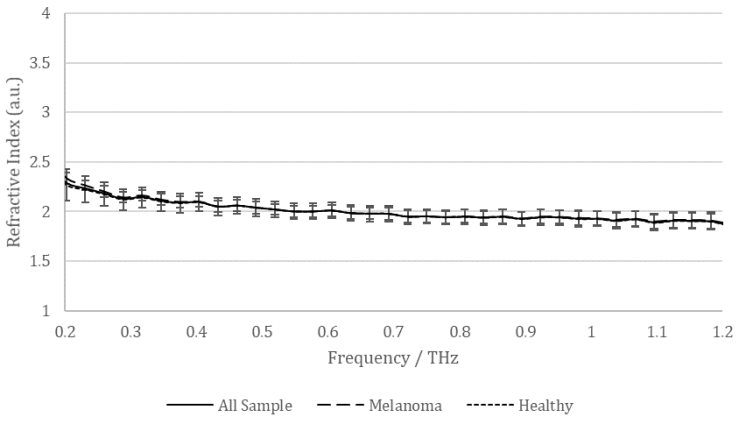

Figure 7-16: Averaged frequency dependant refractive index of sample 9 pressed onto the sample holder (N=2197) including IVR and EVR with standard deviation from 0.l to 1.2 THz

cies, the data does not show a statistical significant differences between the two regions. Furthermore, noise in the lower frequency regime leads to a certain instability in the curves, especially when other works found in the literature are consulted (compare [199]). To reduce these effects, fitting is introduced, which may be used not just to filter out noise but also gives (crisp) numbers to describe the frequency-dependent function. In recent years, fitting has been proposed by utilizing the Debye and Double-Debye models, which describe the dielectric relaxation for intermolecular and intramolecular reactions over a wide frequency spectrum and have been intensively used to find those reactions in deionised water [169, 200] and in non-melanoma human skin cancers [201, 202]. Unfortunately, due to the amount of noise and the relatively low resolution in the frequency spectra plus assumptions regarding unknown variables that need to be made for the Double-Debye model, it was found to be inapplicable to the data collected (data not shown). Thus, other, simpler models are studied to describe the waveforms in the range of 0.2 to 1.3 THz, which are evaluated by the R^2-values. In most cases a power fit in the form of $f(x) = ax^b$ has been found to be the most suitable function as it yields the highest R^2-value of 0.94, as indicated in Table 7.6.

Table 7.6: Comparison of fitting function of sample 2 with their respective coefficients and R^2-values.

function	a	b	c	R^2
exponential	2.33	-0.21		0.90
linear	-0.08	2.65		0.56
logarithmic	-0.47	1.82		0.79
polynomial (2nd order)	1.76	-3.03	3.16	0.76
power	1.92	-0.12		0.94

Table 7.7: Power function fitting of benign and malign (IVR) parts of the samples including a and b coefficients as wells as the RMSE and R^2-value with standard deviations.

Sample	Type	a	StdDev. a	b	stdev b	R^2	RMSE	StdDev R^2
1.1	benign	1.92	0.02	-0.12	0.01	0.03	0.94	0.02
1.2	benign	1.97	0.03	-0.11	0.01	0.03	0.94	0.02
1.3	benign	1.91	0.02	-0.14	0.01	0.02	0.96	0.01
2	malign	2.14	0.43	-0.07	0.20	0.06	0.75	0.18
4	malign	2.10	0.08	-0.10	0.02	0.04	0.85	0.10
5	malign	1.97	0.05	-0.13	0.03	0.03	0.91	0.08
7	malign	1.82	0.08	-0.15	0.02	0.10	0.64	0.08
8	malign	1.89	0.11	-0.11	0.02	0.05	0.78	0.05
9	malign	1.93	0.06	-0.08	0.03	0.03	0.84	0.12

The power function is evaluated over all waveforms of each sample but also divided into the IVR and EVR. In this case, it is anticipated to compare the IVR of the malign samples together with the first three benign samples, with the results that the standard deviation of the R^2-values, the coefficients a and b of the benign samples are significant smaller than the malign samples, as shown in Figure 7-17 with data from Table 7.7. This gives rise to the assumption that the variation of the sample containing malignancies is higher than of the benign ones.

7.4 Conlusion

In this chapter, we have evaluated different methods for the determination of the frequency dependant refractive index using different quartz slides with known,

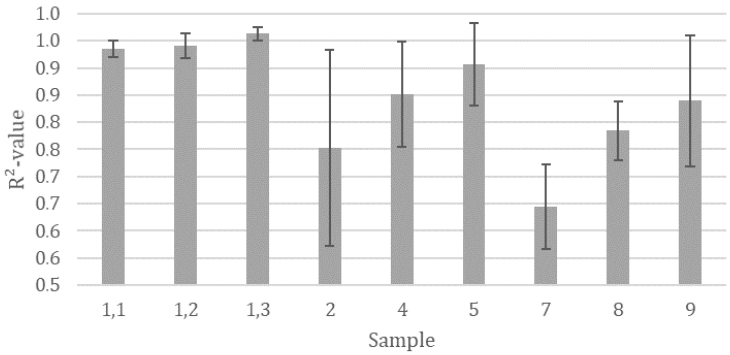

Figure 7-17: Mean R-square values of the samples with standard deviation.

constant refractive indices. We have compared the results to measurements previously taken in transmission mode and established a methodology to calculate the refractive index, which is close to the ones found in the literature. This Method has been applied to the skin sample data and the IVR and EVR were evaluated. At lower frequencies the refractive index on all samples is higher than on higher frequencies. In this region, the IVR is slightly then the EVR but not of statistical importance. To cancel out noise various fitting functions have been applied to the refractive indices with the result that a power-function is mostly to reflect the RI correctly with an R^2-value of 0.94. This fitting function has been applied to the benign samples (1.1 - 1.3) and IVR of the malign samples. The results show a lower R^2-value at the benign samples. However, since the sample size of the benign lesions is very low and originates from the same person which was also much younger (30) it cannot said for certain if this is due to differences in the benign and malign lesions. It could as well beage difference or the size of the sample that causes the changes in the standard deviation of the R^2-values.

Chapter 8

Conclusion and discussion

In this pilot study, a primary investigation of the potential of terahertz imaging in reflection geometry for the early diagnosis of human cutaneous melanoma was carried out using eight samples of MM and three of healthy tissue (moles) *ex-vivo*. By comparing the samples containing melanoma with histopathology findings, there is potential that THz might show regions not visible by the naked eye or with the dermascope where the tumour is active in infiltrating surrounding tissue and creating fibroblasts around the lesion as a side-product. While this analysis would require further confirmation, it can be said that the terahertz images obtained show similarities with the visual taken with a digital camera.

To further investigate these similarities, a quantitative analysis of the EVR and IVR was performed with different datasets on a per sample basis. The raw dataset per sample shows a positive prediction between the EVR and the IVR using a linear classifier or a neural network, which makes this method comparable to similar research performed with NIR-machines. To ensure that the data obtained from the reflected terahertz beams is not purely random with respect to the layout of the data obtained, predictive modelling techniques were applied to the data using resubstitution and 10-fold cross-validation.

The results showed that the linear discriminant analysis and the neural network performed well over all samples with a specificity of up to 79% and a sensitivity of 96%, which has been shown to be in good agreement over all samples, as the cross-validation showed few outliers. Therefore, we conclude, that malignancy is encoded within the terahertz. Furthermore, due to the high sensitivity, the models are good in identifying healthy skin as such. By using the ReliefF, it was found that almost all variables that contain the area-under-the-curve are positive prediction values and furthermore evidence to secondary peaks as cause of the malignancy. Interestingly, the main maximum peak is not a high predictor, which may be due to normalisation but is most likely because the energy wave conceals a secondary signal, if present. The initial negative peak is also found to be a positive predictor, which could mean that the malignancy is already detectable at the very front of the skin, i.e., at the stratum corneum. The high predictors behind the maximum wave are different regarding there position of the optical delay from sample to sample and may indicate different depths of the tumours. However, to investigate the depth of a malignancy, further histological data would be required that could shows a correlation of the histological found tumour depth and the positive prediction values obtained from the ReliefF on the raw waveforms. Unfortunately, for this study, depth information from the histologists could not be retrieved due to regulations and privacy concerns.

Further analysis utilising the PCA and manually chosen variables did not show a better result than those obtained from the raw datasets, which indicates that the information for the differentiation is manifold and that a dimension reduction cannot be performed using the PCA.

While it was anticipated that we would find a predictive modelling technique suitable for all samples which did not show any good results, an investigation of the samples on the complex refractive index was carried out. An exponential

fitting function was applied to the frequency-dependant refractive indices on all samples between 0.3 and 1.3 THz to further quantify the results. It was found that all samples have different refractive indices, which is most likely due to different thickness and water absorption and position on the body of the excised lesion. A comparison of the moles with the infiltrated tissue (IVR) showed that the standard deviation of the fit, the noise, is much lower on the healthy tissue than on the infiltrated tissue. However, this should be investigated further, as the sample size of the healthy tissue was low, as it contained three moles from different sides of the body of the same patient.

One of the biggest limitations of this study is that all samples have been put in saline for transportation to prevent the sample from drying out before undergoing standard histology procedure. Due to the high content of surrounding saline it is most likely that the sample cells saturate which may account for a higher amount of noise but also for a higher absorption rate, which makes it difficult to find relevant data behind the maximum energy wave, if present. The same limitation of sample collection accounts for the relatively small time window in which samples were scanned. To make sure that samples would not degrade before arriving at the histologist, the sample acquisition time has been set to a maximum of 30 minutes. Therefore, we had to make sure that a complete scan of the sample was taken out in around 20 minutes. Without this limitation, one could scan a sample point multiple times and take the average value to reduce noise during the scanning process.

The analysis carried out in this thesis shows that terahertz imaging in reflection geometry indeed has the potential to be beneficial for the diagnosis of melanoma; however, further research need to be performed in this field.

With the new development of external probes for terahertz emission and detection, it would be interesting to collect data from patients before excision by

scanning healthy skin close to the potential lesion and using it as a baseline before scanning the actual lesion. Furthermore, by cutting the excised lesion, a B-scan could be performed which then could be compared to histology findings more precisely than in this study to further investigate the infiltration of surrounding tissue during the RGP.

Appendix A

TNM Staging system after AJCC

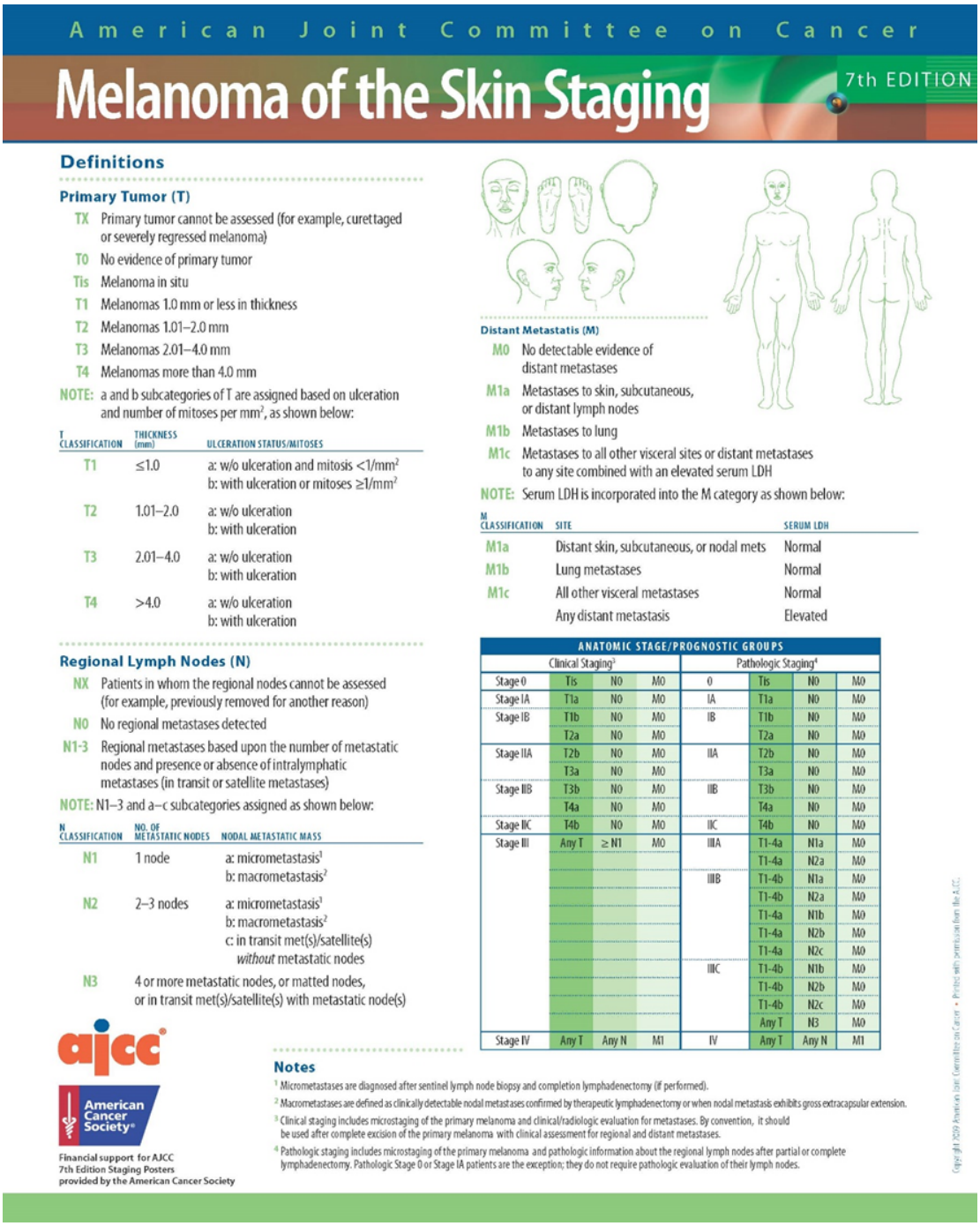

Figure A-1: TNM Staging System after AJCC

Appendix B

Waterfall images and results of the ReliefF algorithm on the raw terahertz data per sample

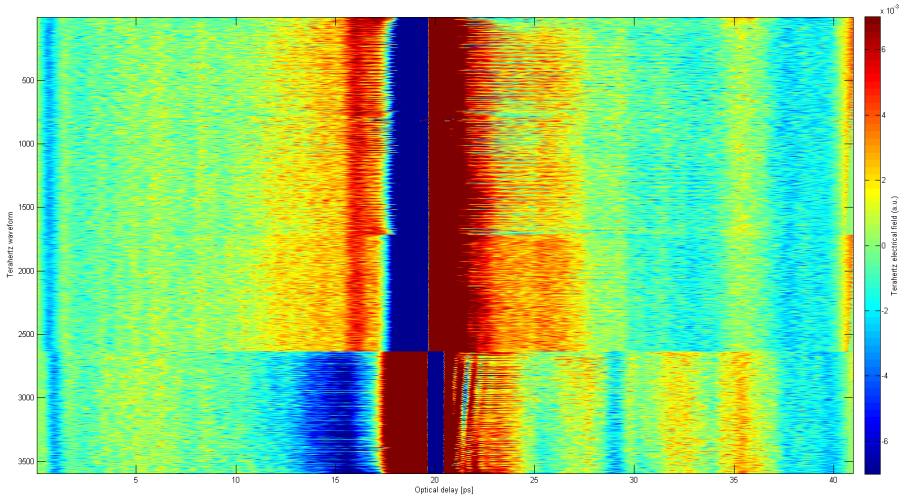

Figure B-1: False colour waterfall diagram from patient 2 of the sample (top) and air (bottom) waveforms transformed into 2D.

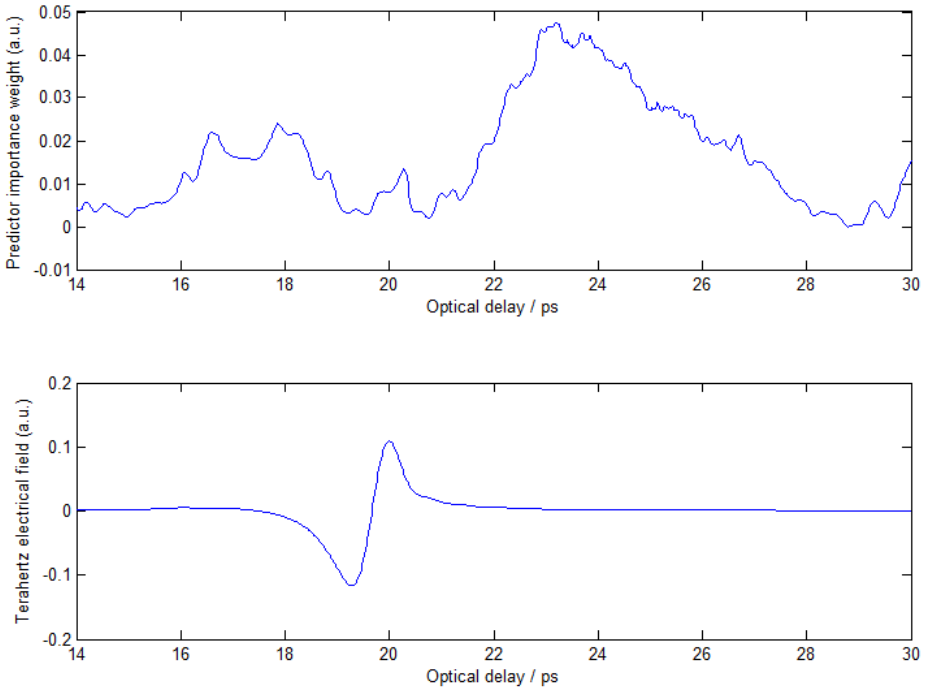

Figure B-2: Mean waveform of patient 2 skin data (top) and corresponding predictor importance weight of the ReliefF algorithm (bottom).

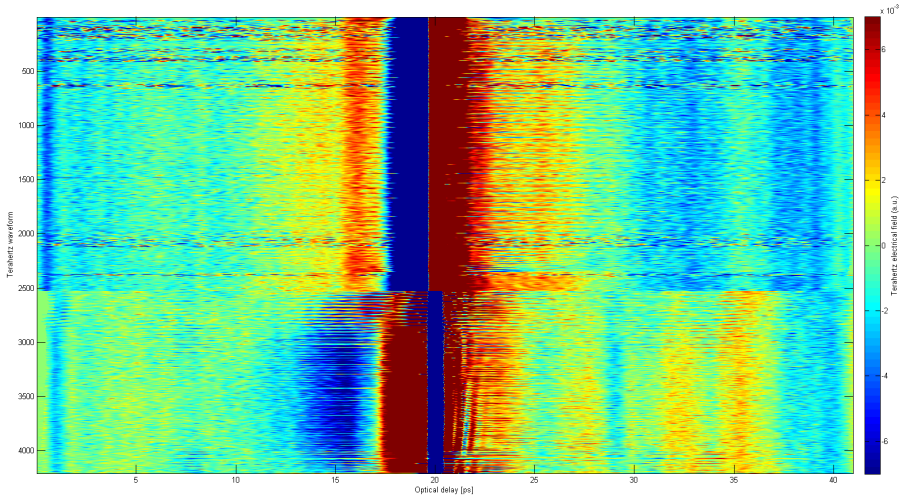

Figure B-3: False colour waterfall diagram from patient 4 of the sample (top) and air (bottom) waveforms transformed into 2D.

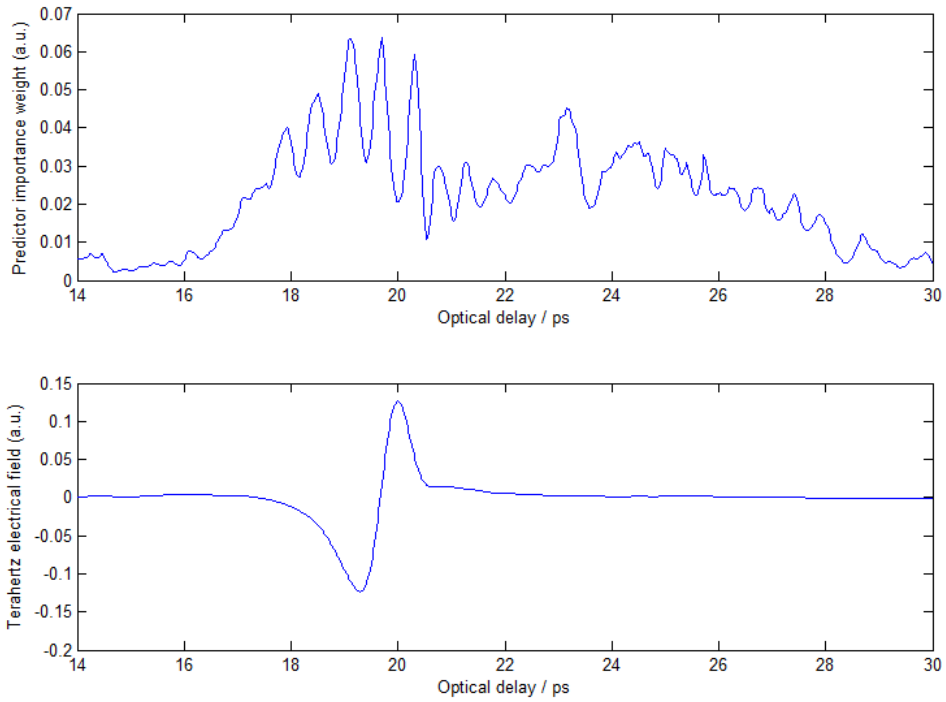

Figure B-4: Mean waveform of patient 4 skin data (top) and corresponding predictor importance weight of the ReliefF algorithm (bottom).

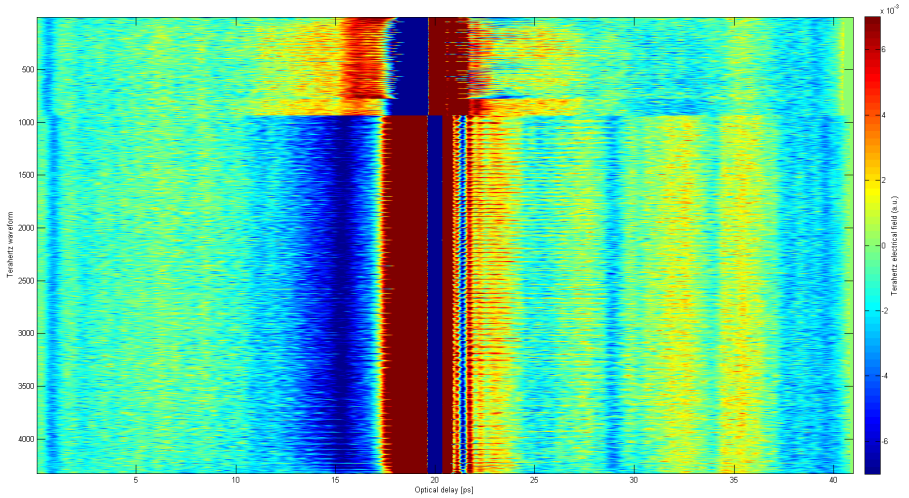

Figure B-5: False colour waterfall diagram from patient 5 of the sample (top) and air (bottom) waveforms transformed into 2D.

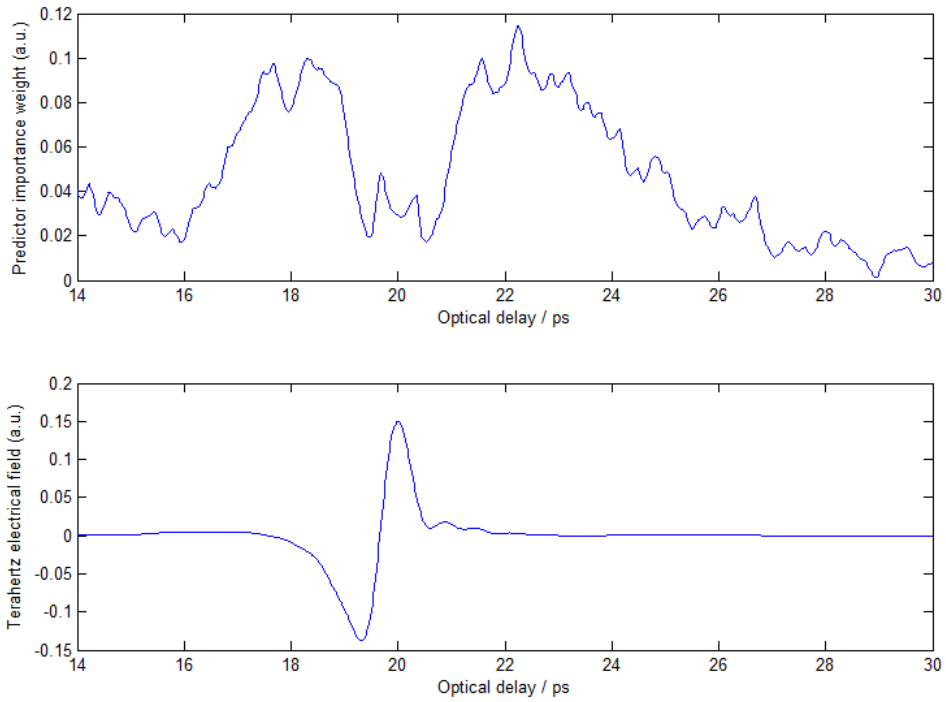

Figure B-6: Mean waveform of patient 5 skin data (top) and corresponding predictor importance weight of the ReliefF algorithm (bottom).

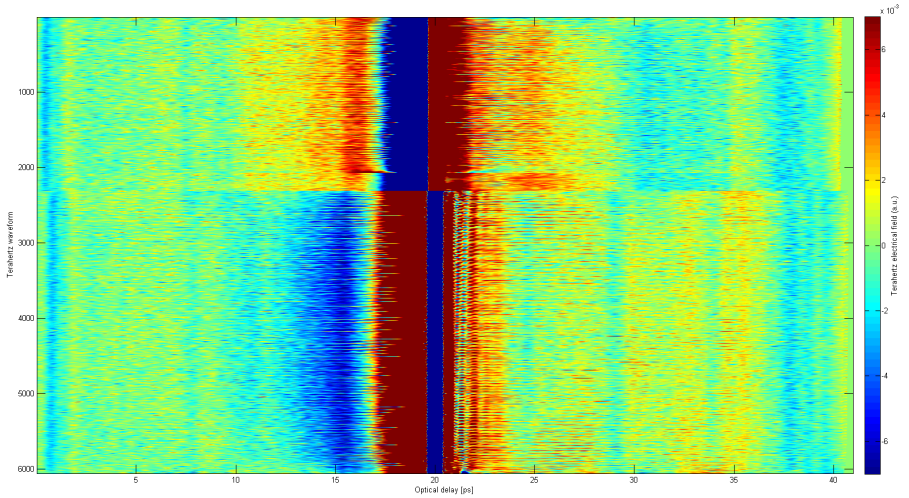

Figure B-7: False colour waterfall diagram from patient 6 of the sample (top) and air (bottom) waveforms transformed into 2D.

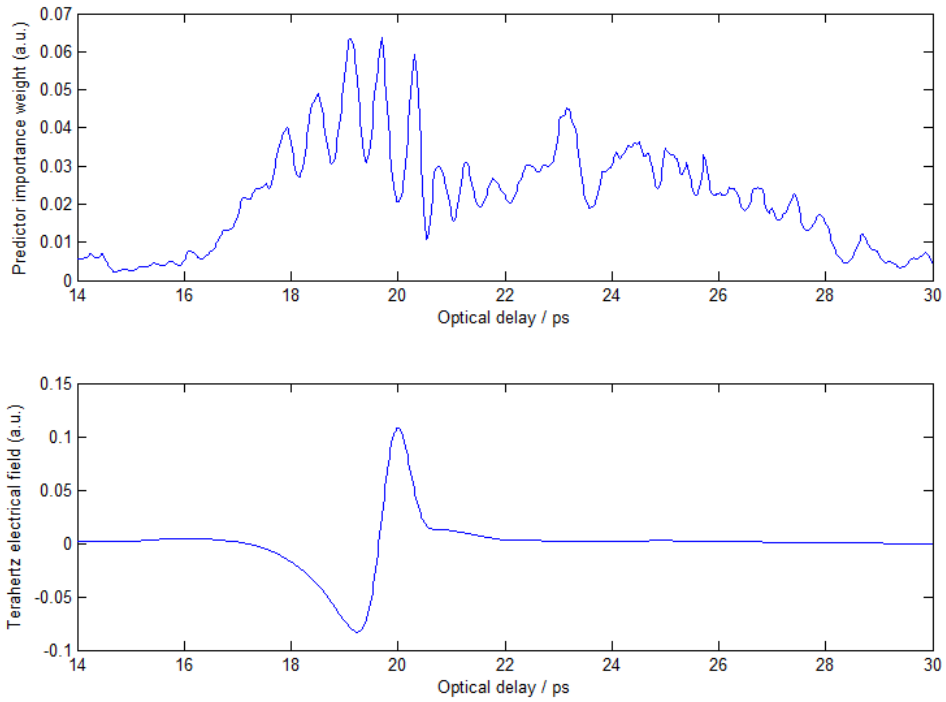

Figure B-8: Mean waveform of patient 6 skin data (top) and corresponding predictor importance weight of the ReliefF algorithm (bottom).

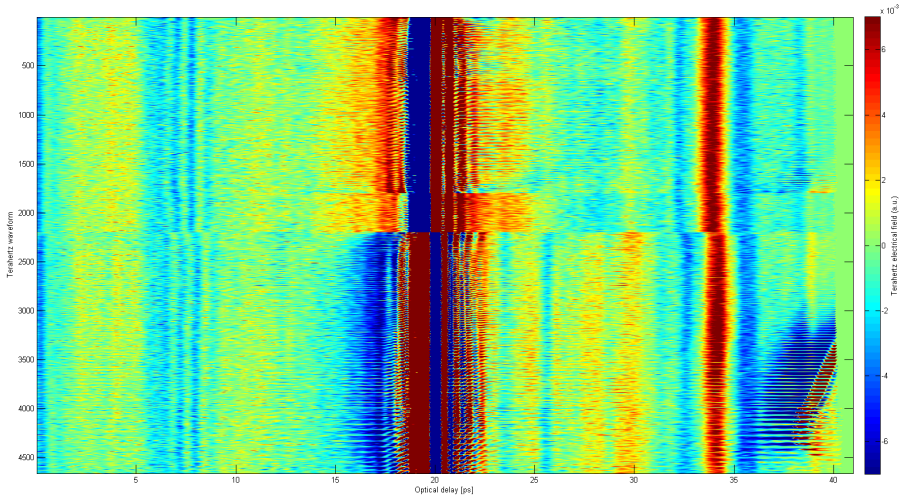

Figure B-9: False colour waterfall diagram from patient 7 of the sample (top) and air (bottom) waveforms transformed into 2D.

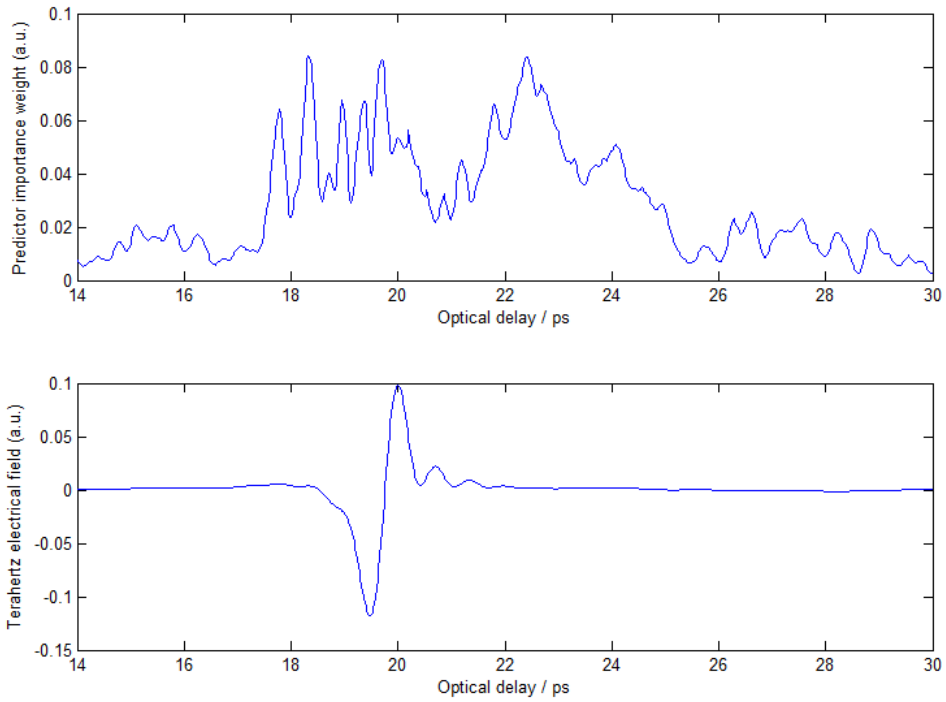

Figure B-10: Mean waveform of patient 7 skin data (top) and corresponding predictor importance weight of the ReliefF algorithm (bottom).

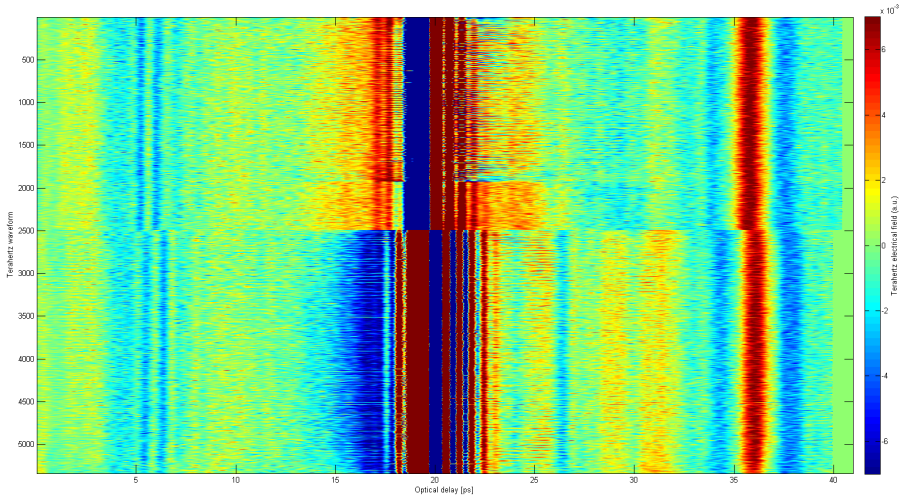

Figure B-11: False colour waterfall diagram from patient 8 of the sample (top) and air (bottom) waveforms transformed into 2D.

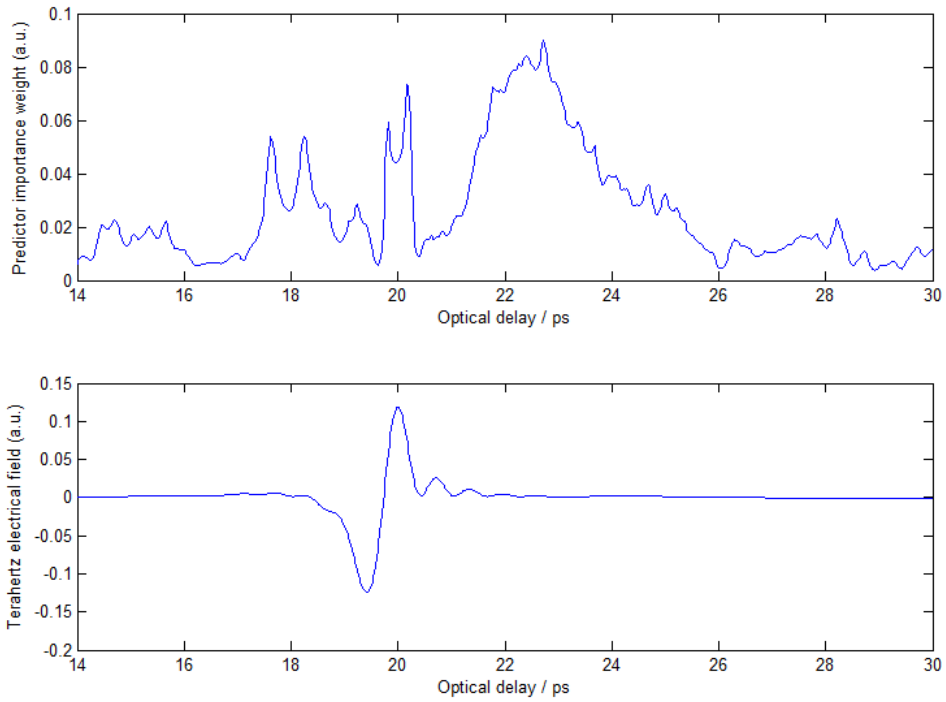

Figure B-12: Mean waveform of patient 8 skin data (top) and corresponding predictor importance weight of the ReliefF algorithm (bottom).

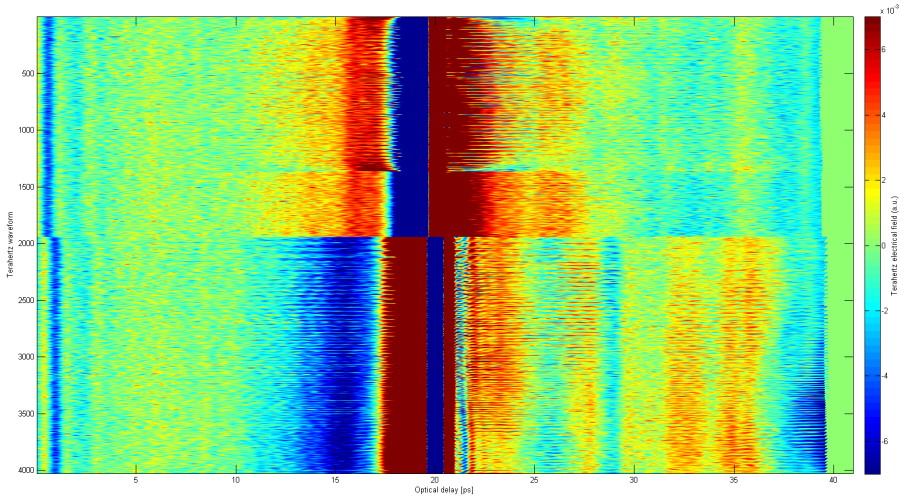

Figure B-13: False colour waterfall diagram from patient 9 of the sample (top) and air (bottom) waveforms transformed into 2D.

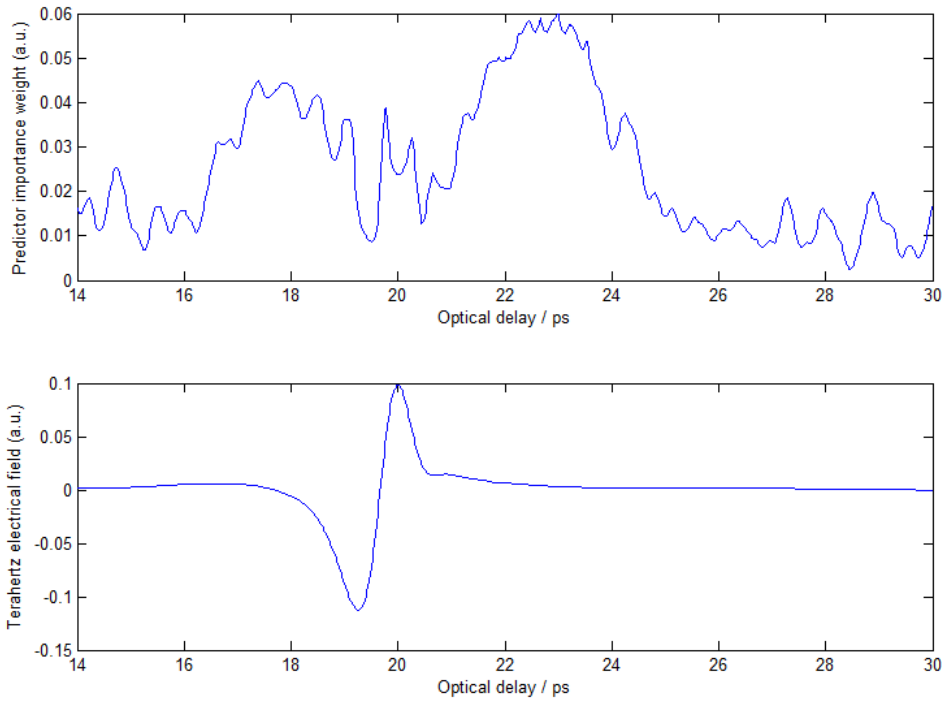

Figure B-14: Mean waveform of patient 9 skin data (top) and corresponding predictor importance weight of the ReliefF algorithm (bottom).

Appendix C

First three principle components from sample data

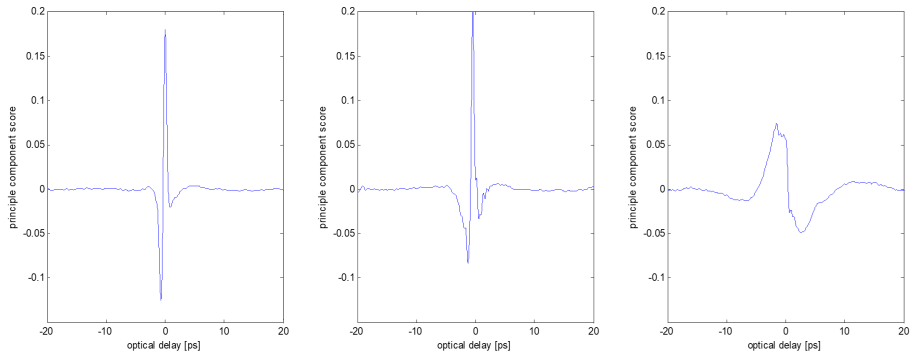

Figure C-1: Principle components coefficients of the first three components of patient 2.

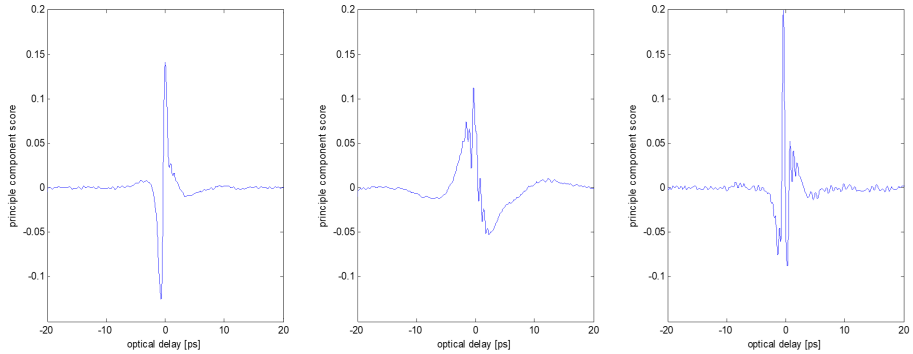

Figure C-2: Principle components coefficients of the first three components of patient 4.

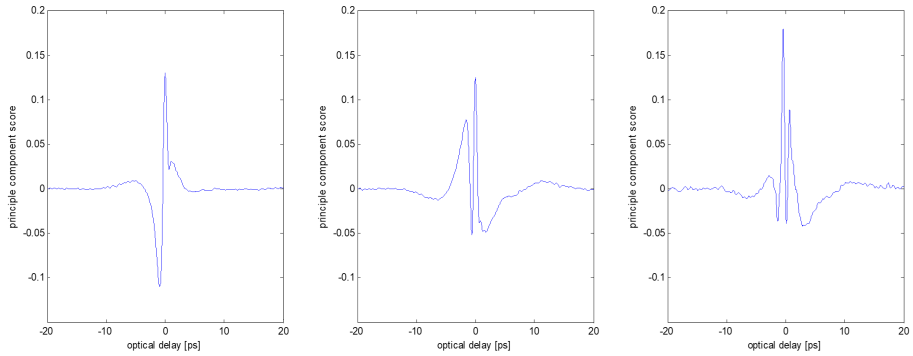

Figure C-3: Principle components coefficients of the first three components of patient 5.

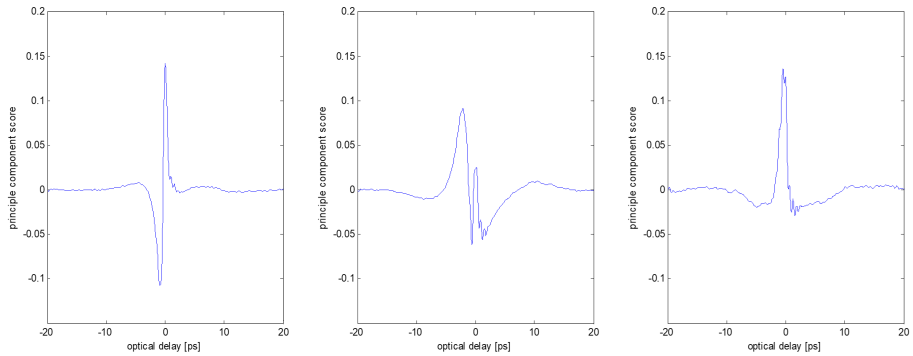

Figure C-4: Principle components coefficients of the first three components of patient 6.

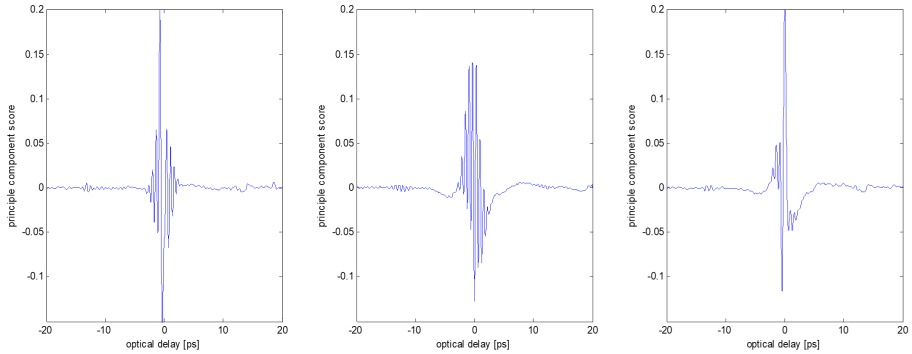

Figure C-5: Principle components coefficients of the first three components of patient 7.

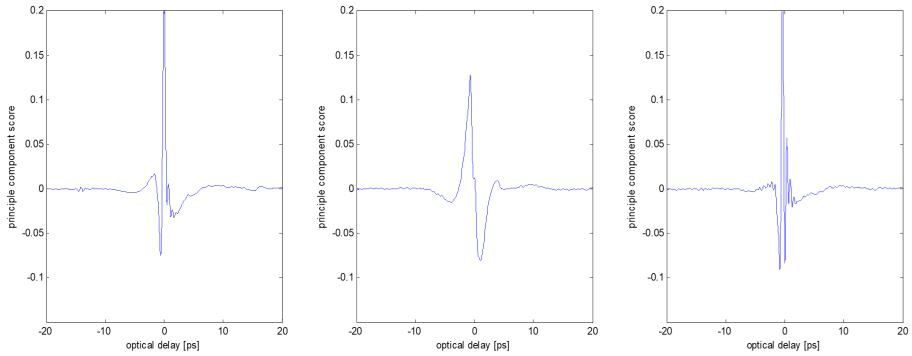

Figure C-6: Principle components coefficients of the first three components of patient 8.

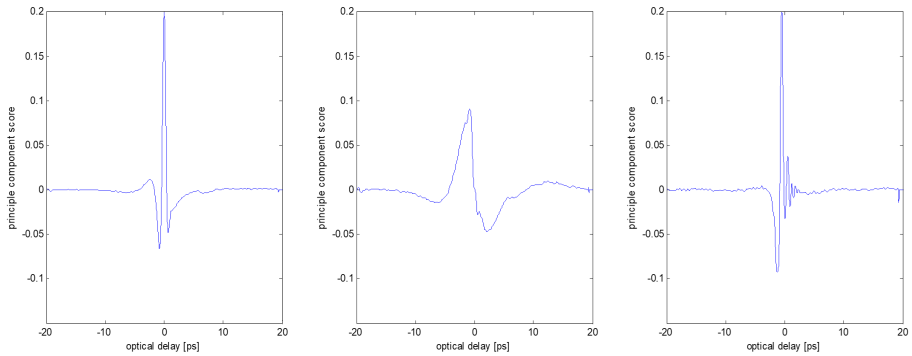

Figure C-7: Principle components coefficients of the first three components of patient 9.

Appendix D

2D images of manual extracted features from the samples terahertz data

The images shown in this appendix show all 27 extracted variables from the terahertz time domain waveform data per sample. The data is structured so that the first values are from the EVR whereas the latter ones are from the IVR shown in Table D.1.

Table D.1: Overview of sample collection and classification in EVR and IVR.

Sample	**Overall data waveforms**	**Classified as EVR**	**Classified as IVR**
Sample 2	2549	1626	923
Sample 4	2523	2349	174
Sample 5	935	775	160
Sample 6	2310	2072	238
Sample 7	2196	1793	403
Sample 8	2493	1926	567
Sample 9	1931	1353	578

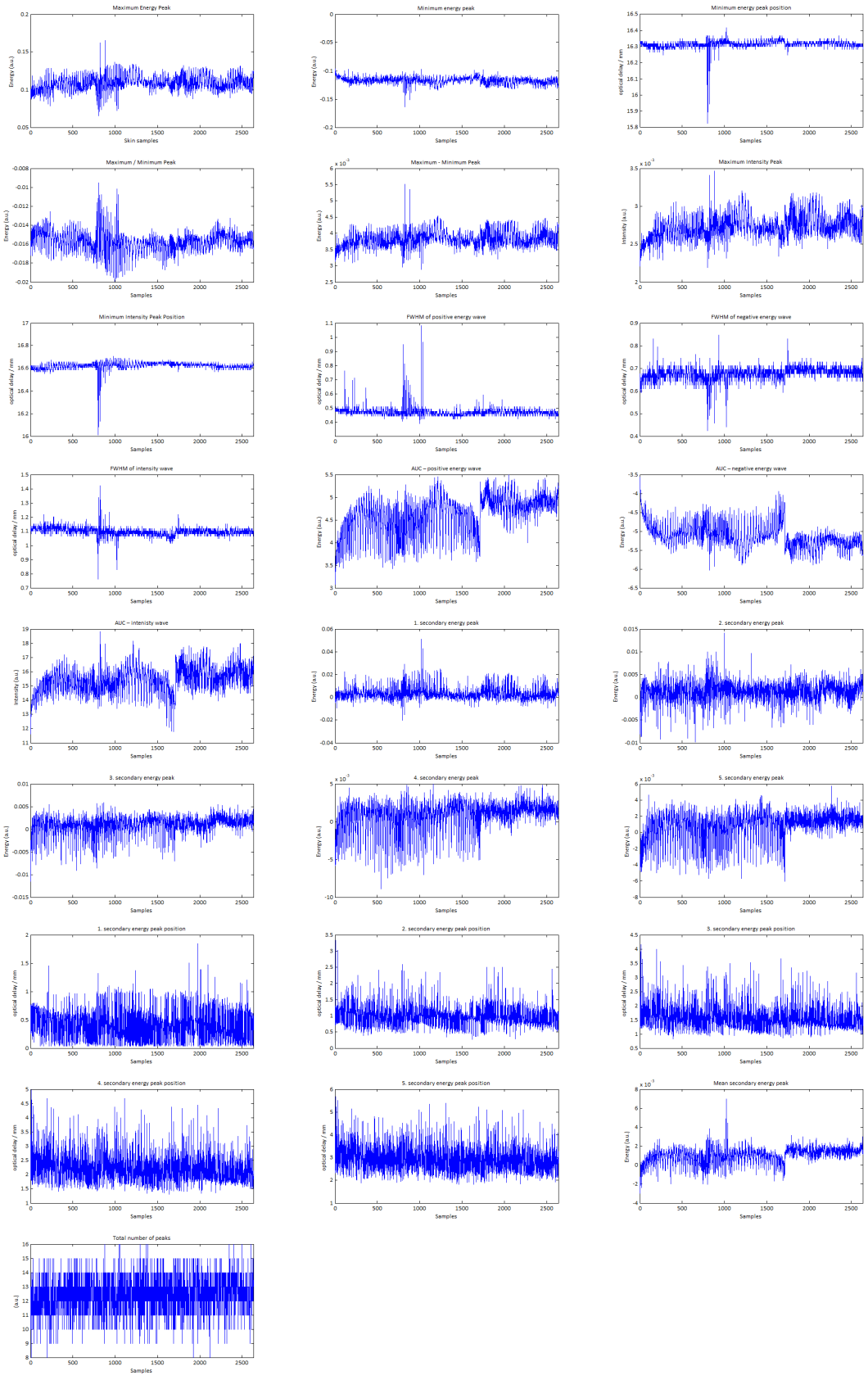

Figure D-1: Manually extracted features from sample 2.

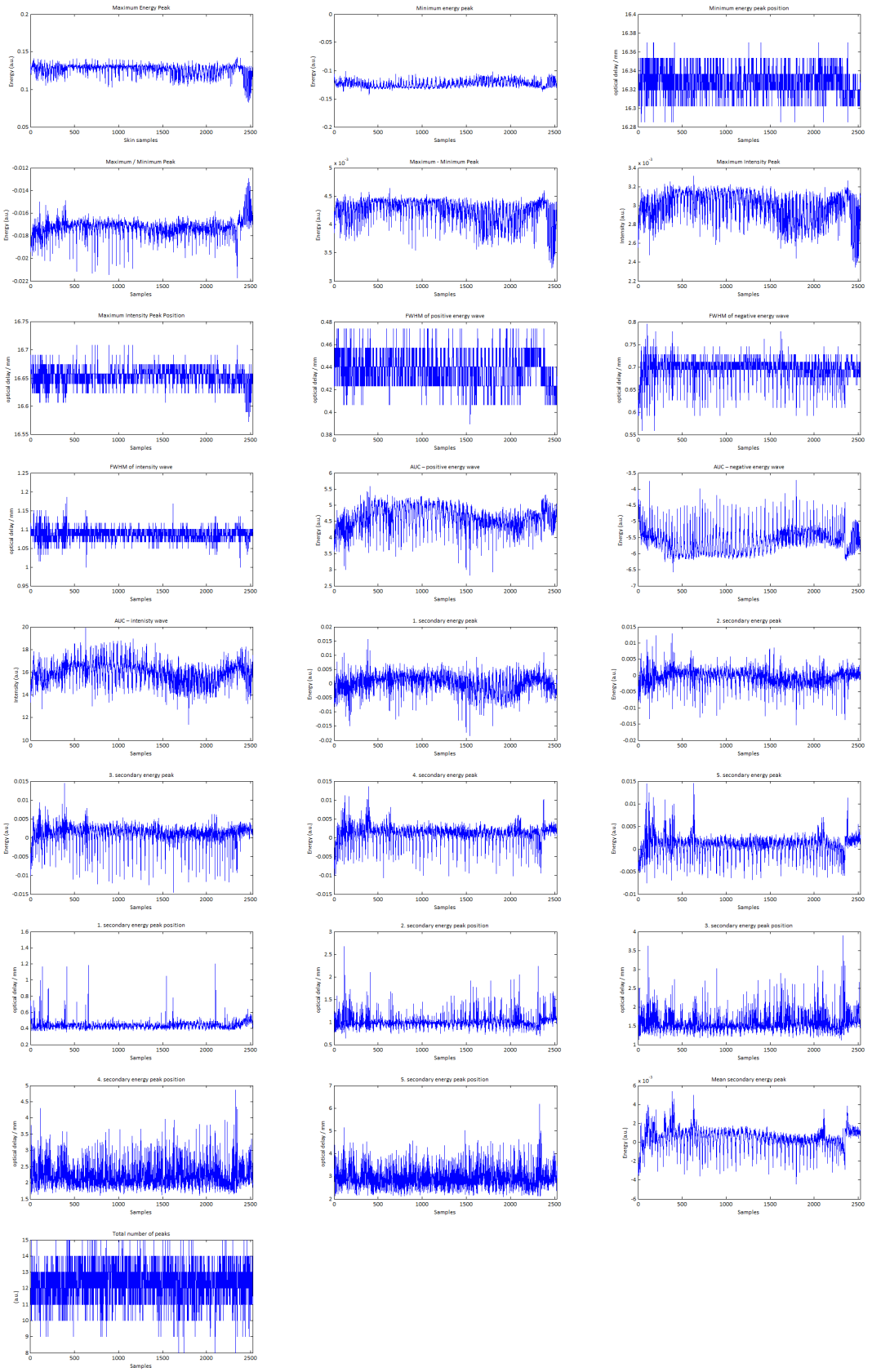

Figure D-2: Manually extracted features from sample 4.

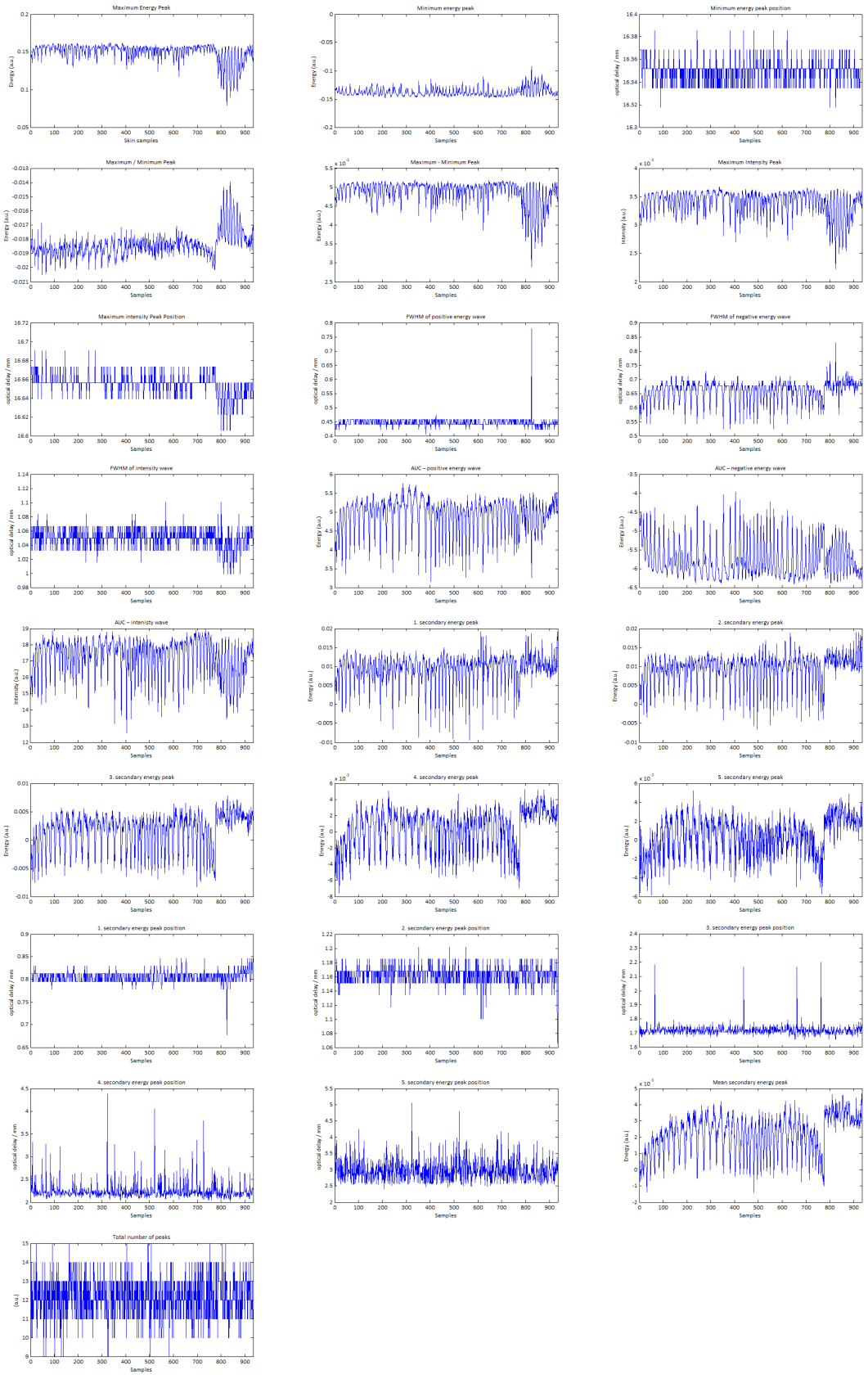

Figure D-3: Manually extracted features from sample 5.

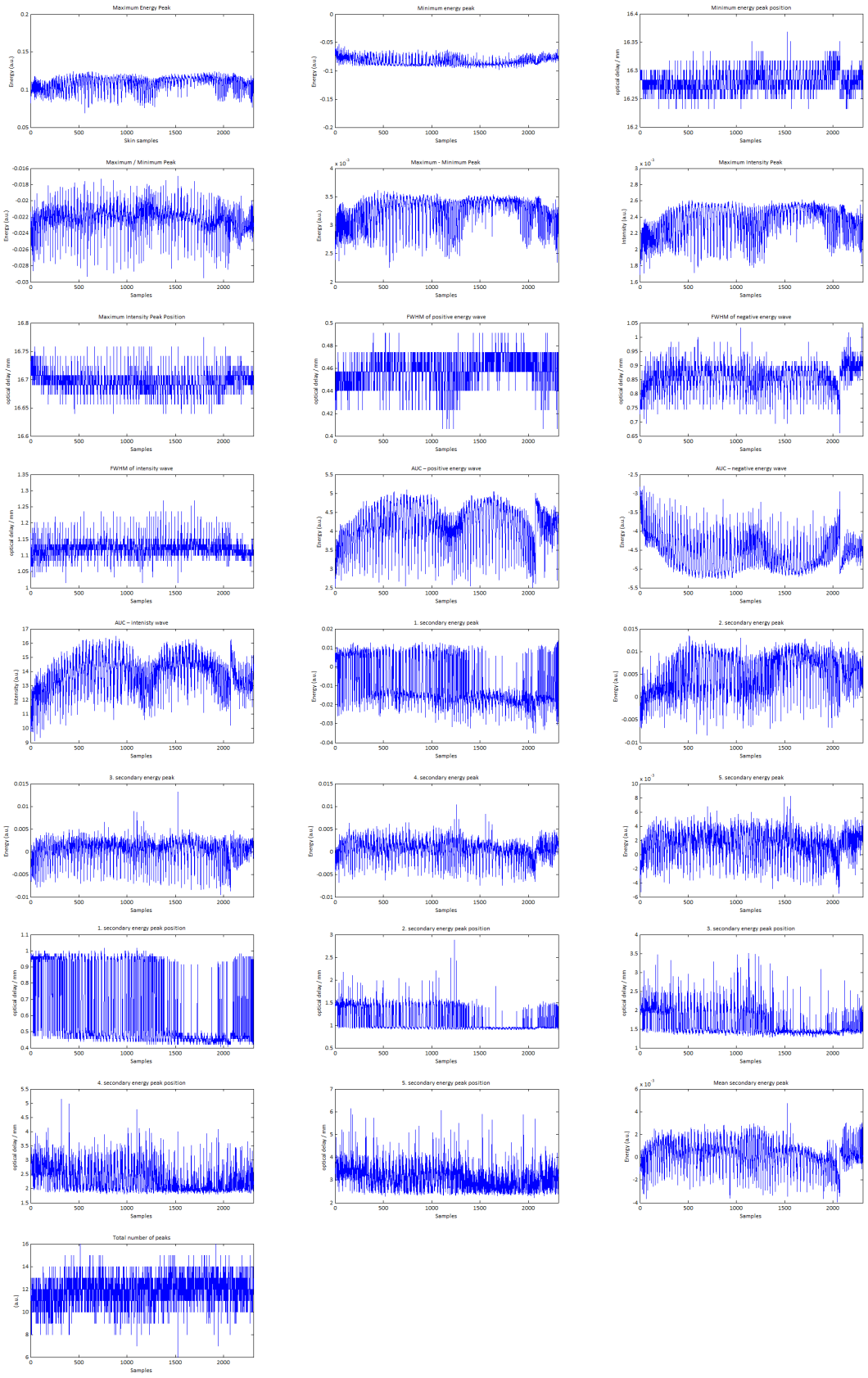

Figure D-4: Manually extracted features from sample 6.

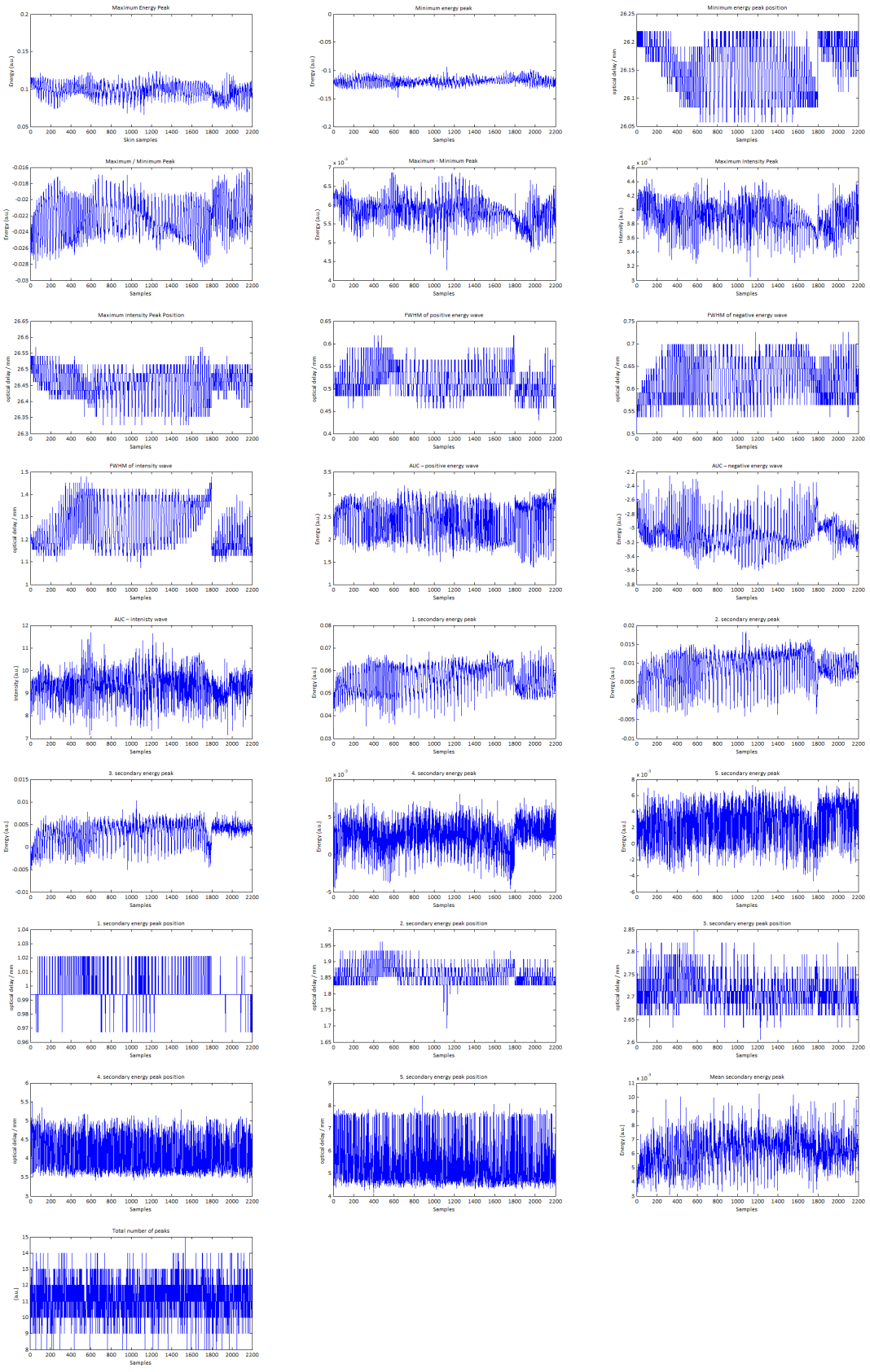

Figure D-5: Manually extracted features from sample 7.

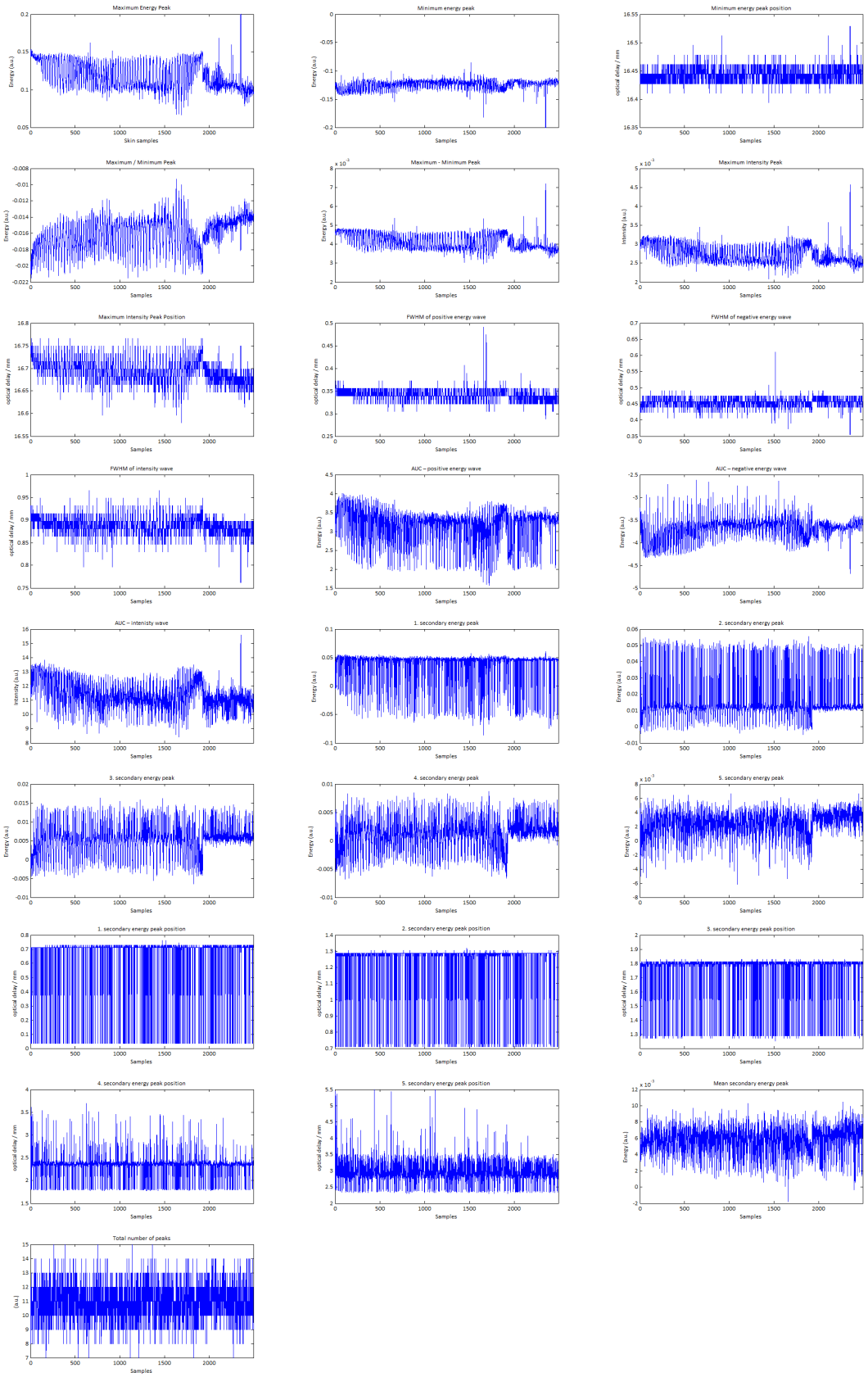

Figure D-6: Manually extracted features from sample 8.

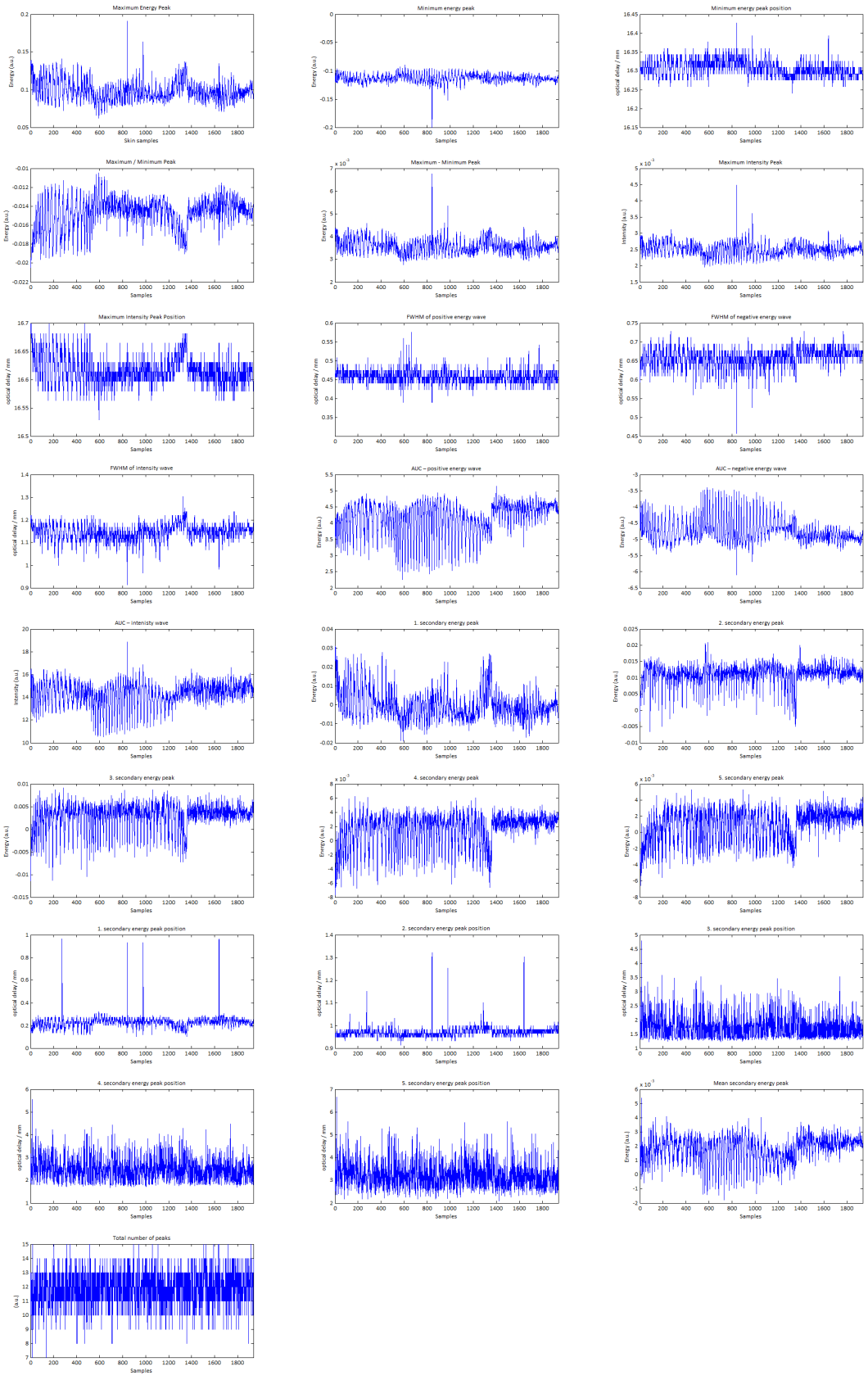

Figure D-7: Manually extracted features from sample 9.

Bibliography

[1] L. M. Hollestein, S. A. W. van den Akker, T. Nijsten, H. E. Karim-Kos, J. W. Coebergh, and E. de Vries, "Trends of cutaneous melanoma in the netherlands: increasing incidence rates among all breslow thickness categories and rising mortality rates since 1989," *Annals of Oncology*, vol. 23, no. 2, pp. 524–530, May 2011.

[2] J. Barbarić and A. Znaor, "Incidence and mortality trends of melanoma in croatia, 1988-2008," *Croatian Medical Journal*, vol. 53, no. 2, pp. 135–140, Apr. 2012.

[3] D. E. Godar, "Worldwide increasing incidences of cutaneous malignant melanoma," *Journal of Skin Cancer*, vol. 2011, pp. 1–6, 2011.

[4] Roche, X.-C. Wu, V. Chen, E. Hamilton-Byrd, F. Groves, A. Jemal, H. J. Martin, and C. C. McLaughlin, "Cutaneous melanoma incidence and survival among black, asian and pacific islander and white populations in the united states," *Clinical Medicine Insights: Dermatology*, p. 15, Aug. 2010.

[5] D. S. Rigel and J. A. Carucci, "Malignant melanoma: prevention, early detection, and treatment in the 21st century," *CA: A Cancer Journal for Clinicians*, vol. 50, no. 4, pp. 215–236, Jul. 2000.

[6] B. Diffey, "The future incidence of cutaneous melanoma within the u.k." *British Journal of Dermatology*, vol. 151, no. 4, pp. 868–872, Oct. 2004.

[7] E. L. Rager, E. P. Bridgeford, and D. W. Ollila, "Cutaneous melanoma: update on prevention, screening, diagnosis, and treatment." *American family physician*, vol. 72, pp. 269–276, Jul. 2005.

[8] G. Argenziano, G. Fabbrocini, P. Carli, V. D. Giorgi, E. Sammarco, and M. Delfino, "Epiluminescence microscopy for the diagnosis of doubtful melanocytic skin lesions," *Archives of Dermatology*, vol. 134, no. 12, Dec. 1998.

[9] J. P. Banky, J. W. Kelly, D. R. English, J. M. Yeatman, and J. P. Dowling, "Incidence of new and changed nevi and melanomas detected using baseline images and dermoscopy in patients at high risk for melanoma," *Archives of Dermatology*, vol. 141, no. 8, Aug. 2005.

[10] E. L. Psaty and A. C. Halpern, "Current and emerging technologies in melanoma diagnosis: the state of the art," *Clinics in Dermatology*, vol. 27, no. 1, pp. 35–45, Jan. 2009.

[11] Y. Wang, L. Zhang, C. Deng, W. Li, H. Zhong, and C. Zhang, "Feature extraction and identification of explosive materials in reflective terahertz spectroscopic imaging system," in *2008 International Conference on Optical Instruments and Technology: Microelectronic and Optoelectronic Devices and Integration*, X. Zhang, W. J. Bock, X. Bao, and P. Shum, Eds. SPIE, Dec. 2008.

[12] L. Jofre, J. Romeu, S. Capdevila, J. Abril, E. Nova, and M. Alonso, "The "challenging" world of terahertz radiation and imaging," in *Proc. 5th European Conf. Antennas and Propagation (EUCAP)*, Apr. 2011, pp. 3470–3475.

[13] H. Wu, E. J. Heilweil, A. S. Hussain, and M. A. Khan, "Process analytical technology (pat): quantification approaches in terahertz spectroscopy for pharmaceutical application." *Journal of pharmaceutical sciences*, vol. 97, pp. 970–984, Feb. 2008.

[14] J. R. Peacock, "Millimetre wave permittivity of water near 25 c," *Journal of Physics D: Applied Physics*, vol. 42, no. 20, p. 205501, 2009. [Online]. Available: http://stacks.iop.org/0022-3727/42/i=20/a=205501

[15] Y. X. Wu, B. Su, J. He, C. Zhang, H. Zhang, S. Zhang, and C. Zhang, "An effective way to reduce water absorption to terahertz," in *2017 International Conference on Optical Instruments and Technology: Optical Systems and Modern Optoelectronic Instruments*, L. Dong, Y. Wang, B. Jia, and K. Tatsuno, Eds. SPIE, Jan. 2018.

[16] E. Berry, G. C. Walker, A. J. Fitzgerald, N. N. Zinov'ev, M. Chamberlain, S. W. Smye, R. E. Miles, and M. A. Smith, "Do in vivo terahertz imaging systems comply with safety guidelines?" *Journal of Laser Applications*, vol. 15, no. 3, pp. 192–198, Aug. 2003.

[17] J. Zeitler, Y. Shen, C. Baker, P. F. Taday, M. Pepper, and T. Rades, "Analysis of coating structures and interfaces in solid oral dosage forms by three dimensional terahertz pulsed imaging," *Journal of Pharmaceutical Sciences*, vol. 96, no. 2, pp. 330–340, Feb. 2007.

[18] C. Yu, S. Fan, Y. Sun, and E. Pickwell-Macpherson, "The potential of terahertz imaging for cancer diagnosis: A review of investigations to date." *Quantitative imaging in medicine and surgery*, vol. 2, pp. 33–45, Mar. 2012.

[19] D. B. Bennett, Z. D. Taylor, P. Tewari, R. S. Singh, M. O. Culjat, W. S. Grundfest, D. J. Sassoon, R. D. Johnson, J.-P. Hubschman, and E. R. Brown, "Terahertz sensing in corneal tissues." *Journal of biomedical optics*, vol. 16, p. 057003, May 2011.

[20] A. Fitzgerald, E. Berry, N. Zinov'ev, S. Homer-Vanniasinkam, R. Miles, J. Chamberlain, and M. Smith, "Catalogue of human tissue optical properties at terahertz frequencies," *Journal of Biological Physics*, vol. 29, no. 2-3, p. 123, Jun. 2003.

[21] H. Hoshina, S. Nakajima, M. Yamashita, C. Otani, and N. Miyoshi, "Terahertz imaging diagnostics of the cancer tissues with chemometrics technique," in *Proc. Joint 31st Int. Conf. Infrared Millimeter Waves and 14th Int. Conf. Teraherz Electronics*, Sep. 2006, p. 195.

[22] M. Schwerdtfeger, S. Lippert, M. Koch, A. Berg, S. Katletz, and K. Wiesauer, "Terahertz time-domain spectroscopy for monitoring the curing of dental composites," *Biomedical Optics Express*, vol. 3, no. 11, p. 2842, Oct. 2012.

[23] C. H. Reid, "Spectroscopic methods for medical diagnosis at terahertz wavelengths," Ph.D. dissertation, University College London, 2009.

[24] P. H. Siegel, "Terahertz technology in biology and medicine," *IEEE Transactions on Microwave Theory and Techniques*, vol. 52, no. 10, pp. 2438–2447, Oct. 2004.

[25] J. W. Bowen, "Terahertz spectroscopy of biological systems," in *Biophotonics: Spectroscopy, Imaging, Sensing, and Manipulation.* Springer Netherlands, Oct. 2010, pp. 287–303.

[26] R. M. Woodward, B. E. Cole, V. P. Wallace, R. J. Pye, D. D. Arnone, E. H. Linfield, and M. Pepper, "Terahertz pulse imaging in reflection geometry of human skin cancer and skin tissue," *Physics in Medicine and Biology*, vol. 47, no. 21, pp. 3853–3863, Oct. 2002.

[27] J. R. Knab, J. Chen, S. Ye, Y. He, and A. G. Markelz, "Protein conformational dynamics measured with terahertz time domain spectroscopy," in *2006 Joint 31st International Conference on Infrared Millimeter Waves and 14th International Conference on Teraherz Electronics*, Sep. 2006, pp. 183–183.

[28] A. G. Markelz, J. R. Knab, J. Y. Chen, and Y. He, "Protein dynamical transition in terahertz dielectric response," *Chemical Physics Letters*, vol. 442, no. 4-6, pp. 413–417, Jul. 2007.

[29] J. R. Knab, J. Chen, Y. He, and A. G. Markelz, "Terahertz measurements of protein relaxational dynamics," *Proceedings of the IEEE*, vol. 95, no. 8, pp. 1605–1610, Aug. 2007.

[30] B. Born, S. J. Kim, S. Ebbinghaus, M. Gruebele, and M. Havenith, "The terahertz dance of water with the proteins: the effect of protein flexibility on the dynamical hydration shell of ubiquitin," *Faraday Discuss.*, vol. 141, pp. 161–173, 2009.

[31] K. B. Reed, J. D. Brewer, C. M. Lohse, K. E. Bringe, C. N. Pruitt, and L. E. Gibson, "Increasing incidence of melanoma among young adults: an epidemiological study in olmsted county, minnesota." *Mayo Clinic proceedings*, vol. 87, pp. 328–334, Apr. 2012.

[32] M. Cristofolini, S. Boi, D. Cattoni, M. C. Sicher, A. Decarli, and R. Micciolo, "A 10-year follow-up study of subjects recruited in a health campaign for the early diagnosis of cutaneous melanoma: Suggestions for the screening timetable," *Dermatology*, vol. 231, no. 4, pp. 345–352, 2015.

[33] C. E. M. Griffiths, J. Barker, T. Bleiker, R. Chalmers, and D. Creamer, Eds., *Rook's Textbook of Dermatology*. Wiley John + Sons, Jul. 2016.

[34] K. A. Young, J. A. Wise, P. DeSaix, D. H. Kruse, B. Poe, E. Johnson, J. E. Johnson, O. Korol, J. G. Betts, and M. Womble, *Anatomy & Physiology*. OpenStax College, 2013.

[35] P. A. J. Kolarsick, M. A. Kolarsick, and C. Goodwin, "Anatomy and physiology of the skin," *Journal of the Dermatology Nurses' Association*, vol. 3, no. 4, pp. 203–213, Jul. 2011.

[36] T. P. Habif, *Clinical Dermatology*. Elsevier LTD, Oxford, 2015, vol. 16.

[37] B. Alberts, D. Bray, and J. Lewis, *Molecular Biology of the Cell*. Taylor & Francis, 2002.

[38] M. Kerscher, *Dermatokosmetik (German Edition)*. Steinkopff-Verlag Darmstadt, 2004.

[39] P. B. Janetta Bensouilah, *Aromadermatology*. Taylor & Francis Ltd, Oct. 2006.

[40] R. Schmidt, F. Lang, and M. Heckmann, *Physiologie des Menschen: Mit Pathophysiologie*, ser. Springer-Lehrbuch. Springer Berlin Heidelberg, 2011.

[41] K. Qian, T. Jiang, M. Wang, X. Yang, and J. Zhang, *Feline Soft Tissue and General Surgery*. Saunders Ltd., 2013, vol. 27.

[42] M. Hejmadi, *Introduction to Cancer Biology*. Ventus Publishing, 2009.

[43] C. S. M. Wong, "Basal cell carcinoma," *BMJ*, vol. 327, no. 7418, pp. 794–798, Oct. 2003.

[44] J. T. Lear, B. B. Tan, A. G. Smith, W. Bowers, P. W. Jones, A. H. Heagerty, R. C. Strange, and A. A. Fryer, "Risk factors for basal cell carcinoma in the uk: case-control study in 806 patients." *Journal of the Royal Society of Medicine*, vol. 90, pp. 371–374, Jul. 1997.

[45] A. Sánchez-Danés, E. Hannezo, J.-C. Larsimont, M. Liagre, K. K. Youssef, B. D. Simons, and C. Blanpain, "Defining the clonal dynamics leading to mouse skin tumour initiation," *Nature*, vol. 536, no. 7616, pp. 298–303, Aug. 2016.

[46] M. L. Ramsey and L. Sewell, "Basal cell carcinoma," *Medicine*, pp. 1–10, 2004.

[47] R. A. Schwartz, "Squamous cell carcinoma," in *Skin Cancer*. Blackwell Publishing Ltd, 2008, pp. 47–65.

[48] T. J. Minton, "Contemporary mohs surgery applications," *Current Opinion in Otolaryngology & Head and Neck Surgery*, vol. 16, no. 4, pp. 376–380, Aug. 2008.

[49] D. C. Whiteman, W. J. Pavan, and B. C. Bastian, "The melanomas: a synthesis of epidemiological, clinical, histopathological, genetic, and biological aspects, supporting distinct subtypes, causal pathways, and cells of origin." *Pigment cell & melanoma research*, vol. 24, pp. 879–897, Oct. 2011.

[50] C. Garbe, *Management des Melanoms*. Springer Berlin Heidelberg, Aug. 2006.

[51] C. Hasney, R. B. Butcher, and R. G. Amedee, "Malignant melanoma of the head and neck: a brief review of pathophysiology, current staging, and management." *The Ochsner journal*, vol. 8, pp. 181–185, 2008.

[52] D. Guerry, M. Synnestvedt, D. E. Elder, and D. Schultz, "Lessons from tumor progression: the invasive radial growth phase of melanoma is common, incapable of metastasis, and indolent." *The Journal of investigative dermatology*, vol. 100, pp. 342S–345S, Mar. 1993.

[53] L. Hershkovitz, J. Schachter, A. J. Treves, and M. J. Besser, "Focus on adoptive t cell transfer trials in melanoma," *Clinical and Developmental Immunology*, vol. 2010, pp. 1–11, 2010.

[54] A. Spatz, P. A. Gimotty, M. G. Cook, J. J. van den Oord, N. Desai, A. M. Eggermont, U. Keilholz, D. J. Ruiter, and M. C. Mihm, "Protective effect of a brisk tumor infiltrating lymphocyte infiltrate in melanoma: An eortc melanoma group study," *Journal of Clinical Oncology*, vol. 25, no. 18_suppl, pp. 8519–8519, 2007.

[55] F. S. Hodi, "Well-defined melanoma antigens as progression markers for melanoma: insights into differential expression and host response based on stage." *Clinical cancer research : an official journal of the American Association for Cancer Research*, vol. 12, pp. 673–678, Feb. 2006.

[56] F. de Braud, D. Khayat, B. B. Kroon, R. Valdagni, P. Bruzzi, and N. Cascinelli, "Malignant melanoma," *Critical Reviews in Oncology/Hematology*, vol. 47, no. 1, pp. 35–63, Jul. 2003.

[57] J. Kasprzak and Y. Xu, "Diagnosis and management of lentigo maligna: a review," *Drugs in Context*, vol. 4, pp. 1–16, May 2015.

[58] A. Breslow, "Thickness, cross-sectional areas and depth of invasion in the prognosis of cutaneous melanoma." *Annals of surgery*, vol. 172, pp. 902–908, Nov. 1970.

[59] H. Tsao, J. M. Olazagasti, K. M. Cordoro, J. D. Brewer, S. C. Taylor, J. S. Bordeaux, M.-M. Chren, A. J. Sober, C. Tegeler, R. Bhushan, and W. S. Begolka, "Early detection of melanoma: Reviewing the ABCDEs," *Journal of the American Academy of Dermatology*, vol. 72, no. 4, pp. 717–723, Apr. 2015.

[60] W. H. Clark, L. From, E. A. Bernardino, and M. C. Mihm, "The histogenesis and biologic behavior of primary human malignant melanomas of the skin." *Cancer research*, vol. 29, pp. 705–727, Mar. 1969.

[61] I. Zalaudek, G. Argenziano, H. Soyer, R. Corona, F. Sera, A. Blum, R. Braun, H. Cabo, G. Ferrara, A. Kopf, D. Langford, S. Menzies, G. Pellacani, K. Peris, and S. S. and, "Three-point checklist of dermoscopy: an open internet study," *British Journal of Dermatology*, vol. 154, no. 3, pp. 431–437, Mar. 2006.

[62] C. M. Balch, J. E. Gershenwald, S. jaw Soong, J. F. Thompson, M. B. Atkins, D. R. Byrd, A. C. Buzaid, A. J. Cochran, D. G. Coit, S. Ding, A. M. Eggermont, K. T. Flaherty, P. A. Gimotty, J. M. Kirkwood, K. M. McMasters, M. C. Mihm, D. L. Morton, M. I. Ross, A. J. Sober, and V. K. Sondak, "Final version of 2009 AJCC melanoma staging and classification," *Journal of Clinical Oncology*, vol. 27, no. 36, pp. 6199–6206, Dec. 2009.

[63] G. Annessi, R. Bono, F. Sampogna, T. Faraggiana, and D. Abeni, "Sensitivity, specificity, and diagnostic accuracy of three dermoscopic algorithmic methods in the diagnosis of doubtful melanocytic lesions," *Journal of the American Academy of Dermatology*, vol. 56, no. 5, pp. 759–767, May 2007.

[64] H. Pehamberger, A. Steiner, and K. Wolff, "In vivo epiluminescence microscopy of pigmented skin lesions. i. pattern analysis of pigmented skin lesions." *Journal of the American Academy of Dermatology*, vol. 17, pp. 571–583, Oct. 1987.

[65] R. P. Braun, H. S. Rabinovitz, M. Oliviero, A. W. Kopf, and J.-H. Saurat, "Dermoscopy of pigmented skin lesions," *Journal of the American Academy of Dermatology*, vol. 52, no. 1, pp. 109–121, Jan. 2005.

[66] D. G. Altman and J. M. Bland, "Diagnostic tests. 1: Sensitivity and specificity." *BMJ (Clinical research ed.)*, vol. 308, p. 1552, Jun. 1994.

[67] S. Goldsmith and A. Solomon, "A series of melanomas smaller than 4 mm and implications for the ABCDE rule," *Journal of the European Academy of Dermatology and Venereology*, vol. 21, no. 7, pp. 929–934, Aug. 2007.

[68] A. Bono, E. Tolomio, C. Bartoli, A. Carbone, S. Tomatis, S. Zurrida, and M. Santinami, "Metamorphosis of melanoma. trends in size and thickness of cutaneous melanoma over one decade at the istituto nazionale tumori, milan," *Tumori Journal*, vol. 94, no. 1, pp. 11–13, Jan. 2008.

[69] F. Nachbar, W. Stolz, T. Merkle, A. B. Cognetta, T. Vogt, M. Landthaler, P. Bilek, O. Braun-Falco, and G. Plewig, "The abcd rule of dermatoscopy. high prospective value in the diagnosis of doubtful melanocytic skin lesions." *Journal of the American Academy of Dermatology*, vol. 30, pp. 551–559, Apr. 1994.

[70] A. Bono, S. Tomatis, C. Bartoli, G. Tragni, G. Radaelli, A. Maurichi, and R. Marchesini, "The abcd system of melanoma detection: a spectrophotometric analysis of the asymmetry, border, color, and dimension." *Cancer*, vol. 85, pp. 72–77, Jan. 1999.

[71] P. Shetty and V. Turkar, "Article: Melanoma decision support system for dermatologist," *IJCA Proceedings on International Conference on Recent Trends in Information Technology and Computer Science (ICRTITCS-2011)*, vol. icrtitcs, no. 2, pp. 28–30, Mar. 2012.

[72] H. Lorentzen, K. Weismann, R. O. Kenet, L. Secher, and F. G. Larsen, "Comparison of dermatoscopic abcd rule and risk stratification in the diagnosis of malignant melanoma." *Acta dermato-venereologica*, vol. 80, pp. 122–126, 2000.

[73] C. A. Morton and R. M. Mackie, "Clinical accuracy of the diagnosis of cutaneous malignant melanoma." *The British journal of dermatology*, vol. 138, pp. 283–287, Feb. 1998.

[74] B. Lindelöf and M. A. Hedblad, "Accuracy in the clinical diagnosis and pattern of malignant melanoma at a dermatological clinic." *The Journal of dermatology*, vol. 21, pp. 461–464, Jul. 1994.

[75] M. F. Healsmith, J. F. Bourke, J. E. Osborne, and R. A. Graham-Brown, "An evaluation of the revised seven-point checklist for the early diagnosis of cutaneous malignant melanoma." *The British journal of dermatology*, vol. 130, pp. 48–50, Jan. 1994.

[76] H. P. Soyer, G. Argenziano, I. Zalaudek, R. Corona, F. Sera, R. Talamini, F. Barbato, A. Baroni, L. Cicale, A. D. Stefani, P. Farro, L. Rossiello,

E. Ruocco, and S. Chimenti, "Three-point checklist of dermoscopy," *Dermatology*, vol. 208, no. 1, pp. 27–31, 2004.

[77] S. W. Menzies, C. Ingvar, and W. H. McCarthy, "A sensitivity and specificity analysis of the surface microscopy features of invasive melanoma." *Melanoma research*, vol. 6, pp. 55–62, Feb. 1996.

[78] A. Katsambas, T. Lotti, C. Dessinioti, and A. D'Erme, *European Handbook of Dermatological Treatments*. Springer Berlin Heidelberg, 2015.

[79] J. M. Ashfaq Marghoob, Ralph Braun, *An Atlas of Dermoscopy, Second Edition*. Taylor & Francis Ltd, Jul. 2012.

[80] C. Dolianitis, J. Kelly, R. Wolfe, and P. Simpson, "Comparative performance of 4 dermoscopic algorithms by nonexperts for the diagnosis of melanocytic lesions," *Archives of Dermatology*, vol. 141, no. 8, Aug. 2005.

[81] J. S. Henning, J. A. Stein, J. Yeung, S. W. Dusza, A. A. Marghoob, H. S. Rabinovitz, D. Polsky, and A. W. Kopf, "CASH algorithm for dermoscopy revisited," *Archives of Dermatology*, vol. 144, no. 4, Apr. 2008.

[82] J. S. Henning, S. W. Dusza, S. Q. Wang, A. A. Marghoob, H. S. Rabinovitz, D. Polsky, and A. W. Kopf, "The CASH (color, architecture, symmetry, and homogeneity) algorithm for dermoscopy," *Journal of the American Academy of Dermatology*, vol. 56, no. 1, pp. 45–52, Jan. 2007.

[83] H. P. Soyer, G. Argenziano, V. Ruocco, and S. Chimenti, "Dermoscopy of pigmented skin lesions (part ii)." *European journal of dermatology : EJD*, vol. 11, pp. 483–498, 2001.

[84] D. S. Rigel, J. Russak, and R. Friedman, "The evolution of melanoma diagnosis: 25 years beyond the ABCDs," *CA: A Cancer Journal for Clinicians*, vol. 60, no. 5, pp. 301–316, Jul. 2010.

[85] G. Argenziano, G. Ferrara, S. Francione, K. D. Nola, A. Martino, and I. Zalaudek, "Dermoscopy—the ultimate tool for melanoma diagnosis," *Seminars in Cutaneous Medicine and Surgery*, vol. 28, no. 3, pp. 142–148, Sep. 2009.

[86] C. Garbe, K. Peris, A. Hauschild, P. Saiag, M. Middleton, L. Bastholt, J.-J. Grob, J. Malvehy, J. Newton-Bishop, A. J. Stratigos, H. Pehamberger, and A. M. Eggermont, "Diagnosis and treatment of melanoma. european consensus-based interdisciplinary guideline – update 2016," *European Journal of Cancer*, vol. 63, pp. 201–217, Aug. 2016.

[87] M. Helfand, S. M. Mahon, K. B. Eden, P. S. Frame, and C. T. Orleans, "Screening for skin cancer." *American journal of preventive medicine*, vol. 20, pp. 47–58, Apr. 2001.

[88] M. Vestergaard, P. Macaskill, P. Holt, and S. Menzies, "Dermoscopy compared with naked eye examination for the diagnosis of primary melanoma: a meta-analysis of studies performed in a clinical setting," *British Journal of Dermatology*, Jun. 2008.

[89] H. Kittler, H. Pehamberger, K. Wolff, and M. Binder, "Diagnostic accuracy of dermoscopy." *The Lancet. Oncology*, vol. 3, pp. 159–165, Mar. 2002.

[90] I. Kuzmina, I. Diebele, D. Jakovels, J. Spigulis, L. Valeine, J. Kapostinsh, and A. Berzina, "Towards noncontact skin melanoma selection by multispectral imaging analysis," *Journal of Biomedical Optics*, vol. 16, no. 6, p. 060502, 2011.

[91] M. Elbaum, A. W. Kopf, H. S. Rabinovitz, R. G. Langley, H. Kamino, M. C. Mihm, A. J. Sober, G. L. Peck, A. Bogdan, D. Gutkowicz-Krusin, M. Greenebaum, S. Keem, M. Oliviero, and S. Wang, "Automatic differentiation of melanoma from melanocytic nevi with multispectral digital dermoscopy: A feasibility study," *Journal of the American Academy of Dermatology*, vol. 44, no. 2, pp. 207–218, Feb. 2001.

[92] S. Tomatis, M. Carrara, A. Bono, C. Bartoli, M. Lualdi, G. Tragni, A. Colombo, and R. Marchesini, "Automated melanoma detection with a novel multispectral imaging system: results of a prospective study," *Physics in Medicine and Biology*, vol. 50, no. 8, pp. 1675–1687, Mar. 2005.

[93] C. Fink and H. A. Haenssle, "Non-invasive tools for the diagnosis of cutaneous melanoma," *Skin Research and Technology*, vol. 23, no. 3, pp. 261–271, Nov 2016.

[94] I. Diebele, I. Kuzmina, J. Kapostinsh, A. Derjabo, and J. Spigulis, "Melanoma-nevus differentiation by multispectral imaging," in *Clinical and Biomedical Spectroscopy and Imaging II*. OSA, 2011.

[95] B. Farina, C. Bartoli, A. Bono, A. Colombo, M. Lualdi, G. Tragni, and R. Marchesini, "Multispectral imaging approach in the diagnosis of cutaneous melanoma: potentiality and limits." *Physics in medicine and biology*, vol. 45, pp. 1243–1254, May 2000.

[96] S. Tomatis, A. Bono, C. Bartoli, M. Carrara, M. Lualdi, G. Tragni, and R. Marchesini, "Automated melanoma detection: Multispectral imaging and neural network approach for classification," *Medical Physics*, vol. 30, no. 2, pp. 212–221, Jan. 2003.

[97] M. Aboras, H. Amasha, and I. Ibraheem, "Early detection of melanoma using multispectral imaging and artificial intelligence techniques," in *American Journal of Biomedical and Life Sciences*, 2015, pp. 29–33.

[98] M. Pereyra, N. Dobigeon, H. Batatia, and J. Tourneret, "Segmentation of skin lesions in 2-d and 3-d ultrasound images using a spatially coherent generalized rayleigh mixture model," *IEEE Transactions on Medical Imaging*, vol. 31, no. 8, pp. 1509–1520, Aug. 2012.

[99] N. Lassau, A. Spatz, M. F. Avril, A. Tardivon, A. Margulis, G. Mamelle, D. Vanel, and J. Leclere, "Value of high-frequency US for preoperative assessment of skin tumors." *RadioGraphics*, vol. 17, no. 6, pp. 1559–1565, Nov. 1997.

[100] M.-H. Schmid-Wendtner and D. Dill-Müller, "Ultrasound technology in dermatology," *Seminars in Cutaneous Medicine and Surgery*, vol. 27, no. 1, pp. 44–51, Mar. 2008.

[101] L. Machet, V. Belot, M. Naouri, M. Boka, Y. Mourtada, B. Giraudeau, B. Laure, A. Perrinaud, M.-C. Machet, and L. Vaillant, "Preoperative measurement of thickness of cutaneous melanoma using high-resolution 20 MHz ultrasound imaging: A monocenter prospective study and systematic review of the literature," *Ultrasound in Medicine & Biology*, vol. 35, no. 9, pp. 1411–1420, Sep. 2009.

[102] C. Wassef and B. K. Rao, "Uses of non-invasive imaging in the diagnosis of skin cancer: an overview of the currently available modalities," *International Journal of Dermatology*, vol. 52, no. 12, pp. 1481–1489, Nov. 2013.

[103] L. Smith and S. MacNeil, "State of the art in non-invasive imaging of cutaneous melanoma," *Skin Research and Technology*, vol. 17, no. 3, pp. 257–269, Feb. 2011.

[104] V. R. Korde, G. T. Bonnema, W. Xu, C. Krishnamurthy, J. Ranger-Moore, K. Saboda, L. D. Slayton, S. J. Salasche, J. A. Warneke, D. S. Alberts, and J. K. Barton, "Using optical coherence tomography to evaluate skin sun damage and precancer," *Lasers in Surgery and Medicine*, vol. 39, no. 9, pp. 687–695, 2007.

[105] M. Mogensen, T. M. oergensen, B. M. Nürnberg, H. A. Morsy, J. B. Thomsen, L. Thrane, and G. B. E. Jemec, "Assessment of optical coherence tomography imaging in the diagnosis of non-melanoma skin cancer and benign lesions versus normal skin," *Dermatologic Surgery*, vol. 35, no. 6, pp. 965–972, Jun. 2009.

[106] J. Welzel, "Optical coherence tomography in dermatology: a review." *Skin research and technology : official journal of International Society for Bioengineering and the Skin (ISBS) [and] International Society for Digital Imaging of Skin (ISDIS) [and] International Society for Skin Imaging (ISSI)*, vol. 7, pp. 1–9, Feb. 2001.

[107] T. Gambichler, G. Moussa, M. Sand, D. Sand, P. Altmeyer, and K. Hoffmann, "Applications of optical coherence tomography in dermatology," *Journal of Dermatological Science*, vol. 40, no. 2, pp. 85–94, Nov. 2005.

[108] V. de Giorgi, M. Stante, D. Massi, L. Mavilia, P. Cappugi, and P. Carli, "Possible histopathologic correlates of dermoscopic features in pigmented melanocytic lesions identified by means of optical coherence tomography," *Experimental Dermatology*, vol. 14, no. 1, pp. 56–59, Jan. 2005.

[109] Y.-Q. Xiong, Y. Mo, Y.-Q. Wen, M.-J. Cheng, S.-T. Huo, X.-J. Chen, and Q. Chen, "Optical coherence tomography for the diagnosis of malignant skin tumors: a meta-analysis," *Journal of Biomedical Optics*, vol. 23, no. 02, p. 1, Feb.b 2018.

[110] A. Rajabi-Estarabadi, J. M. Bittar, C. Zheng, V. Nascimento, I. Camacho, L. G. Feun, M. Nasiriavanaki, M. Kunz, and K. Nouri, "Optical coherence tomography imaging of melanoma skin cancer," *Lasers in Medical Science*, vol. 34, no. 2, pp. 411–420, Dec. 2018.

[111] Z. Turani, E. Fatemizadeh, T. Blumetti, S. Daveluy, A. F. Moraes, W. Chen, D. Mehregan, P. E. Andersen, and M. Nasiriavanaki, "Optical radiomic signatures derived from OCT images to improve identification of melanoma," in *Optical Coherence Imaging Techniques and Imaging in Scattering Media III*, S. A. Boppart, M. Wojtkowski, and W.-Y. Oh, Eds. SPIE, Jul. 2019.

[112] L. M. McIntosh, M. Jackson, H. H. Mantsch, J. R. Mansfield, A. Crowson, and J. W. Toole, "Near-infrared spectroscopy for dermatological applications," *Vibrational Spectroscopy*, vol. 28, no. 1, pp. 53–58, Feb. 2002.

[113] N. Wald and E. Goormaghtigh, "Infrared imaging of primary melanomas reveals hints of regional and distant metastases," *The Analyst*, vol. 140, no. 7, pp. 2144–2155, 2015.

[114] L. Rey-Barroso, F. Burgos-Fernández, X. Delpueyo, M. Ares, S. Royo, J. Malvehy, S. Puig, and M. Vilaseca, "Visible and extended near-infrared multispectral imaging for skin cancer diagnosis," *Sensors*, vol. 18, no. 5, p. 1441, May 2018.

[115] C. Herman and M. P. Cetingul, "Quantitative visualization and detection of skin cancer using dynamic thermal imaging," *Journal of Visualized Experiments*, no. 51, May 2011.

[116] J. Pawley, Ed., *Handbook of Biological Confocal Microscopy*. Springer Nature, Jun. 2006.

[117] A. Esmaeili, A. Scope, A. C. Halpern, and A. A. Marghoob, "Imaging techniques for the in vivo diagnosis of melanoma," *Seminars in Cutaneous Medicine and Surgery*, vol. 27, no. 1, pp. 2–10, Mar 2008.

[118] A. Stevenson, S. Mickan, S. Mallett, and M. Ayya, "Systematic review of diagnostic accuracy of reflectance confocal microscopy for melanoma diagnosis in patients with clinically equivocal skin lesions," *Dermatology Practical & Conceptual*, vol. 3, no. 4, Oct. 2013.

[119] A. Gerger, S. Koller, W. Weger, E. Richtig, H. Kerl, H. Samonigg, P. Krippl, and J. Smolle, "Sensitivity and specificity of confocal laser-scanning microscopy for in vivo diagnosis of malignant skin tumors," *Cancer*, vol. 107, no. 1, pp. 193–200, 2006.

[120] C. A. Charles, A. A. Marghoob, K. J. Busam, L. Clark-Loeser, and A. C. Halpern, "Melanoma or pigmented basal cell carcinoma: a clinical-pathologic correlation with dermoscopy, in vivo confocal scanning laser microscopy, and routine histology." *Skin research and technology : official journal of International Society for Bioengineering and the Skin (ISBS) [and] International Society for Digital Imaging of Skin (ISDIS) [and] International Society for Skin Imaging (ISSI)*, vol. 8, pp. 282–287, Nov. 2002.

[121] C. C. Harland, S. G. Kale, P. Jackson, P. S. Mortimer, and J. C. Bamber, "Differentiation of common benign pigmented skin lesions from melanoma by high-resolution ultrasound." *The British journal of dermatology*, vol. 143, pp. 281–289, Aug. 2000.

[122] S. Koganti, , , , T. Kotecha, and R. D. Rakhit, "Choice of intracoronary imaging: When to use intravascular ultrasound or optical coherence tomography," *Interventional Cardiology Review*, vol. 11, no. 1, p. 11, 2016.

[123] F. G. Bechara, T. Gambichler, M. Stucker, A. Orlikov, S. Rotterdam, P. Altmeyer, and K. Hoffmann, "Histomorphologic correlation with routine histology and optical coherence tomography," *Skin Research and Technology*, vol. 10, no. 3, pp. 169–173, Aug. 2004.

[124] R. M. Woodward, V. P. Wallace, R. J. Pye, B. E. Cole, D. D. Arnone, E. H. Linfield, and M. Pepper, "Terahertz pulse imaging of ex vivo basal cell carcinoma," *Journal of Investigative Dermatology*, vol. 120, no. 1, pp. 72–78, Jan. 2003.

[125] M. Rajadhyaksha, S. González, J. M. Zavislan, R. R. Anderson, and R. H. Webb, "In vivo confocal scanning laser microscopy of human skin II: Advances in instrumentation and comparison with histology11the authors have declared conflict of interest." *Journal of Investigative Dermatology*, vol. 113, no. 3, pp. 293–303, sep 1999.

[126] G. Pellacani, A. M. Cesinaro, and S. Seidenari, "Reflectance-mode confocal microscopy of pigmented skin lesions - improvement in melanoma diagnostic specificity," *Journal of the American Academy of Dermatology*, vol. 53, no. 6, pp. 979–985, Dec. 2005.

[127] L. M. McIntosh, R. Summers, M. Jackson, H. H. Mantsch, J. R. Mansfield, M. Howlett, A. N. Crowson, and J. W. Toole, "Towards non-invasive screening of skin lesions by near-infrared spectroscopy," *Journal of Investigative Dermatology*, vol. 116, no. 1, pp. 175–181, Jan. 2001.

[128] V. R. Kondepati, H. M. Heise, and J. Backhaus, "Recent applications of near-infrared spectroscopy in cancer diagnosis and therapy," *Analytical and Bioanalytical Chemistry*, vol. 390, no. 1, pp. 125–139, Oct. 2007.

[129] K. Ajito and Y. Ueno, "Thz chemical imaging for biological applications," *IEEE Transactions on Terahertz Science and Technology*, vol. 1, no. 1, pp. 293–300, Sep. 2011.

[130] B. Ferguson and X.-C. Zhang, "Materials for terahertz science and technology," *Nature materials*, vol. 1, pp. 26–33, Oct. 2002.

[131] K.-E. Peiponen, A. Zeitler, and M. Kuwata-Gonokami, Eds., *Terahertz Spectroscopy and Imaging*. Springer Berlin Heidelberg, Oct. 2012.

[132] E. Hecht, *Optics*. Pearson, 2016.

[133] R. Paschotta, *Field Guide to Laser Pulse Generation*. SPIE, Jan. 2009.

[134] Y. Huang, N. Khiabani, Y. Shen, and D. Li, "Terahertz photoconductive antenna efficiency," in *2011 International Workshop on Antenna Technology (iWAT)*. IEEE, Mar. 2011.

[135] Y.-S. Lee, "Generation and detection of broadband terahertz pulses," in *Principles of Terahertz Science and Technology*. Springer US, 20089, pp. 1–66.

[136] J. X. Xi-Cheng Zhang, *Introduction to THz Wave Photonics*. Springer-Verlag GmbH, Dec. 2009.

[137] S. L. Dexheimer, Ed., *Terahertz Spectroscopy: Principles and Applications (Optical Science and Engineering)*. CRC Press, 2007.

[138] L. Wei, L. Yu, H. Jiaoqi, H. Guorong, Z. Yang, and F. Weiling, "Application of terahertz spectroscopy in biomolecule detection," *Frontiers in Laboratory Medicine*, 2019.

[139] Y.-C. Shen, "Terahertz pulsed spectroscopy and imaging for pharmaceutical applications: A review," *International Journal of Pharmaceutics*, vol. 417, no. 1-2, pp. 48–60, Sep. 2011.

[140] R. Gente, N. Born, N. Voß, W. Sannemann, J. Léon, M. Koch, and E. Castro-Camus, "Determination of leaf water content from terahertz time-domain spectroscopic data," *Journal of Infrared, Millimeter, and Terahertz Waves*, vol. 34, no. 3-4, pp. 316–323, Mar. 2013.

[141] E. Castro-Camus, M. Palomar, and A. A. Covarrubias, "Leaf water dynamics of arabidopsis thaliana monitored in-vivo using terahertz time-domain spectroscopy," *Scientific Reports*, vol. 3, no. 1, Oct. 2013.

[142] M. Tonouchi, "Cutting-edge terahertz technology," *Nature photonics*, vol. 1, pp. 97–105, Jan. 2007.

[143] J. Johnson, T. Dorney, and D. Mittleman, "Interferometric imaging with terahertz pulses," *IEEE Journal of Selected Topics in Quantum Electronics*, vol. 7, no. 4, pp. 592–599, 2001.

[144] J. L. Johnson, T. D. Dorney, and D. M. Mittleman, "Enhanced depth resolution in terahertz imaging using phase-shift interferometry," *Applied Physics Letters*, vol. 78, no. 6, pp. 835–837, Feb. 2001.

[145] Y. Sun, M. Y. Sy, Y.-X. J. Wang, A. T. Ahuja, Y.-T. Zhang, and E. Pickwell-Macpherson, "A promising diagnostic method: Terahertz pulsed imaging and spectroscopy." *World journal of radiology*, vol. 3, pp. 55–65, Mar. 2011.

[146] E. Pickwell-MacPherson, "Advancing in vivo terahertz imaging," *SPIE Newsroom*, Feb. 2011.

[147] M. R. Grootendorst, A. J. Fitzgerald, S. G. B. de Koning, A. Santaolalla, A. Portieri, M. V. Hemelrijck, M. R. Young, J. Owen, M. Cariati, M. Pepper, V. P. Wallace, S. E. Pinder, and A. Purushotham, "Use of a handheld terahertz pulsed imaging device to differentiate benign and malignant breast tissue," *Biomedical Optics Express*, vol. 8, no. 6, p. 2932, May 2017.

[148] Y. B. Ji, E. S. Lee, S.-H. Kim, J.-H. Son, and T.-I. Jeon, "A miniaturized fiber-coupled terahertz endoscope system," *Optics Express*, vol. 17, no. 19, p. 17082, Sep. 2009.

[149] P. Doradla, K. Alavi, C. Joseph, and R. Giles, "Single-channel prototype terahertz endoscopic system," *Journal of Biomedical Optics*, vol. 19, no. 8, p. 080501, Aug. 2014.

[150] E. Pickwell-MacPherson, "Biomedical THz imaging and spectroscopy: High sensitivity is both a blessing and a curse," in *2016 41st International Conference on Infrared, Millimeter, and Terahertz waves (IRMMW-THz)*. IEEE, Sep. 2016.

[151] X. Yin, B. W. H. Ng, and D. Abbott, *Terahertz Imaging for Biomedical Applications*. Springer New York, Mar. 2012.

[152] E. Pickwell-MacPherson, "Practical considerations for in vivo thz imaging," *Terahertz Science and Technology*, vol. 3, no. 4, pp. 163–171, 2010.

[153] P. Tewari, C. P. Kealey, D. B. Bennett, N. Bajwa, K. S. Barnett, R. S. Singh, M. O. Culjat, A. Stojadinovic, W. S. Grundfest, and Z. D. Taylor, "In vivo terahertz imaging of rat skin burns." *Journal of biomedical optics*, vol. 17, p. 040503, Apr. 2012.

[154] V. P. Wallace, A. J. Fitzgerald, S. Shankar, N. Flanagan, R. Pye, J. Cluff, and D. D. Arnone, "Terahertz pulsed imaging of basal cell carcinoma ex vivo and in vivo." *The British journal of dermatology*, vol. 151, pp. 424–432, Aug. 2004.

[155] V. P. Wallace, A. J. Fitzgerald, E. Pickwell, R. J. Pye, P. F. Taday, N. Flanagan, and T. Ha, "Terahertz pulsed spectroscopy of human basal cell carcinoma." *Applied spectroscopy*, vol. 60, pp. 1127–1133, Oct. 2006.

[156] D. D. Arnone, C. M. Ciesla, A. Corchia, S. Egusa, M. Pepper, J. M. Chamberlain, C. Bezant, E. H. Linfield, R. Clothier, and N. Khammo, "Applications of terahertz (THz) technology to medical imaging," in *Terahertz Spectroscopy and Applications II*, J. M. Chamberlain, Ed. SPIE, Sep. 1999.

[157] T. Löffler, T. Bauer, K. J. Siebert, H. G. Roskos, A. Fitzgerald, and S. Czasch, "Terahertz dark-field imaging of biomedical tissue," *Opt. Express*, vol. 9, no. 12, pp. 616–621, Dec. 2001.

[158] R. M. Woodward, V. P. Wallace, D. D. Arnone, E. H. Linfield, and M. Pepper, "Terahertz pulsed imaging of skin cancer in the time and frequency domain." *Journal of biological physics*, vol. 29, pp. 257–259, Jun. 2003.

[159] E. Pickwell, B. E. Cole, A. J. Fitzgerald, V. P. Wallace, and M. Pepper, "Simulation of terahertz pulse propagation in biological systems," *Applied Physics Letters*, vol. 84, no. 12, pp. 2190–2192, Mar. 2004.

[160] B. E. Cole, R. M. Woodward, D. A. Crawley, V. P. Wallace, D. D. Arnone, and M. Pepper, "Terahertz imaging and spectroscopy of human skin in vivo," in *Commercial and Biomedical Applications of Ultrashort Pulse Lasers; Laser Plasma Generation and Diagnostics*, J. Richard F. Haglund, J. Neev, and R. F. Wood, Eds. SPIE, May 2001.

[161] E. Pickwell, B. E. Cole, A. J. Fitzgerald, M. Pepper, and V. P. Wallace, "In vivo study of human skin using pulsed terahertz radiation," *Physics in Medicine and Biology*, vol. 49, no. 9, pp. 1595–1607, Apr. 2004.

[162] E. Pickwell and V. P. Wallace, "Biomedical applications of terahertz technology," *Journal of Physics D: Applied Physics*, vol. 39, no. 17, p. R301, 2006.

[163] A. J. Fitzgerald, V. P. Wallace, M. Jimenez-Linan, L. Bobrow, R. J. Pye, A. D. Purushotham, and D. D. Arnone, "Terahertz pulsed imaging of human breast tumors," *Radiology*, vol. 239, no. 2, pp. 533–540, May 2006.

[164] P. C. Ashworth, E. Pickwell-MacPherson, E. Provenzano, S. E. Pinder, A. D. Purushotham, M. Pepper, and V. P. Wallace, "Terahertz pulsed spectroscopy of freshly excised human breast cancer." *Optics express*, vol. 17, pp. 12 444–12 454, Jul. 2009.

[165] E. Pickwell-MacPherson, A. Fitzgerald, B. E Cole, P. Taday, R. J Pye, T. Ha, M. Pepper, and V. Wallace, "Simulating the response of terahertz radiation to basal cell carcinoma using ex vivo spectroscopy measurements," *Journal of biomedical optics*, vol. 10, p. 064021, Nov. 2005.

[166] E. Berry, J. W. Handley, A. J. Fitzgerald, W. Merchant, R. D. Boyle, N. Zinov'ev, R. E. Miles, J. Chamberlain, and M. A. Smith, "Multispectral classification techniques for terahertz pulsed imaging: an example in histopathology," *Medical Engineering & Physics*, vol. 26, no. 5, pp. 423–430, Jun. 2004.

[167] Y. C. Sim, J. Y. Park, K.-M. Ahn, C. Park, and J.-H. Son, "Terahertz imaging of excised oral cancer at frozen temperature." *Biomedical optics express*, vol. 4, pp. 1413–1421, 2013.

[168] Y. C. Sim, K.-M. Ahn, J. Y. Park, C.-S. Park, and J.-H. Son, "Temperature-dependent terahertz imaging of excised oral malignant melanoma," *IEEE Journal of Biomedical and Health Informatics*, vol. 17, no. 4, pp. 779–784, Jul. 2013.

[169] H. J. Liebe, G. A. Hufford, and T. Manabe, "A model for the complex permittivity of water at frequencies below 1 THz," *International Journal of Infrared and Millimeter Waves*, vol. 12, no. 7, pp. 659–675, Jul. 1991.

[170] C. Zhang, K.-S. Lee, X.-C. Zhang, X. Wei, and Y. R. Shen, "Optical constants of ice ih crystal at terahertz frequencies," *Applied Physics Letters*, vol. 79, no. 4, pp. 491–493, Jul. 2001.

[171] Z. Vilagosh, A. Lajevardipour, and A. W. Wood, "Computational phantom study of frozen melanoma imaging at 0.45 terahertz," *Bioelectromagnetics*, vol. 40, no. 2, pp. 118–127, Jan. 2019.

[172] K. I. Zaytsev, K. G. Kudrin, V. E. Karasik, I. V. Reshetov, and S. O. Yurchenko, "In vivo terahertz spectroscopy of pigmentary skin nevi: Pilot study of non-invasive early diagnosis of dysplasia," *Applied Physics Letters*, vol. 106, no. 5, p. 053702, Feb. 2015.

[173] K. I. Zaytsev, K. G. Kudrin, I. V. Reshetov, A. A. Gavdush, N. V. Chernomyrdin, V. E. Karasik, and S. O. Yurchenko, "In vivo spectroscopy of healthy skin and pathology in terahertz frequency range," *Journal of Physics: Conference Series*, vol. 584, no. 1, p. 012023, 2015.

[174] J. Y. Park, H. J. Choi, H. Cheon, S. W. Cho, S. Lee, and J.-H. Son, "Terahertz imaging of metastatic lymph nodes using spectroscopic integration technique." *Biomedical optics express*, vol. 8, pp. 1122–1129, Feb. 2017.

[175] W. L. Chan, J. Deibel, and D. M. Mittleman, "Imaging with terahertz radiation," *Reports on Progress in Physics*, vol. 70, no. 8, pp. 1325–1379, Jul. 2007.

[176] V. Lucarini, Y. Ino, K.-E. Peiponen, and M. Kuwata-Gonokami, "Detection and correction of the misplacement error in terahertz spectroscopy by application of singly subtractive kramers-kronig relations," *Phys. Rev. B*, vol. 72, p. 125107, Sep. 2005.

[177] M. Bernier, F. Garet, J.-L. Coutaz, H. Minamide, and A. Sato, "Accurate characterization of resonant samples in the terahertz regime through a technique combining time-domain spectroscopy and kramers–kronig analysis," *IEEE Transactions on Terahertz Science and Technology*, vol. 6, no. 3, pp. 442–450, May 2016.

[178] G. P. Gallerano and S. Biedron, "Overview of terahertz radiation sources," *Proceedings of the 2004 FEL Conference*, Jan. 2004.

[179] J. F. Federici, D. Gary, B. Schulkin, F. Huang, H. Altan, R. Barat, and D. Zimdars, "Terahertz imaging using an interferometric array," *Applied Physics Letters*, vol. 83, no. 12, pp. 2477–2479, Sep. 2003.

[180] B. Ferguson and D. Abbott, "De-noising techniques for terahertz responses of biological samples," *Microelectronics Journal*, vol. 32, pp. 943–953, Apr. 2001.

[181] Y. Xiaoxia, B. Ng, B. Ferguson, and D. Abbott, "Wavelet based local tomographic image using terahertz techniques," *Digital Signal Processing*, pp. 750–763, Jul. 2009.

[182] S. Hadjiloucas, G. Walker, J. Bowen, H. Paiva, R. Galvao, and R. Dudley, "Apodisation, denoising and system identification techniques for THz transients in the wavelet domain," in *2007 Joint 32nd International Conference on Infrared and Millimeter Waves and the 15th International Conference on Terahertz Electronics*. IEEE, Sep. 2007.

[183] Y. Chen, S. Huang, and E. Pickwell-MacPherson, "Frequency-wavelet domain deconvolution for terahertz reflection imaging and spectroscopy," *Optics Express*, vol. 18, no. 2, p. 1177, Jan. 2010.

[184] U. Jacobi, M. Kaiser, R. Toll, S. Mangelsdorf, H. Audring, N. Otberg, W. Sterry, and J. Lademann, "Porcine ear skin: an in vitro model for human skin." *Skin research and technology : official journal of International Society for Bioengineering and the Skin (ISBS) [and] International Society for Digital Imaging of Skin (ISDIS) [and] International Society for Skin Imaging (ISSI)*, vol. 13, pp. 19–24, Feb. 2007.

[185] N. Sekkat, Y. Kalia, and R. Guy, "Biophysical study of porcine ear skin in vitro and its comparison to human skin in vivo," *Journal of Pharmaceutical Sciences*, vol. 91, no. 11, pp. 2376–2381, Nov. 2002.

[186] S. J. Oh, S.-H. Kim, K. Jeong, Y. Park, Y.-M. Huh, J.-H. Son, and J.-S. Suh, "Measurement depth enhancement in terahertz imaging of biological tissues," *Optics Express*, vol. 21, no. 18, p. 21299, Sep. 2013.

[187] L. H. Eadie, C. B. Reid, A. J. Fitzgerald, and V. P. Wallace, "Optimizing multi-dimensional terahertz imaging analysis for colon cancer diagnosis," *Expert Systems with Applications*, vol. 40, no. 6, pp. 2043–2050, May 2013.

[188] M.-A. Brun, F. Formanek, A. Yasuda, M. Sekine, N. Ando, and Y. Eishii, "Terahertz imaging applied to cancer diagnosis," *Physics in Medicine and Biology*, vol. 55, no. 16, pp. 4615–4623, Jul. 2010.

[189] K. J. Max Kuhn, *Applied Predictive Modeling*. Springer New York, May 2013.

[190] A. T. Azar and S. M. El-Metwally, "Decision tree classifiers for automated medical diagnosis," *Neural Computing and Applications*, vol. 23, no. 7-8, pp. 2387–2403, Oct. 2012.

[191] V. Podgorelec, P. Kokol, B. Stiglic, and I. Rozman, "Decision trees: An overview and their use in medicine," *Journal of Medical Systems*, vol. 26, no. 5, pp. 445–463, 2002.

[192] A. C. C. Coolen, R. Kuehn, and P. Sollich, *Theory of neural information processing systems*. Oxord Univeristy Press, Sep. 2005.

[193] T. D. Dorney, R. G. Baraniuk, and D. M. Mittleman, "Material parameter estimation with terahertz time-domain spectroscopy," *Journal of the Optical Society of America A*, vol. 18, no. 7, p. 1562, Jul. 2001.

[194] C. Stoik, M. Bohn, and J. Blackshire, "Nondestructive evaluation of aircraft composites using reflective terahertz time domain spectroscopy," *NDT & E International*, vol. 43, no. 2, pp. 106–115, Mar. 2010.

[195] P. U. Jepsen, U. Møller, and H. Merbold, "Investigation of aqueous alcohol and sugar solutions with reflection terahertz time-domain spectroscopy," *Optics Express*, vol. 15, no. 22, p. 14717, 2007.

[196] A. Kumar, A. Singh, D. Amrish Kumar Panwar, and H. Kim, "Terahertz imaging system for biomedical applications: Current status," *International Journal of Engineering & Technology IJET-IJENS*, vol. 13, pp. 33–39, Jan. 2013.

[197] L. Thrane, R. Jacobsen, P. U. Jepsen, and S. Keiding, "THz reflection spectroscopy of liquid water," *Chemical Physics Letters*, vol. 240, no. 4, pp. 330–333, Jun. 1995.

[198] D. S. Venables and C. A. Schmuttenmaer, "Far-infrared spectra and associated dynamics in acetonitrile–water mixtures measured with femtosecond THz pulse spectroscopy," *The Journal of Chemical Physics*, vol. 108, no. 12, pp. 4935–4944, Mar. 1998.

[199] K. I. Zaytsev, A. A. Gavdush, N. V. Chernomyrdin, and S. O. Yurchenko, "Highly accurate in vivo terahertz spectroscopy of healthy skin: Variation of refractive index and absorption coefficient along the human body," *IEEE Transactions on Terahertz Science and Technology*, vol. 5, no. 5, pp. 817–827, Sep. 2015.

[200] K. Tielrooij, D. Paparo, L. Piatkowski, H. Bakker, and M. Bonn, "Dielectric relaxation dynamics of water in model membranes probed by terahertz spectroscopy," *Biophysical Journal*, vol. 97, no. 9, pp. 2484–2492, Nov. 2009.

[201] B. C. Q. Truong, H. D. Tuan, H. H. Kha, and H. T. Nguyen, "Debye parameter extraction for characterizing interaction of terahertz radiation with human skin tissue," *IEEE Transactions on Biomedical Engineering*, vol. 60, no. 6, pp. 1528–1537, Jun. 2013.

[202] B. C. Q. Truong, H. D. Tuan, V. P. Wallace, A. J. Fitzgerald, and H. T. Nguyen, "The potential of the double debye parameters to discriminate between basal cell carcinoma and normal skin," *IEEE Transactions on Terahertz Science and Technology*, vol. 5, no. 6, pp. 990–998, Nov. 2015.